Search of X-ray activity cycles in young solar-like stars

Dissertation

der Mathematisch-Naturwissenschaftlichen Fakultät

der Eberhard Karls Universität Tübingen

zur Erlangung des Grades eines

Doktors der Naturwissenschaften

(Dr. rer. nat.)

vorgelegt von

Martina Coffaro

aus Torino (Italien)

Tübingen

2020

Gedruckt mit Genehmigung der Mathematisch-Naturwissenschaftlichen Fakultät der Eberhard Karls Universität Tübingen.

Tag der mündlichen Qualifikation:	15.10.2020
Stellvertretender Dekan:	Prof. Dr. József Fortágh
1. Berichterstatterin:	Prof. Dr. Beate Stelzer
2. Berichterstatter:	Prof. Dr. Andrea Santangelo

Search of X-ray activity cycles in young solar-like stars

Abstract

Die Erforschung der magnetischen Aktivität von sonnenähnlichen Sternen wird in der astrophysikalischen Gemeinschaft intensiv diskutiert und ist bis heute noch nicht gut verstanden. Aus bodengebundenen Langzeitbeobachtungen der Chromosphäre ist bekannt, dass $\sim$ 60% der sonnenähnlichen Hauptreihensterne magnetische Aktivitätszyklen zeigen, deren Zyklusdauern im Bereich von einigen Jahren bis zu einigen Jahrzehnten liegen. Die Untersuchung der magnetischen Aktivität der Korona im Röntgenlicht ist jedoch eine Herausforderung, da langfristige Röntgenüberwachungskampagnen für eine signifikante Anzahl von Sternen nicht durchführbar sind. Das Weltraumteleskop *XMM-Newton* konnte solche Röntgenaktivitätszyklen bislang nur für sieben Sterne bestätigen. Die Mehrheit dieser Sterne sind alt (Alter von wenigen Milliarden Jahre) und weisen lange Röntgenzyklusperioden (zwischen 8 und 12 Jahre) auf.

Ziel dieser Doktorarbeit ist es daher, folgende Fragen zu beantworten: a) Treten Röntgenzyklen nur bei alten Sternen auf? Oder zeigen auch junge sonnenähnliche Sterne Röntgenzyklen? b) Wenn es koronale Zyklen auch bei jüngeren Sternen gibt, in welchem Alter und auf welchem Aktivitätsniveau setzt der Zyklus ein? c) Gibt es einen Zusammenhang zwischen dem Alter des Sterns und den Eigenschaften des Zyklus, insbesondere der Amplitude der Zyklusvariation? Wenn ja, was ist der Grund?

Während meines Promotionsprojekts führte ich Röntgenuntersuchung bei drei jungen sonnenähnlichen Sternen durch: ι Horologii, ε Eridani und Kepler 63. ι Horologii ist der erste junge Stern (600 Mio. Jahre), bei dem ein sehr kurzer Röntgenzyklus (1, 6 Jahre) gefunden wurde. ε Eridani ist sogar noch jünger als ι Horologii (400 Mio. Jahre). Sein Röntgenaktivitätszyklus wurde in diesem Projekt zum ersten Mal gemessen und charakterisiert. Auch ε Eridani zeigt eine kurze Zyklusperiode von 2, 92 Jahren. Darüber hinaus weisen beide Sterne eine hohe Röntgenleuchtkraft und kleine Variabilitätsamplituden auf. Eine mögliche Erklärung für die geringe Variation der Röntgenleuchtkraft während des Aktivitätszyklus könnte ein Mangel an zusätzlichem Platz für magnetische Strukturen auf der Sternoberfläche sein.

Im Fall von ε Eridani habe ich die Entwicklung seines Röntgenzyklus im Hinblick auf solare magnetische Strukturen untersucht, um die oben genannte Hypothese über die kleine Amplituden während des Zyklus zu überprüfen. Ich habe eine neuartige Methode angewendet, die darauf basiert, Röntgenspektren der in der Sonnenkorona beobachteten magnetischen Strukturen so zu simulieren, als ob der Röntgensatellit *XMM-Newton* sie beobachtet hätte. Ich habe diese simulierten Spektren dann mit den Beobachtungen von ε Eridani verglichen, um zu bestimmen, wie viel Prozent der Korona des Sterns zu jedem Zeitpunkt seines Röntgenaktivitätszyklus durch magnetische Strukturen bedeckt sind. Ich fand heraus, dass während des Zyklusminimums 74% der Korona von ε Eridani magnetische Strukturen aufweist, und dass während des Maximums diese Bedeckung auf 94% ansteigt. Die hohe Röntgenhelligkeit von ε Eridani und seine kleine Variabilitätsamplitude sind somit das Ergebnis eines hohen magnetischen Füllfaktors der Korona. Höchstwahrscheinlich zeigen junge sonnenähnliche Sterne im Allgemeinen dasselbe Verhalten.

Um diese Hypothese zu überprüfen erweiterte ich meine Suche nach Röntgenaktivitätszyklen bei jungen sonnenähnlichen Sternen. Die Europäische Weltraumorganisation genehmigte mir 2018 eine Röntgenkampagne für den Stern Kepler 63 (210 Mio. Jahre). Die Beobachtungskampagne begann Anfang 2019. Kepler 63 ist jünger als ι Horologii und ε Eridani und ist damit der jüngste sonnenähnliche Stern in meiner Arbeit. Im optischen Wellenlängenbereich wurde ein Aktivitätszyklus der Photosphere mit einer Periode von 1, 27 Jahren detektiert. Durch eine Analyse der Röntgenspektren fand ich heraus, dass Kepler 63 zwar von allen Sternen mit bekannten Röntgenaktivitätszyklen die größte Röntgenleuchtkraft aufweist, jedoch war während der Überwachungskampagne keine Röntgenvariabilität messbar.

Contents

«It is not too much to hope that in the not too distant future we shall be competent to understand so simple a thing as a star»

Sir Arthur Stanley Eddington, 1926.

1 Introduction

Connecting the stellar physics to the solar physics has always been a major goal in stellar astrophysics. In particular, probing the magnetic activity in solar-like stars is under an intense debate in the astrophysical community and still not well understood.

Solar-like stars are commonly defined as stars that show similar characteristics in mass and evolutionary stage to the Sun. Thus, physically their internal structure is similar to the solar one, i.e. it is composed by an inner radiative core, where the energy produced by thermonuclear fusion is transported via radiative transfer, and an outer convective zone, where the energy transport occurs through convective cells. As defined by Cayrel de Strobel (1996), solar-like stars have spectral class of about F8V to K2V, or 0.50 to 1.00 in B-V color index [1].

The internal structure of the Sun and of solar-like stars explains how the stellar magnetic field can be maintained. As a matter of fact, the magnetic field is driven by a cyclic magnetic dynamo ($\alpha - \Omega$ dynamo) operating in the interior of the Sun and whose basic ingredients are the turbulent motions in the convective zone and the differential rotation of the Sun. During a cycle of the dynamo, the

[1] The color index is a quantity that expresses the color of a star and, consequentially, its temperature. It is computed as the difference between two magnitudes at different wavelengths. Historically, the most widely used were the blue (B; 4420 Å) and the visual (V; 5400 Å) that are computed to form the B-V color.

configuration of the magnetic field changes from a poloidal configuration to a toroidal one, and back again to poloidal. Let imagine thus to follow this change of the magnetic field configuration and to have at the beginning a poloidal configuration of the magnetic field. Because of the differential rotation of the star, these lines start to be twisted (Ω effect), reaching a toroidal configuration that emerges in the surface because of the magnetic buoyancy in the convective zone. The poloidal configuration is then restored by helical turbulent motions, that rotate because of the Coriolis force and in turn twist the toroidal field (a effect)[2]. The time needed to go from the poloidal configuration to the toroidal one, and back to the poloidal, is the length of the stellar magnetic cycle and commonly known as *activity cycle*.

A consequence of the twisting of the magnetic lines combined with the buoyancy is the formation of small-scale magnetic structures on the surface of the star, that thus are linked to the activity cycle of a star. These magnetic structures are responsible for variations that are referred to as *stellar activity*. The magnetic structures pervade the whole stellar atmosphere and consequentially associated emissions are manifest throughout the stellar atmosphere. In solar-like stars the atmosphere is composed of three layers: the photosphere, the chromosphere and the corona. In Figure 1.0.1, the temperature structure of the solar atmosphere is shown as function of the height. The plot shows also the spectral lines that originate in the atmosphere in different layers.

The photosphere is the inner layer, characterized by a negative gradient of temperature that goes from $\sim$ 6000 K to $\sim$ 4500 K. At $\sim$ 500 km there is an inversion in the temperature gradient and this denotes the beginning of the next atmospheric layer, i.e. the chromosphere. Here, the temperature starts to increase through non-radiative processes to a maximum of around 10000 K . At $\sim$ 2000 km the temperature rapidly increases and this region, called transition region, denotes the upper boundary of the chromosphere. The next and outermost layer is the corona, where the temperature reaches values $> 10^6$ K. The reason for the changes of the temperature in the outer atmosphere is not entirely understood. It is believed that the cause is the non-radiative heating process due to the magnetic field (see Narain et al. (1996) for a review of all theories on heating processes in the stellar atmosphere given in the last century). Because of the presence of the temperature gradient, different emission processes take place, making the stellar atmosphere a multi-wavelength emitter, from the optical emission in the photosphere and the UV emission in the chromosphere to the X-rays in the corona. Thus,

[2]The dynamo theory explains well the changes from the poloidal configuration to the toroidal one, i.e. the Ω effect. However, the restoration of the magnetic field lines in the poloidal configuration is still debated. The a-effect is the most plausible explanation given so far and supported by numerical simulations and thus it remains the favoured magnetic field generation mechanism. For a more detailed discussion on dynamo models I refer the reader to the review of Charbonneau (2020).

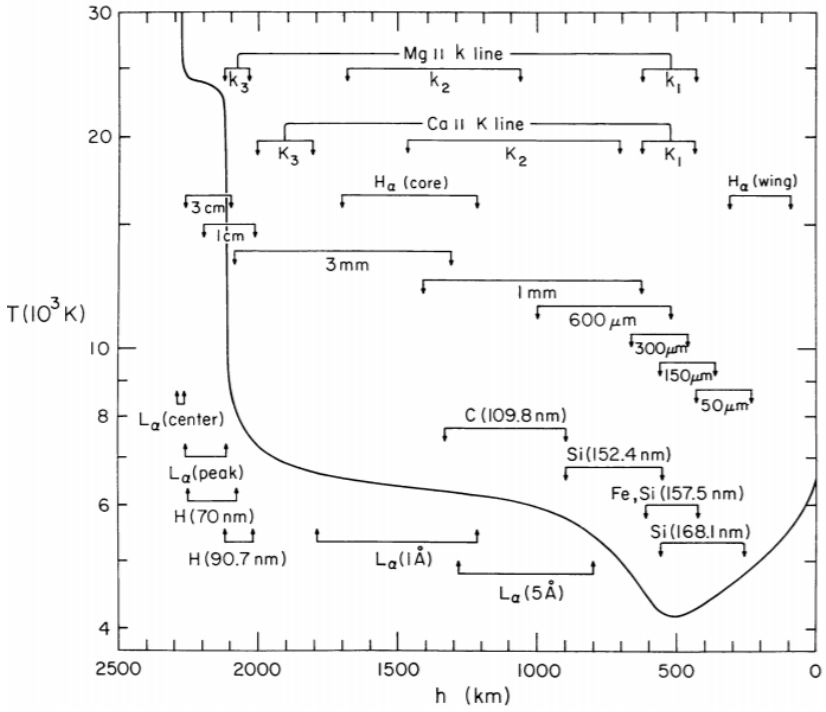

Figure 1.0.1: Gradient of the temperature in the solar atmosphere as function of the height. The spectral lines that form at different heights of the atmosphere are also shown (Vernazza et al., 1981).

we can monitor the activity of stars in different wavebands of the electromagnetic spectrum.

In the photosphere of the Sun its magnetic surface structures, the so-called sunspots, are directly observed and spatially resolved, while in other stars we can indirectly identify these structures (starspots) through photometry. During the activity cycle of the Sun and of solar-like stars, a maximum and a minimum of the cycle are identified as a maximum and minimum coverage of these spots on the surface. Thus, by monitoring the evolution of the spots on the surface of the Sun and of other stars, we obtain the length of the activity cycle.

When a starspot is present on the stellar surface, in the chromosphere an emission of the cores of Ca II H&K lines is seen in the spectra. Therefore, during the magnetic cycle, the flux of these lines is periodically varying, with a period length corresponding to the activity cycle seen in the photosphere.

Several studies of these indicators have shown that $\sim$ 60% of the main-sequence solar-like stars show Ca II H&K activity cycles, with a cycle period lasting from a couple of years to few decades. Finding the X-ray counterparts of the chromospheric cycles is challenging. The difficulties for probing the X-ray activity cycles are several, but the common denominator is the feasibility of such X-ray monitoring because of the length of the magnetic activity cycles. The stars with confirmed X-ray activity

cycles, besides the Sun, are up to date seven: α Cen A and B, 61 Cyg A and B, HD 81809, ι Horologii and ε Eridani. These stars can be divided into two groups according to their age and their activity level. The first group includes α Cen A and B, 61 Cyg A and B and HD 81809: they are stars with age of $\sim 3-6$ Gyr, with an X-ray activity cycle lasting $\sim 7-15$ yr and X-ray luminosity comparable to the Sun, i.e. $logL_X\,[\mathrm{erg/s}] \sim 26.5-28.5$. In the second group there are the stars ι Horologii and ε Eridani: they are young stars, with age of $400-600$ Myr, with short X-ray period cycles of $1.6-2.9$ yr and high X-ray luminosity $logL_X\,[\mathrm{erg/s}] > 28.5$.

This PhD project was dedicated to the characterization of the X-ray activity cycles of these latter stars, i.e. young solar-like stars that might be proxies for our Sun at its early evolutionary stages. In particular the X-ray cycle of ε Eridani, the youngest star that up to date is known to show a coronal cycle, has been discovered within this project.

Before this PhD project, three major questions on X-ray activity cycles were still unanswered:

a) Are X-ray cycles frequent only among old stars? Or do young solar-like stars also commonly exhibit X-ray activity cycles?

b) If it is common to find coronal cycles also in younger stars, at which age and at which activity level does the cycle set in?

c) Is there a relation between stellar age and cycle properties, such as the amplitude of the cycle variation, and if so, what is the reason?

In this thesis I want to guide the reader through the study of three young solar-like stars (ε Eridani, ι Horologii and Kepler 63) that allowed me to provide first answers to these questions.

Chapter 2 and chapter 3 present a review of our knowledge about stellar activity cycles. In particular, first I summarize how the activity cycles can be detected and characterized in the photosphere and in the chromosphere of the Sun and of other solar-like stars (chapter 2). Then, I discuss how the first X-ray coronal cycles were discovered during the last decade (chapter 3).

After this overview on stellar activity cycles, I introduce the X-ray satellite that I used to observe my targets in these last three years, i.e. the X-ray satellite *XMM-Newton* (chapter 4). In chapter 5 and chapter 6 I present the young solar-like stars ι Horologii and ε Eridani that were observed and analysed during my PhD project. In particular with great details I discuss my discovery of the X-ray activity cycle of ε Eridani (chapter 6).

In chapter 7 I present a novel method that allowed me to describe the activity cycle of ε Eridani in terms of magnetic structures similar to those observed on the Sun. The method consists in simulating

the spectra of the magnetic structures observed in the corona of the Sun as if the X-ray satellite *XMM-Newton* observed them. By then comparing the simulated spectra with the observations of ε Eridani, I was able to associate a percentage of magnetic structures covering the corona of ε Eridani during each state of its X-ray cycle. This method was particularly helpful for answering the question c laid out above.

In chapter 8 the X-ray monitoring campaign on the young solar-type star Kepler 63 is presented, that was recently carried out (between 2019 and early 2020). The *XMM-Newton* observations of this star were granted in late 2018 by the European Space Agency with the highest observational priority (PI: Martina Coffaro). The aim of this campaign was to search for an X-ray activity cycle in a star even younger than ε Eridani (question b above).

Finally, in chapter 9 I conclude this thesis with an outline of further studies that can be carried out in the future for enhancing our knowledge on X-ray activity cycles in young solar-like stars.

Part I

The state of the art

2

Stellar activity cycles in the photosphere and the chromosphere

Contents

The study of magnetic activity cycles starts with the Sun. In fact, the interpretation of stellar activity often relies on the so-called *solar-stellar connection*, i.e. explaining the variable phenomena observed in late-type stars using analogous solar phenomena and their interpretation as a reference. In this thesis, in particular, I use the Sun as a template to study magnetic structures on young solar-like stars, and their evolution in time caused by a dynamo cycle. The Sun is the key to understand the stellar dynamics because it is the nearest star that can be studied and, thus, the information collected from its observations are much more detailed.

For a comprehensive view it is useful here to introduce and briefly explain the main properties of the solar activity cycle and to discuss how during the last centuries the astrophysicists tried actively to link the stellar physics to the solar one.

This summary on the solar and stellar activity cycles starts with the photospheric manifestations of cyclic behaviour (section 2.1). Then, the characterization of the activity cycle in the chromosphere is discussed, highlighting in particular the main findings of the Mount Wilson Project, also known as the *HK project*, which represents up to date the most complete catalogue of solar-like active stars (section 2.2).

2.1 Sunspots and photospheric activity cycles

Probing the magnetic activity in the photosphere of the Sun and stars can be done by monitoring the so-called *sunspots* and *starspots*. A sunspot is a region on the visible solar surface darker than the surrounding photosphere. Its darkness is due to reduced temperature caused by a concentration of magnetic flux that inhibits the convective transfer of heat from the interior. However, when sunspots were observed for the first time, their magnetic nature and their cyclic behaviour on the solar surface were not immediately understood.

The first recorded proofs of sunspots date back to the ancient Greece around 325 BC when these black dots were observed with the naked eye [1]. However, the first people who directly observed the sunspots and tried to find an explanation of their existence where Galileo Galilei in Padua and Christoph Scheiner in Ingolstadt in the 17th century thanks to the invention of optical telescopes. From their observations, lasting a couple of years, they noticed that the spots rotated with the Sun and that they always were located near the solar equator. They then wrongly defined them as clouds above the Sun.

However, the cyclic evolution of the sunspots was only discovered a couple of centuries later by the

[1] Sunspots are mentioned for the first time in the manuscript "De Signis", that contains a collection of observational weather signs, and it is ascribed to the Greek philosopher Theophrastus (371-287 BC).

astronomer Heinrich Schwabe. He systematically observed the Sun for 43 years and in 1843 came to the conclusion that the number of sunspots had a possible 10-year periodicity.

After the discovery of Schwabe, it was natural to wonder if it was possible to trace back in time the sunspot cycle. Thus, in 1848 the astronomer Rudolf Wolf introduced the *relative sunspot number* $\mathcal{R}$ (also known as the *Zurich number*), defined as $\mathcal{R} = k(10g+f)$, where g is the number of groups of spots seen on the surface, f is the number of single detected spots and k is a correction factor with different value for each set of observations. By computing this value, Wolf was able to trace the sunspot cycle back to the beginning of the 17th century, henceforth labelled *Cycle 1*. In Figure 2.1.1, the sunspot cycle, starting from the 1600s by applying the *relative sunspot number* and updated until the 2000s, is shown. Here, the periodicity of the sunspot number is clearly seen, having a period length on average equal to 11 years. It is also evident that between 1645 and 1715 the number of the sunspots was at a

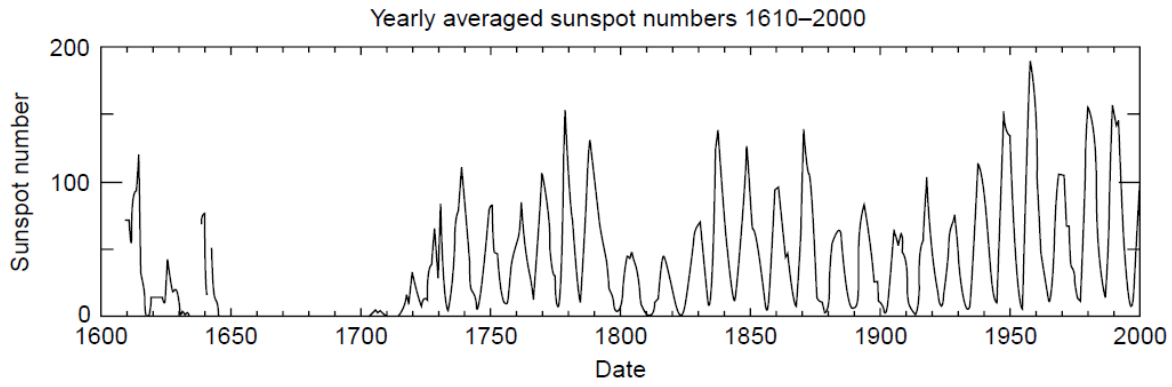

Figure 2.1.1: Cyclic sunspots activity from 1610 to 2000 (Thomas et al., 2008).

historical minimum, called *Maunder minimum* after the two astronomers Annie and Edward Maunder. The minimum is not an artefact of the *relative sunspot number* calculation nor it is due to a lack of observations during that period: there is for example a well reported observing campaign of the Sun, carried at the Observatory of Paris between 1610s and 1690s, during which no more than 50 sunspots were seen in total (see Usoskin et al. (2015) for a well reported review of the historical observations of the Sun). It is not entirely clear what could have happened on the Sun at that time, but surely this minimum corresponds to the lowest activity level of our star in its recent history.

Thus, in the middle 1800s, it was known that the Sun has a cyclic behaviour with a period of 11 years but the magnetic origin of this periodicity had not yet been discovered. Only in 1908, George Hale proved the presence of a magnetic field in the Sun. By looking at the sunspot images, shown in Figure 2.1.2, Hale (1908) considered the possibility of a magnetic field since the picture was resembling

the lines of a magnetic field force. Moreover, some years before, Zeeman had discovered the so-called *Zeeman effect*: for a laboratory light source which emits a line spectrum in a laboratory magnetic field, the spectral lines split into several components and the separation of the lines increases as the magnetic field strength increases. Thus, Hale analysed several spectra acquired from the sunspots, detecting the splitting of some magnetically sensitive lines, such as the iron lines at 6213.14Å ,6301.72Å and 6337.05 Å , and calculating a magnetic field strength of $\sim$ 3000 G. It was the first time that an extraterrestrial magnetic field was detected.

Moreover, from the observations and the spectral analysis, he also discovered what is now known as *Hale's polarity laws*:

- Sunspots generally appear in pairs of opposite magnetic polarity;
- The polarity of the spot in the direction of the Sun's rotation is the same for all pairs in the same hemisphere, but opposite in the other hemisphere;
- The groups of sunspot in each hemisphere reverse their polarity in the next cycle, and thus the magnetic cycle has a period twice that of the sunspot cycle, i.e. 22 years.

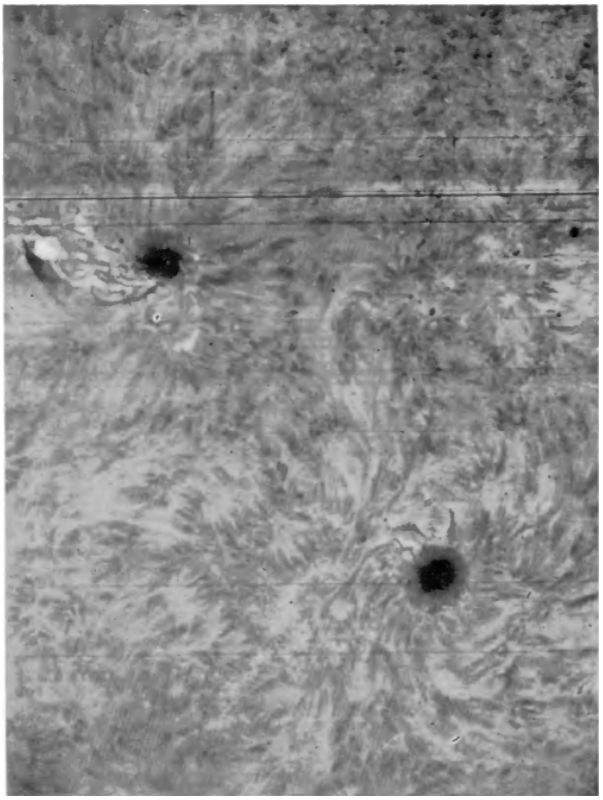

Figure 2.1.2: Images of sunspots acquired by Hale (1908).

The Zeeman effect became thus the tool to directly measure the magnetic field and some years later it was applied to detect the first stellar magnetic field in the star HD 215441 by Babcock (1960).

When we want to characterize the activity cycle of another star, we have the limitation that, differently to the Sun, it is not possible to spatially resolve these structures on the stellar surface and thus we can not trace their evolution. However, different techniques can be applied in order to overcome these problems and gain indirect information on starspots.

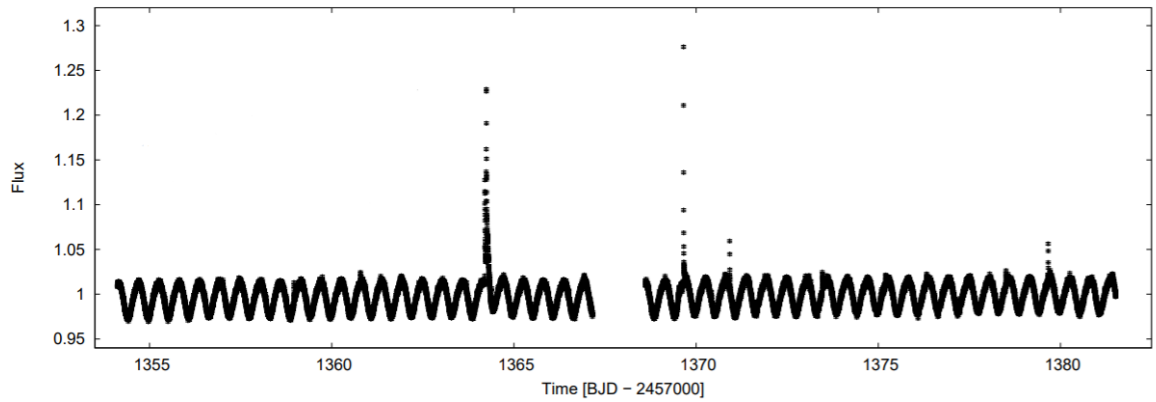

Figure 2.1.3: Example of lightcurve of a M2 dwarf seen by *TESS*. The modulation due to the starspots is very well visible in the lightcurve as a sinusoidal signal. The peaks in the lightcurve are flares occurring in the stellar surface. The plot is adapted from Raetz et al. (2020).

One way of characterizing an activity cycle in the stellar photosphere, i.e. in the optical waveband, is through photometry. As a matter of fact, especially with the advent of space-based observatories, like the NASA satellites *Kepler* and *TESS*[2], it is possible to monitor stellar variability with high precision. When monitoring the brightness of a star, a variability in the lightcurve is detected if starspots are present. In particular, being the spots darker and cooler than the average stellar surface, a decrease of the flux is registered. As the starspots rotate on the surface, they produce a periodic modulation in the lightcurve. In Figure 2.1.3, an example of a starspot modulated lightcurve observed by *TESS* is shown. During that observation, also stellar flares were observed and they correspond to the peaks in the lightcurve. Flaring events are defined as a sudden increase of the surface brightness of a star that last from some seconds to even hours. They result from a sudden release of energy stored in the magnetic field.

Different techniques are in use to model the periodic variability in the lightcurves in order to gain information on the position and shape of the detected starspots. However, the analysis of starspots is not the topic of this PhD project and I refer the reader to the review of Berdyugina (2005) and to section 8.1 where I will describe one method to characterize the starspots and, therefore, the magnetic cycle of the star Kepler 63 through photometry.

[2]*TESS* (Transiting Exoplanet Survey Satellite) is a NASA satellite designed for exoplanets using the transit method. IT was launched in 2018 and it is currently operating.

2.2 Chromospheric activity cycles and the *HK project*

In the upper region of the atmosphere, i.e. in the chromosphere, the H&K lines of Ca II are visible in the solar spectrum at the wavelengths 3968 Å and 3933 Å respectively. In particular, these lines show broad absorption profiles. When an area of concentrated magnetic field is present on the surface, i.e. a starspot, this translates in an emission of the cores of the Ca II H&K lines.

Thus, measurements of flux variation of the Ca II H&K lines represent a good proxy for investigating magnetic activity cycles in stars. Furthermore, this method overcomes the problem of not being able to spatially resolve the magnetic structures on the surface of stars, since we only need to carry out spectroscopic analysis.

As investigation of magnetic activity cycles in the chromosphere, the most fruitful project was the so-called *HK project*, started by Olin Wilson at the Mount Wilson Observatory (MWO) in 1966. The project was dedicated to the long-term monitoring of the Ca II H&K lines in high resolution spectra of more than 2000 solar-like stars and lasted until 2003.

The highlights of this long monitoring are reported by Baliunas et al. (1995) and it still represents the most complete catalogue of chromospheric activity cycles of solar-like stars. The *HK project* led to the definition of the MWO "activity index", S_{MWO}, a dimensionless quantity dependent on the stellar index color:

$$S_{\mathrm{MWO}} = \alpha \frac{H+K}{V+R} \tag{2.1}$$

where H and K are the fluxes in two passbands (1 Å narrow) centred on each line of the Ca II doublets and V and R are the fluxes in two 20 Å wide passbands centred on 3900 Å (red) and 4000 Å (violet), used to estimate a continuum in the spectrum. In Figure 2.2.1 an example of the Ca II H&K lines is shown, where with dotted lines the 1 Å passband for the H and K lines are shown as well as the passbands used for the continuum. The coefficient α is an instrumental calibration factor.

For the complete sample of stars monitored at the MWO, Baliunas et al. (1995) found that:

a) 60% of the solar-like stars show a periodic, or quasi-periodic, variation in the S_{MWO}-index and the cycles last from some years up to $\sim$ 30 years;

b) 25% are variable but do not show an obvious periodicity;

c) 15% do not show any significant variability and they might be in a sort of Maunder Minimum.

An example of S_{MWO}-index lightcurves for each of these three categories is shown in Figure 2.2.2.

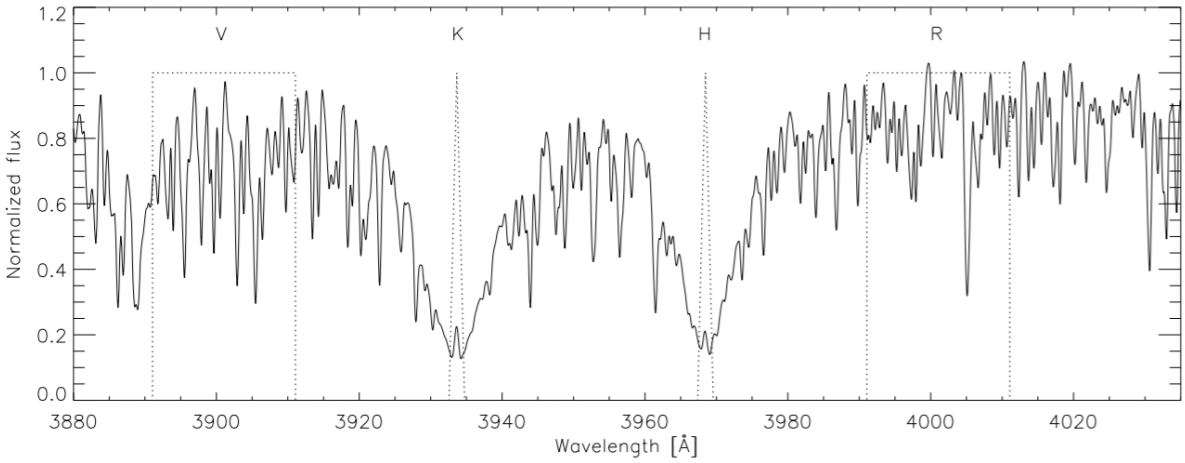

Figure 2.2.1: Ca II H and K lines of the star HD 48676 (Schröder et al., 2009) with filter profiles used for the measurements of the S_{MWO}-index overlaid.

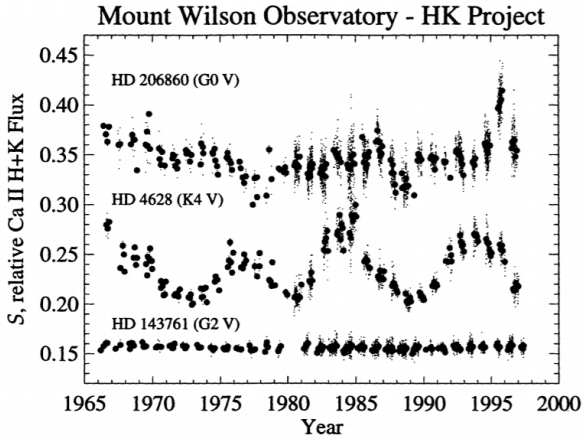

Figure 2.2.2: Examples of S_{MWO}-index lightcurves of three Mount Wilson stars: on the top an example of a variable target, on the middle an example of a (significant) cyclic variability and on the bottom an example of a non-variable target (Baliunas et al., 1998).

Since the mechanism that drives the magnetic dynamo in stars involves the stellar differential rotation, different studies were dedicated on investigating a correlation between the rotational periods and activity cycle periods.

As a star ages, its rotation slows down. The rotational evolution of solar-like stars was first studied by Skumanich (1972) who, from the analysis of young stars (with age 100 − 600 Myr), showed that the rotational velocity decreases with the age following a power law at $t^{-0.5}$, where t is the stellar age [3]. Thus, it is expected that older stars show longer periods of their activity cycles. An investigation of the rotation-activity correlation was carried out by many authors, such as Brandenburg et al. (1998), Saar et al. (1999), Böhm-Vitense (2007), and Brandenburg et al. (2017).

In the most recent study of this relation, Brandenburg et al. (2017) analysed a sample of 35 stars, composed by solar-like stars of spectral class from F to K. In the sample 27 stars were part of the *HK project* and already analysed by Böhm-Vitense (2007). In Figure 2.2.3 I show the plot of the activity period ($P_{\rm cyc}$) in years as function of the rotational period ($P_{\rm rot}$) in days, that I produced with the data from Böhm-Vitense (2007) and Brandenburg et al. (2017).

From this plot, the first evidence is that the sample is divided into two main branches, identified as the *active* branch and the *inactive* branch. These two branches were already identified in the early studies on the rotation-activity relation and they are confirmed in subsequent works. In Figure 2.2.3 the stars belonging to the inactive branch are plotted with black dots, while the stars on the active branch are plotted with crosses. For some of the stars in this sample two cycle periods are identified, residing thus in both branches. These stars are plotted with grey squares and the two periods of each star are connected with grey dashed lines. The Sun is plotted with the orange symbol and lays between the two branches (see below for an explanation).

In each sequence the cycle period is proportional to the rotational period, i.e. the ratio between $P_{\rm cyc}$ and $P_{\rm rot}$ is constant for each sequence. This ratio thus represents the number of rotations that each star undergoes before completing one activity cycle. For the inactive branch the number is $\sim$ 90 and for the active branch it is 300 − 500 (Böhm-Vitense, 2007). Thus, the stars belonging to the inactive sequence complete their activity cycle with less rotational revolutions than the stars on the active branch. Therefore, Böhm-Vitense (2007) suggested that the division into two branches is not due to dynamos of different nature, but rather the zones of the stars where the dynamo is operating may be different. In the active branch, the dynamo may operate near the stellar surface: the large number of rotations to complete the cycle suggests that those stars have a thin convective layer and

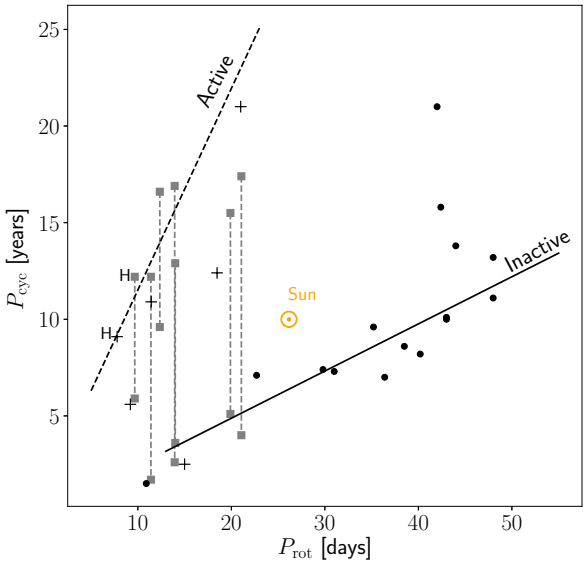

Figure 2.2.3: Period (P_{cyc}) of the chromospheric activity cycle as function of the rotational period (P_{rot}). The black dots represent the stars of the inactive branch, whereas the black crosses are the stars belonging to the active branch. The stars that show two periods, each associated with one of the branches, are plotted as grey squares. The plot was produced within this thesis and comprises the stars originally studied by Böhm-Vitense (2007) plus other targets added by Brandenburg et al. (2017).

the toroidal field needs more time to become strong enough for emerging because of the magnetic buoyancy. On the other hand, in the inactive branch the dynamo may operate at the bottom of the convective zone: in deeper layers of the convective zone it is expected that the velocity gradients are larger than at the top and thus it explains the need of few rotations for the toroidal field to emerge.

The stars laying simultaneously in both the active and the inactive branches show the coexistence of long and short period cycles, suggesting then that the stellar dynamo is working at different depth of the convective zone at different time. These stars are the youngest stars (with age < 2.3 Gyr) in the studied sample. It can be therefore hypothesised that in young stars the dynamo is still unstable and for this reason multiple cycles can be detected.

Finally, the Sun is located between the two branches and, thus, in light of the previous arguments, the dynamo may simultaneously operate at different zones. Böhm-Vitense (2007) therefore stated that the Sun might not be a good standard star for the discussion of stellar activity, and this has motivated in recent years different studies to interpret better the position of the Sun on this matter. In particular, Salabert et al. (2016) studied the chromospheric activity of several solar analogues, that are

[3]More recently this relation was confirmed by Barnes et al. (2016) who analysed older stars than the sample of Skumanich (1972).

defined as solar-like stars with a mass between 0.9 and 1.1 solar masses, chemical composition within 10% similar to the Sun, similar temperatures and luminosity. Some stars of the sample (28 in total) were chosen from the *HK project* survey and other stars (18 in total) were new solar analogues that Salabert et al. (2016) identified from *Kepler* observations.

In Figure 2.2.4, I show the results of Salabert et al. (2016). The plot shows the dependence of chromospheric activity parameter $R'_{\rm HK}$ on the rotational period. R'_{HK} is a quantity related to the flux of the Ca II lines and is equal to

$$R'_{\rm HK} = \frac{(F_{HK} - F_{\rm phot})}{\sigma T_{\rm eff}^4}, \tag{2.2}$$

where F_{HK} is the sum of the fluxes of each Ca II lines, $F_{\rm phot}$ is the photospheric flux (i.e. the flux of the continuum in the spectrum), $T_{\rm eff}$ is the effective temperature of the star and σ is the Stefan–Boltzmann constant[4] (R'_{HK} was defined in this way by Noyes et al. (1984)). From this plot, Salabert et al. (2016) noticed that the chromospheric activity level of the Sun (black circle with a centred dot) is overall compatible with the one of the solar analogues. Thus, they concluded that the Sun does not occupy any peculiar position in the $P_{\rm cyc} - P_{\rm rot}$ diagram and the statement of Böhm-Vitense (2007) was rather motivated by a lack of stars with characteristics more similar to the Sun in her sample.

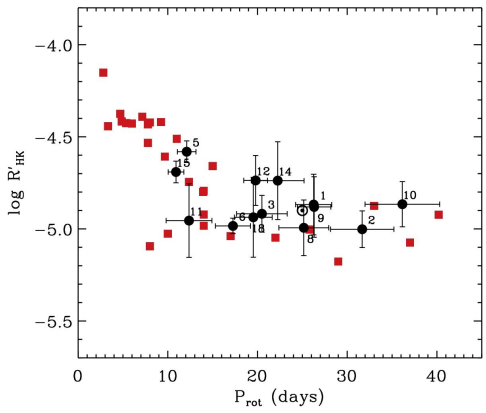

Figure 2.2.4: Chromospheric activity index $R'_{\rm HK}$ as function of the rotational period for a sample of solar analogues (Salabert et al., 2016). The red squares are stars present in the *HK project* catalogue. The black dots are stars observed with the *Kepler* satellite. The Sun is plotted with its usual symbol, i.e. black open circle with a centred dot.

[4]The superscript in R'_{HK} denotes that the flux in the H and K lines is corrected for the photospheric contribution $F_{\rm phot}$.

3

X-ray activity cycles

Contents

We have seen that the magnetic activity can be characterized through the monitoring of the magnetic structures that rise on the surface of the star, evolve and decay. Since these structures pervade all layers of the stellar atmosphere, we can characterize the stellar activity cycles through observations of the photosphere, the chromosphere and the corona. In chapter 2 we have seen that in the photosphere the evolution of sunspots and starspots traces the magnetic activity cycle and in the chromosphere these same structures emit the Ca II H&K lines in the optical waveband. The question is now how we can characterize also the coronal cycles of the stars in the X-ray. When observing the Sun in the X-ray band, its X-ray luminosity is periodically variable with a period compatible with its magnetic cycle. Thus, it is expected that also solar-like stars should show coronal X-ray cycles, with the length period of their photospheric and chromospheric counterparts.

While the photosphere and the chromosphere can be observed with ground-based telescopes, X-ray observations can be performed only with satellites outside the Earth's atmosphere. At present, as X-ray observatories the ESA *XMM-Newton* satellite (chapter 4) and the NASA *Chandra* satellite are widely used for investigations of stellar X-ray emission.

Employing a satellite for such scientific studies rises some difficulties. These two X-ray satellites are not employed only for stellar observations, but their scientific goals comprise different astrophysical studies. On the other hand, the dedicated *HK project* (section 2.2) was exclusively thought for the monitoring and characterization of stellar activity cycles. Moreover, from the Mount Wilson project we know that activity cycles last from few years up to few decades and this would imply long-term X-ray monitoring campaigns of activity cycles, depriving observational time to the other studies. Last but not least, it is advantageous to have homogeneous observations provided by the same X-ray instrument to avoid problems of cross-calibration of data. Because of these arguments, little is still known about stellar X-ray cycles.

Monitoring of coronal cycles requires thus a long-lasting X-ray mission, such as *XMM-Newton* (see chapter 4 for details on the satellite). Up to date, *XMM-Newton* has confirmed that seven stars show X-ray activity cycles: α Centauri A and B of the triple system α Centauri, 61 Cygnus A and B of the binary system 61 Cygnus, HD 81809, ι Horologii and ε Eridani.

In section 3.1 I summarize the characterization of the solar X-ray cycle provided by the study "The Sun as an X-ray star" conducted in the early 2000s. The results of that study were used during this PhD project. "The Sun as an X-ray star" has provided a collection of spatially resolved emission measure distributions of the magnetic structures on the Sun at X-ray wavelengths. These solar distributions can now be compared with X-ray observations of other active stars. The aim is thus to describe stellar X-ray activity cycles in terms of surface coverage factors of solar magnetic structures and their variation throughout the cycle. In chapter 7 the details of the application of the study "The Sun as an X-ray star"

is given.

In section 3.2, I present a summary of the X-ray studies of stellar cycles that had been performed before this thesis started. First I describe the characterization of the X-ray activity cycles for α Centauri, 61 Cygnus and HD 81809. Then, in subsection 3.2.3 I describe a first application of the study "The Sun as an X-ray star" to HD 81809.

In the light of the knowledges acquired from the X-ray activity cycles of the stars mentioned above, in section 3.3 I conclude this chapter with the motivations that have brought to start this PhD project and the X-ray monitoring campaign of ι Horologii and ε Eridani. The studies carried out on these two targets are discussed in details in subsequent chapters (chapter 5 and chapter 6).

3.1 The Sun as an X-ray star

The solar satellite *Yohkoh*, launched in 1991 and dismissed 10 years later, observed the Sun for its full mission lifetime in the X-ray waveband. *Yohkoh* comprised four instruments: two spectrometers, the Bragg Crystal Spectrometer (BCS) and the Wide Band Spectrometer (WBS), and two X-ray telescopes, the Soft X-Ray Telescope (SXT), sensible to soft X-ray energies in the $0.25 - 4.0$ keV range, and the Hard X-Ray Telescope (HXT), sensible to the energy range $14 - 93$ keV. In the context of the study "The Sun as an X-ray star" (Orlando et al., 2000; Peres et al., 2000; Reale et al., 2001; Orlando et al., 2001), several images acquired by *Yohkoh/SXT* were analysed: in particular the observations of the solar corona analysed in the context of this study covered part of the 22nd activity cycle of the Sun[1] from its maximum to its minimum.

In the first paper of this study, Orlando et al. (2000) analysed only one full image of the Sun, the one taken by *Yohkoh* in January 1992. In Figure 3.1.1, the image of the whole solar corona is shown in panel a. By analysing each image pixel[2], they retrieved a table of emission measures *EM*s as function of the temperature T, i.e. the solar emission measure distribution ($EMD_{\odot}$) representative of the whole solar corona. In the determination of $EMD_{\odot}$, they rejected the pixels where the number of photon counts (n_{phot}) was less than 10 because those pixels overestimate the emission measures at temperatures $T < 10^6$ K. Panel b of Figure 3.1.1 shows the $EMD_{\odot}$ of the solar corona obtained by the analysis of the image: the thick solid line is the $EMD_{\odot}$ of the image with $n_{phot} > 10$, while the thin line is the $EMD_{\odot}$ obtained from all the image pixels.

In the second paper (Peres et al., 2000), the study was extended to other solar images acquired

[1] The 22nd cycle of the Sun started in 1986 and ended in August 1996

[2] This was achieved using the analysis software of the satellite *Yohkoh*, called SYAS (Standard *Yohkoh* Analysis System).

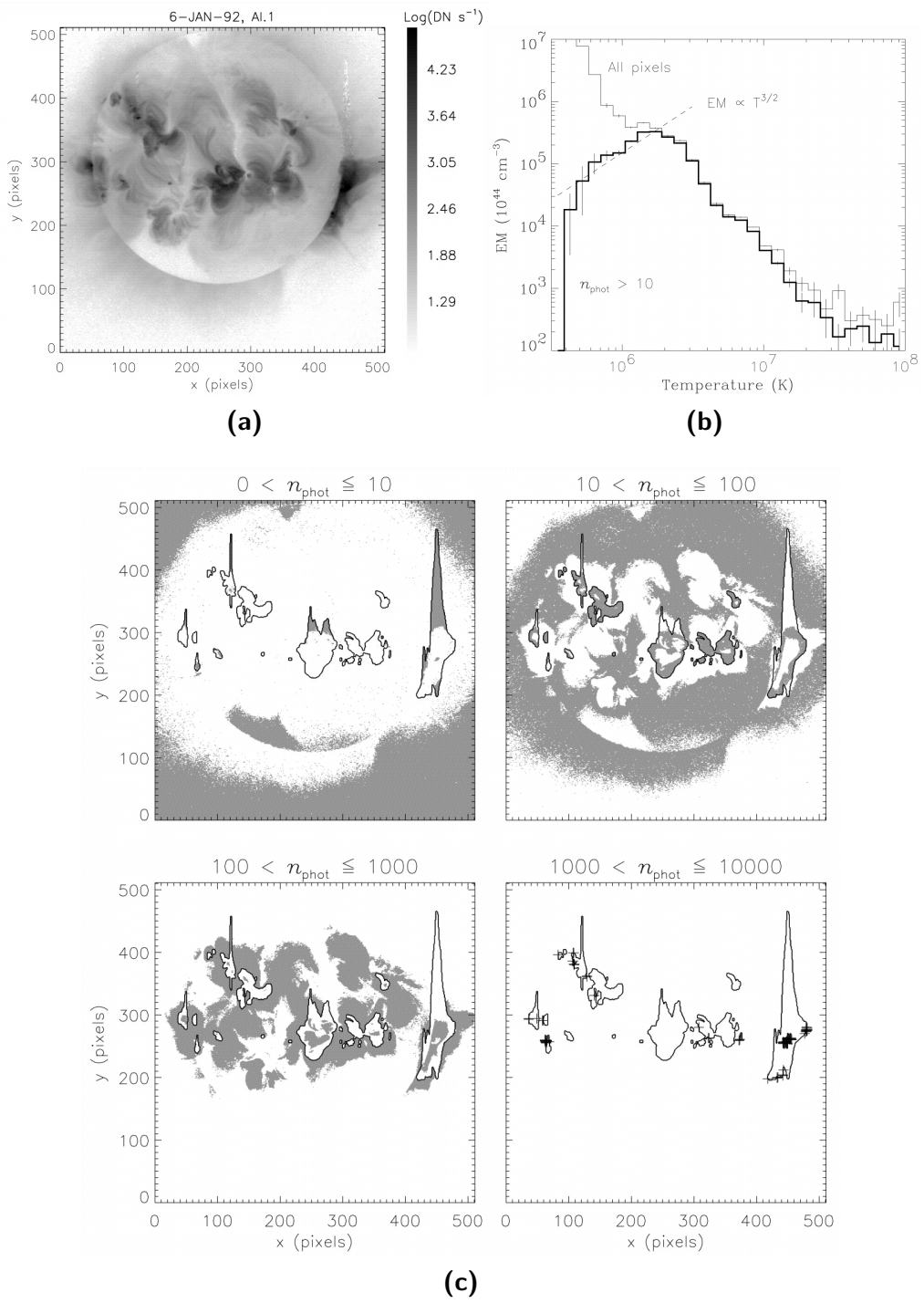

Figure 3.1.1: *Panel a*: the whole image of the Sun observed by *Yohkoh* in January 1992. *Panel b*: emission measures as function of the temperature obtained from the analysis of each pixel of the image in panel a. *Panel c*: The image of panel a divided in four ranges according to the photon counts measured in each pixel image (Orlando et al., 2000).

by *Yohkoh*, representing the maximum of the solar cycle (January 1992), an intermediate state of the cycle (July 1993) and the minimum of the cycle (June 1994). Moreover, a procedure to obtain the synthetic spectra of these observations as they were obtained from other non-solar X-ray satellites was developed. The $EMD_{\odot}$ of each state of the solar cycle was produced by analysing each image pixel with the same threshold that the authors gave in the first paper, i.e. the number of photon counts greater than 10.

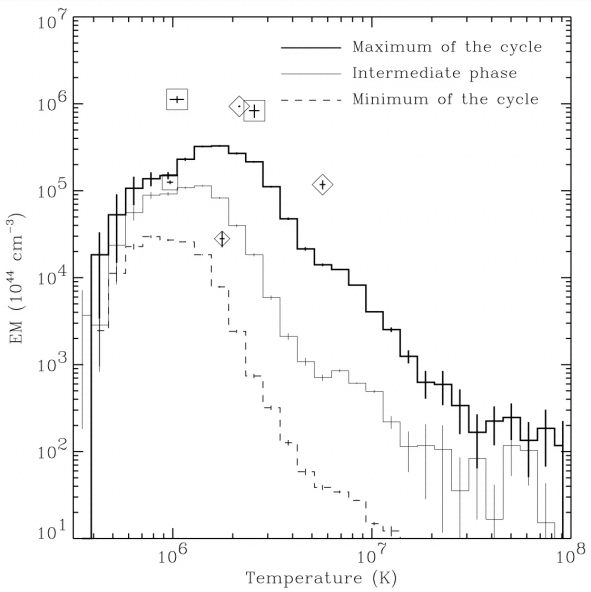

Figure 3.1.2: $EMD_{\odot}$ of the 22nd solar cycle monitored by *Yohkoh* in the 1990s. The thick line is the EMD of the maximum of the solar cycle. The thin line is the EMD of an intermediate state of the solar cycle. The dashed line is the EMD of the minimum. Overplotted are also the best-fitting spectral parameters retrieved from the synthetic spectra extracted from the maximum of the cycle (large symbols) and from the minimum (small symbols). The spectra were synthesized as if the Sun was observed by *ROSAT* (square symbols) and by *ASCA* (diamonds symbols) (Peres et al., 2000).

In Figure 3.1.2 the $EMDs_{\odot}$ at the maximum of the solar cycle, at an intermediate state and at the minimum are shown. The overall shape of the emission measures is in general the same for the three phases of the cycle. However, the peak of the temperature, and the corresponding emission measure, decrease from the maximum to the minimum of the solar cycle, and the high-temperature slope of the emission measure is steeper during the minimum.

Starting from these $EMDs_{\odot}$, the authors generated the corresponding synthetic spectra as if the Sun were observed by another X-ray satellite. At the time when this procedure was developed, the most used satellites for stellar X-ray observations were *ROSAT* and *ASCA*. A given $EMD_{\odot}$ distribution

consists in N bins, each characterized by a pair k of values of plasma temperature and corresponding emission measure ($EM(T_k)$). For each of these pairs, the emitted spectrum ($P(T_k, E)$ where E is the energy of the photons), i.e. the spectrum emitted by an optically thin isothermal plasma, was computed using the MEKAL code (Mewe et al., 1986; Kaastra, 1992; Mewe et al., 1995). For the entire $EMD_\odot$, the spectrum is calculated by summing up the contribution to emission from all the N bins of the distribution:

$$C_j = \sum_k \frac{P\left(T_k, E\right) EM(T_k)}{E} \tag{3.1}$$

where C_j is the number of counts in the jth spectral channel of the detector. However, at this stage, Equation 3.1 does not take into account the characteristic of the satellite nor the stellar parameters. Thus, it is required to include the distance of the star, a value of exposure time of the simulated observation and the spectral response of the detector of interest. By including these variables, equation 3.1 becomes:

$$C_i = \frac{t}{4\pi d^2} \int dE \frac{A(E)M(j,E)}{E} \sum_k P\left(T_k, E\right) EM(T_k) \tag{3.2}$$

where t is the (assumed) exposure time of the observation, d is the distance of the star, $A(E)$ is the effective area of the instrument and $M(j, E)$ is its response matrix [3]. Now, the integral over the energy takes into account also the instrumental response and the produced synthetic spectrum can be treated with the usual software for spectral analysis, like `xspec` (Arnaud, 1996).

With this procedure, Peres et al. (2000) generated two pairs of synthetic spectra of the Sun, simulating the observations of the minimum and the maximum of the solar cycle as if they were acquired by *ROSAT* and *ASCA*, respectively. In Equation 3.2, the distance of the Sun was set to 1 pc. They then proceeded on the spectral analysis using the software `xspec`: the spectrum of the maximum of the cycle was fitted assuming a 2-T spectral model APEC [4], while the minimum assuming a 1-T spectral model APEC. The best-fitting parameters that they retrieved from the spectral analysis are overplotted in Figure 3.1.2: the square symbols are the values obtained from the *ROSAT*-like spectra; the diamond symbols are the values obtained from the *ASCA*-like spectra. The small symbols refer to the spectra of the minimum of the cycle, whereas the large symbols to the spectra of the maximum of the cycle. Effectively, the procedure has downgraded the $EMD_\odot$ to an EMD represented by 1- or 2-temperatures only, which is the typical approach to study stellar X-ray observations that provide much less detail than available for the Sun. From Figure 3.1.2, it can be seen that in general the parameters of the best-fitting 1- and 2-T model follow the trend of the $EMD_\odot$ constructed directly from

[3] The response matrix of a detector represents the probability that a photon of energy E is detected in the jth channel. See also section 6.3.

[4] See section 6.5 for a detailed description of the spectral model APEC.

Yohkoh images: during the maximum of the cycle the emission measure results higher than during the minimum, and the best-fitting temperatures of the 1-T and 2-T model represent well the $EMD_{\odot}$. Thus, the synthetic spectra, simulated following the aforesaid procedure, are consistent with the real observations of the Sun, albeit describing them with much lower details.

The third paper of the study "The Sun as an X-ray star" (Reale et al., 2001) was entirely dedicated to the analysis of the flaring events observed by *Yohkoh*: the solar satellite was able to observe the Sun in the so-called "flaring mode" for which only the flaring events occurring on the solar surface were monitored. Reale et al. (2001) selected in total eight flares of different classes, from a low energetic class (class C) to the highest energetic one (class X). These flares have all been observed with two hard SXT filter passbands (199 μm Be filter and 11.4 μm Al filter) that are sensitive to plasma around and above 10^7 K. Moreover, one of the eight flares, a flare of class M of intermediate energy, was also observed with two soft SXT filters (1265 Å-thick Al filter, Al/Mg filter), highlighting that also plasma at low temperatures gives an important contribution to the flare EMD. The flares were all analysed in separate phases of their evolution, from the rise to decay. The authors analysed the pixel images of each phase of the observed flares and they obtained the corresponding flare emission measure distribution ($EMD_{FL\odot}$) following the approach of the first and of the second paper.

In the fourth paper of this study (Orlando et al., 2001), the *Yohkoh* images of the Sun were analysed again, but following an approach different from the one of Peres et al. (2000): Orlando et al. (2001) identified three different classes of coronal magnetic regions by looking at the image brightness (I) of the SXT images representative of different phases of the solar corona during its cycle. From each of these images, the brightness was calculated in each pixel and a histogram of these values was produced. The range of intensities was divided into 50 bins of constant size. The histogram is shown in Figure 3.1.3. The authors identified a maximum of intensity at $I = 40$ DN(data numbers) s^{-1} $pixel^{-1}$ and a change in the slope at $I = 6 \times 10^3$ DN(data numbers) s^{-1} $pixel^{-1}$. These two thresholds are highlighted in Figure 3.1.3 with dashed vertical lines. The regions with intensities lower than the maximum were identified as quiet regions (BKC - BacKground Corona). The regions between the two thresholds were identified as the active regions (ARs). The regions at $I \geq 6 \times 10^3$ DN(data numbers) s^{-1} $pixel^{-1}$ were identified as the cores of active regions (COs), which, in the images, are the most intensively emitting regions at the center of active regions.

These thresholds were then applied to all images of the Sun in order to identify the three classes of magnetic structures and the corresponding $EMD_{\odot}$s as done in the previous papers. Thus for each observation of the Sun the total $EMD_{\odot}$ can be described by the sum of the individual contributions from each of the three classes of magnetic structures: the ARs ($EMD_{AR\odot}$), the COs ($EMD_{CO\odot}$) and

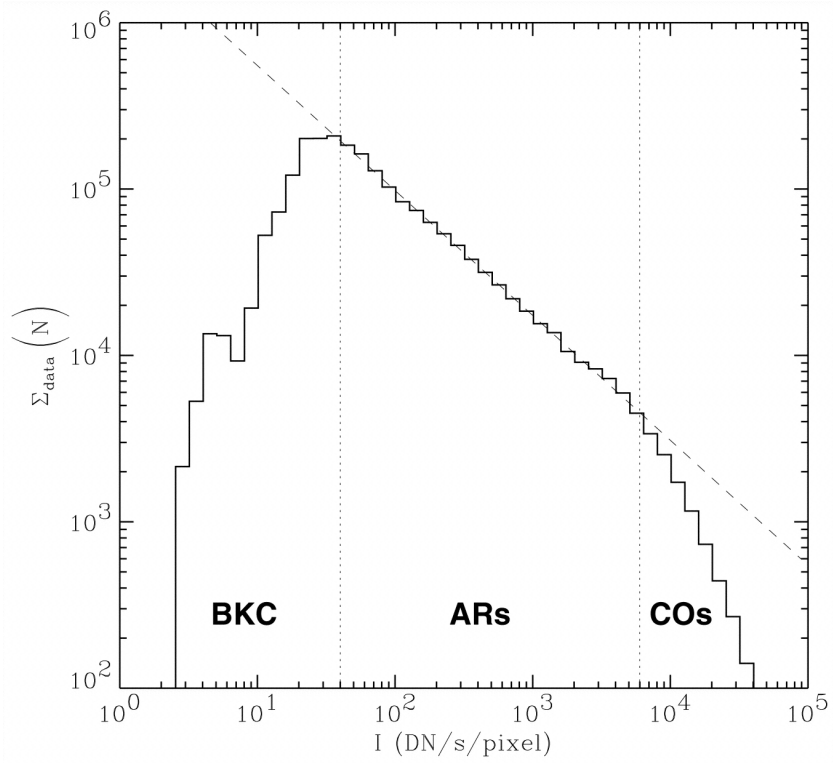

Figure 3.1.3: Histogram of the brightness I for each pixel of the SXT images. The vertical dashed lines are the two thresholds individuated by the authors and that denote three different types of solar magnetic structures identified in the images (Orlando et al., 2001).

the BKCs ($EMD_{BKC\odot}$). Also the $EMD_{FL\odot}$ contribute to the total $EMD_{\odot}$. However, the flares could be observed only separately from the other magnetic structures because, when a flare occurs on the Sun, the images saturate and events other than the flares can not be detected. Thus, only with the "flaring mode" it is possible to identify in the images the flares at the expense of the other classes of magnetic structures. For these reasons, the solar cycle was described in Orlando et al. (2001) only in terms of ARs, COs and BKCs.

In Figure 3.1.4, the $EMD_{\odot}$ of the maximum (top panel) and of the minimum of the cycle (bottom panel), together with the corresponding *Yohkoh* images, are shown. The main result was that during the maximum of the solar cycle, the $EMD_{\odot}$ is strongly influenced by the ARs, while during the minimum the main contribution to the total $EMD_{\odot}$ comes from the BKCs.

In 1996, one active region was present on the solar surface and observed by *Yohkoh*. During that observation the corresponding core was also observed from the moment when it emerged in the surface of the Sun (July 1996) to the time of its disappearance (October 1996). The analysis presented by

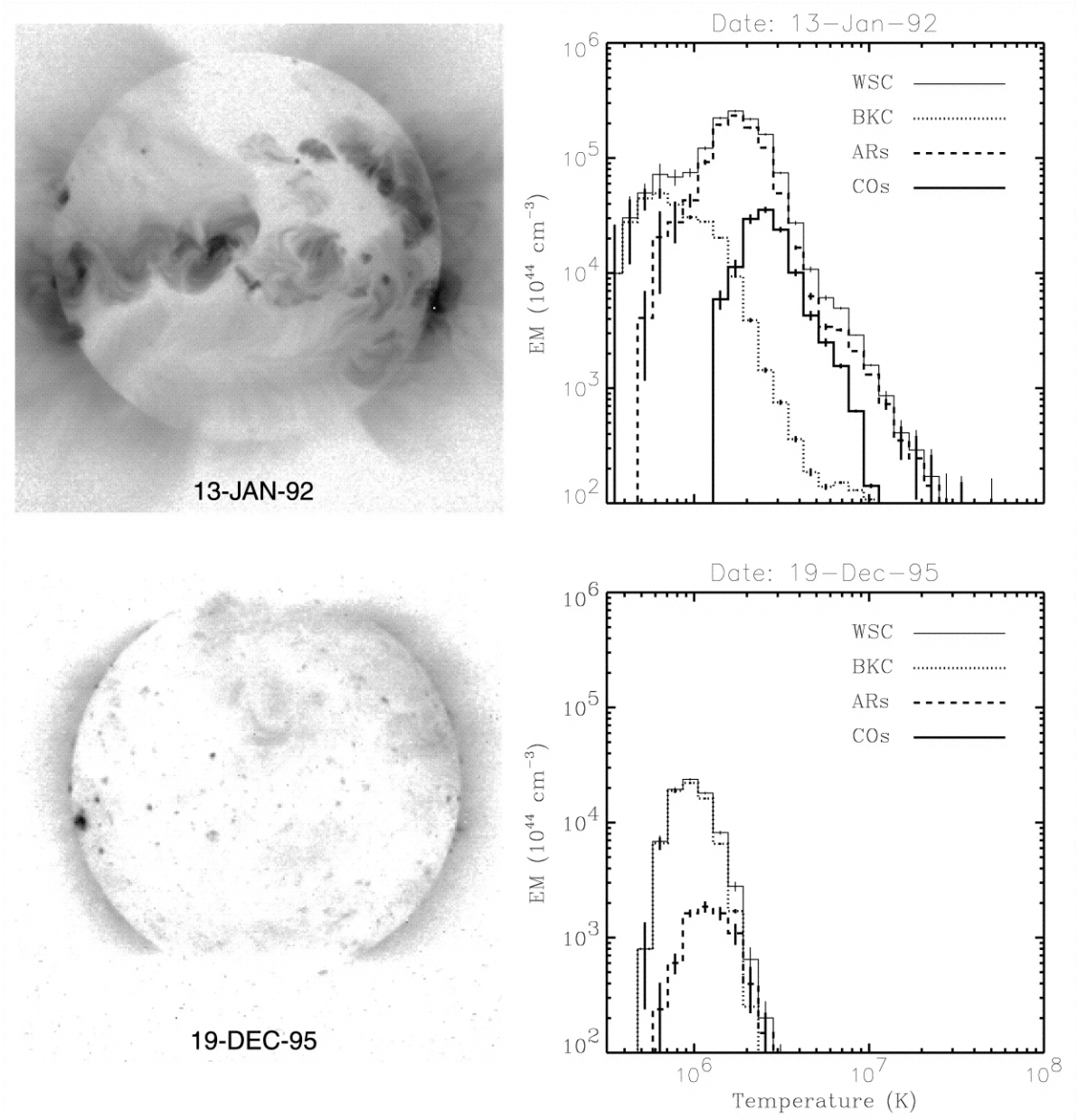

Figure 3.1.4: On the left the solar images acquired by *Yohkoh* during the maximum (top) and the minimum (bottom) of the solar cycle. On the right the corresponding $EMD_{\odot}$ are shown. The thin line is the total contribution of all three types of magnetic structures, i.e. the whole-solar corona (WSC); the thick line is the $EMD_{CO\odot}$; the thick dashed line is the $EMD_{AR\odot}$; the thin dashed line is the $EMD_{BKC\odot}$. (Orlando et al., 2001)

Orlando et al. (2001) was also applied to this observation, yielding information on how the $EMD_{AR\odot}$ and the $EMD_{CO\odot}$ evolve throughout the AR lifetime (Orlando et al., 2004).

To summarize, the most important products of the study "The Sun as an X-ray star" are:

- a grid of emission measures as function of the temperatures, emission measure distributions, representative of the whole solar corona ($EMD_{\odot}$);
- a classification of the solar magnetic structures: quiet regions (BKCs), active regions (ARs) and cores of active regions (COs), based on the intensity brightness of solar images;
- the emission measure distributions of each type of magnetic structure on the surface of the Sun ($EMD_{AR\odot}$, $EMD_{CO\odot}$ and $EMD_{BKC\odot}$), and the identification of the main contribution from each of these regions during the maximum and minimum of the solar cycle;
- the emission measure distributions of different classes of solar flares ($EMD_{FL\odot}$) that are obtained separately for each phase of the flaring event, from its rise to its decay;
- the procedure to extract from each kind of $EMD_{\odot}$ synthetic spectra that represent the Sun as if it was observed by another X-ray satellite.

Among these products, the last has interesting applications. In fact, the synthetic solar spectra can be simulated assuming the characteristic of any other star and not only of the Sun. In this way, they simulate a star in which the same solar phenomena are occurring and then they can be defined as *pseudo-solar* synthetic spectra. Thus, by studying their characteristics and comparing them with the actual observations of the star of interest, they can actually be used as a benchmark to see if the behaviour of a star is similar or not to the solar case. We will see direct applications of this study in the case of the star HD 81809 (subsection 3.2.3) and for the star ε Eridani (chapter 7), being the latter the core of my PhD project.

3.2 Stars with known X-ray activity cycles

In this section, I review the stars that show an evidence of an activity cycle in the X-ray band, all observed with the X-ray satellite *XMM-Newton*. This regards the stellar systems α Centauri, 61 Cygnus and HD 81809.

3.2.1 The triple systems α Centauri

The stellar system α Centauri (α Cen) is composed of three stars: α Centauri A of spectral class G2V, α Centauri B of spectral class K1V and the M5 dwarf Proxima Centauri. The system is at 1.5 pc, one of the nearest stellar systems to our Solar System. α Cen is estimated to have an age similar to the Sun, between 4.2 and 6.8 Gyr, and both α CenA and B are slow rotators with a period of 29 and 37 days respectively (Barnes, 2007; Epstein et al., 2014).

A comprehensive analysis of the X-ray observations of the system was provided by Robrade et al. (2012). The observations were taken with *XMM-Newton* and the system was irregularly observed from 2003 to 2010. Proxima Centauri was not in the field of view of the observations and thus only α CenA and B were monitored by *XMM-Newton*.

When Robrade et al. (2012) started to observe the system in 2003, no chromospheric long-term monitoring data of the system was available. However, some years later Buccino et al. (2008) found a cycle period of 8.4 yr for α CenB from the Ca II measurements taken at the Complejo Astronomico El Leoncito (CASLEO) in Argentina.

From the analysis of *XMM-Newton* spectra of the two stars, Robrade et al. (2012) calculated the X-ray luminosities in the energy band $0.2 - 2.0$ keV. The X-ray lightcurves of α CenA and B are shown in Figure 3.2.1. The X-ray observations of α CenA (top panel in Figure 3.2.1) show an X-ray luminosity that varies between $\sim 7 \times 10^{25}$ erg/s and $\sim 6 \times 10^{26}$ erg/s, but does not show a periodic variability in its lightcurve. However, the authors speculated that, if this trend observed during 7 years of X-ray monitoring was associated to an activity cycles, the observations would indicate a cycle period longer than 10 yr and at that time α Cen A was showing a broad minimum. Thus, they proposed an X-ray cycle period of α CenA lasting $12 - 15$ yr.

On the other hand, α CenB (bottom panel in Figure 3.2.1) shows an X-ray variability with an X-ray luminosity going from $\sim 4 \times 10^{26}$ erg/s to 2.5×10^{27} erg/s. However the lightcurve does not cover the full chromospheric cycle: the X-ray luminosity displays a likely maximum between the end of 2003 and early 2004 and a clear minimum between the end of 2007 and early 2008, followed by a rise until 2010. Thus, the X-ray observations, by covering almost completely the choromospheric 8-yr cycle found by Buccino et al. (2008), supported the presence of a coronal cycle.

In the following years, Ayres (2014) also studied the α Cen system, trying to constrain the possible X-ray cycle for α CenA. He took into account not only the *XMM-Newton* observations, but also X-ray observations coming from *Chandra* and the German X-ray satellite *ROSAT*[5]. From his X-ray analysis,

[5]The satellite *ROSAT* was a German X-ray mission launched in 1990. Designed at the beginning as a 18-months mission, the satellite actually operated for over eight years, finally shutting down in 1999.

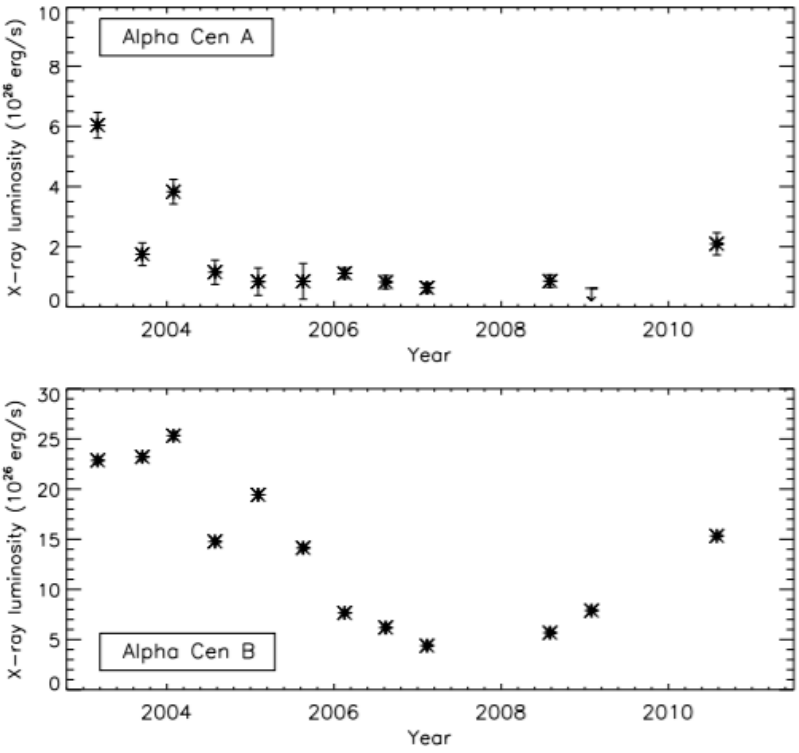

Figure 3.2.1: X-ray lightcurves of α CenA (top panel) and α CenB (bottom panel) (Robrade et al., 2012).

Ayres (2014) was not able to find a clear periodicity in the X-ray lightcurve of α CenA concluding that the result was related to an inappropriate cross-calibration of the observations.

The M dwarf Proxima Cen was also monitored in the optical waveband and in the X-ray band by Wargelin et al. (2017). The optical study, conducted within the *All Sky Automated Survey* project (ASAS) that observes stars in the visual and infrared band, included fifteen years of observations and showed that Proxima Cen is also an active star with a cycle lasting $\sim$ 7 yr. In the X-ray band the star was observed with the satellite *Swift* and four years of observations were acquired. Although the X-ray observations were not covering the full length of the cycle, a maximum and a minimum was observed in the X-ray lightcurve. However, Proxima Cen is not catalogued as a solar-like star and thus I did not include it in the sample of X-ray active star in this thesis.

3.2.2 The binary system 61 Cygnus

The binary system 61 Cygnus (61 Cyg), at a distance of 3.5 pc, consists of two stars, 61 Cyg A and B, of spectral class K5V and K7V respectively. Both stars are slow rotators, with periods of 35 and 38 days

(Donahue et al., 1996). The age of the system is estimated to be between 2 and 3 Gyr (Barnes, 2007) up to 6 Gyr (Epstein et al., 2014). The two stars were part of the *HK project* and they were found to be cyclic with a chromospheric period of 7.3 yr for 61 CygA and 11.7 yr for 61 CygB (Baliunas et al., 1995).

The binary system was studied in the X-rays by Robrade et al. (2012). They observed the stars with *XMM-Newton*, taking snapshots of the system regularly twice per year, from 2002 to 2011. Analogous to the analysis of the α Cen system, Robrade et al. (2012) calculated the X-ray luminosity of the two stars in the energy band of $0.2 - 2.0$ keV. In Figure 3.2.2 the X-ray lightcurve of 61 CygA (top panel) and 61 CygB (bottom panel) are shown.

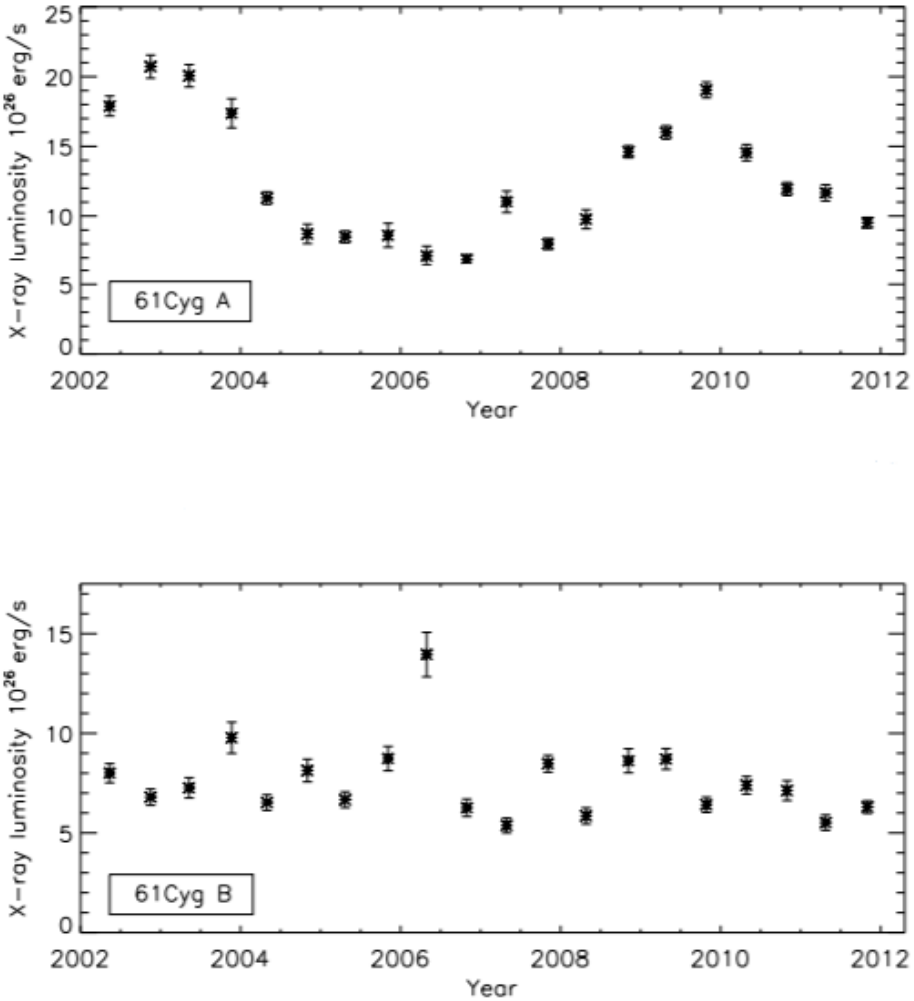

Figure 3.2.2: X-ray lightcurves of 61 CygA (top panel) and 61 CygB (bottom panel) (Robrade et al., 2012).

The lightcurve of 61 CygA (top panel Figure 3.2.2) shows a clear cyclic variability of the X-ray luminosity, having a minimum value at $\sim 7 \times 10^{26}$ erg/s and a maximum value at 2.1×10^{27} erg/s. In the plot two maxima of the cycle are located, the first at mid/end 2002 and second at the end of 2009, covering the chromospheric cycle of 7.3 yr and confirming the presence of an X-ray activity cycle. In contrast, although the companion 61 CygB has a chromospheric cycle of $\sim$ 11 yr, the star does not show a clear X-ray variability in its lightcurve (bottom panel Figure 3.2.2) where the trend of the X-ray luminosity is irregular with a mean value at 8×10^{26} erg/s and not smooth as for 61 CygA. In the past 61 CygB was also observed with *ROSAT* and in those observations that cover five years a significant variability was present and the *ROSAT* X-ray luminosity was varying from 4×10^{26}erg/s to 10^{27}erg/s (Hempelmann et al., 2006). Although the results obtained with *XMM-Newton* were unexpected when comparing them to the *ROSAT* observations, Robrade et al. (2012) noticed that also the chromospheric cycle of 61 CygB showed irregularities. Nevertheless, the X-ray observations followed the trend of more recent Ca II measurements of 61 CygB (Hall et al., 2007), first published by Baliunas et al. (1995) (see the Ca II measurements plotted in Figure 3.2.3). This evidence led Robrade et al. (2012) to conclude that the X-ray data point to a cycle probably shorter, between 10-11 yr, than the one found by Baliunas et al. (1995).

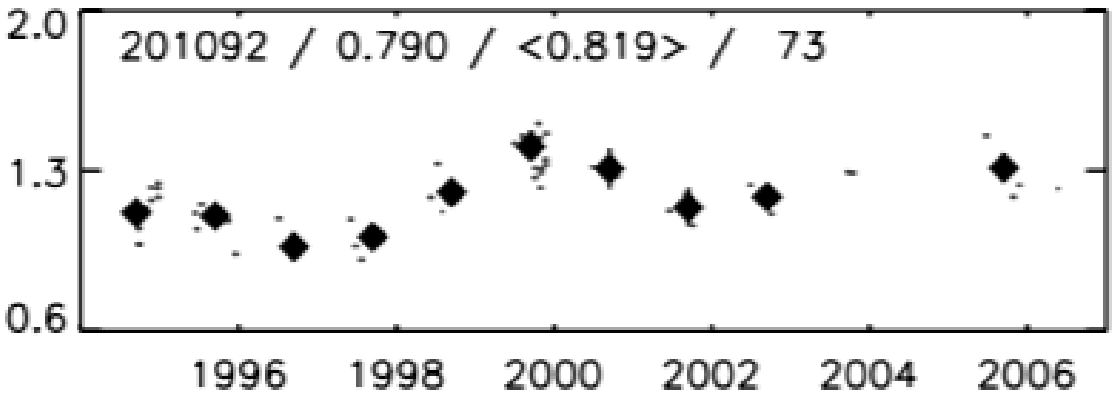

Figure 3.2.3: Ca II H&K measurements of 61 CygB (*y-axis*) during eleven years (*x-axis*) (Hall et al., 2007). In the legend of the plot, the *HD* name, the Strömgren *b-y* color index, the mean of the S_{MWO}-index measurements (y-axis) and the total number of observations are reported from the left to the right.

3.2.3 HD 81809

HD 81809 is a close visual binary where the two components have a separation of about 0.4 arcsec and an orbital period of 35 yr that make tidal effects likely negligible (Pourbaix, 2000). The two stars have spectral class G2V and G9V, respectively. Both components are slow rotators with a rotational period of 40.2 days (Donahue et al., 1996).

Baliunas et al. (1995) reported a well defined chromospheric cycle that lasts 8.2 yr. However, the binary system is not resolved and thus it is not clear if the activity comes from one of the two components.

The X-ray activity cycle was investigated and characterized by Favata et al. (2004), Favata et al. (2008) and Orlando et al. (2017). Favata et al. (2008) analysed the first seven years of observations taken by *XMM-Newton* regularly twice per year starting from 2001. Figure 3.2.4 shows the long-term

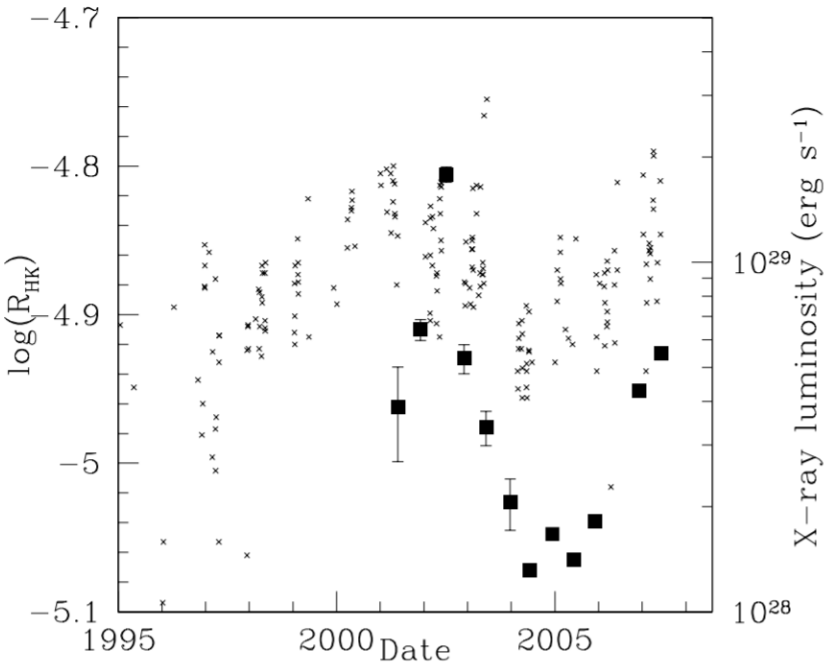

Figure 3.2.4: Long-term lightcurve of HD 81809 (Favata et al., 2008). The square symbols are the X-ray luminosity calculated from the *XMM-Newton* spectra. The cross-symbols are the chromospheric Ca II H&K activity.

lightcurve of the X-ray measurements collected by Favata et al. (2008) from 2001 to 2007. In the plot also the chromospheric data, taken in the same period of the X-ray monitoring campaign of HD 81809, are shown. From the lightcurve, Favata et al. (2008) concluded that HD 81809 shows an X-ray vari-

ability that is consistent with its chromospheric activity cycle, and the X-ray luminosity throughout the cycle covers a range of $(1.4 - 6.4) \times 10^{28}$ erg/s.

The *XMM-Newton* monitoring campaign of HD 81809 continued during the following years, providing thus fifteen years of observations that allowed a more detailed characterization of the X-ray activity cycle. In particular, Orlando et al. (2017) had applied the study "The Sun as an X-ray star" (section 3.1), with the aim to investigate if the coronal X-ray cycle of HD 81809 can be ascribed to solar-like phenomena, i.e. if the magnetic structures of HD 81809 are of the same nature as the solar ones.

Their study can be summarized in four steps:

- choosing the solar EMDs of the coronal magnetic structures, obtained in the study "The Sun as an X-ray star", that potentially best represent the spectra of HD 81809. They chose the ARs, the COs and the FLs, whereas the BKC regions were excluded because a high percentage of covering fraction would be required to reproduce the X-ray luminosity of the star and, thus, little space on the surface would have remained for the other magnetic structures that instead better reproduce the spectra of HD 81809;

- assuming a percentage coverage fraction of the magnetic structures and allowing them to vary on the surface of the star throughout the cycle, having thus different combinations of ARs, COs and FLs that contribute to the total EMD;

- for each combination of magnetic structures, producing the corresponding EMD and obtaining a grid of EMDs that artificially reproduces a solar-like corona with the physical characteristics of HD 81809;

- for each EMD in the grid, synthesizing a pseudo-solar spectrum to be compared to the observed *XMM-Newton* spectra of HD 81809.

Among the ARs and COs observed by *Yohkoh*, they chose to consider the active region and the core that were observed in 1996 from the rise to the decay and time-resolved by Orlando et al. (2004). These $EMD_{AR\odot}$ and $EMD_{CO\odot}$ were obtained by averaging over time each EMD corresponding to a certain phase in the evolution of these structures. The $EMD_{FL\odot}$ was built considering all eight solar flares discussed by Reale et al. (2001): they averaged over time each $EMD_{FL\odot}$ throughout the evolution of each flare observed by *Yohkoh*.

At this stage, the chosen EMDs for each magnetic structure are still representative of the Sun. Thus, the authors scaled the $EMD_{AR\odot}$, the $EMD_{CO\odot}$ and the $EMD_{FL\odot}$ to the surface of HD 81809: henceforth, these distributions are labelled as $\overline{EMD}_{AR\odot}$, $\overline{EMD}_{CO\odot}$ and $\overline{EMD}_{FL\odot}$ to stress that these $\overline{EMD}$s

are describing the magnetic structures of the Sun on the stellar surface of HD 81809, i.e. they are describing a *pseudo-Sun*.

Starting from these three $\overline{EMD}$s, the authors assumed that ARs, COs and FLs contribute each with a certain percentage value to the surface coverage of HD 81809 with magnetic structures. In particular they assumed that $P_{AR} = 60\%$ of the surface of HD 81809 is occupied by ARs, that the COs can cover from $P_{CO} = 4\%$ to $P_{CO} = 40\%$ of the stellar surface and that the FLs are tied to the COs varying from $P_{FL} = 0\%$ to $P_{FL} = 1\%$ of the coverage of the COs [6]. Finally, for each combination of magnetic structures ($P_{AR} + P_{CO} + P_{FL}$) within the pre-defined grid of values they produced the corresponding $\overline{EMD}$ and the synthetic spectrum according to Equation 3.2. In Equation 3.2, d was set on the distance of HD 81809 ($\sim$ 31 pc) and the effective area and the response matrix were assumed to be the ones of the EPIC/pn detector of *XMM-Newton* (see chapter 4). Thus, they obtained a grid of simulated *XMM-Newton* spectra, each of them representing a certain combination in percentage of ARs, COs and FLs. Finally, they fitted the synthetic spectra, adopting the same spectral model used to fit the observed *XMM-Newton* EPIC/pn spectra of HD 81809, i.e. a 2-T APEC model, and they compared the best-fitting parameters of the synthetic spectra to those obtained from the spectral analysis of HD 81809.

A first comparison was carried out between the X-ray luminosity (L_X) and the so-called average temperature (T_{av}) of the synthetic spectra and the observed spectra of HD 81809. Here, the average temperature is defined as:

$$T_{av} = \frac{\sum_i T_i \cdot EM_i}{\sum_i EM_i} \tag{3.3}$$

where the index i denotes the i-th parameter of the spectral model (thus, in this case, $i = 1, 2$). The results are shown in the left panel of Figure 3.2.5 where the X-ray luminosity is plotted as function of the average temperature: the red dots are the best-fitting parameters calculated from the observations of HD 81809; the magenta stars refer to the average temperature and the X-ray luminosity calculated directly from the *Yohkoh* observations of the Sun; the blue and the green symbols are the best-fitting parameters retrieved from the synthetic pseudo-solar spectra. In particular, the blue plus-symbols are the average temperatures and the X-ray luminosity calculated from those spectra that were extracted from $\overline{EMD}_{AR+CO_\odot}$, i.e. an EMD that is built by considering only contributions of ARs and COs. On the other hand, the green diamonds are the values calculated from the EMD that considers also the $\overline{EMD}_{FL_\odot}$. With the same symbol coding, all best-fitting parameters, $T_{1,2}$ and $EM_{1,2}$ of both synthetic

[6] As mentioned in section 3.1, the flares are not separately resolved from ARs and COs in the images of the Sun. Thus, to add the flaring contribution to the total EMD, since it is physically plausible that a FL arises in a CO, the most active magnetic structure, the percentage of flaring events is tied to the percentage of COs on the surface.

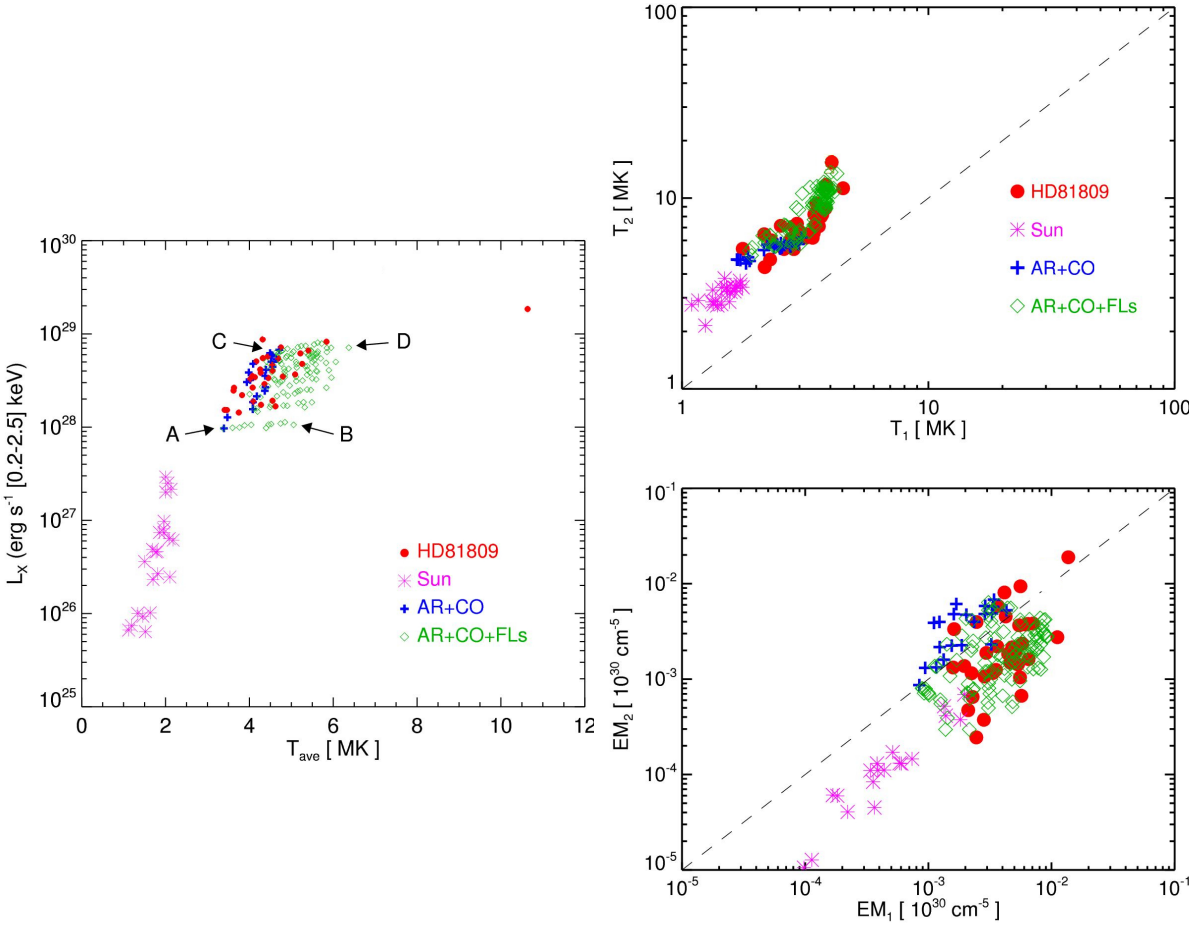

Figure 3.2.5: *Left panel*: L_X as function of the T_{av}. The red dots are the values obtained from the spectral fit of HD 81809 X-ray observations. The magenta diamonds are the L_X and T_{av} of the solar spectra acquired by *Yohkoh*. The blue and green symbols are the values calculated from the synthetic spectra extracted from the $\overline{EMD}_{AR+CO\odot}$ and from the $\overline{EMD}_{AR+CO+FL\odot}$ respectively. The points A, B, C and D denote each a specific percentage of coverage fraction of magnetic structures: A = 4%CO+0%FL, B = 4%CO+1%FL, C = 40%CO+0%FL and D = 40%CO+1%FL. *Right panel*: the best-fitting parameters $kT_{1,2}$ and $EM_{1,2}$. The color coding follows the same of the left panel (Orlando et al., 2017).

spectra and HD 81809 spectra, are plotted in the right panel of Figure 3.2.5 to yield a more detailed comparison of synthetic and observed spectra. From these two panels, it is clear that the observations of HD 81809 can be well reproduced by the synthetic pseudo-solar spectra if the $\overline{EMD}_{FL\odot}$ is contributing to the total $\overline{EMD}_{\odot}$.

As already noticed by Orlando et al. (2004) in the study "The Sun as an X-ray star", the characteristics of the solar X-ray variability due to the coronal cycle and the flaring activity are different: the flares lead to a prominent change of the coronal temperature, while the coronal cycle is mainly characterized by large variations in the X-ray luminosity. This effect is here also visible in panel a and b of Figure 3.2.5. As a matter of fact, an increase of the X-ray luminosity corresponds to an increase of coverage fractions of cores (from point $A = 4\%COs + 0\%FLs$ to point $C = 40\%COs + 0\%FLs$ in the figure). On the other hand, adding the flare contribution to each generated EMD affects mostly the temperature: it is clear from the plots in Figure 3.2.5 that the average temperatures result higher (going from point $A = 4\%COs + 0\%FLs$ to $B = 4\%COs + 1\%FLs$) than the same values obtained by considering only the contributions of ARs and COs to the total EMDs (blue plus-symbols).

From a visual comparison between the parameters presented in Figure 3.2.5, Orlando et al. (2017) concluded that, as the level of activity of HD 81809 increases, a corresponding increase of COs covering the stellar surface is required: the coverage of cores increases from 4% to 40% throughout the activity cycle of the star. Moreover, most of the observations of HD 81809 can be explained if a flare component, representing the solar flaring, is considered.

To summarize, through the synthetic spectra the authors were able to identify the presence of flaring events occurring in the corona of HD 81809 although no evidence of short-term variability was seen in the *XMM-Newton* observations. The analysis thus indirectly revealed the presence of small, unresolved flares. Moreover, compared to the level of activity of the Sun and the magnetic structures that actually cover the solar surface (magenta symbols in Figure 3.2.5), HD 81809 requires higher percentages of magnetic structures that yield to higher luminosity and temperatures. Thus, the authors concluded that HD 81809 can be considered a scaled-up solar version in terms of magnetic structures that cover the surface.

3.3 Motivations for this PhD thesis

If we put in one picture all the stars that show an X-ray activity cycle, we notice that the Sun, α CenA, α CenB, 61 CygA, 61 CygB and HD 81809 have similar characteristics. They are old with age comprised between 3 and 6 Gyr and they are all slow rotators. In the X-ray waveband, overall they appear as moderately active stars, with X-ray luminosity compatible with their long rotational period. All of this

can be summarized in the plots of Figure 3.3.1.

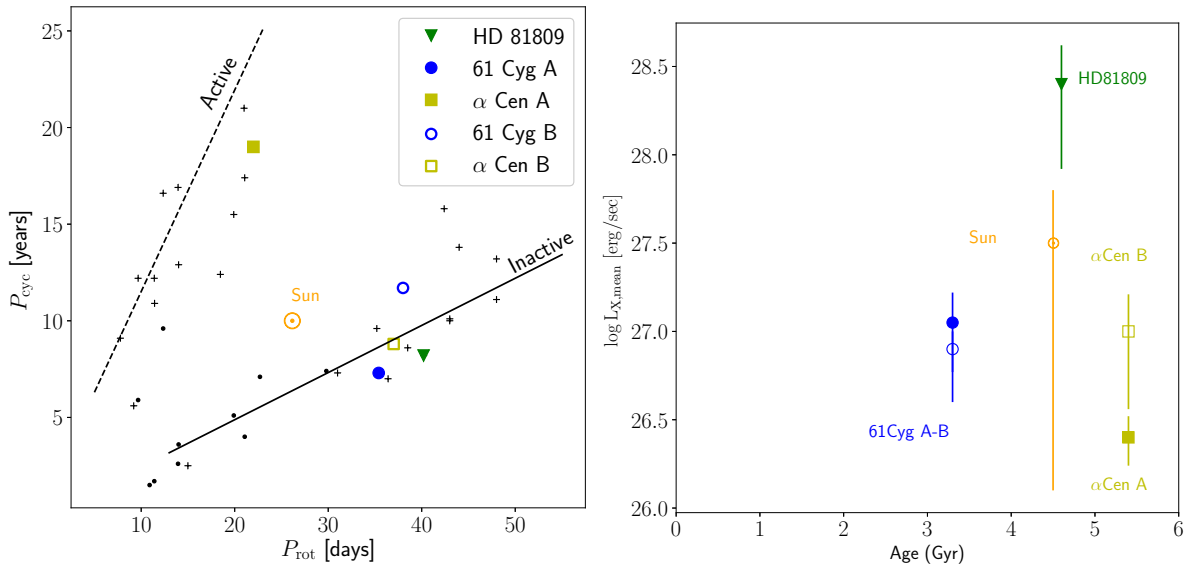

Figure 3.3.1: *Left panel*: $P_{cycl} - P_{rot}$ diagram. The dotted line is the active branch, whereas the solid line is the inactive branch. The crosses and dots are the stars that show a chromospheric cycle and were studied by Böhm-Vitense (2007) and Brandenburg et al. (2017) (see Figure 2.2.3). The stars with a published X-ray activity cycle are plotted with coloured symbols and the name of each star is given in the legend. *Right panel*: X-ray luminosity as function of the age of the published X-ray active stars. The vertical bars represent the amplitude of each X-ray cycle, i.e. the end of the bars represent the largest and smallest values of the X-ray luminosity during the cycle.

In Figure 3.3.1a, the P_{cycl}-P_{rot} diagram presented for the first time by Böhm-Vitense (2007) and Brandenburg et al. (2017) (Figure 2.2.3 in section 2.2) includes also the X-ray active stars I discussed previously in section 3.2. In Figure 3.3.1b, I show the relation between the age and X-ray luminosity of the stars with an X-ray cycle. From the first plot, it seems that for 61 CygA, α CenB and HD 81809 the dynamo is operating in deeper areas of the convective layers, being positioned in the inactive branch of the diagram. 61 CygB may show a coexistence of two operational ways of the dynamo, since it lays between the two branches together with the Sun. Finally, α CenA is the only star in the X-ray sample of cyclic stars that is positioned in the active branch.

From Figure 3.3.1b, it is also evident that overall, as the stars are older, the X-ray luminosity is small. The only exception is in this picture HD 81809, that has a mean X-ray luminosity higher than the other stars. However, HD 81809 is a close binary system that was not resolved with *XMM-Newton* and, thus,

the mean X-ray luminosity comprises both components. If the system would be resolved, the X-ray luminosity of the two components could be disentangled.

Examining in more detail the X-ray luminosity-age relationship, by looking at the amplitude of the X-ray cycle, i.e. the variation between the luminosity at the X-ray minimum of the cycle and its maximum represented by the vertical bars in Figure 3.3.1b, it is also clear that these stars present a large amplitude of the cycle.

However, in the sample of X-ray stars presented here, young stars are missing and thus a natural question would be: *"Are X-ray activity cycles common in old stars as observed until now, or do younger stars show also X-ray cycles? And if so, what are the proprieties of X-ray activity cycles in young stars?"*. If we observe younger stars, the first expectation would be to observe X-ray luminosity greater than what we have seen until now. The decay of the X-ray luminosity with age is a known relationship. For example, Preibisch et al. (2005) and Ribas et al. (2005) showed that pre-main sequence stars (with age between $\sim$ 0.1 Myr and $\sim$ 10 Myr) and solar analogues (with age between 100 Myr and 8 Gyr) have X-ray luminosity that linearly decreases with the age. More recently, Gondoin (2018) showed that the X-ray luminosity decreases with the age of the main-sequence solar-like stars and, moreover, for young stars with age comprised between $\sim$ 1 Myr and $\sim$ 1 Gyr and different rotational period the X-ray luminosity ranges between 10^{28} erg/s and 10^{31} erg/s. Thus, the level of the X-ray activity would be greater than the stars showed in Figure 3.3.1b.

However, would these young stars show also a long-term variability of their X-ray luminosity over time, i.e. an X-ray cycle? In the *HK project* the youngest stars monitored have an age $<$ 2.3 Gyr and they showed chromospheric activity cycles. However, an age $<$ 2.3 Gyr denotes stars relatively old and it would be more interesting to investigate younger stars.

Thus, this PhD project is dedicated to an appropriately targeted X-ray study of *young* stars. In particular, I focused on the study of two young solar-like stars: ι Horologii and ε Eridani (with age of $\sim$ 600 Myr and $\sim$ 400 Myr) monitored with *XMM-Newton* in search of an X-ray activity cycle. In chapter 5, chapter 6 and chapter 7 I discuss the characterization of their activity cycles. In addition to these two stars, a third target, Kepler 63 (with age $\sim$ 200 Myr), was added through a guest observer program I have been granted with *XMM-Newton*. This latter X-ray monitoring campaign is described in chapter 8.

Part II

The X-ray monitoring campaigns

4

The *XMM-Newton* satellite

Contents

The observations of the stars that, up to date, show X-ray activity cycles and that were discussed in the previous chapter (chapter 3), were all performed with the X-ray satellite *XMM-Newton* of the European Space Agency (ESA). This satellite was also employed in the X-ray monitoring campaigns performed during this Phd project.

The X-ray satellite *XMM-Newton* was launched in 1999 by ESA. Initially thought as a three-year space mission, the satellite is still operating after 20 years and the mission was recently extended until 2022. *XMM-Newton* has different important characteristics that still makes it the most widely used X-ray satellite. One of the appealing traits of *XMM-Newton* is its highly elliptical orbit that offers long continuous target visibility up to 40 hours.

The spacecraft is 10 meter long and it represents up to now the largest space mission ever carried out by the ESA. On board two different kind of telescopes are present: three co-aligned Wolter type-1 X-ray telescopes and a 30-cm optical/UV telescope. The telescopes are equipped with different scientific instruments that operate simultaneously: *European Photon Imaging Camera (EPIC)*, *Reflecting Grating Spectrometer (RGS)* and the *Optical Monitor (OM)*. The first two instruments are designed for X-ray studies, and the last one for optical/UV studies. Thus, *XMM-Newton* gives also the important possibility to simultaneously access two windows of the electromagnetic spectrum. In the following a more detailed description of the detectors is given (XMM-Newton SOC, 2019).

4.1 European Photon Imaging Camera (EPIC)

EPIC is composed of three detectors: the *EPIC MOS (Metal Oxide Semiconductor)* CCD, divided into two arrays, *MOS1* and *MOS2*, and the EPIC pn CCD. The *EPIC* cameras can perform sensitive imaging observations over a field of view of 30′ and they cover an energy range from 0.2 to 12 keV, with moderate spectral resolution ($E/\Delta E \sim 20 - 50$), allowing thus also spectral studies of the targets.

The *MOS* arrays consist of 7 individual identical, front-illuminated CCDs, but during the mission two out of the 14 total CCDs were damaged and are not operating any more. The *MOS* cameras are mounted at the prime focus of those X-ray telescopes that also carry *RGS* instruments, placed at the second focal plane. In each telescope a grating stack focuses $\sim 44\%$ of the incoming light in the primary focus, i.e. in the MOS detector, and the remaining incoming light is dispersed towards the RGS detectors in the secondary focus where it will be diffracted by a second grating as discussed in the next section. In Figure 4.1.1 the X-ray light path in the two telescopes where MOS and RGS detectors are located is shown.

The *EPIC pn* camera is a single Silicon wafer with 12 back-illuminated CCDs. It is mounted on the

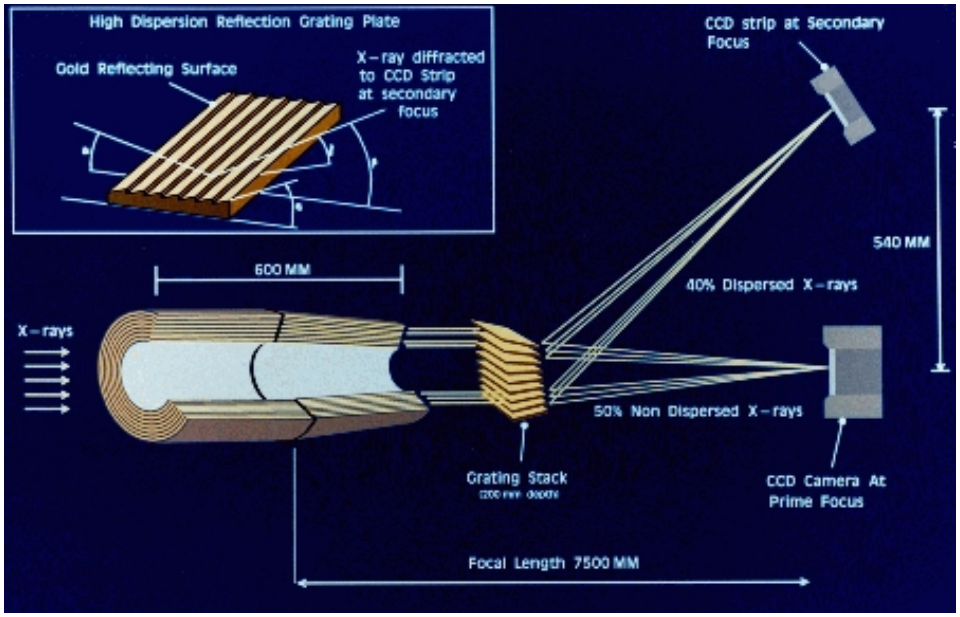

Figure 4.1.1: Sketch of the incoming X-ray light in the two telescopes where both RGS and EPIC MOS are mounted. The EPIC MOS is placed in the prime focal plane of the telescopes, with the RGS is in the second focal plane.

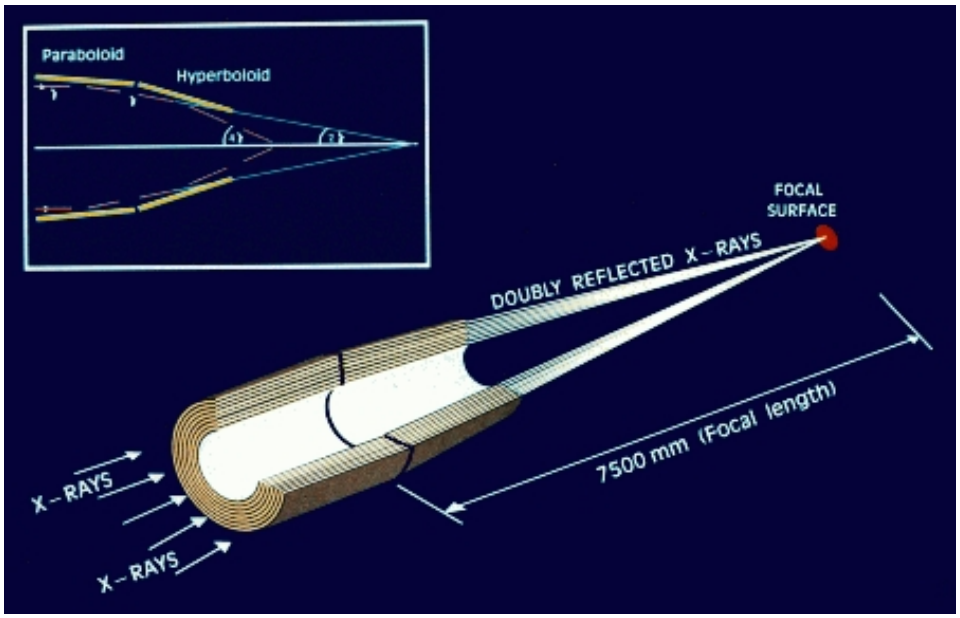

Figure 4.1.2: Sketch of the incoming X-ray light in the telescope where the EPIC/pn detector is mounted.

third telescope alone and, therefore, it receives the total amount of incoming X-ray light. For this latter reason, the *EPIC pn* has a higher sensitivity than the *EPIC* MOS. In Figure 4.1.2 the X-ray light path coming into the EPIC/pn detector is shown.

EPIC allows to operate in different scientific modes. The data can be obtained either when all the CCDs, or half of them, are turned on or when one single CCD is operating. The first two data acquisition modes are called "Full Frame" and "Large Window" mode, and in the first mode all CCDs are read out and thus the entire field of view of the EPIC MOS and EPIC/pn is covered, whereas in the second mode half of the CCDs are read out. The other data acquisition mode is called "Small window", where a part of a CCD is used. In Figure 4.1.3, two examples of the data acquisition of the young solar-like star ε Eridani (chapter 6) are shown: on the left a Full Frame observation is shown, on the right a Small Window observation.

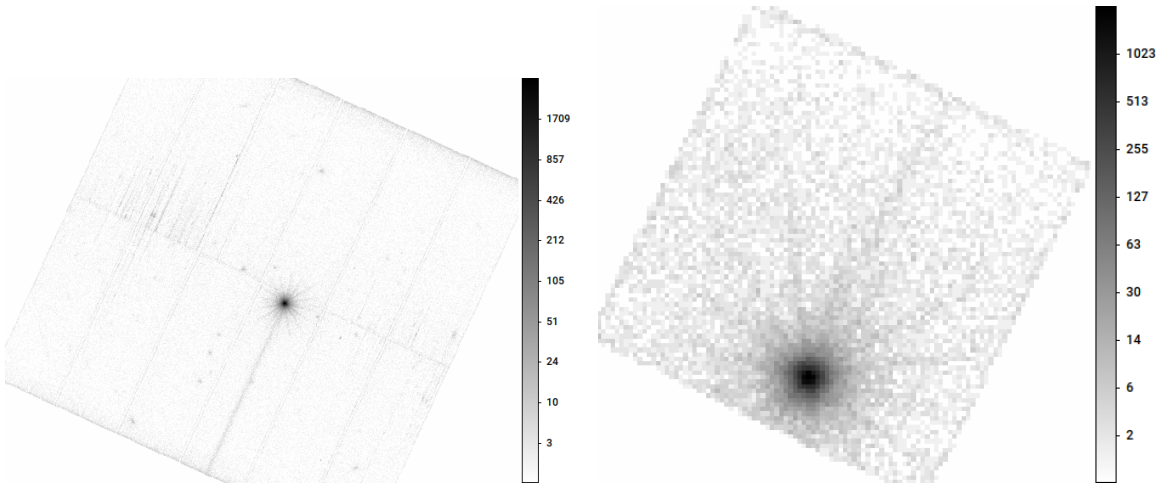

(a) Full Frame image **(b)** Small Window image

Figure 4.1.3: Two examples of images of ε Eridani obtained with EPIC/pn. On the left an image acquired in the Full Frame Mode. On the right an image in Small Window Mode.

During an observation, the following effects occur in the EPIC detectors: a) presence of background, that can be due to interactions with surrounding photons and particles and to the electronic noise of the cameras; b) Out-of-Time (OoT) events, i.e. when the photons are not registered only during the integration interval but also during the readout of the CCD.

The background due to interactions with photons is the *cosmic X-ray background*: at soft energies it is mainly due to the galactic X-ray background and at hard energies to unresolved X-ray sources outside the Milky Way.

The background due to interactions with particles can be divided into two categories: an external component and an internal component. The first component originates from the interaction with soft protons (protons with an energy smaller than few 100 keV) that are funnelled towards the detectors by the X-ray mirrors. These particles are most likely organized in clouds populating the Earth's magnetosphere and the number of clouds that *XMM-Newton* encounters depends on different factors such as the altitude of the satellite, its position with respect to the magnetosphere of the Earth and the amount of solar activity. During my PhD project, I dealt with some X-ray observations affected by a high presence of soft protons and in chapter 8 direct examples of such kind of background are seen.

The internal component is due to the interactions of the structure of the detectors and the detectors themself with high-energy particles with energy greater than 100 MeV. The consequence of these interactions is the creation of fluorescent lines in the background spectrum of the observation.

The effect of the OoT events is to broaden the spectral features in a systematic way, and it can be also affect in the image of the target. An example is the EPIC/pn image in Figure 4.1.3a, where a column of pixels in the readout direction of the CCD appears bright. The effect depends on the data acquisition mode, since the percentage of OoT events registered by the CCDs depends on the ratio of the readout time and the integration time. For example, in the EPIC/pn an observation conducted in Small Window mode has 1.1% of OoT events, while in Full Frame mode 6.3% of OoT events are present. In the XMM-Newton User Handbook (XMM-Newton SOC, 2019), the fraction of OoT events for each detector and each scientific mode is reported, so that these effects can be evaluated before the observation planning.

In section 6.3, the description of how these effects were handled in the observations of ε Eridani is presented in detail.

4.2 Reflecting Grating Spectrometer (RGS)

The *RGS* is suited for high spectral resolution X-ray spectroscopy, covering an energy range from 0.33 keV to 2.5 keV, corresponding to 5 - 38 Å. This energy band is particularly rich of X-ray emission lines: it includes the K-shell and He-like triplet of light elements and the L-shell of heavier elements, providing thus the possibility to carry out detailed studies on the coronal elemental abundances.

The instrument is composed of two identical units, *RGS1* and *RGS2*, that are hosted by the same X-ray telescopes on which the EPIC MOS cameras are mounted and they receive in total $\sim$ 50% of incoming light (see Figure 4.1.1). Each unit consists in an array of reflection gratings (Reflection Grating Assemblies - RGAs) which diffracts the X-rays to an array of dedicated CCD detectors (RGS Focal Cameras RFCs). This latter is composed in total by 9 MOS CCDs, back-illuminated to maximize the

soft energy response and aluminum-coated to shield the optical/UV incoming light. At the present, one CCD in each RGS unit is damaged and no longer in use.

The reflection of the light in the RGAs follows the diffraction geometry: the incoming light, that strikes the gratings at an angle of incidence α, emerges with an angle β according to the dispersion equation $\cos\beta = \cos\alpha + m\lambda/d$, where λ is the radiation wavelength, d the grating spacing and m the spectral order. The X-ray light is reflected into the first and second spectral order, and depending on the spectral order the RGS covers a different wavelength range: at the first order the range from 5 to 38 Å is covered and at the second order the range 5-20 Å. For very bright sources, it is also possible to have a third spectral order in a wavelength range from 5 to 10 Å.

All the RGS CCDs work following the so-called "Frame Store" mode: half of each CCD registers the incoming light and transfers then the signal to the other half, which works as a storage area before the readout. The scientific data acquisition modes are the "Spectroscopy" mode and the "Small Window" mode. The first mode works as the EPIC "Full frame" mode, where all the CCDs are operating. In the second mode only 1/4 of the CCDs operate.

Contrary to the EPIC camera, all different kinds of X-ray background is automatically rejected on board of the satellite, after the CCD readout. The main factors that have an impact on the RGS background are:

- Fluorescence lines, due to the interaction on electrons and ionising particles, that are not fully suppressed by the Au coating on the detectors;
- soft protons entering the mirrors, as in the EPIC camera;
- instrumental background caused by different events, such as particle background and low energy electrons.

4.3 Optical Monitor (OM)

The *OM* is an optical/UV 30-cm telescope that covers a range from 170 nm 650 nm. With the *OM* optical studies of the target can be conducted simultaneously to the X-ray studies. Even if the telescope has a small size, since the observations are conducted outside the atmosphere and, therefore, there is no atmospheric extinction, the *OM* is a powerful instrument, especially suited for faint sources. However, sources with an apparent magnitude less than 7, i.e. optically bright stars, can damage the OM CCDs, and for this reason the *OM* can not be used to observe such targets.

The telescope is equipped with a wheel holding several filters and two grisms, one for the UV and one for the optical bands. The filters cover part of the UV and optical range and they are in total six:

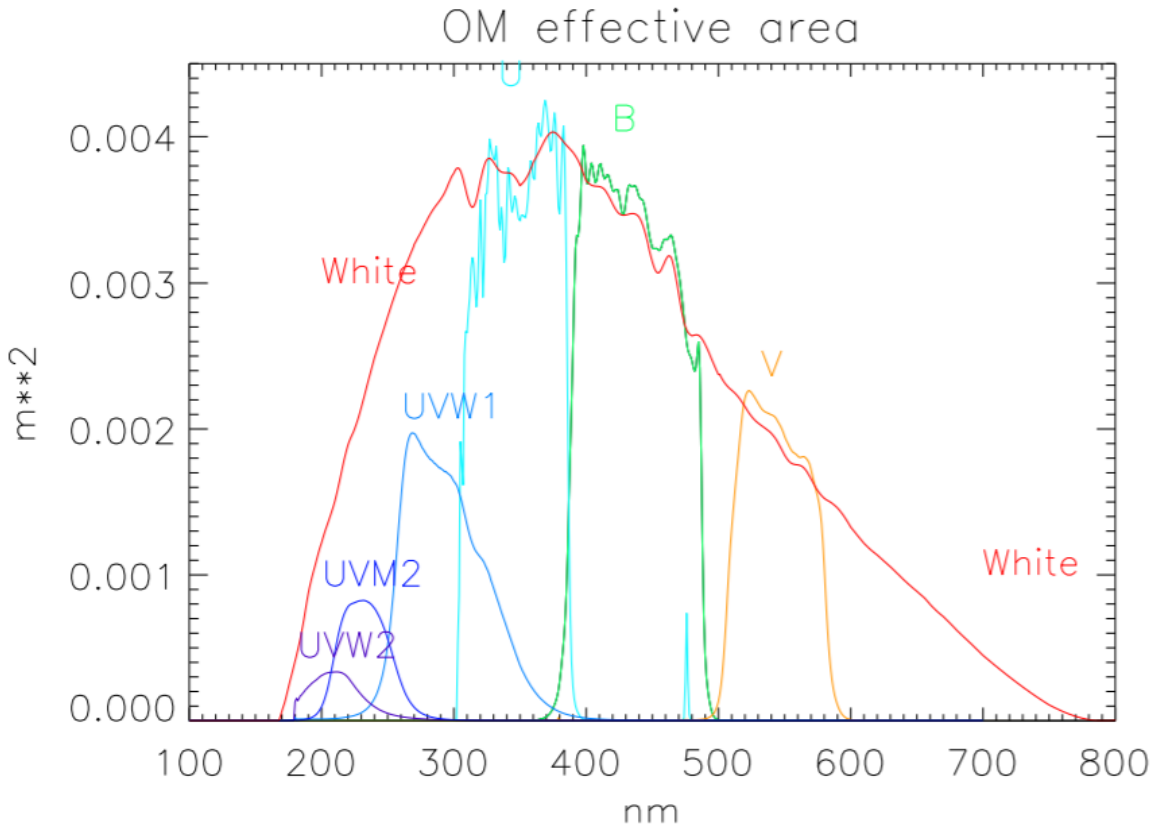

Figure 4.3.1: Transmission curve of the OM filters.

V ($\lambda_{\text{eff}} = 543, \text{nm}\ \Delta\lambda = 70\text{nm}$), B($\lambda_{\text{eff}} = 450, \text{nm}\ \Delta\lambda = 105\text{nm}$), U ($\lambda_{\text{eff}} = 344, \text{nm}\ \Delta\lambda = 84\text{nm}$), UVW1 ($\lambda_{\text{eff}} = 291, \text{nm}\ \Delta\lambda = 83\text{nm}$), UVM2 ($\lambda_{\text{eff}} = 231, \text{nm}\ \Delta\lambda = 48\text{nm}$), UVW2 ($\lambda_{\text{eff}} = 212, \text{nm}\ \Delta\lambda = 50\text{nm}$). In addition a seventh filter (white filter) covers the full wavelength range of the optical monitor. In Figure 4.3.1 the transmission curves of all filters is plotted, i.e. the OM effective area for a given filter including the entire telescope response. The two grisms instead allow to have low resolution spectra of the target, with a resolving power ~ 180. The visible grism covers a wavelength range from 175 nm to 360 nm. The UV grism covers the range from 300 nm to 600 nm.

5

The X-ray activity cycle of ι Horologii

Contents

ι Horologii (ι Hor; HD 17051) is a F8V/G0V star at a distance of 17.24 pc (van Leeuwen, 2007). It hosts a giant planet at a separation of 0.92 AU (Kürster et al., 2000). ι Hor has been proposed as component of the Hyades cluster, and thus this implies an age of $\sim$ 625 Myr (Lebreton et al., 2001). This estimation is also compatible with the age of $\sim$ 500 Myr found from the X-ray luminosity by Sanz-Forcada et al. (2011), with $\sim$ 625 Myr calculated from asteroseismology (Vauclair et al., 2008) and with 740 Myr found from gyrochronology (Barnes, 2007). ι Hor is a fast rotator, with a rotational period estimated 7.70 days from *TESS* photometry (Sanz-Forcada et al., 2019).

The chromospheric cycle of ι Hor was identified by Metcalfe et al. (2010) in Ca II S-index measurements monitored from 2008 to 2010. The period length was estimated to be 1.6 yr. Thus, ι Hor is the star with the shortest period identified in the chromosphere and, therefore, a perfect target to enlarge the sample of X-ray active star, also because of its young age.

The X-ray monitoring campaign started in 2011 with the *XMM-Newton* satellite (PI Sanz-Forcada J.; CoI Stelzer B.), and regularly continued until 2018. In the course of this campaign, the X-ray cycle of ι Hor was discovered (section 5.1,Sanz-Forcada et al. (2013)). In the years following the discovery, the X-ray monitoring of ι Hor continued and a multi-wavelength study of this target was carried out by Sanz-Forcada et al. (2019). Part of this latter work on ι Hor is included in my PhD project and the details are discussed in section 5.2.

5.1 The discovery of the shortest coronal X-ray cycle

In first published study on ι Hor the observations collected with *XMM-Newton* were in total 14, acquired from May 2011 to February 2013. ι Hor was observed with all instruments on board of *XMM-Newton*, but in the article on the discovery of the X-ray cycle Sanz-Forcada et al. (2013) focused only on the EPIC observations.

In Figure 5.1.1 the long-term lightcurve of ι Hor is plotted. The red squares represent the X-ray luminosity calculated from the EPIC spectra. The black circles are the Ca II S-index data, where the filled symbols are the measurements discussed by Metcalfe et al. (2010), dating from 2008 to 2010, whereas the open circles are the Ca II data acquired after the publication of the chromospheric cycle. Overplotted with a solid line in the lightcurve, there is also the sinusoidal fit calculated by Metcalfe et al. (2010) considering the Ca II data from 2008 to 2010. The dashed line is instead the sinusoidal fit obtained from the Ca II data dating from 2010.

The variability found by Metcalfe et al. (2013) for the Ca II S-index data until 2010 highlights the presence of a chromospheric cycle of 1.6 yr. However, after 2010 the Ca II S-index data had an erratic

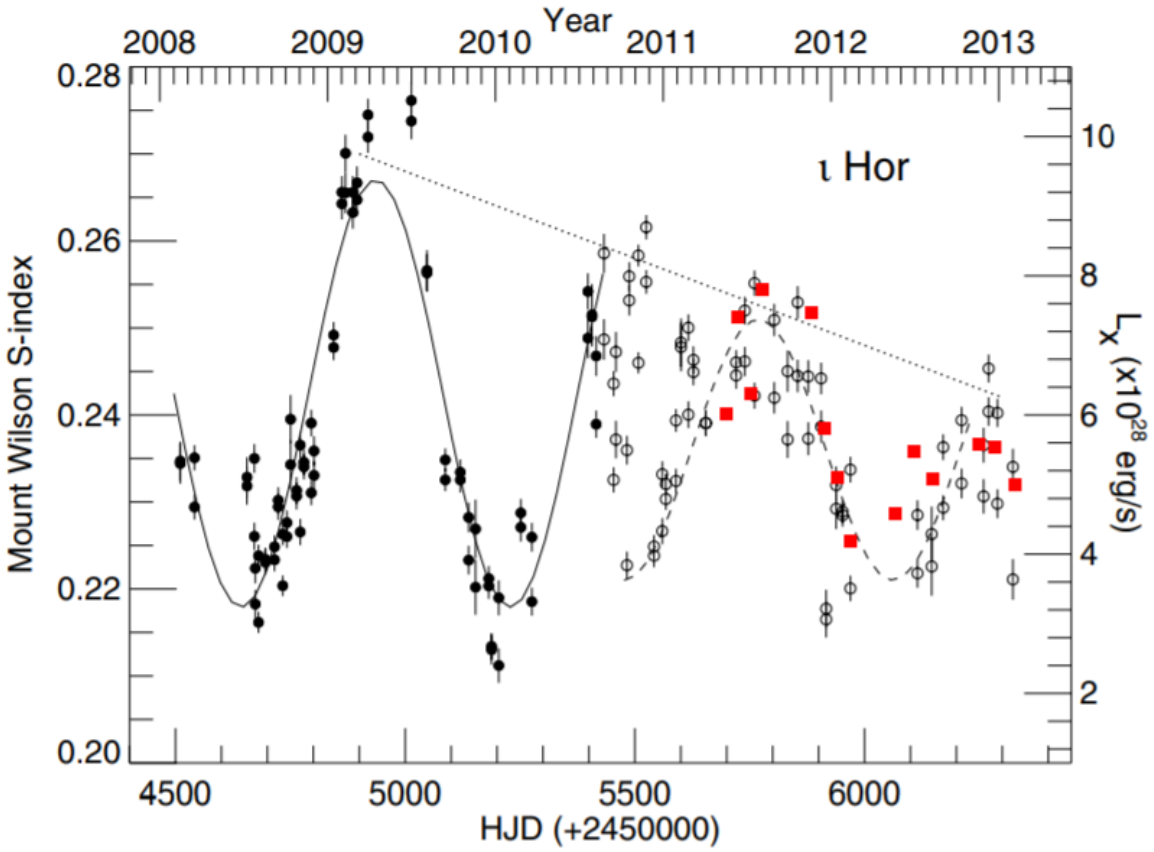

Figure 5.1.1: Lightcurve showing the long-term activity of ι Hor (Sanz-Forcada et al., 2013). The red squares are the X-ray luminosities calculated from the EPIC spectra. The black circles are the Ca II S-index data, where the filled symbols are the measurements published by Metcalfe et al. (2010) and the open symbols are the Ca II S-index data acquired after the study of Metcalfe et al. (2013). The solid line is the sinusoidal fit calculated from the chromospheric data. The dotted line highlights the changes in phase and amplitude of the activity cycle that occurred after 2010.

behaviour, returning after few months to show a periodic variability. Although the period length did not change, the cycle period shows a smaller amplitude with respect to the previous signal. The change of the amplitude of the cycle is highlighted in Figure 5.1.1 with the dotted line. From this lightcurve, it is also visible how Ca II cycle seems to change again at the end of 2013.

The X-ray observations cover only the latter measurement of the Ca II data. From the spectral analysis of EPIC spectra, Sanz-Forcada et al. (2013) calculated the X-ray luminosity. It is clear from the plot that X-ray luminosities are in agreement with the sinusoidal variability of the Ca II data, confirming thus the presence of a coronal X-ray cycle.

Overall, this study provided the evidence of a short X-ray cycle of a duration of 1.6 yr, the shortest measured up to date, that, however, shows also changes on a timescale comparable to the cycle duration itself. Sanz-Forcada et al. (2013), therefore, suggested the presence of a second cycle.

5.2 Multi-wavelength study of the activity cycle of ι Hor

A second article on the long-term X-ray monitoring campaign of ι Hor was published in 2019 (Sanz-Forcada et al., 2019) to which I have contributed. My contribution to this study was in particular to investigate if the changes seen previously in the chromospheric cycle were also present in the coronal cycle (subsection 5.2.1) and to assess the presence of chromospheric excess in the optical/UV observations of *XMM-Newton* (subsection 5.2.2).

5.2.1 First seven years of X-ray observations

In the years after the discovery of the activity cycle (Sanz-Forcada et al., 2019), the *XMM-Newton* observations of ι Hor continued until 2018. Also the monitoring of the Ca II S-index continued over the years. With the larger X-ray database, it was possible to run a period search algorithm on the X-ray lightcurve. First I run a Lomb-Scargle periodogram analysis (see section A.1) on the complete X-ray data set, comprising 32 observations in total. In Figure 5.2.1a the periodogram is shown.

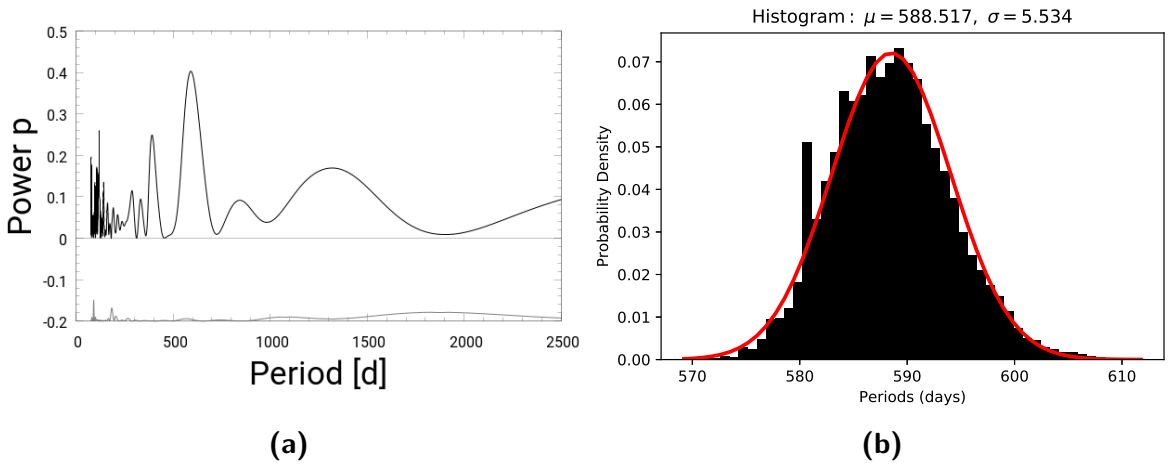

Figure 5.2.1: *Left panel*: the Lomb-Scargle periodogram of X-ray luminosity of ι Hor (Sanz-Forcada et al., 2019) *Right panel*: the distribution of the 1000 peaks found from the Monte-Carlo simulation of the X-ray lightcurve. On the top of the figure, the center of the best-fitting Gaussian model (μ) and its standard deviation (σ) are reported.

The most significant peak was found at 588.5 ± 5.5 days, i.e. at 1.61 ± 0.02 yr. The uncertainty on the period was found through Monte-Carlo simulations. The X-ray lightcurve was simulated 1000 times: each X-ray value of the luminosity was assumed as the mean of a normal distribution and from this a set of 1000 normally distributed random numbers were generated for each data point, having thus 1000 simulated lightcurves. For each simulated lightcurve I then performed the Lombe-Scargle analysis. The corresponding significant peaks were normally distributed. In Figure 5.2.1b the distribution of the 1000 significant peaks are shown. After having fitted the distribution of the periods with a Gaussian model (solid red line in Figure 5.2.1b), I adopted the standard deviation of the best-fitting model as the error of the period.

From the Lomb-Scargle analysis of the X-ray lightcurve, I obtained also the amplitude and the phase of the sinusoidal function that best represent the X-ray activity cycle of ι Hor. From the spectral analysis of the EPIC observations, I obtained the X-ray luminosities. In Figure 5.2.2 the long-term lightcurve of ι Hor is again showed, this time displaying the data of the full 2011-2018 X-ray campaign. The red squares are the X-ray luminosity obtained from the EPIC spectra, whereas the open circles are the Ca II S-index measurements collected during the time-span covered by the X-ray observations. The dashed line is the sinusoidal function obtained from the Lomb-Scargle periodogram analysis applied to the X-ray luminosity. The mean X-ray luminosity throughout the cycle is $\overline{L}_X = 5.8 \times 10^{28}$ erg/s

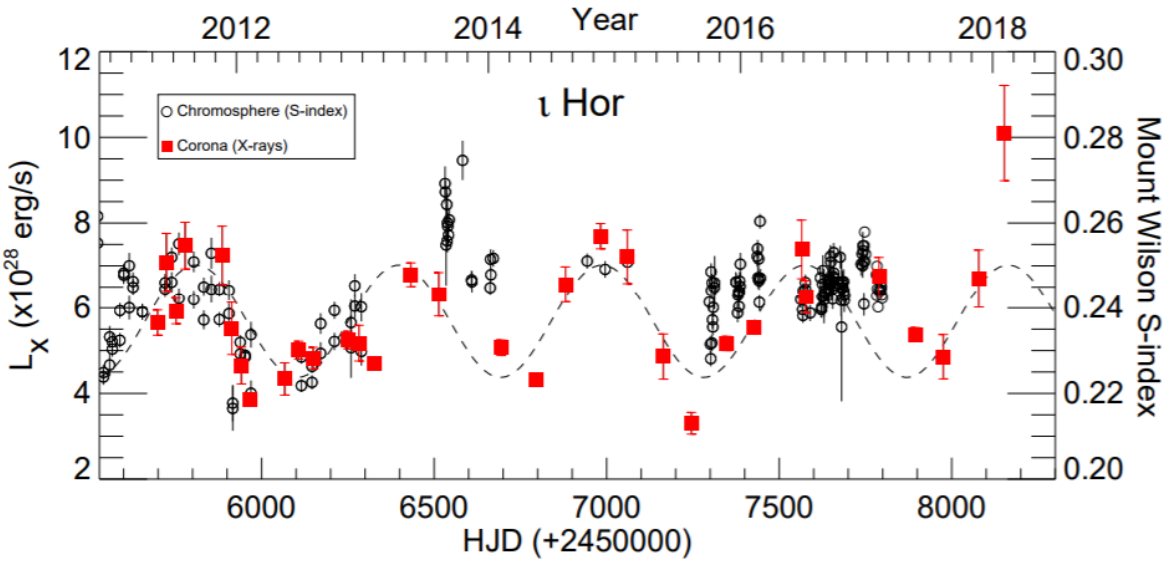

Figure 5.2.2: Long-term lightcurve of ι Hor (Sanz-Forcada et al., 2019). The red squares are the X-ray luminosity calculated from the EPIC spectra. The open circles are the chromospheric S-index values. The dashed line is the sinusoidal fit obtained from the X-ray luminosity values of ι Hor.

with an amplitude $\Delta L_X = 1.4 \times 10^{28}$erg/s.

In Figure 5.2.2 it seems that the Ca II S-index data show again an erratic behaviour between 2013 and 2017, similar to that seen in 2011 just before the start of the X-ray monitoring of ι Hor (Figure 5.1.1). However, the X-ray variability does not show the same trend: the coronal cycle is indeed more regular in duration and amplitude than its chromospheric counterpart. A possible explanation is given by Sanz-Forcada et al. (2019) and is based on the geometry of the star. Because the rotation axis inclination of ι Hor is $i \sim 56^{\circ}$, the chromospheric activity might come from one of the stellar hemispheres and the irregularities might be due to the other more occulted hemisphere. However, since the X-ray emission originates in the corona that is more extended and optically thin, the irregularities due to that effect should be less evident, as the X-ray observations of ι Hor seems to support.

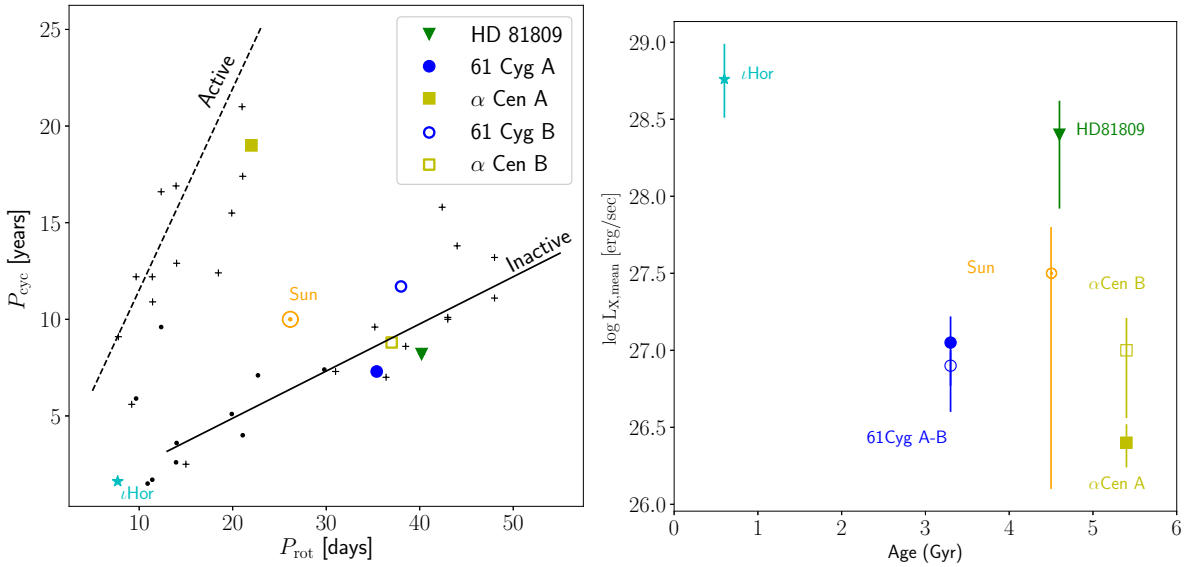

Figure 5.2.3: *Left panel*: $P_{cycl} - P_{rot}$ diagram with ι Hor included in the X-ray sample. The coding of the plot is the same as in Figure 3.3.1. *Right panel*: X-ray luminosity as function of the age with ι Hor included in the X-ray sample. I recall here that the vertical bars represent the amplitude of each X-ray cycle (see section 3.3).

To summarize ι Hor shows an X-ray activity cycle with a 1.6 yr period, consistent with its chromospheric Ca II H&K cycle. Together with its young age, ι Hor is the youngest star with a detected cycle and it exhibits the shortest cycle period. In Figure 5.2.3, I present again the $P_{cycl} - P_{rot}$ diagram and the X-ray luminosity-age relation and I include ι Hor among the other X-ray active stars. It can be seen

that ι Hor is different from the other stars with known X-ray cycle. First, its X-ray luminosity is higher than that of the stars with previously discovered coronal cycles (Figure 5.2.3b), as we might expect because young stars show high X-ray luminosity and fast rotational period. Moreover, the amplitude of ι Hor's X-ray cycle is among the smallest. In Sanz-Forcada et al. (2019), it was hypothesized that a high coronal surface coverage fraction with active structures might cause these findings: the high X-ray luminosity suggests that much of the surface is covered with X-ray emitting regions even during the minimum of the cycle, thus naturally limiting any possible variation throughout the cycle (i.e. leading to small cycle amplitude).

With ι Hor in this picture, the questions, that this PhD aims to answer and presented in the Introduction of this thesis, are strengthened and more stars with similar characteristics to ι Hor need to be observed in the X-ray. In this sense, ε Eridani and Kepler 63 are two suitable targets as it is presented in chapter 6, chapter 7 and chapter 8.

5.2.2 Search for a chromospheric excess

During the monitoring campaign of ι Hor, the star was also observed by the OM on board of *XMM-Newton* with the UVW2 filter ($\lambda = [1800 - 2600]$ Å) and the UVM2 filter ($\lambda = [2000 - 2800]$ Å). In Figure 5.2.4, the UV fluxes calculated from each observation of ι Hor are plotted. From this lightcurve, it is evident that there is no variability compatible with the activity cycle of the star. Moreover, we found that the time-averaged observed flux densities are $F_{\mathrm{UVW2}} = (1.67 \pm 0.01) \times 10^{-12}$ erg/s/cm^2/Å and $F_{\mathrm{UVM2}} = (1.84 \pm 0.06) \times 10^{-12}$ erg/s/cm^2/Å..

The flux density observed in the UV is a combination of contributions coming from the photosphere and the chromosphere. Thus, it is interesting when characterizing an active star to see if a chromospheric excess ($F_{\mathrm{UV,exc}}$), attributed to the activity, is present. In order to do so, I calculated the $F_{\mathrm{UV,exc}}$ as the difference between the actual flux density observed by the OM in the two UV filters and the flux density predicted from photospheric atmosphere models in the corresponding wavebands. Moreover, the excess flux density was also calculated for the *GALEX*[1] measurement (Shkolnik, 2013) in the far ultraviolet band (FUV; $\lambda_{\mathrm{FUV}} = [1350 - 1750]$ Å).

The first step was to identify the photospheric model that best describes the spectral shape of ι Hor at the visible and infrared wavelengths, where there is no chromospheric contribution to the emission. To this end, I retrieved all published photometric data of ι Hor, using the VizieR database[2]. The sub-

[1] The *Galaxy Evolution Explorer (GALEX)* was an orbiting ultraviolet space telescope which was launched by NASA in 2003 and dismissed in early 2012.

[2] http://vizier.unistra.fr/vizier/sed/

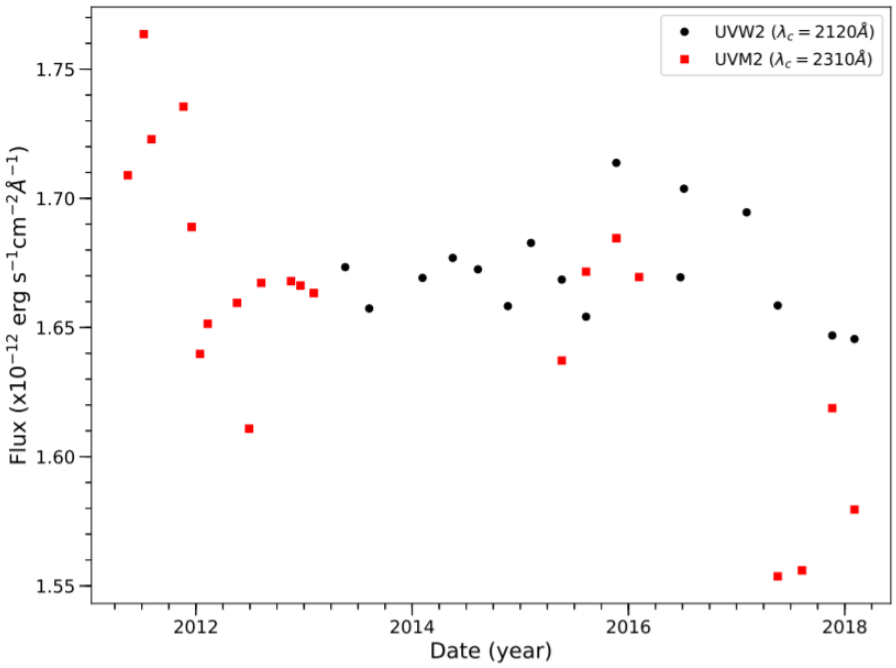

Figure 5.2.4: UV lightcurve of ι Hor obtained with the OM on *XMM-Newton* (Sanz-Forcada et al., 2019).

sequent analysis was performed with the online tool Virtual Observatory SED Analyzer (VOSA; Bayo et al., 2008). In Figure 5.2.5 all the photometric data, except for the OM flux densities, are shown.

The spectral energy distribution (SED) of ι Hor was then fitted using the spectral model BT-Settl-CIFIST (Baraffe et al., 2015) in the VOSA environment. BT-Settl-CIFIST is a grid of theoretical spectral models of stellar atmospheres, where each model of the grid has a certain value of effective temperature ($T_{\rm eff}$), gravity (g) and photometric abundances. The fitting serves to find the grid point that best matches ι Hor.

Since the SED based on the photometry is sensitive to $log\ (g)$ and the metal abundance $[Fe/H]$, I could effectively only determine the effective temperature of ι Hor. I, thus, chose those spectral models in the grid that have the closest values of gravity and metallicity to the ones found in the literature for ι Hor, i.e. $log\, g = 4.37 \pm 0.10$ and $[Fe/H] = 0.15 \pm 0.06$ dex (Fuhrmann et al., 2017). The BT-Settl grid points that come closest to these values have $log\, g = 4.5$ and $[Fe/H] = 0.$ dex. I then fitted the SED of ι Hor using those spectra and keeping as only free parameter the effective temperature. From the fitting, I thus retrieved the best value of the effective temperature, which is 6000 ± 50 K. This is in agreement with the $T_{\rm eff}$ found by Fuhrmann et al. (2017) for ι Hor from spectroscopic studies($6057 \pm$

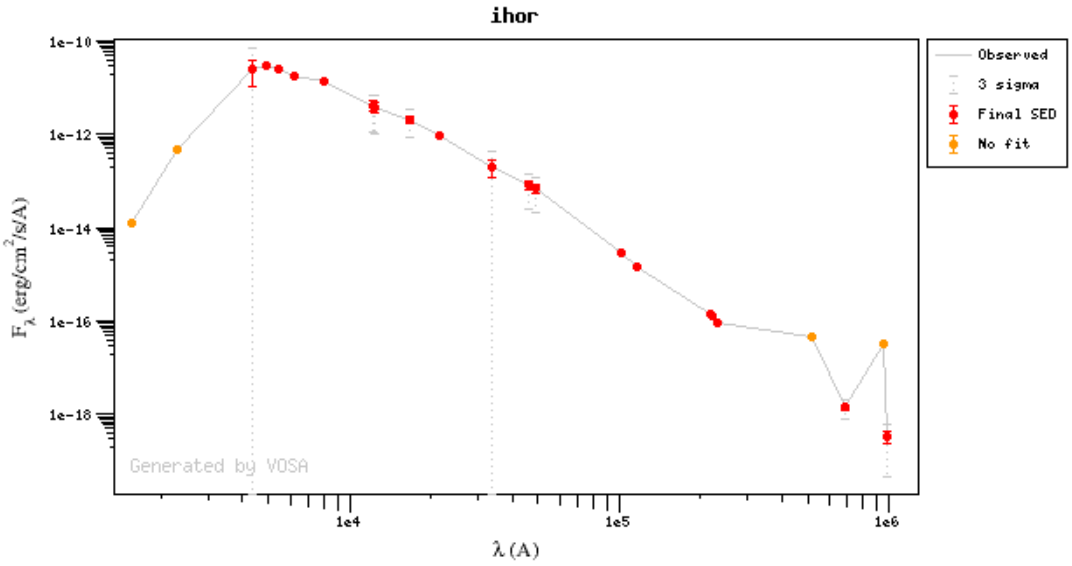

Figure 5.2.5: Spectral energy distribution of ι Hor, extracted from the VizieR catalogue.

60 K). In Figure 5.2.6 the SED of ι Hor is shown again, this time together with the best fitting BT-Settl model.

I then calculated the predicted photospheric flux, i.e. the *synthetic* flux, from the following equation:

$$F_{sy} = \int F_{mod}(\lambda)\tau_{filter}(\lambda)d\lambda. \tag{5.1}$$

Here, F_{mod} is the flux density of the best-fitting BT-Settl-CiFIST model, i.e. the spectrum with T_{eff} equal to 6000 K, $log\, g = 4.5$ and $[Fe/H] = 0$. dex. $\tau_{filter}(\lambda)$ is the normalized transmission curve of the UV filter applied in the OM observations of ι Hor (see in chapter 4 Figure 4.3.1) and of the *GALEX* instrument[3]. In Figure 5.2.7, the BT-Settl-CFIST spectrum is shown as a solid black line. In the same plot, the best-fitting model of VOSA is overplotted with the solid blue line, together with the OM and the GALEX FUV densities fluxes (magenta, green and yellow symbols respectively). The two circles and the star symbol are the flux densities seen in the waveband of interest.

Finally, I calculated the expected synthetic flux for each of the OM filters, UVM2 and UVW2, and

[3]The trasmission curve of *GALEX* is available in VOSA at the web page http://svo2.cab.inta-csic.es/theory/fps/index.php?mode=browse&gname=GALEX

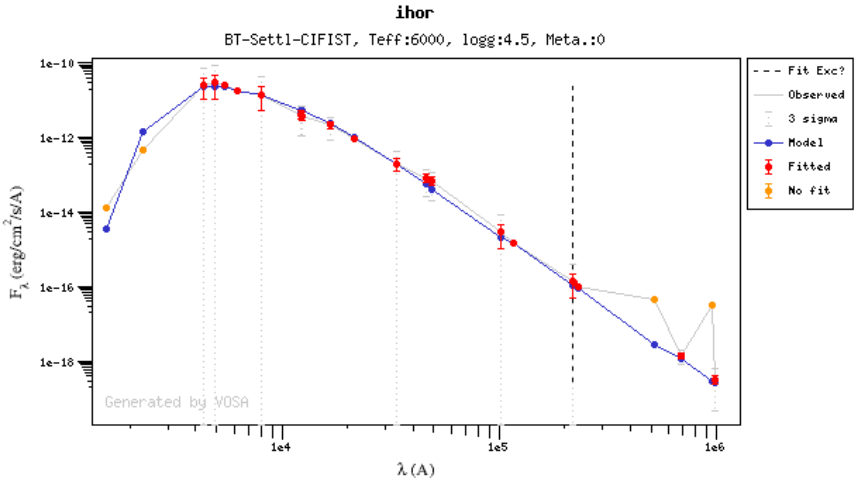

Figure 5.2.6: Fitting of the spectral energy distribution of ι Hor, performed with the VOSA tool. The red and the orange dots are the photometry values retrieved from VizeR: the orange data points are those value automatically excluded by VOSA during the fitting procedure. The dotted grey vertical bars represent a confidence level of 3σ. The blue solid line is the best-fitting BT-Settl model with $T_{\rm eff} = 6000 \pm 50$, $log(g) = 4.5$ and $[Fe/H] = 0.0$.

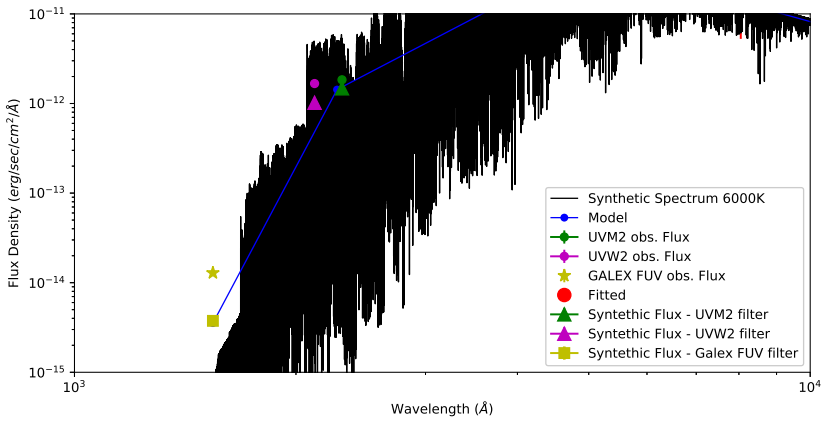

Figure 5.2.7: Synthetic spectrum (black line) and best-fitting model (blue line) that best represent the photometry of ι Hor. The yellow symbols are the observed (star symbol) and the synthetic (square symbol) fluxes of the GALEX FUV. The magenta and green symbols are the observed (filled circles) and synthetic (triangles symbols) fluxes of the OM filters UVW2 and UVM2 respectively.

for GALEX FUV using Equation 5.1, and the corresponding values are plotted in Figure 5.2.7 with the triangles and the square symbol respectively. Already from this plot, it can been noticed that the observed fluxes are greater than the fluxes predicted from the synthetic spectra. The synthetic fluxes were then subtracted to the observed density fluxes. In Table 5.2.1 the difference in percentage is reported, where it can bee seen that the chromospheric excess decrease when the wavelength increases.

Filter	λ_{eff} (Å)	$F_{\lambda,\text{obs}}$ (erg/s/cm^2/Å)	$F_{\lambda,\text{exc}}$ (%)
GALEX/FUV	1516	$(1.29 \pm 0.03) \times 10^{-14}$	71 ± 3
OM/UVW2	2120	$(1.67 \pm 0.01) \times 10^{-12}$	39 ± 4
OM/UVM2	2310	$(1.84 \pm 0.06) \times 10^{-12}$	20 ± 7

Table 5.2.1: Observed UV flux densities and chromospheric excess calculated for ι Hor (Sanz-Forcada et al., 2019).

6

The activity cycle of ε Eridani

Contents

ε Eridani (ε Eri; HD 22049) is a young solar-type dwarf star with spectral type K2V (Keenan et al., 1989). Its mass is estimated to be $0.8 M_{\odot}$ and its radius is $0.74 R_{\odot}$ (Di Folco et al., 2004). It is located in the southern constellation of Eridanus and, at a distance of 3.2 pc (van Leeuwen, 2007), is the third-closest star visible to the unaided eye. Similarly to ι Horologii (chapter 5), it is quite young: its age is estimated to be between 200 Myr and $\sim$ 900 Myr [1] (Song et al., 2000; Fuhrmann, 2004; Barnes, 2007). It hosts two Jupiter-like planets with a semimajor axis of 3.4 AU and 40 AU respectively (Hatzes et al., 2000; Quillen et al., 2002).

ε Eri was widely studied at all wavelengths, from the radio to the gamma waveband, and in particular it was part of the Mt. Wilson Project (see section 2.2). The complete Ca II data was studied and analysed by Gray et al. (1995), comprising all the observations conducted within the project from the 1960s to the 1990s. The authors had catalogued the star as a variable target, stating that the period of the chromospheric variability was $\sim$ 5 yr. Later, Metcalfe et al. (2013) found that ε Eri shows two periods, at $\sim$ 12 and $\sim$ 3 yr, by re-analysing the Mt. Wilson data and adding new chromospheric data coming from other observatories. The presence of a second short cycle, and the similarities with ι Horologii, make ε Eri the perfect target to be studied in the context of the activity cycles on young solar-like stars.

In the following sections, the chromospheric activity of ε Eri is presented, discussing the results of the literature as well as new results obtained during this PhD project (section 6.1). In section 6.2 the X-ray monitoring campaign, the heart of this PhD project, is described, presenting the X-ray data extraction (section 6.3) and the data analysis (section 6.4 and section 6.5), and discussing the main results accomplished from the project (section 6.6).

6.1 Chromospheric activity cycle

ε Eri was monitored within the Mt. Wilson project for the entire life-time of the project, i.e. from the 1960s to the 1990s. The first study of its chromospheric activity cycle was published by Baliunas et al. (1995) in the first review of all Mt. Wilson targets. The authors catalogued the star as variable target with a possible long cycle, but they did not calculate the period length. In Figure 6.1.1 the historical record of the Ca II S-index variation is shown. Later, Gray et al. (1995) dedicated a work entirely focused on ε Eri, analysing the Mt. Wilson data and finding evidence of a cycle that lasts roughly 5 years.

[1] The age of ε Eridani was found using different methods. During this PhD thesis I adopted the value of 440 Myr found by Barnes (2007) through gyro-chronology.

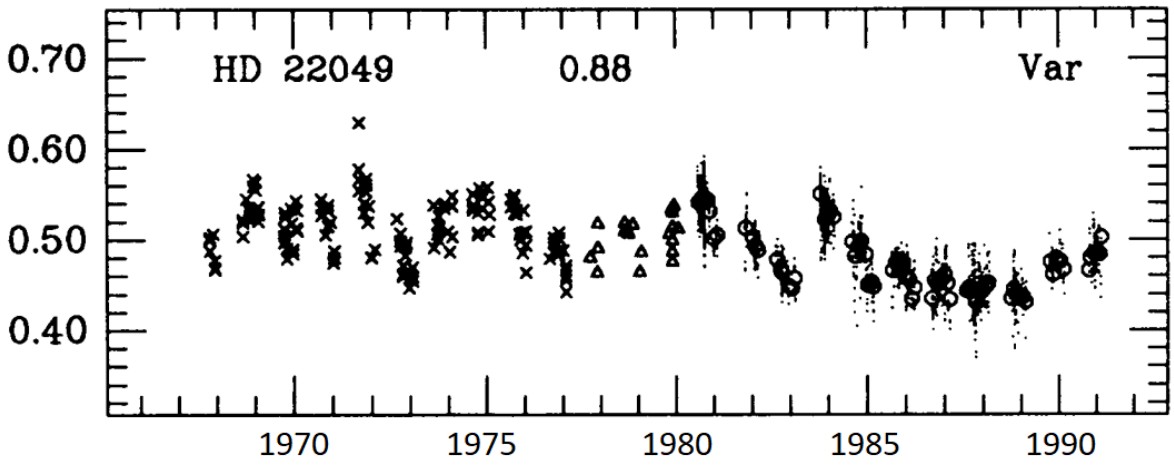

Figure 6.1.1: H&K S-index variation of ε Eri, recorded by the Mt. Wilson Observatory between the 1965 and the 1992 (Baliunas et al., 1995). The x-axis is the time where the data were acquired, whereas the y-axis are the Ca II S_{MWO} – index measurements.

The chomospheric monitoring of ε Eri did not stop with the Mt. Wilson project, but many other observatories started to observe and record its H&K S-index variation. In 2013 Metcalfe et al. (2013) published their Ca II monitoring campaign of ε Eri, started in 2007 using the Small and Moderate Aperture Research Telescope System (SMARTS) 1.5-m at Cerro Tololo Inter-American Observatory (CTIO - Chile). Moreover, the authors added to their SMARTS measurements all available published data of ε Eri, in order to cover a wide time range. In particular the additional data set comprised Ca II S-index data taken with the Solar-Stellar Spectrograph (SSS) at the Lowell Observatory from 1994 to 2013 (Hall et al., 2007); the measurements obtained at the Complejo Astronomico El Leoncito (CASLEO) in Argentina from 2001 to 2011 (Mauas et al., 2012); the data taken at the Keck Observatory in Hawaii with the HIRES instrument between 2002 and 2010 (California Planet Search (CPS); Isaacson et al. (2010)); additional published data from the HARPS spectrograph from 2004 and 2008 (Anglada-Escudé et al., 2012); the historical data of the Mt. Wilson Observatory.

The Ca II S-index is calculated according to Equation 2.1. Since the chromospheric measurements that Metcalfe et al. (2013) took into account came from different observatories, it was necessary to scale the data as if they were acquired by the same telescope. The standard procedure is to calibrate the S-index on the Mt. Wilson observatory. In order to do so, each data set of S-index measurements were correlated to the Mt. Wilson data and from a linear fitting they found the multiplicative scale factors for each data set.

To search for periodicities in their chromospheric activity measurements, they performed a Lomb-Scargle periodogram analysis (see section A.1 for the details on this analysis technique) in the whole

data set and in two subsets of the data, the first comprising measurements from 1968 to 1992, i.e. the historical Mt. Wilson data, and the second comprising the measurements from 1994 to 2012, in order to understand if the long period seen in the historical data set is still dominant. The data were also binned according to the visibility window of ε Eri (seasonal means) and to the nightly observations (nightly means). In Figure 6.1.2 the periodograms from Metcalfe et al. (2013) are shown. The Mt. Wilson Observatory historical data (1968–1992) are plotted with the red dotted line, the data in the time range 1994–2012 with the blue dashed line and the full data set (1968–2012) with the black solid line. The first subset of data (historical data set) showed a primary periodicity at roughly 13 yr and two shorter periodicities near 3 and 5 yr. The periodogram of the second data set (i.e. the most recent Ca II measurements) showed a peak at 3 yr, with a smaller peak at 7 yr.

The peaks at 5 yr and 7 yr were rejected by the authors because the first appeared only in the early observations of the Mt. Wilson Observatory and the second was associated to the orbital period of the exoplanet. The peaks at 3 and 12 yr had both a False Allarm Probability $< 10^{-6}$. Thus, they stated that these two periods are the most significant ones in the periodogram. This is an indication that, since the beginning of the chromospheric monitoring of ε Eri, its cycle has been variable and it can not be excluded that in the future other changes might occur.

Thus, I collected all available Ca II S-index measurements that cover the time range of the X-ray monitoring campaign of ε Eri (section 6.2), i.e. from 2002 up to now, in order to work with two data sets consistent with each other in terms of observational epochs. Excluding the historical S-index data is motivated by the aim to assess the most recent behaviour of the activity cycle of ε Eri where in the chromosphere the shorter cycle is dominant. The data set I built comprises the published S-index data of Isaacson et al. (2010) with the HIRES instrument, the SMARTS telescope data (Metcalfe et al., 2013) and the Lowell Observatory data (Hall et al., 2007) with the SSS instrument. The latter data set was also extended including new measurements the authors carried out in the years after their publication. Moreover, I made use of data obtained in support of this thesis with the *TIGRE* telescope at La Luz Observatory in Mexico from 2013 to 2019. All these data are published in Coffaro et al. (2020). In Table 6.1.1 a summary of the Ca II data used during this PhD project is presented.

I received the S-index already calculated from the spectra, although for some data sets it was necessary to place them onto the Mt. Wilson scale. The SMARTS data were already scaled to the common Mt. Wilson S-index (S_{MWO}-index). The TIGRE data and the Lowell data were scaled using respectively the following relations:

$$S_{MWO} = 0.0360 + 20.02 \cdot S_{TIGRE}$$

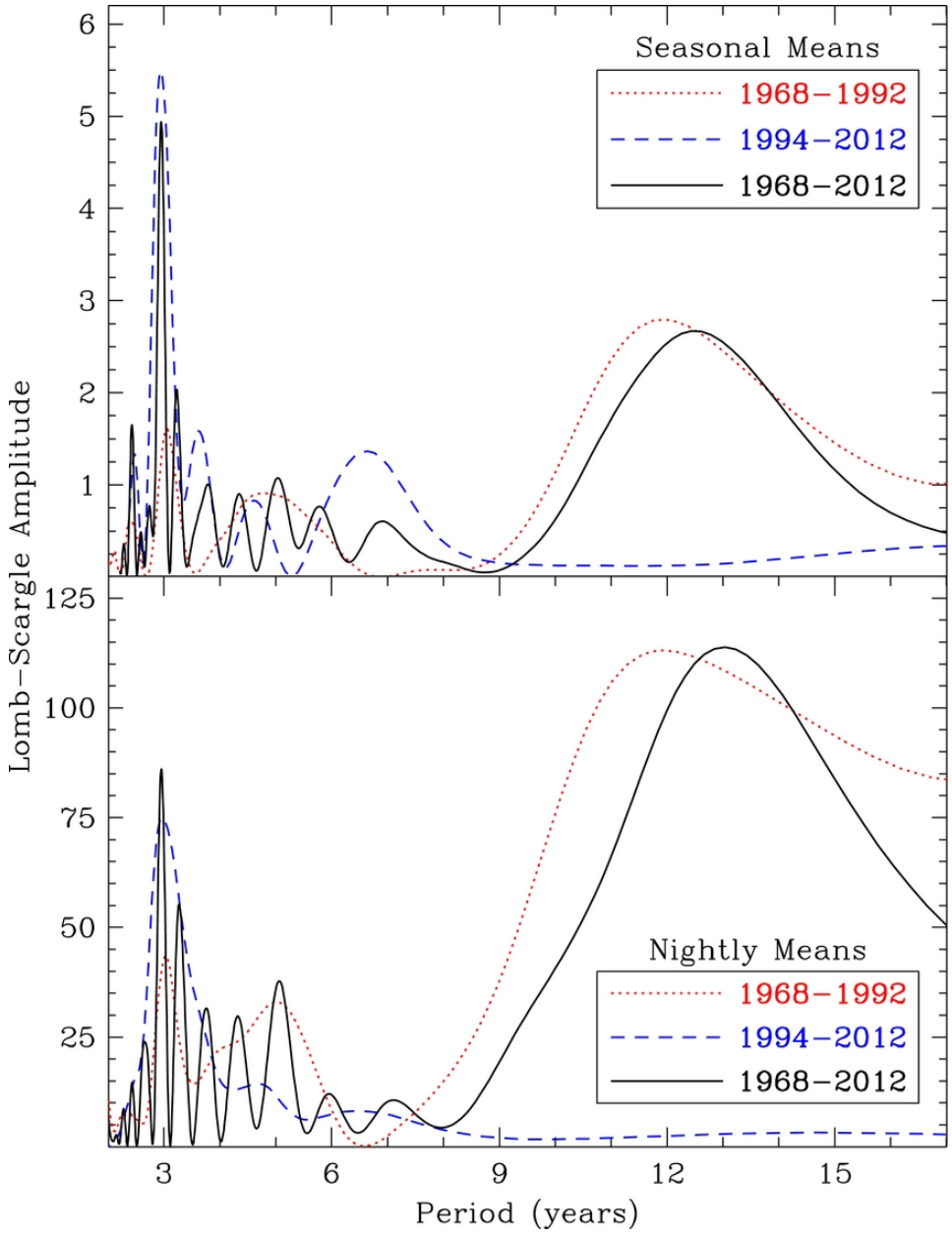

Figure 6.1.2: Lomb–Scargle periodograms of the seasonal (top panel) and nightly (bottom panel) mean S_{MWO}-index measurements published in Metcalfe et al. (2013). The Mt. Wilson Observatory historical data (1968–1992) are plotted with the dotted line, the data in the time range 1994–2012 with the dashed line and the full data set (1968–2012) with the solid line.

Instrument	No. Observations	S_{MWO}-index mean	Time range	
			published	unpublished [a]
TIGRE	86	0.514	\	2013-mid 2019
SMARTS	148	0.513	2007-2013	\
SSS	260	0.528	1994-2013	2013-2018
HIRES	168	0.511	2002-2010	\

[a] "Unpublished" means that these data were not published prior to this PhD project and they are presented for the first time in Coffaro et al. (2020).

Table 6.1.1: Ca II S-index data set analysed in this thesis. The number of collected observations for each instrument and the corresponding mean S_{MWO}-index are reported in the second and third column. The time range of the observations taken by each telescope is shown in the last columns.

$$S_{MWO} = 0.0044 + 0.976 \cdot S_{SSS},$$

according to Mittag et al. (2016) and Hall et al. (2020 in prep.).

The values of the S_{MWO}-index obtained from each instrument employed in this work are in good agreement with each other. In Figure 6.1.3 the Ca II S_{MWO}-index is plotted as function of time. The short-term scatter of the S_{MWO}-index seen in the figure is probably due to the rotational modulation of ε Eri. This was tested by performing a Lomb-Scargle analysis on each seasonal sub-set of the Ca II S_{MWO}-index. For each subset, a period comprised between 9 days and 12 days was found, values close to the 11.1 d period that was previously reported for the rotation of ε Eri (Gray et al., 1995). However, the investigation of the rotational effects was not the scope of this study.

The entire data set covers a different time range than the data set considered by Metcalfe et al. (2013). Thus, I performed again a period search by analysing the Lomb-Scargle periodogram with the software `GLS` (see subsection A.1.2 for the details on the software). In Figure 6.1.4a the periodogram and its window function are shown. The most significant peak is found at 1067.12 days, with a False Alarm Probability (FAP) of 1.5×10^{-6} (see subsection A.1.2).

To associate an error to the value of the period, I performed a Monte-Carlo simulation on the data set. I simulated 1000 data sets of Ca II S_{MWO}-index measurements: each data point was randomly drawn from a normal distribution within the observed standard deviation around the measured S_{MWO}-index. Then, I performed the Lomb-Scargle analysis for each simulated data set, obtaining 1000 values of the period. In Figure 6.1.4b the distribution of the 1000 periods is shown. From this distribution, I calculated the mean and the standard deviation applying a Gaussian fit, showed as red solid line in the

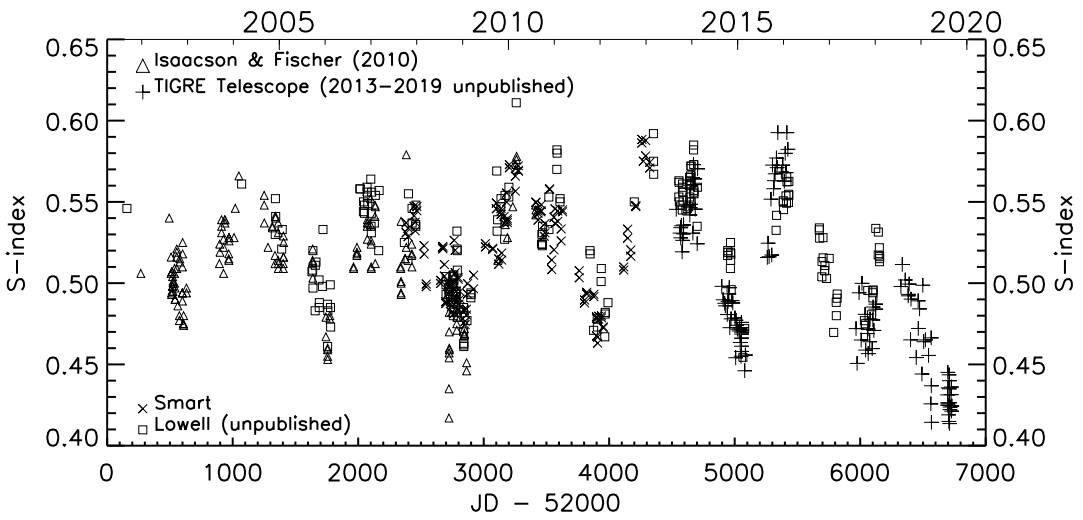

Figure 6.1.3: Ca II Mount Wilson S-index of ε Eri. The data set covers the time range from 2002 to 2019 and comprises the observations of different instruments: SMARTS telescope (cross-symbols), SSS spectrograph (squared-symbols), HIRES spectrograph (triangle-symbols) and TIGRE telescope (plus-symbols) (Coffaro et al., 2020).

figure. The resulting standard deviation is the error I associated to the value of the period. Summarizing, from the Lomb-Scargle periodogram I found the period of the data is $P_{cyc} = 1067.12 \pm 10.95$ days, equal to 2.93 ± 0.02 yr.

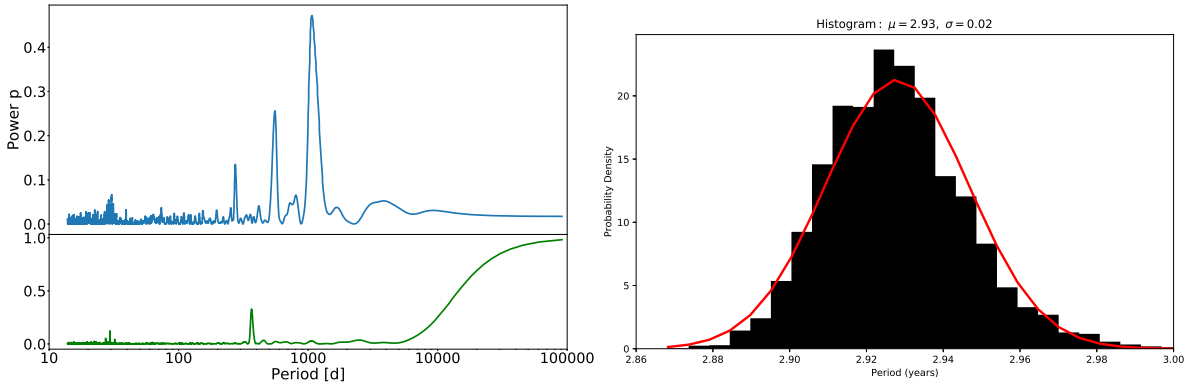

Figure 6.1.4: In the left panel, the Lomb-Scargle periodogram resulting from the GLS software, with on the bottom its window function (Coffaro et al., 2020). In the right panel, the distribution of the 1000 simulated data sets of the Ca II S_{MWO}-index measurements, with the Gaussian fit overplotted as the red solid line.

In Figure 6.1.5 the curve describing the sinusoidal variation of the data is shown. The sinusoidal function is retrieved by GLS, which as output parameters of the Lomb-Scargle analysis provides also the amplitude and the phase of the sinusoidal signal corresponding to the significant peak at 1067.12 days(see subsection A.1.2).

This analysis shows that, indeed, the short cycle identified by Metcalfe et al. (2013) in the data from 1968 to 2012 is still dominant. Interestingly, there is also a hint that the activity cycle starts to change again: from Figure 6.1.5, it is clear that the maximum expected in early 2019 did not take place, but instead the S_{MWO}-index was at a historical minimum.

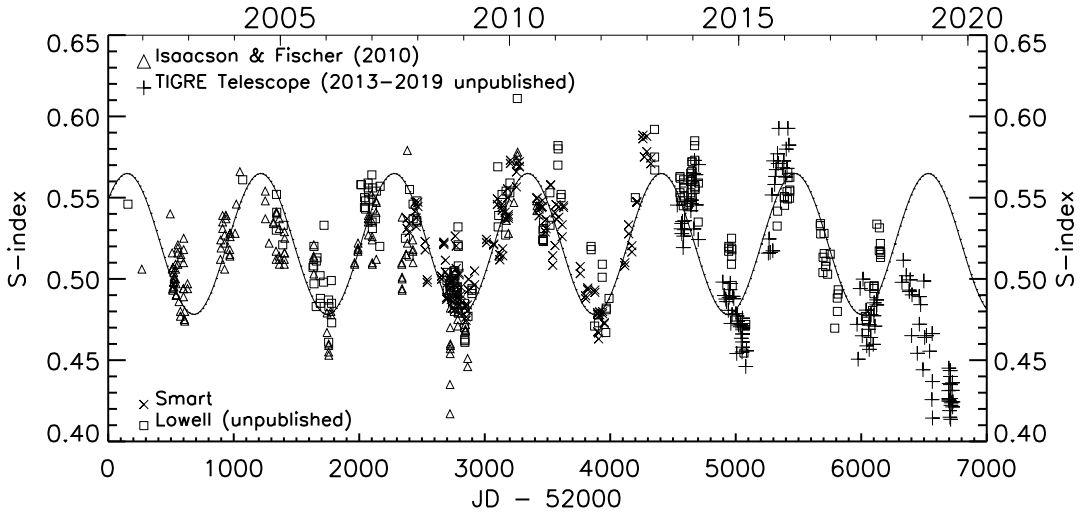

Figure 6.1.5: Same data set of the Ca II Mount Wilson S-index of ε Eri as in Figure 6.1.3 with overplotted the sinusoidal function obtained from the Lomb-Scargle periodogram analysis. The symbols have the same meaning as in Figure 6.1.3 (Coffaro et al., 2020).

The chromospheric period, found in this analysis, is used as benchmark for the X-ray data obtained from the *XMM-Newton* monitoring campaign described in the following sections.

6.2 X-ray monitoring campaign

The X-ray observations of ε Eri analysed during this PhD project comprise in total twelve snapshots taken by the *XMM-Newton* satellite (chapter 4). The dedicated campaign (PI Beate Stelzer) started in July 2015, continuously observing the star with a cadence of two observations every year. Two other observations of ε Eri were found in the *XMM-Newton* archive, dating back to January 2003 and January 2015.

The observations were carried out both with EPIC and with RGS [2]. In this PhD project I gave priority to the EPIC/pn observations. The RGS data were extracted and a preliminary analysis was performed. In chapter 9 more details are provided on the RGS data, in particular discussing the future prospective that these data offer.

In Table 6.2.1 the observing log of all EPIC observations of ε Eri is given, where the chosen operating mode of the detectors and the exposure time of each observation are shown. The first two observations, found in the archive, were taken in the Full Frame and Large Window mode respectively. Since the Full Frame mode is the one affected the most by the OoT events, the subsequent observations were taken in Small Window mode (see section 4.1).

Date	ID	Science Mode	Exposure Time	
		EPIC	EPIC/pn	EPIC MOS
2003-01-19	0112880501 [a,b]	Full Frame	11.5 ks	13.2 ks
2015-02-02	0748010101 [a,b]	Large Window	16.7 ks	18.7 ks
2015-07-19	0760490301 [b]	Small Window	6.5 ks	6.7 ks
2016-01-31	0760490401 [b]	Small Window	7.7 ks	7.9 ks
2016-07-19	0780240101 [b]	Small Window	8.9 ks	9.7 ks
2017-01-16	0780240201 [b]	Small Window	6 ks	6.3 ks
2017-08-26	0801160301 [b]	Small Window	8.8 ks	8.9 ks
2018-01-16	0801160401 [b]	Small Window	6.5 ks	6.7 ks
2018-07-20	0820070201 [b]	Small Window	19.6 ks	20 ks
2019-01-19	0820070301	Small Window	17 ks	15.8 ks
2019-07-19	0843450301	Small Window	7.7 ks	7.4 ks
2020-01-19	0843450401	Small Window	6.8 ks	6.5 ks

[a] Archival observations carried out prior to our *XMM-Newton* campaign.
[b] published in Coffaro et al. (2020)

Table 6.2.1: Observation log of EPIC data of ε Eri.

[2] ε Eri was not observed in the optical/UV waveband because of its magnitude that in the visual band is $\sim$ 3 mag. Thus, this value is higher than the brightness limit of the *OM* (section 4.3)

6.3 XMM-Newton EPIC data extraction procedures

In the following section, the data reduction of the X-ray observations of ε Eri is described. The set of *XMM-Newton* data files, corresponding to each given observation, is composed of the so-called *Observation Data Files* (ODF). These files include raw event science files, commonly called *event lists*, from the EPIC and RGS detectors, ready to be extracted and analysed using the software *Science Analysis System* (SAS; v 17.0.0; ESA: XMM-Newton SOC, 2019).

In section 6.3, the steps to generate calibrated and cleaned event lists of the EPIC camera are described. The extraction procedure of EPIC event lists consists of three steps:

1. Preparation of the analysis environment To carry out the analysis correctly it is necessary to create the *Calibration Index File* (CIF): this file comprises a list of the necessary calibration data appropriate for the observations and they are created with the SAS task `cifbuild`. In addition to the CIF, it is also required to create the ODF summary file using the SAS task `odfingest`.

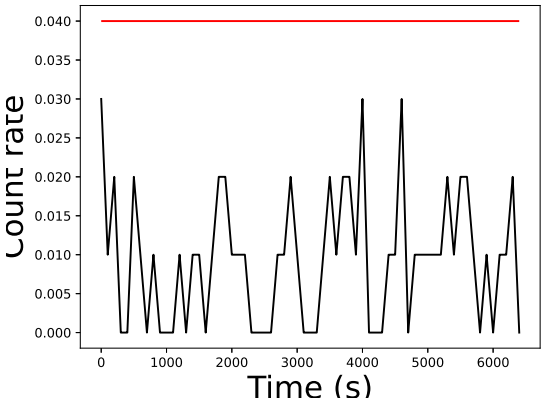

Figure 6.3.1: Detector background lightcurve in one of the EPIC/pn observations of ε Eri. The observation is the one of July 2015. The red solid line is the chosen threshold for the GTI.

2. Calibration of the event lists As discussed in chapter 4, EPIC event lists need to be cleaned from background events of different nature that can undermine the quality of the final scientific products. The first cleaning handles the background events of instrumental nature, such as bad pixels of the CCDs, events registered outside the field of view of the detectors, readout noise, dead pixels, etc. The elimination of this kind of events is achieved by the SAS task `evselect` using a filtering option that includes the minimum energy, *PI*, at which the source is detected and a set of flags, XMMEA_EP (pn) and XMMEA_EM (MOS), that encode all the instrumental bad events of the CCDs. In this analysis the minimum *PI* was set on 0.15 keV for both EPIC detectors.

The second cleaning of the EPIC event lists is the determination of the so-called *Good Time Intervals* (GTIs), a table that includes the time intervals where there is no high background. In order to define

this table, the first step is to produce the high energy background lightcurve: this is also achieved by the task `evselect` with the additional option `withrateset` that generates as output the lightcurve of the detector. By inspecting this lightcurve, the appropriate count rate used as threshold for the GTI can be defined. Usually, for standard observations a good reference value of the count rate is 0.4 cnt/s for the EPIC/pn and 0.35 cnt/s for EPIC MOS: all time intervals within these threshold are stored in the GTI table. In the case of ε Eri, I applied the standard cuts suggested by the manual. In Figure 6.3.1, an example of the detector background registered in one of the observations is shown. In this plot also the standard cut at 0.4 cnt/s is highlighted as red solid line.

A final (and optional) step in the calibration of the event lists is to apply a filtering for the energy: the user can decide to have the final cleaned event list restricted to a particular energy band of the satellite. In general, the most used energy bands are: the soft band, from 0.2 keV to 2. keV; the hard band, from 2 keV to 12 keV; the XID band, from 0.5 keV to 4.5 keV; the total energy band of EPIC, from 0.2 keV to 12 keV. The observations of ε Eri were all extracted in the soft energy band.

3. Source detection and extraction of the scientific products Using the filtered event list, now it is possible to carry out the source detection, i.e. generating a single list of the sources detected in an EPIC image, as well as a number of associated products such as background and sensitivity maps. The list of the detected sources in the images is a region file that can be easily overplotted on the image the user is analysing and that also comprises the count rates in the selected energy bands and the coordinates of each identified source. In the case of ε Eri, the source region successfully detected the star in all observations. In the Figure 6.3.2, two examples of the source detection performed on ε Eri are shown: on the left the source detection for the observation in Full Frame mode of January 2003 is shown; on the right the one for the observation in Small Window mode of July 2015 is shown. On these images, the regions of the sources detected with the source detection procedure are overplotted in blue, whereas in red there are the regions chosen to be the background regions (dashed line) and the source regions (solid lines), these latter centred on the coordinates resulting from the source detection.

After having identified the two regions for the source and the background, the lightcurves and the spectra of the target can be extracted from the event lists. The lightcurves are extracted with the SAS task `evselect`: the additional options applied on the task include a spatial filtering, where the source and background regions are given as input, and the option `timebinsize`, where the size of the time bin is given. The lightcurves of ε Eri were all extracted by choosing a time bin size of 300 seconds. The outputs of this task are the lightcurve extracted in the background region (background lightcurve)

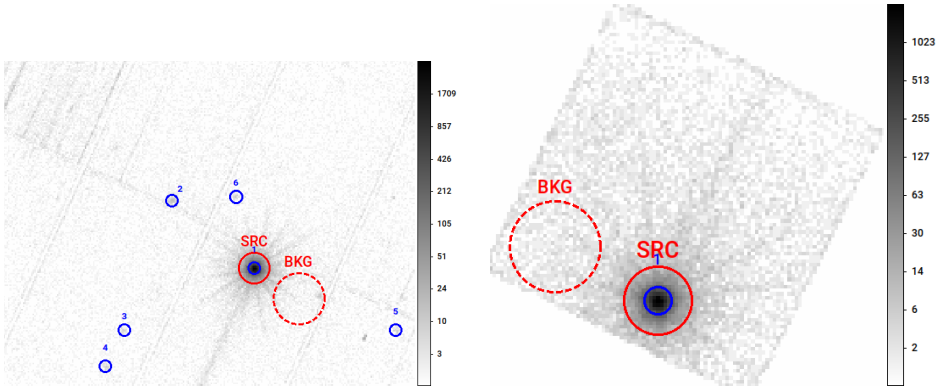

Figure 6.3.2: Two images of ε Eri observations taken with the EPIC/pn instrument. On the left the observation of January 2003 in Full Frame mode. On the right the one of July 2015 in Small Window mode. The solid blue lines denote the targets detected by the source detection procedure. The red lines are the region chosen for the source (solid lines) and the background (dashed lines) for the extraction of lightcurves and spectra.

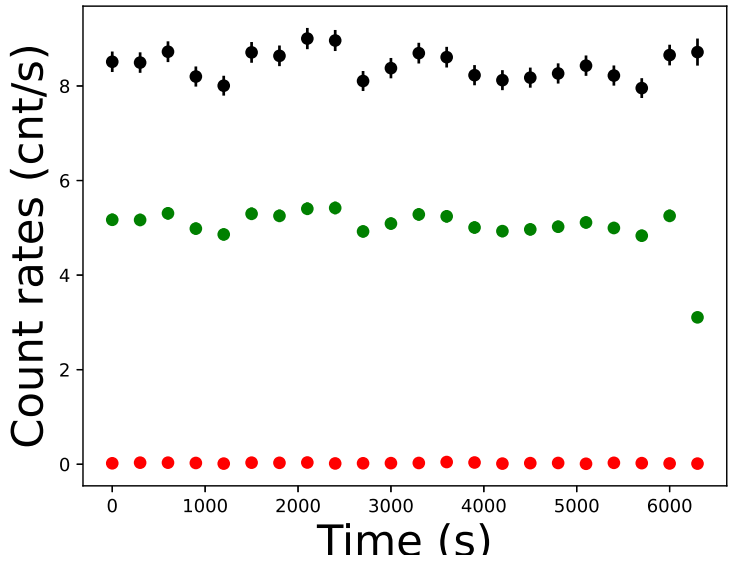

Figure 6.3.3: Example of a X-ray lightcurve of ε Eri. The observation is the one of July 2015. The background-subtracted lightcurve is plotted with black symbols. The background lightcurve is plotted with red symbols, whereas the green symbols represent the source lightcurve.

and the lightcurve of the source region (source lightcurve, not yet corrected from the background). The final step is then to subtract the lightcurve of the background region from the one of the source region, having at the end a background corrected lightcurve ready to be analysed. This latter task

is not a simple subtraction between background and source count rates, but SAS takes into account technical effects on the cameras such as the exposure correction, that is the time inside each frame where the CCD is taking data correctly, and the dead time correction, that is the time where the CCD is not active. These corrections influence the background-subtracted lightcurve by making the count rates greater than the ones of the source lightcurve. In Figure 6.3.3, an example of EPIC/pn lightcurve of ε Eri is shown. The final lightcurve, i.e. the background-subtracted lightcurve, is plotted with the black symbols. The background lightcurve and the source lightcurve are plotted with the red and green symbols respectively.

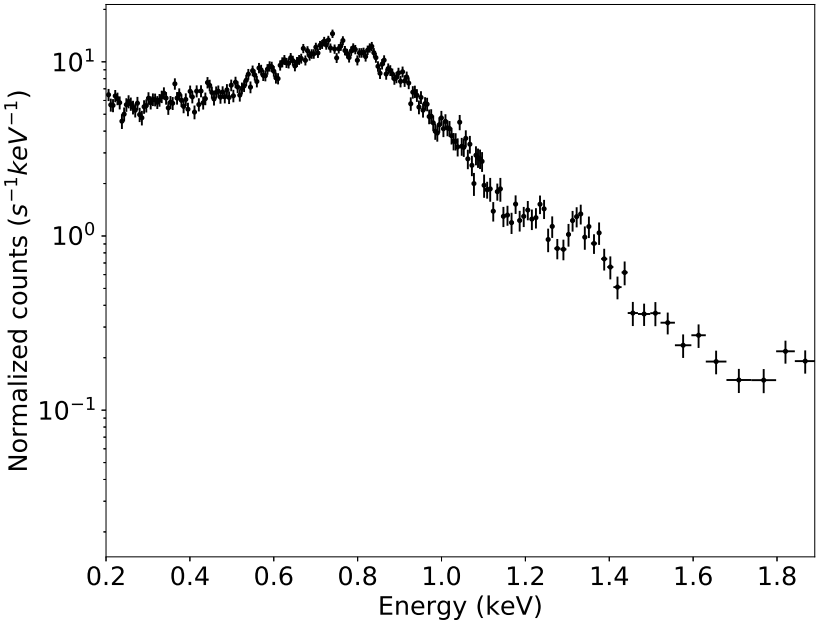

Figure 6.3.4: Example of EPIC/pn spectrum for one of the observations of ε Eri. The observation is the one of July 2015.

The spectra are extracted in a similar way: the SAS task `evselect` is also used where in this case the additional option is `withspectrumset`. The outputs are one spectrum for the source region and one for the background region. Both spectra are scaled to the area of the chosen region with the command `backscale`. A second step is to generate the Redistribution Matrix File (RMF) and the Ancillary Response File (ARF). The software used for analysing the spectra requires a characterization of the EPIC detector response to simulate an output spectrum. The response function gives the probability that an incoming photon of energy E will be detected in a channel I. This discrete function can be calculated as a product of the RMF by the ARF. The RMF is obtained using the SAS task `rmfgen`, whereas the ARF with the task `arfgen`. The final step is then to group all these outputs into a single

file, in order to simplify the uploading of the spectra to the analysis software. This is achieved by the SAS task `specgroup` where also the minimum number of counts for each energy bin is specified. The spectra of ε Eri were all grouped with a minimum of 40 counts per bin. An example of EPIC/pn (background-subtracted) spectrum is shown in Figure 6.3.4.

During the extraction procedure of the spectra, the Out-Of-Time (OoT) events are also removed. Among all the possible options, the SAS task `evselect` also provides the possibility to extract the spectra limited to the OoT events for each observation. Once these spectra are extracted, the counts in each energy channel are first scaled to the percentage of OoT events that is given by the observing mode dependent ratio of readout time and integration time. The values corresponding to each scientific mode can be retrieved from the XMM-Newton User Handbook (XMM-Newton SOC, 2019). In Table 6.3.1 I show the percentage of OoT events that influence the scientific mode used to observe ε Eri. As final step, the scaled spectra of the OoT events are then subtracted from the spectra of the whole observations.

Detector	Scientific Mode	Fraction OoT (%)
EPIC/pn	Full Frame	6.3
	Large Window	0.16
	Small Window	1.1

Table 6.3.1: EPIC/pn Out-of-Time (OoT) events. The percentage of OoT events is given by the mode dependent ratio of readout time and integration time (XMM-Newton SOC, 2019).

6.4 Analysis of the EPIC X-ray lightcurves

The EPIC lightcurves were all extracted in the soft energy band and with a time bin size of 300 s (see section 6.3). In Table 6.4.1, the mean count rates registered in each observation are reported. The values are obtained as the average over all count rates of each lightcurve and the uncertainties are the standard deviation.

The EPIC/pn lightcurves were systematically checked for short-term variability in the count rates during the observation with the *changepoint* routines in the R statistics packages (see section A.2 for the details of this analysis technique). In Appendix B the lightcurves of all observations and their segmentations are shown. Each segmentation in the lightcurve denotes a change in mean and variance of the count rate registered during the given observation, i.e. the lightcurve shows short-term variability.

Date	Average count rates	
	EPIC/pn (cnt/s)	EPIC MOS (cnt/s)
January 2003	6.2 ± 0.7	1.5 ± 0.2
February 2015	5.4 ± 0.3	1.3 ± 0.2
July 2015	8.4 ± 0.3	1.8 ± 0.1
January 2016	8.1 ± 0.2	1.8 ± 0.1
July 2016	9.8 ± 1.1	2.2 ± 0.3
January 2017	7.4 ± 0.4	1.6 ± 0.1
August 2017	6.7 ± 0.4	1.5 ± 0.1
January 2018	10.1 ± 0.7	2.3 ± 0.2
August 2018	10.7 ± 1.2	2.4 ± 0.3
January 2019	5.8 ± 0.5	1.2 ± 0.2
August 2019	9.5 ± 1.7	2.1 ± 0.4
January 2020	6.0 ± 0.4	1.3 ± 0.1

Table 6.4.1: Average count rates measured in each lightcurve of ε Eri. The errors are the uncertainties calculated as the standard deviation of the count rates.

According to this analysis, six out of twelve observations show this variability. These observations are the ones from January 2003, July 2016, January 2018, August 2018, January 2019 and August 2019.

In the context of the study for searching for stellar X-ray flares in the *XMM-Newton* catalogue, Pye et al. (2015) presented a large-scale survey of X-ray flare emission analysing more than 3000 EPIC lightcurves of solar-like stars. These lightcurves were characterized by a variability in the count rate and Pye et al. (2015) catalogued these changes as: *flare*, when the variability corresponds to a clear rise and fall towards a quiescent state; *trend*, when there is either a rise or a fall in the count rate during the observation; *gradual*, when there is a rise and then a fall of the count rate, but without a fast rise; *indeterminate*, when the changes of the count rate do not show an evolution similar to any of those mentioned above. Adopting these definitions, the lightcurves of ε Eri with short-term variability are not showing clear *flare* events, but rather a *gradual* and *indeterminate* variability. Thus, these increases in the count rates can be better defined as *flare-like* events. In Figure 6.4.1, one of the lightcurves presented by Pye et al. (2015) (panel a) is shown and compared with one of the lightcurves of ε Eri (panel b). In panel a, the top plot is the EPIC/pn lightcurve of the star HD 14716, whereas the bottom panel is the corresponding observation acquired by the *XMM-Newton* OM instrument where there is an increase similar to the X-ray short-term variability. In panel b, the solid red line denotes the variability found with the `changepoint` procedure in the observation of ε Eri. Here, the short-term change seems to belong to the *gradual* category since the highest value of count rate is reached slowly.

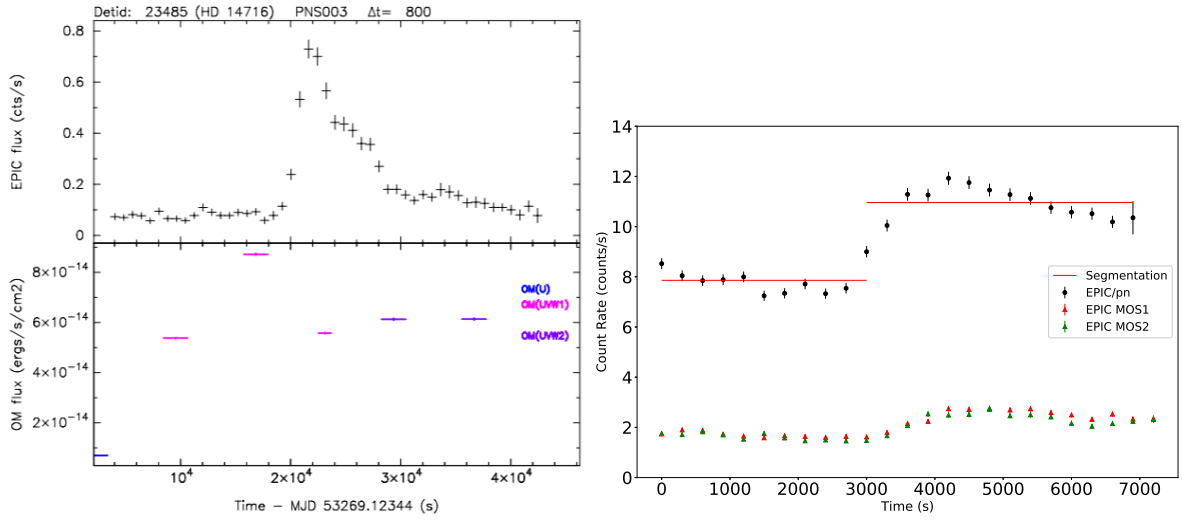

Figure 6.4.1: Panel a: example of an X-ray flare observed in the star HD 14716 by *XMM-Newton* (Pye et al., 2015). The top panel is the EPIC/pn lightcurve with a bin size (Δt) of 800 seconds. The bottom panel is the OM lightcurve, where an increase of the count rate similar to the X-ray count rate is registered. Panel b: example of an X-ray lightcurve of ε Eri (August 2019) where a short-term variability is present and highlighted with the solid red line.

6.5 Analysis of the EPIC X-ray spectra

The EPIC/pn spectra of ε Eri were all analysed with the software `xspec` (version 12.10; Arnaud 1996). The signal-to-noise ratio of these spectra is higher than the ones of EPIC MOS, so that I focused on the spectral analysis of only the EPIC/pn. Moreover, by considering only the EPIC/pn spectra the subsequent analysis carried out for ε Eri was simplified (see chapter 7).

The spectral model suitable for describing the stellar corona is for optically thin plasmas in collisional ionization equilibrium. In `xspec` this spectral model is the *Astrophysical Plasma Emission Code* - APEC - model and the chemical abundances of the plasma are calculated by looking up the ATOMdb atomic database. As input, the APEC model requires four initial values:

- the temperature kT [keV] of the plasma;
- the metal abundance, Z, (average of the elements C, N, O, Ne, Mg, Al, Si, S, Ar, Ca, Fe, Ni), relative to the Solar abundances;

- the redshift, z;
- the normalization parameter n, equal to

$$\frac{10^{-14}}{4\pi D^2 (1+z)^2} \int n_e n_H dV \tag{6.1}$$

where D is distance of the source (cm), n_e and n_H are the electron and H densities (cm^{-3}), respectively.

In Equation 6.1, an important quantity is the integral called *emission measure*, that provides information about how much material is emitted per unit of volume at a given temperature.

By assuming only one isothermal model, i.e. an APEC model with as input only one temperature, the spectra of ε Eri result to be poorly fitted. Therefore, the number of temperature components was increased until the statistics of the fit improved. In particular the best-fitting model results to be a 3-T APEC model, i.e. the spectra of ε Eri are well fitted by a coronal plasma emitting at three different temperatures kT.

To determine the initial parameters of the model, first I carried out a fitting considering all of the observations of ε Eri merged in one spectrum. The details of this procedure is described in subsection 6.5.1. Using then the results from this exercise, the spectrum of each observation was analysed separately (subsection 6.5.2).

6.5.1 Fitting of the merged EPIC/pn spectrum

Using the SAS task `epicspeccombine`, it is possible to merge several spectra in one spectrum with higher signal-to-noise ratio. I, thus, combined all spectra of all observations of ε Eri. Within this project fitting this spectrum had the goal to derive the best-fitting temperatures and abundances to be used later as a starting point for the fitting procedure of each individual observation.

The APEC models tested for the fitting procedure are the following: 1-T spectral model, 2-T spectral model, 3-T spectral model and a 4-T spectral model. In all the tested spectral models, the input parameters were all set on 1.0 as initial values. The temperatures kT and the normalizations n were left free to vary during the fitting procedure. The global metal abundances of each thermal component were tied to each other and they were left free to vary. In Table 6.5.1, the best-fitting parameters obtained for each spectral model fitted to the merged spectrum are shown.

For all tested models, the reduced χ^2, henceforth $\overline{\chi}^2$, is high. As matter of fact, since this spectrum is the result of merging all available spectra of ε Eri, the signal-to-noise ratio is much higher than that

Model	kT_1 [keV]	kT_2 [keV]	kT_3 [keV]	kT_4 [keV]	Abundances Z $[Z_\odot]$	$\overline{\chi}^2$	d.o.f.
1-T APEC	0.46				0.08	33.11	252
2-T APEC	0.25	0.68			0.22	7.64	250
3-T APEC	0.18	0.34	0.78		0.25	5.08	248
4-T APEC	0.11	0.20	0.35	0.76	0.25	5.0	246

Table 6.5.1: Best-fitting parameters obtained from the fitting procedures of each tested spectral model applied to the merged EPIC/pn spectrum. The abundances Z are given by `xspec` in units of solar metal abundances $Z_\odot$ in the photosphere of the Sun. $\overline{\chi}^2$ is the reduced χ^2 and d.o.f stands for the degrees of freedom.

of each individual spectrum, i.e. the spectrum gives more information on the corona observed during this last 5 years than the spectrum of an individual observation, but it averages out any possible spectral variations between one observation and another.

Among the $\overline{\chi}^2$ of each tested spectral model, the best value is given by the 3-T APEC and the 4-T APEC model. However, for the subsequent analysis I did not consider the 4-T APEC model. As a matter of fact, the $\overline{\chi}^2$ of both two models are very similar and thus adding a fourth component does not yield an improved fit. Moreover, adding more spectral parameters in the analysis of the individual spectra would only complicate the next step of the analysis presented in chapter 7. Thus, I chose to fit each individual spectrum with a 3-T APEC model, where the best-fitting parameters resulting from the spectral analysis of the merged spectrum are used as input parameters. The 3-T best-fitting model (solid red line) to the merged spectra (black dots) is shown in Figure 6.5.1, together with the residuals of the fitting in the bottom panel.

From the bottom panel of Figure 6.5.1, it can be noticed that the residuals of the fitting show some systematics. The spectral model APEC does not treat each metal abundance separately, but all the typical elements present in the corona are averaged and scaled to the solar metal abundances in the photosphere of the Sun. Thus, if the abundances are treated individually, using for example VAPEC [3] as spectral model, the fitting would have a better statistics.

[3] This spectral model considers the metal abundances C, N, O, Ne, Mg, Al, Si, S, Ar, Ca, Fe and Ni as separated spectral components.

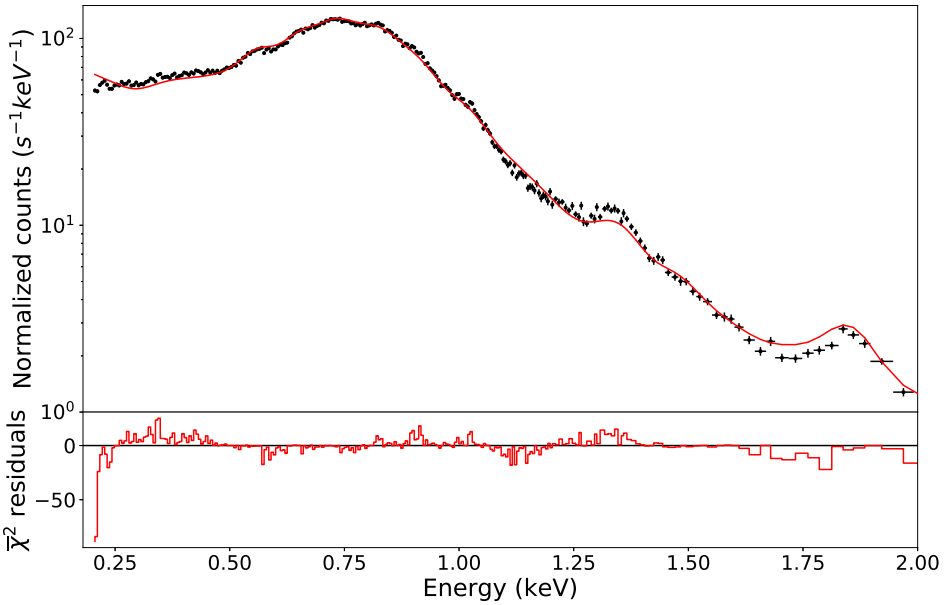

Figure 6.5.1: Merged EPIC/pn spectrum of all the available observations of ε Eri (black dots). The solid red line is the best-fitting 3-T APEC model. The bottom panel shows the residuals of the fitting.

6.5.2 Fitting of the individual EPIC/pn spectra

Building on the results of the fitting procedure of the merged spectrum, each individual spectrum of ε Eri was fitted assuming a 3-T APEC model. Two different procedures were applied: the first where the global abundances were free to vary during the fitting procedure; the second where they were instead kept frozen at $0.3Z_{\odot}$, where this latter value for the metal abundances is motivated by the best-fit of the merged spectrum, by the subsequent fit of all individual observations and by the literature, as explained in the next paragraphs. The choice of keeping the global abundances frozen was made in order to minimize the free fit parameters and, consequentially, to simplify the subsequent analysis, in which the best-fitting parameters of the spectra of ε Eri (three temperatures and three emission measures) are compared to same set of parameters obtained from fitting pseudo-solar simulated spectra (chapter 7).

In Table C 1 the best-fitting parameters obtained when the global metal abundances were free to vary are shown. For each observation, the X-ray flux was calculated in the soft energy band of *XMM-Newton* ($0.2 - 2$ keV), using the `xspec` command `flux`. The logarithms of the emission measures were calculated from Equation 6.1. The uncertainties associated to the temperatures, the abundances and the fluxes are retrieved from `xspec` through the command `error`, where the errors of the best-fitting parameters are calculated within a confidence region that for default is equal to 90%. The errors

associated to the emission measures are instead calculated with error propagation [4].

The average value of the abundances obtained from all twelve observations with this procedure is equal to $(0.27 \pm 0.05)Z_{\odot}$, in good agreement with what was found from the fitting of the merged spectrum. Thus, in the second procedure, as already anticipated, the metal abundances are kept frozen at $0.3Z_{\odot}$ [5].

In Table C 2, the best-fitting parameters obtained from the second procedure are shown, i.e. the fit performed when the global abundances are fixed to $0.3Z_{\odot}$. The uncertainties, the fluxes and the emission measures are calculated as mentioned above for Table C 1. The temperatures and the emission measures are similar to the ones obtained when the abundances are left free during the fitting. The spectra of all twelve observations with overplotted both the best-fitting spectral models presented here are shown in Appendix C.

Spectral analysis of the flare-like events

From the analysis of the EPIC/pn X-ray lightcurves (section 6.4), I found that six out of twelve observations show short-term variability in their lightcurves. I defined these "bumps" seen in the lightcurves as flare-like events. Since these events contribute to the X-ray variability of the star and they may thus influence the search for long-term cyclic activity, the flare-like events were disentangled.

The event lists of the observations of ε Eri affected by short-term variability were extracted again following the same procedure described in section 6.3 but demanding from the SAS task `evselect` to take into account only the events that happened outside the flare-like event, i.e. the events registered with the lowest count rate during the observation. Analogously, I extracted each event list during the flare-like event. Thus, for those observations where a flare-like event is present, there are three spectra for each observation: one extracted from the whole duration of the observation, one extracted in the time interval of the quiescent state and one in the time interval during the short-term variability of the count rate. These two latter spectra were separately analysed with a 3-T APEC model with the abundances set on $0.3Z_{\odot}$ and kept frozen during the fitting.

In Table C 3 the best-fitting parameters obtained from the analysis of spectra in the quiescent state

[4] According to Equation 6.1, the emission measure is $EM = \frac{4\pi D^2}{10^{-14}} n \Rightarrow logEM = log\left(\frac{4\pi D^2}{10^{-14}} n\right)$. For error propagation, the uncertainty to associate to the logarithm of EM is $\Delta logEM = \frac{\partial logEM}{\partial n}\Delta n = \frac{\Delta n}{n \cdot ln(10)}$, where Δn is the error of the normalization calculated by `xspec` with the command `error`.

[5] This value is also in good agreement with the literature (see for example Sanz-Forcada et al. 2004 and Ness et al. 2008)where from the studies on high resolution X-ray spectra, Fe is found equal to $0.5Z_{\odot} \pm 0.2Z_{\odot}$. Since the stellar coronae are usually rich of iron, Fe, it is a good parameter to be compared to the global metal abundance Z of low resolution spectra.

and during the flaring event are shown. Since a flare-like event are here defined as a change in the count rate, by examining separately the flare-like and quiescent spectra, it is possible to search for a change in temperature associated with the brightness change. Such changes are, indeed, expected for flares because they are the result of coronal heating events.

As I defined the flare-like event as an increase in the count rate, the spectra of these events for each observation have a higher flux than those of the quiescent state. However, the three temperatures of quiescent and flare-like spectra do not appreciably change.

In the subsequent analysis, to search for the presence of a coronal X-ray cycle, the flare-like events were excluded from the analysis, since they are influencing the X-ray variability of ε Eri.

6.6 Identification of an X-ray activity cycle

To search for a coronal X-ray cycle in ε Eri, first the X-ray fluxes obtained from the fitting procedure of subsection 6.5.2 were compared to the S-index values obtained in section 6.1. To better visualize the trend of the S-index variations, the Ca II data were binned: the data set was divided in sub-sets, each of them with a bin size that corresponds to $\sim$ 360 days, such that each averaged S-index represents approximately one observing season, the duration of which is represented by the horizontal bars in Figure 6.6.1. The value assigned to each bin is the mean of the S-index found within the chosen time range and errors are calculated as the standard deviation and represented by vertical bars. In the same figure, the X-ray fluxes are overplotted in red. For those observations that show short-term variability in the EPIC/pn lightcurves both the fluxes obtained outside the flaring events (values in Table C 3 - *Quiescent* columns) and the fluxes calculated over the whole observation (values in Table C 2) are plotted with two different symbols, red open symbols and red filled symbols respectively.

From a visual comparison, the X-ray fluxes show a variability similar to the Ca II data, i.e. the X-ray data follow the sinusoidal function given by the Lomb-Scargle periodogram analysis performed on the Ca II data (section 6.1). However, two X-ray observations have unexpected values: the observations of January 2016 and January 2019 do not show the maximum expected from the sinusoidal function, although the latter is in agreement with the Ca II data.

To better constrain the evidence of an X-ray cycle, a correlation test between the S-index and the X-ray data was performed, evaluating the Pearson's coefficient, r (see section A.3 for the details on this analysis technique). For correlating the two data sets, first I binned in a new way the Ca II S-index: I choose a time range spanning 50 days before and after each *XMM-Newton* observation and I calculated the mean of the Ca II S-index inside that time range. Each S-index mean was then correlated to the

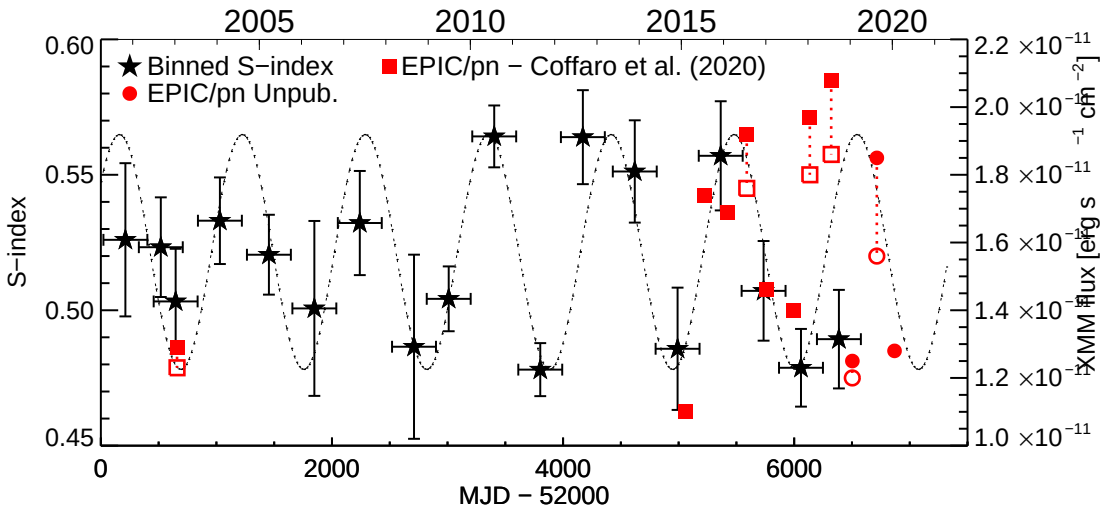

Figure 6.6.1: Long-term lightcurve of ε Eri obtained from the *XMM-Newton* data and Ca II data. The star symbols are the binned Ca II S-index data, where the horizontal bars are the bin size equal to 380 days and the vertical bars are the errors associated to the binned S-index and calculated as the standard deviation of the S-index data found within the chosen temporal range. The red symbols are the X-ray fluxes retrieved from the spectral analysis of the X-ray observations (subsection 6.5.2). For those observations that show a flaring event in the EPIC/pn lightcurves the X-ray flux was also calculated outside the event and is plotted with an opened red symbol. Finally, the red squares are the X-ray fluxes of those observations published by Coffaro et al. (2020), whereas the red circles are the observations not yet published.

corresponding X-ray fluxes, for which I chose to consider the ones of the quiescent state in the case of those observations with short-term variability.

In Figure 6.6.2, the zoom of the long-term lightcurve of ε Eri is shown to better visualize the new binning I adopted for this correlation test. The lightcurve includes the X-ray observations from early 2015 to early 2020 and in the plot they are shown with the red numbers, chronologically ordered. The grey intervals in the figure represent the time range I chose for calculating the average value of the S-index data for each XMM-Newton observation time. All individual S-index measurements are plotted with black open circles, while the means are the blue numbers, each of them corresponding to the given X-ray flux. From this plot, it can be seen that the X-ray observation number 5 and number 12 (July 2016 and January 2020 respectively) do not have S-index measurements close in time and, thus, they were excluded from the correlation analysis.

For carrying out the analysis, I used the software R. In Figure 6.6.3a, the scatter plot of the two variables is shown. The Pearson's coefficient results equal to 0.45 with p-value of 0.19%. I chose to set the significance level at 5%. Consequentially, the statistics of the coefficient r is significant and, moreover,

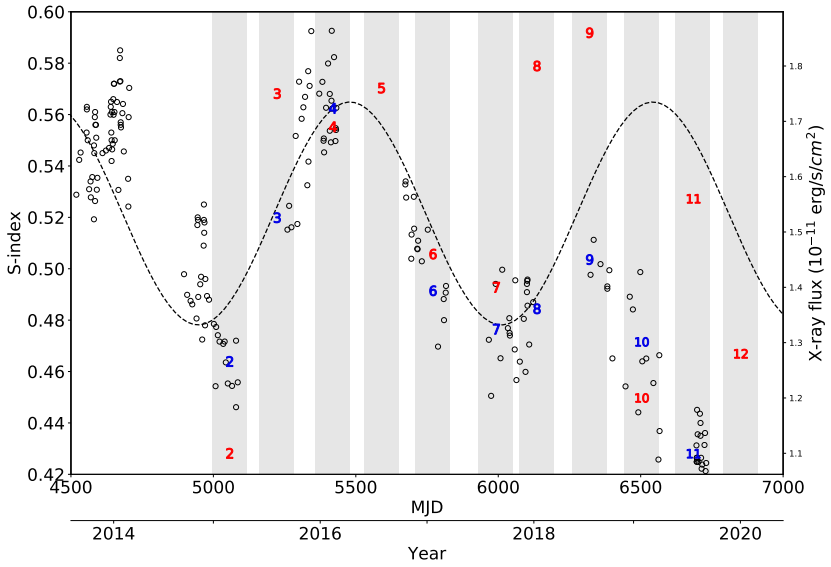

Figure 6.6.2: Long-term lightcurve of ε Eri observations, from early 2015 to early 2020. The open circles are the Ca II S-index measurements. The red numbers are the EPIC/pn X-ray fluxes. The grey intervals represent the time range (size of 50 days) chosen for calculating the mean S-index values for the correlation test. The corresponding means are plotted with as blue numbers.

the linear correlation is positive, i.e. the X-ray flux linearly increases with the S-index. In the plot of Figure 6.6.3a the confidence range corresponding to the retrieved p-value is also overplotted: here two observations (number 4 and 11, i.e. January 2016 and August 2019) are outside the confidence level. The observation of August 2019 has an X-ray flux strongly deviating from the corresponding S_{MWO}-index measure recorded in the same period and, thus, it is expected that these two measures do not follow a linear correlation. Thus, due to the evident departure of the chromospheric S-index data and the coronal X-ray flux during summer 2019, a new correlation test was carried out excluding the observation of August 2019. The result of this new test is shown in Figure 6.6.3b: by eliminating that observation, the coefficient r results ~ 0.62 with a p-value of 0.08% indicating a stronger correlation with higher significance than the first test. However, the observation of January 2016 (number 4) is still outside the confidence range. This can be due to the fact that the S-index measurement recorded at that time shows a higher scatter than in the other time ranges where the S-index data are binned. Moreover, also the X-ray flux of this observation is not at the expected maximum of the cycle (see also the non-zoomed Figure 6.3.3 where it is more evident that this observation should have been one of the maximum of the cycle). These two aspects together lead to the conclusion that during that period of time the Ca II S-index is increasing towards the maximum of the cycle with a different way than the corresponding X-ray flux.

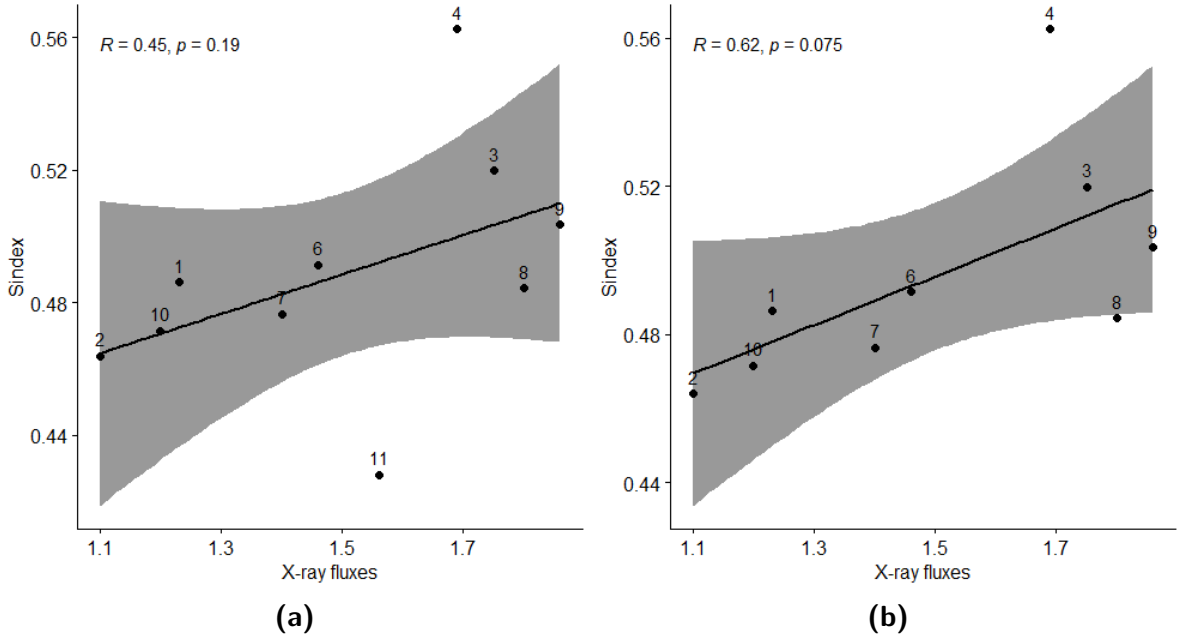

Figure 6.6.3: Linear correlation tests. On the left (panel a) the correlation is investigated when among the X-ray observations the observation of July 2016 and January 2020 are excluded because there is no corresponding S-index data. On the right (panel b) the correlation is tested for the same X-ray observations of panel a, but excluding the observation of August 2019, when the X-ray and the Ca II cycles are diverging from each other. The correlation coefficients of both tests are given in the legend of the plots, together with the corresponding p-values. The gray range overplotted in both panels is the confidence level corresponding to the retrieved p-value. The overplotted numbers refer to each X-ray observation and follow a chronological order.

Overall, the correlation tests statistically prove the presence of the X-ray cycle of ε Eri. However, it seems that from early 2019 some drastic change seems to happen to the cycle of ε Eri. This statement can be proved or disproved only with further monitoring of both the corona and of the chromosphere of ε Eri (chapter 9).

7

The X-ray activity cycle of ε Eridani in terms of solar magnetic structures

Contents

The study of ε Eri revealed that this star with its age of $\sim$ 400 Myr is the youngest star, among the targets considered so far, where a coronal X-ray cycle is present. Moreover, the amplitude of ε Eri's activity cycle, similarly to ι Hor, is among the shortest. As a matter of fact, from the spectral analysis (section 6.5), I found that ε Eri has a mean X-ray luminosity of 2.0×10^{28} erg/s and the amplitude of the cycle is 1.3×10^{28} erg/s. In Figure 7.0.1, these results provided by my analysis are shown.

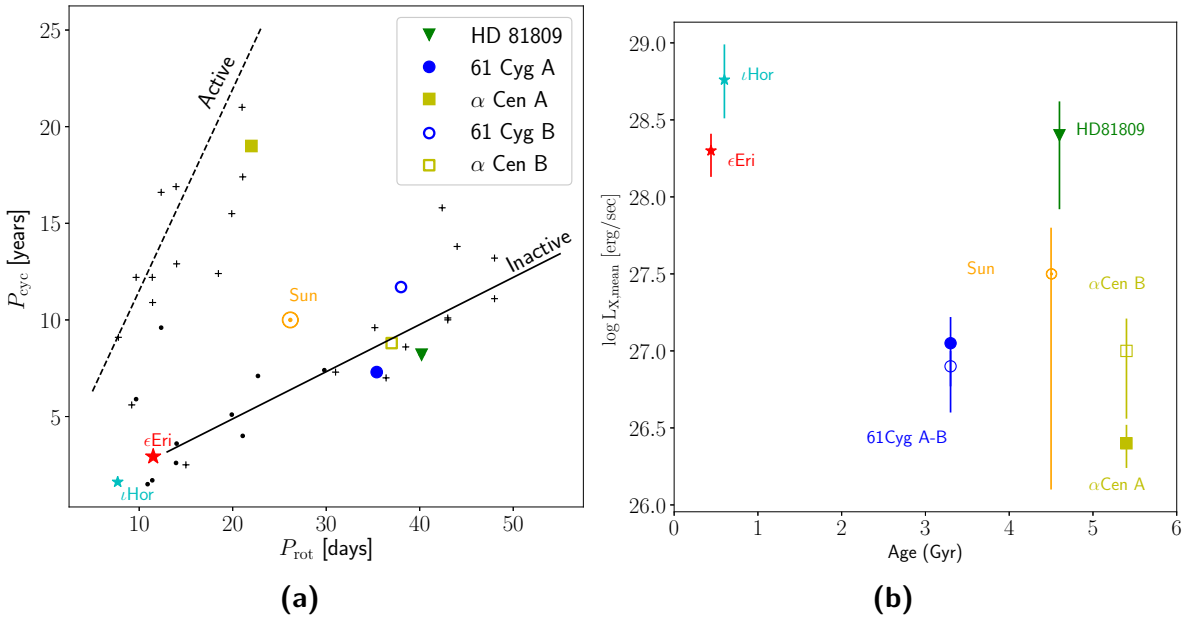

Figure 7.0.1: *Left panel*: $P_{cycl} - P_{rot}$ diagram with ε Eri included in the X-ray sample. The coding of the plot is the same as in Figure 3.3.1. *Right panel*: X-ray luminosity as function of the age with ε Eri included. The vertical bars represent the amplitude of each X-ray cycle.

Thus, with ε Eri now in the picture, it is interesting to investigate if there is a relation between the stellar age and cycle properties, such as the evidence of a low amplitude, and, if it exists, what might be the reasons. In particular, from the observations of the stars that show the highest X-ray luminosity and the smallest amplitude (Figure 7.0.1b), one might speculate that the cycle amplitude is limited by the available space in the corona, especially for active stars in which already during the cycle minimum a significant part of the surface might be covered with many magnetic structures.

This issue has been addressed in this PhD project with an unconventional approach, based on the study "The Sun as an X-ray star" (section 3.1). To summarize, the study "The Sun as an X-ray star" comprises an analysis of various X-ray images of the Sun that characterize the different coronal magnetic structures on the surface of the Sun. Moreover, from each of these images a synthetic X-ray spectrum can be extracted as if each solar magnetic structures were observed by any X-ray satellite.

How the solar studies can be used to characterize stellar activity cycles was shown by Favata et al. (2004) and Orlando et al. (2017) in the case of HD 81809. This was achieved by generating various X-ray synthetic spectra, so that each spectrum represent different percentage contributions of the different types of solar magnetic structures to the surface coverage of HD 81809. Then, by comparing the synthetic spectra to the observations of HD 81809 carried out with *XMM-Newton*, a certain combination of magnetic structures in the corona of HD 81809 was assigned to each phase of the X-ray activity cycle of the star.

Within this PhD project, the study of the"Sun as an X-ray star" was also applied to ε Eri. As a matter of fact, ε Eri is ideal target for this approach: the high signal-to-noise ratio of the EPIC/pn spectra allow a detailed description of its corona and, consequentially, a better and more detailed comparison with the different types of solar magnetic structures than in the case of HD 81809. Moreover, due to the young age of ε Eri, this approach allows a deeper understanding of the activity cycle during critical evolutionary phases.

The goal is to describe the evolution of the X-ray activity cycle of ε Eri in terms of solar magnetic structures observed by *Yohkoh* and, by comparing the X-ray spectra of ε Eri with pseudo-solar spectra representing the solar magnetic structures, to understand the reasons of a low amplitude during the X-ray cycle.

7.1 Introduction to simulation method

Compared to HD 81809, the available spectra of ε Eri show a significantly higher signal-to-noise ratio, providing thus more information on the temperature profile of the corona. As shown in subsection 6.5.2, a spectral model composed of three temperatures is required for a good description of the X-ray observations of ε Eri, and correspondingly the pseudo-solar spectra simulated for describing the X-ray activity of ε Eri need also to be treated with a 3-T spectral model as compared to the 2-T spectral model for HD 81809. Consequently, the number of spectral parameters to be compared between the synthetic and observed spectra is higher than in the study of HD 81809 by Orlando et al. (2017), i.e. six parameters (three kT and three EM) versus four parameters for HD 81809. Moreover, it will be shown in the subsequent sections that the higher quality spectra available for ε Eri require a refinement of the solar EMDs, as the standard EMDs (described in section 3.1) do not match the observations. In particular the flare EMD had to be changed.

The procedure with which I compared the X-ray spectra of ε Eri to those representing the solar magnetic structures can be summarized in the following steps (and the detailed description is the topic of this chapter):

- Among the different types of magnetic structures described in the study "The Sun as an X-ray star", I chose the ones that best describe the X-ray luminosity and the average temperature of the corona of ε Eri.

- I extracted the EMDs for each magnetic structure, investigating four intervals of different percentage coverage of each of those structures on the stellar corona. The result was four grids of EMDs, where each grid point represents a certain percentage fraction. From each grid point, the synthetic spectra were also extracted and fitted in the same way as the observed spectra of ε Eri, obtaining the X-ray luminosity and average temperature for each spectrum.

- I compared the X-ray luminosity and average temperatures of the synthetic spectra with the spectra of ε Eri in order to set an upper limit of magnetic structures that may be covering ε Eri surface.

- Once the maximum of covering magnetic structures was determined, and thus one of the grids was chosen, I performed a more detailed comparison between the synthetic spectra and the X-ray observations of ε Eri by comparing the kT and the EM of each spectrum obtained from the fitting procedures.

In section 7.2 I describe the solar magnetic structures, and the corresponding EMDs and spectra, chosen for the comparison with ε Eri. In subsection 7.2.1 the method I developed for comparing the spectra of ε Eri and the simulated pseudo-solar spectra is presented. In section 7.3 and in section 7.4, the results of the comparison are presented and discussed in section 7.5. The results of this study are presented by Coffaro et al. (2020) for the first *XMM-Newton* EPIC/pn observations of the monitoring campaign.

7.2 Preparation of the simulated grid of (standard) pseudo-solar spectra

Among the coronal structures described and analysed in the study "The Sun as an X-ray star", active regions (ARs), cores of active regions (COs) and flares (FLs) were considered. The emission measure of ε Eri is much higher than the solar one. Thus, the background coronal regions (BKCs) were ignored because, among all types of structures, they have the lowest intensity (see Figure 3.1.4) and a high percentage of coverage would be required to produce a significant contribution to the total EMD[1].

[1]Based on the same argument, the BKCs regions were also not considered in the study of HD 81809 (subsection 3.2.3).

This would considerably reduce the available surface for the other magnetic structures, that instead, given their higher intensity, are better suited to reproduce the bright X-ray emission of ε Eri.

I chose the same $\overline{EMD}_{AR\odot}$ and $\overline{EMD}_{CO\odot}$ considered by Orlando et al. (2017) for HD 81809 (subsection 3.2.3), but scaled to the surface of ε Eri by multiplying the EMDs by $4\pi R_\star^2$ where $R_\star = 0.74 R_\odot$ (Di Folco et al., 2004). In a first analysis the same $\overline{EMD}_{FL\odot}$ were used as in Orlando et al. (2017), i.e. the time average of the eight flares discussed by Reale et al. (2001). However, my analysis showed that different $\overline{EMD}_{FL\odot}$ that I constructed from the observed *Yohkoh* flares were required to yield a good description of the *XMM-Newton* observations of ε Eri. These latter $\overline{EMD}_{FL\odot}$ will be described in details in the next section 7.4, together with the motivations to test a grid of EMDs different than the standard solar one, i.e. the solar EMD where the flaring contribution is given by all kind of flares observed by *Yohkoh* in 1990s.

In the context of the study "The Sun as an X-ray star", the EMDs of each solar magnetic structure had been extracted considering solar metal abundances, $Z_\odot$. However, from the fitting of ε Eri spectra (subsection 6.5.2), the metal abundances result $\sim 0.3 Z_\odot$, i.e. ε Eri has a lower metallicity than the Sun. This requires to introduce a scale factor to take into account of the reduced radiative losses of ε Eri with respect to the Sun because of its lower metal abundance. For a given magnetic structure, the corresponding X-ray flux in the solar corona and in ε Eri corona would be equivalent if there are no the radiative losses. Thus, in this case the radiative loss rate (E_R) would be

$$E_R = n^2 \Lambda(T) \equiv E_{R_{SUN}} = n^2_{SUN} \Lambda(T)_{SUN} \tag{7.1}$$

where n^2 is the density of the ions and $\Lambda(T)$ is the radiative loss function per unit of emission measure. However, this latter function in ε Eri is 0.3 times lower than the one of the Sun because of the lower metal abundance, i.e. $\Lambda(T)_{\varepsilon\ Eri} = 0.3 \Lambda(T)_{SUN}$. Thus, Equation 7.1 reads:

$$n^2 \Lambda(T) = n^2 0.3 \Lambda(T)_{SUN} \equiv n^2_{SUN} \Lambda(T)_{SUN} \Rightarrow n^2_{\varepsilon\ Eri} \sim 3 n^2_{SUN} \tag{7.2}$$

Since the emission measure is proportional to n^2 (Equation 6.1), the scale factor to consider in the extraction procedure of each $\overline{EMD}_{AR\odot}$, $\overline{EMD}_{CO\odot}$ and $\overline{EMD}_{FL\odot}$ is equal to 3. Henceforth, I label the obtained distributions as $\overline{EMD}_{AR\overline{\odot}}$, $\overline{EMD}_{CO\overline{\odot}}$ and $\overline{EMD}_{FL\overline{\odot}}$ to stress that they also take into account the correction for the reduced radiative losses.

The task is now to determine the relative contribution of ARs, COs and FLs to the X-ray emission of ε Eri. Here, as a first step, I followed the approach applied to HD 81809. I constructed thus a grid of $EM(T)$ distributions where each grid point represents a different percent coverage of the

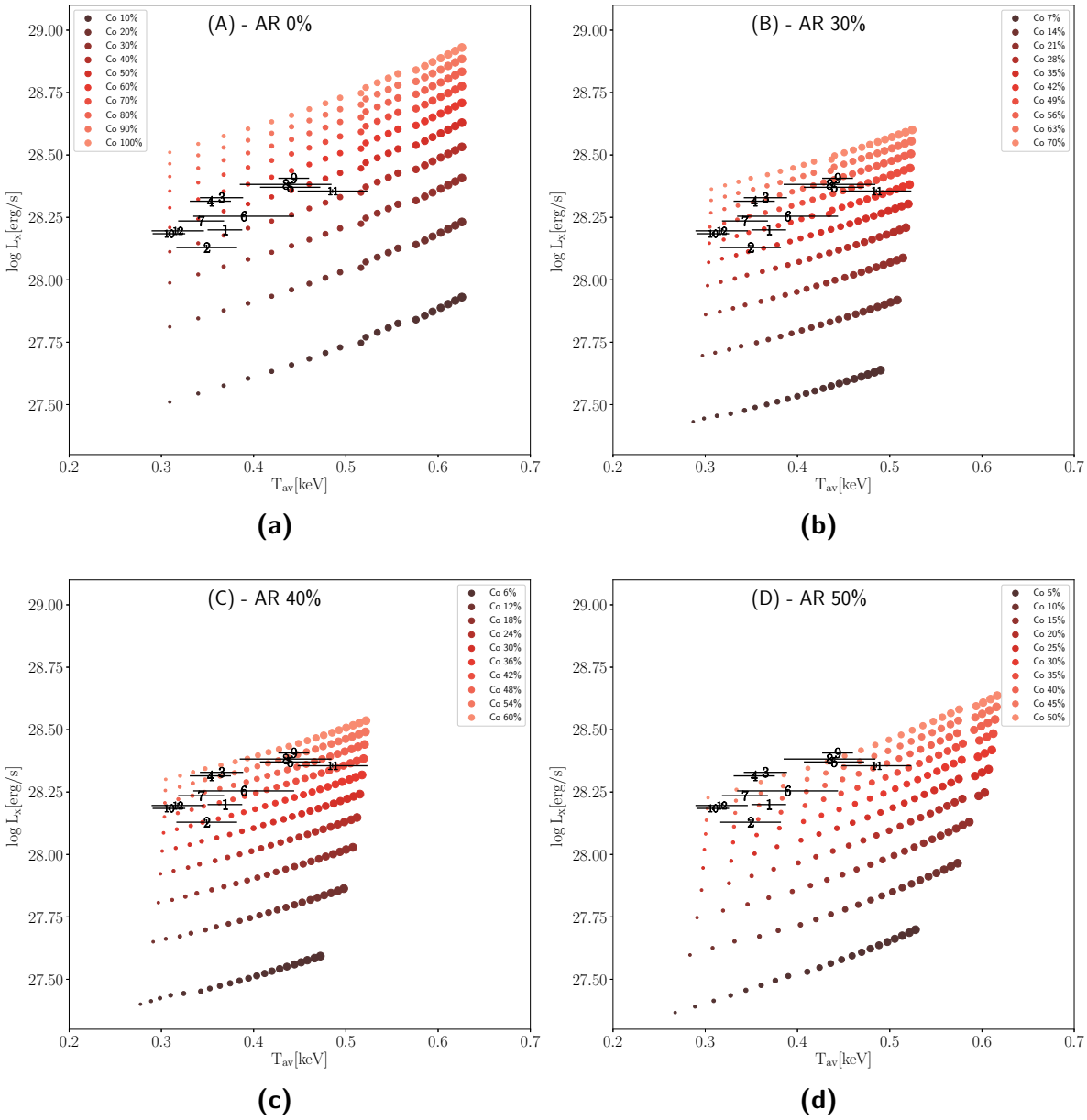

Figure 7.2.1: Grids of X-ray luminosity as function of average temperature. Each panel refers to a different percentage coverage of magnetic structures: (a) $ARs = 0\%$, $COs = 10\% - 100\%$ and $FLs = 0\% - 2\%$; (b) $ARs = 30\%$, $COs = 7\% - 70\%$ and $FLs = 0\% - 2\%$; (c) $ARs = 40\%$, $COs = 6\% - 60\%$ and $FLs = 0\% - 2\%$; (d) $ARs = 50\%$, $COs = 5\% - 50\%$ and $FLs = 0\% - 2\%$ (Coffaro et al. (2020), updated with new observations no. 10, 11 and 12).

coronal structures on the surface of ε Eri ($P_{AR} + P_{CO} + P_{FL}$). The $\overline{EMD}$s of each magnetic structure were multiplied by the surface area of ε Eri within a range of coverage fraction. Starting from the $\overline{EMD}_{(AR+CO+FL)\odot}$ grid, the EPIC/pn spectra were synthesized for each grid point of the composite $EM(T)$ characterized by different fractional contributions of the three magnetic structures. Then, each synthetic spectrum was analysed in the same way as for the observed spectra of ε Eri, i.e. I fitted them with a 3-T thermal APEC model with metal abundance fixed at 0.3 $Z_{\odot}$ (subsection 6.5.2). Finally I calculated for each grid point the X-ray luminosity (L_X) and the average temperature (T_{av}) as defined in Equation 3.3 with $i = 1, 2, 3$.

In Figure 7.2.1a-d it is shown how different combinations of ARs, COs and FLs produce different combinations of L_X and T_{av}. In these panels the results for the synthetic spectra are represented by circles. The L_X and the T_{av} from the spectra of ε Eri (see Table C 2 in Appendix C) are overplotted onto this grid with numerical symbols, denoting the chronological order of the observations. The four panels represent four different test-grids. In Figure 7.2.1a the AR coverage fraction is set to 0%, while the COs are varying between 10% and 100% as shown in the inset. The FLs vary between 0% and 2% of the area covered by the COs, with a step size of 0.1%. The symbol size and the color in the plots represent, respectively, the variation of the percentage of FLs and COs. It can be seen that an increase in the coverage fraction of the FLs influences mainly the average temperature, whereas an increase in the coverage fraction of the COs influences the luminosity, as already found by Orlando et al. (2004) for the Sun and by Orlando et al. (2017) for HD 81809. It can be seen that to cover the (L_X, T_{av}) pairs of all observations of ε Eri a surface coverage of COs of at most 60% is needed.

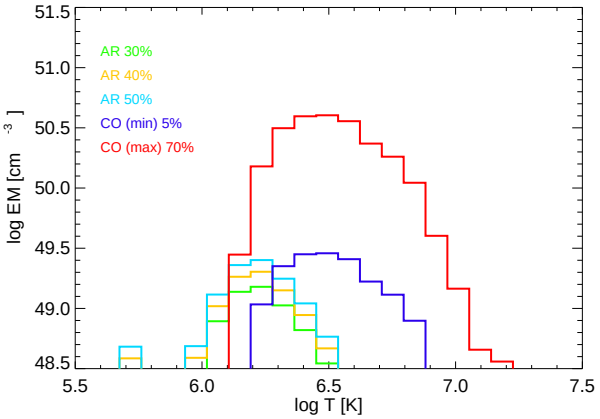

Figure 7.2.2: $\overline{EMD}_{AR\odot}$ and $\overline{EMD}_{CO\odot}$ at different percentage coverage fraction: the green, the yellow and the turquoise lines are the $\overline{EMD}_{AR\odot}$ at 30%, 40% and 50% respectively; the blue and red lines are the minimum percentage (5%) and the maximum percentage (70%) of $\overline{EMD}_{CO\odot}$ among the four grid plotted in Figure 7.2.1 (Coffaro et al., 2020).

Thus, I explored different percentage of coverage fraction around the percentage of the COs of 60% in order to constrain the relative contribution of ARs and COs. In particular, I explored the combinations reported in Table 7.2.1 where the ARs are constant and the COs and FLs are varying

	ARs (%)	COs (min-max %)	FLs (min-max %)	Plot
1st grid	30	$7-70$	$0-2$	Figure 7.2.1b
2nd grid	40	$6-60$	$0-2$	Figure 7.2.1c
3rd grid	50	$5-50$	$0-2$	Figure 7.2.1d

Table 7.2.1: Combination in percentage of ARs, COs and FLs considered to constrain the relative contribution of ARs and COs on the corona of ε Eri. The plots of the X-ray luminosity as function of the average temperature, calculated for each of these combination, are shown in Figure 7.2.1 (panel b,c and d).

with a certain range. The flare contribution varies for each combination between 0% and 2% of the percentage of COs with a step size of 0.1%. In Figure 7.2.2 the EMDs of the ARs for each of these combinations are shown, together with the minimum and maximum of the considered COs fraction.

From a visual inspection of the panels in Figure 7.2.1, all combinations can potentially reproduce the observational data. Figure 7.2.2 shows that changing the AR coverage within the range explored in Figure 7.2.1 (i.e. AR from 30% to 50%) does not have an appreciable impact on the total EMD. Therefore, I chose for further analysis the combination with a coverage of ARs equal to 40%, a coverage of COs that varies from 6% to 60% and FLs varying from 0% to 2% (Figure 7.2.1c), without excluding that the surface of ε Eri can be also covered with a lower fraction of ARs. The other combination with ARs equal to 30% (Figure 7.2.1b) could be representative of the data of ε Eri. In Figure 7.2.2 it can be seen that the EMD of the minimum coverage fraction of COs, i.e. 5%, has an emission measure comparable to the maximum coverage fraction of ARs, i.e. 50%, indicating thus that the contribution of any percentage of ARs affects little the total EMDs and, moreover, the difference between this contribution for different percentage of ARs is small. Therefore, it is not possible to set a lower limit on the ARs coverage. Figure 7.2.1 suggests an upper limit of ARs of 40% as panel d (with ARs$=$ 50%) covers the data of ε Eri only at the limit.

7.2.1 The selection criterion for the bast-matching emission measure distributions

For a more detailed investigation of the compatibility between the observed spectra of ε Eri and the synthetic spectra derived from the pseudo-solar $EM(T)$, I proceeded to a comparison of the individual spectral best fit parameters, i.e. the three temperatures and the three emission measures obtained from the best-fitting procedure of the synthetic spectra and of the spectra of ε Eri.

Figure 7.2.3 shows the best-fit parameters obtained from the synthetic spectra for the chosen combination of standard solar structures (case Figure 7.2.1c), together with the ones of the best fit to the

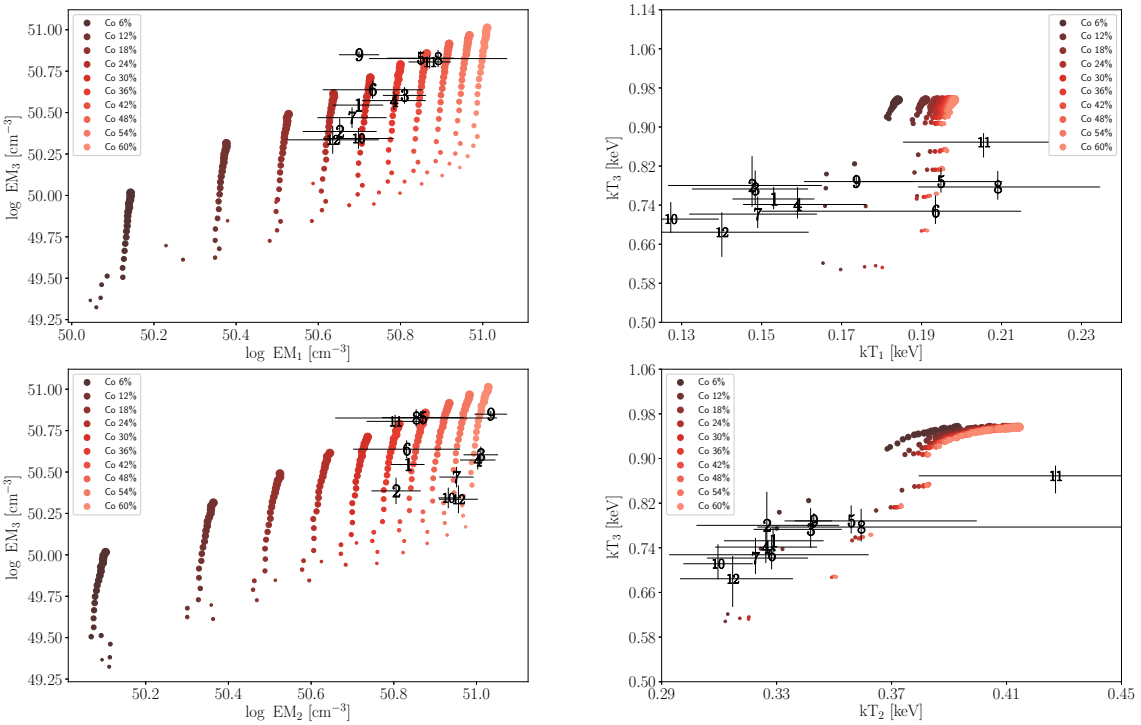

(a) **(b)**

Figure 7.2.3: Best-fitting parameters, $EM_{1,2,3}$ (left) and $kT_{1,2,3}$ (right), of the synthetic spectra with overlaid the spectral parameters of the observations of ε Eri. The variation of the color shape (from a dark red to a light one) highlights the variation of the coverage fraction of COs, as illustrated in the legend of the plots. The variation of the symbol size indicates the variation in percentage of FLs, from 0% (smallest symbols) to 2% (largest symbols). The spectral parameters of the observations of ε Eri are plotted using numerical symbols and chronologically ordered (Coffaro et al. (2020) updated to include the new observations no. 10, 11 and 12).

observed spectra of ε Eri (see Table C 1). Analogous to Figure 7.2.1, the variation of the colors represents the percent coverage of COs, while the symbol sizes the percentage of FLs. As can be seen from Figure 7.2.3, an increase of COs on the surface influences the two lower-temperature components of the spectral model, while an increase of the flaring coverage influences mostly the third component, i.e. the hottest one.

Contrary to the case of HD 81809, where the best-fitting parameters were compared only visually, I performed an analytical comparison to find a match, as close as possible, between the EMDs retrieved

from the observations of ε Eri and the simulated $\overline{EMD}_{(AR+CO+FL)\overline{\odot}}$. To explain how the match was done, I will use as example the $\overline{EMD}_{(AR+CO+FL)\overline{\odot}}$ obtained by considering as solar flare $\overline{EMD}_{FL\overline{\odot}}$ the one built using the eight typical solar flares discussed by Reale et al. (2001), i.e. the standard solar EMD (see previous subsection and subsection 3.2.3). The same procedure was then applied to the other tested $\overline{EMD}_{\overline{\odot}}$ (see section 7.4).

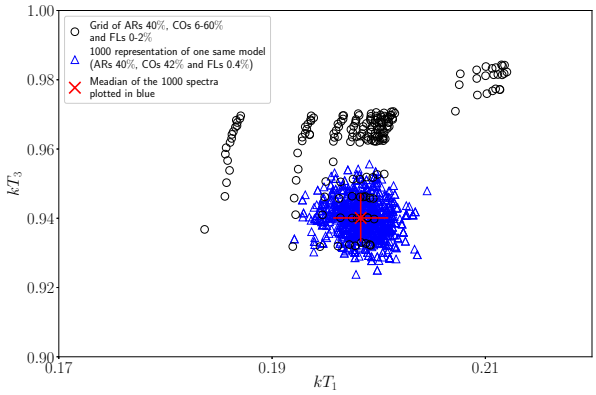

Figure 7.2.4: Example showing the effect of the Poisson statistics on the retrieved spectral parameters (kT_1 vs. kT_3) of the synthetic spectra of the grid with ARs 40%, COs $6-60\%$ and FLS $0-2\%$. *Blue triangles*: 1000 best-fitting parameters representing one specific combination of magnetic structures (ARs 40%, COs 42%, FLs 0.4%) highlighted here as an example; *Red cross*: median of the 1000 representations (blue dots) of the model chosen as example; *Black circles*: medians of the 1000 representations of each grid point, i.e. the equivalents of the red cross for all grid points; (Coffaro et al., 2020).

A major improvement with respect to the previous work on HD 81809 is the evaluation of the uncertainties associated with the synthetic spectra, that impact on the accuracy with which a certain coverage fraction with magnetic structures can be assigned to the star's corona. To this end, I introduced a statistical noise in the synthetic spectra as follows.

Each grid point in Figure 7.2.1c and consequently in Figure 7.2.3[2] was extracted 1000 times by introducing a statistical randomization. In this way the ith spectrum, representing a certain amount in percentage of magnetic structures, is different from the $(i+1)$th spectrum, representing the same combination of ARs, COs and FLs, only in that it has a different level of statistical noise. In this way, a certain combination of ARs, COs and FLs is not univocally represented by only one spectrum, but by 1000 spectra. All spectra for each combination of magnetic structures were then fitted with a 3-T APEC model and, therefore, I retrieved 1000 sets of best-fitting parameters, each of them describing a certain combination of ARs, COs and FLs and with a random distribution. An example of the effect of the statistical noise can be seen in Figure 7.2.4 that shows a zoom of the $kT_1 - kT_3$ plot of Figure 7.2.3c. Here, the blue triangles are the best-fitting parameters of the 1000 spectra representing a specific combination of magnetic structures, that in this example is ARs $= 40\%$, COs $= 42\%$ and FLs $= 0.4\%$. For this specific combination its median is highlighted in red, where the error bars are calculated as the

[2]Here, each spectrum represents the combination of ARs equals to 40%, COs varying between 6% and 60% and FLs varying between 0% and 2%

percentile at 10% and 90% of the 1000 best-fitting values. The black dots are the median of the 1000 best-fitting parameters for each combination of magnetic structures in the range of temperatures displayed in the plot. Figure 7.2.4 highlights the presence of a significant spread defined by these 1000 values. If the uncertainties of the spectral parameters of each grid point is considered (i.e. the red error bars shown for the example in Figure 7.2.4), a given observation of ε Eri is compatible with different grid points, alias different combinations of ARs, COs and FLs. One can therefore define a *range* of synthetic best-fitting parameters that can match a given observation, *instead of only one precise set of parameters*. This translates into a range of best-fitting combinations of AR, CO, and FL coverage for each observation.

To determine this range of best-fitting combinations (AR+CO+FL), a match between observed and synthetic model parameters is performed as follows. For clarity, in the following I denote the six spectral parameters ($kT_{1,2,3}$ and $EM_{1,2,3}$) by P_i, with $i = 1, \ldots, 6$. To find the best-fitting combination of magnetic structures, I matched the best fit parameters P_i^{obs} for each observation with each of the corresponding synthetic parameters $P_{i,j,k}^{syn}$ derived for the 1000 sets (henceforth labeled with j) of all 201 different combinations of solar regions (grid points; henceforth labeled with k), where $j = 1, \ldots, 1000$ and $k = 1, \ldots, 201$ [3]. As selection criterion the following six equations were evaluated according to:

$$P_i^{obs} - \Delta P_i^{obs} \cdot \sigma \leq P_{i,j,k}^{syn} \leq P_i^{obs} + \Delta P_i^{obs} \cdot \sigma \tag{7.3}$$

with a unique parameter σ for all six spectral parameters. σ defines thus the global confidence range of the match between observed values P_i^{obs} and synthetic values $P_{i,j,k}^{syn}$ with $i = 1, \ldots, 6$. I then picked for each of the 1000 sets (j) of combinations of solar regions as best-matching model the one among all grid points (k) that provides the smallest value for σ. The results of this procedure are 1000 best-fitting representations (for each observation). As final best-matching combination of ARs, COs and FLs the median of the 1000 values retrieved with this selection procedure was considered and I associated an uncertainty on this result as the 10% and 90% quantile of the 1000 values.

[3] The match was applied also on the other tested $\overline{EMD}_{\odot}$ where the flaring contributions were modified and that will be deeper discussed in the next subsection. Therefore, the index k changes according to the number of combinations of magnetic structures present in the given grid. In this case, i.e. for the standard solar $\overline{EMD}_{\odot}$, this number is 201. In the subsequent cases, the number of combinations changes according to the kind of $\overline{EMD}_{FL\odot}$ considered, going from 402 to 1206.

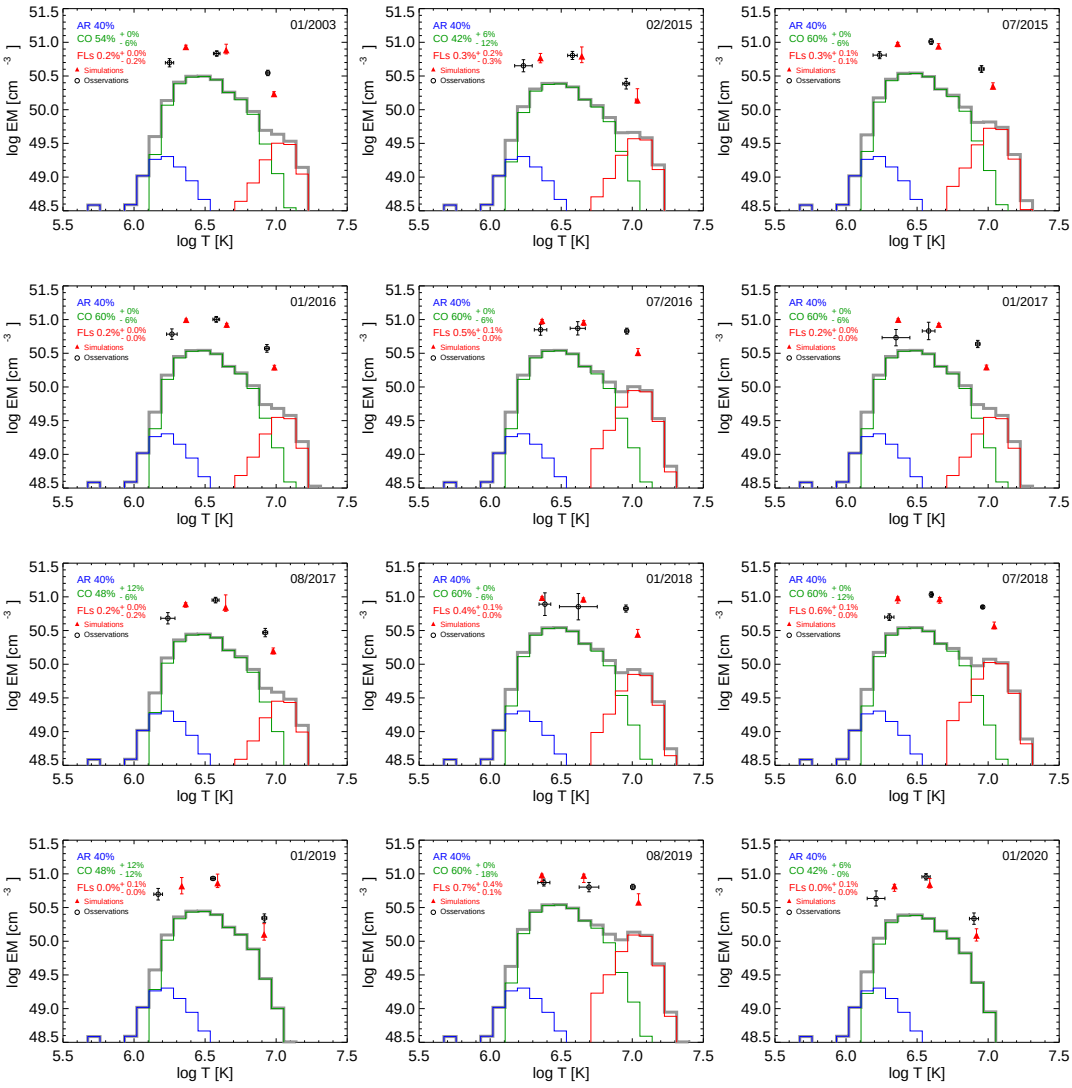

Figure 7.2.5: Best-matching EMDs composed by ARs (blue distribution), COs (green distribution) and FLs (red distribution) for each observed spectrum of ε Eri. The sum of the contribution of all magnetic structures is the gray distribution. Each observation is represented by a different fraction of surface coverage with AR, CO and FL selected as described in subsection 7.2.1 and reported in the legend. Red triangles are the medians of the 1000 best-fit parameters of the selected synthetic spectra. Black dots are the best-fit parameters of the observations (Coffaro et al. (2020) updated with new observations no. 10, 11, and 12).

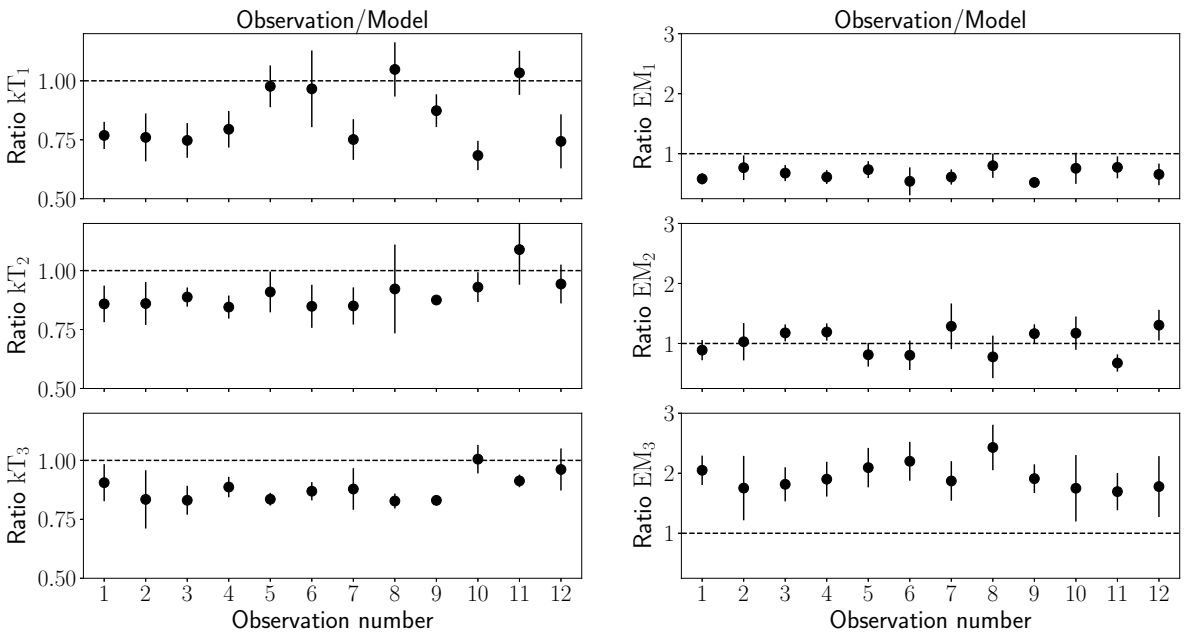

Figure 7.3.1: Ratio of the best-fitting parameters of ε Eri over the same parameters selected for the synthetic grid with ARs 40%, COs $6-60\%$ and FLs $0-2\%$, i.e. $\frac{P_i^{obs}}{P_{i,j,k}^{syn}}$. The vertical bars are the errors on the ratios found from error propagation, using both the uncertainties of the observed spectral parameters and the 10% and 90% percentiles of the 1000 selected representations (Coffaro et al. (2020) updated with the new observations).

7.3 Comparison with standard pseudo-solar emission measure distributions

The $EMD_{\odot}$ corresponding to the models selected with this procedure as the best match to the observations are shown in Figure 7.2.5. The total contribution of all coronal structures is the gray distribution, whereas the blue is the contribution from ARs, the green from COs and the red from FLs. The red triangles are the medians of the best-fit parameters of the 1000 best-matching spectra. The red error bars are the percentiles at 10% and 90% of these 1000 representations, denoting the minimum and the maximum of the error bars respectively. The corresponding best-matching area coverage fraction (as defined above as the median of the 1000 best-fitting results from the simulations) is given in the legend, together with the associated errors (i.e. the percentiles at 10% and 90% of the distribution of the 1000 best fits). In addition, the best-fit parameters of the 3-T model fitted to the observed spectra of ε Eri with the associated errors are plotted (black circles; Table C 2).

Figure 7.3.1 shows a summary of the correspondence between the observed and synthetic pseudo-solar 3-T best-fitting parameters: the ratio between the best-fit parameters of ε Eri and the medians of best-fit parameters of the corresponding selected $EM(T)$ are plotted. The ratios of the temperatures result systematically < 1, i.e. the temperatures of the selected synthetic spectra are higher than the ones of the observed spectra. While the first and the second component of the emission measures give also a ratio < 1, the EM_3 of the selected model is drastically lower than the observed values. Among the six parameters, the hottest component of the emission measure shows the most drastic discrepancy (see also the discrepancy between the black circles and the red triangles in Figure 7.2.5).

To summarize, the grid of solar coronal structures with ARs fixed on 40%, COs between 6% and 60% and FLs between 0% and 2% is able to reproduce the X-ray luminosity and the average coronal temperature of all observed EPIC/pn spectra of ε Eri (Figure 7.2.1c), but the more detailed investigation showed that the $EM(T)$ structure does not match very well its spectral shape (Figure 7.2.3, Figure 7.2.5)

For this reason, I decided to test other combinations of magnetic structures, different from the standard solar one.

7.4 Comparison with modified pseudo-solar emission measure distributions

As shown in section 7.3, the most severe discrepancy between synthetic and observed spectra is given by the third component of the EM: the synthetic EM_3 is systematically lower than the observed ones (Figure 7.3.1). The standard $\overline{EMD}_{\odot}$ previously tested comprises values of EM_3 sufficiently high to be compatible with the observed values (see Figure 7.2.3). However, high values of EM_3 in the grid correspond to high values of kT_3, which do not agree with the observed kT_3, and consequentially are rejected by the selection procedure (subsection 7.2.1). Thus, in order to find models that match both the temperature and the emission measure of the hottest spectral component, it was necessary to modify the $\overline{EMD}_{FL\odot}$ because FLs are the structures that influence most strongly the hottest component.

In the context of "The Sun as an X-ray star" (section 3.1), we have seen that Reale et al. (2001) presented the analysis of eight flares of different energetic class observed by *Yohkoh*, and we have also seen that all these flares were observed with the hard filters of *Yohkoh*/SXT sensitive to plasma around and above 10^7 K. However, among these eight flares, two of class M were also observed with the soft filters of the telescope on board of the satellite, and the analysis showed that a contribution from plasma at temperatures lower than 10^7 K is also important [4]. Thus, the soft emission from these flares modifies the flare $EM(T)$ by adding an extended low-temperature tail. I thus replaced the standard $\overline{EMD}_{FL\odot}$

[4] Reale et al. (2001) published only the results of one these two M class flares.

with the average between these two M class flares (henceforth $\overline{EMD}_{FL\overline{\odot}_M}$) and I tested it (together with the previous $\overline{EMD}_{(AR+CO)\overline{\odot}}$) considering different combination of filters in use and different phase of the flare event. In particular I tested:

1. $\overline{EMD}_{FL\overline{\odot}'_M}$ accounting for two solar flares of class M observed with soft and hard filters;
2. $\overline{EMD}_{FL\overline{\odot}''_M}$ accounting for two solar flares of class M observed with soft and hard filters only during the decay phase;
3. $\overline{EMD}_{FL\overline{\odot}'''_M}$ accounting for two solar flares of class M observed with hard filters only during the decay phase;

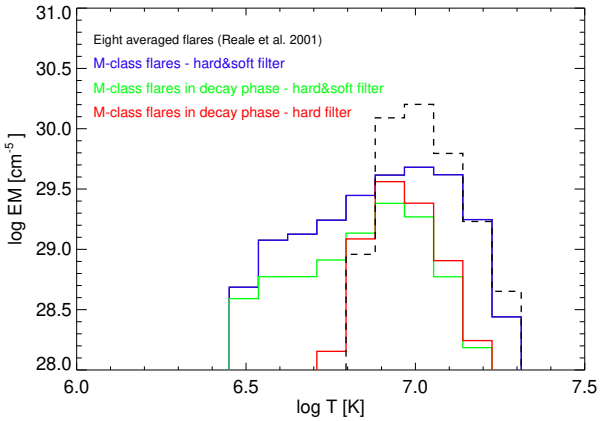

Figure 7.4.1: Pseudo-solar flare $EM(T)$ distributions, normalized to unit surface. *Black distribution* - time-averaged flares typical of the solar corona (Reale et al., 2001); *blue distribution* - Flares at soft and hard energies; *green distributions* - Flares in the decay phase; *red distribution* - Flares at the lowest temperatures (Coffaro et al., 2020).

These three new $\overline{EMD}_{FL\overline{\odot}_M}$ and the original standard one tested in section 7.2 are compared in Figure 7.4.1. The blue distribution is the first modified $\overline{EMD}_{FL\overline{\odot}'_M}$, the green distribution is the second one ($\overline{EMD}_{FL\overline{\odot}''_M}$) and the red distribution is the third one ($\overline{EMD}_{FL\overline{\odot}'''_M}$). The dashed distribution is the original standard solar $\overline{EMD}_{FL\overline{\odot}}$ first tested for ε Eri (see section 7.2 and section 7.3) that was also adopted in the case of HD 81809.

For each modified $\overline{EMD}_{\overline{\odot}}$, I generated a new grid where the percentage coverage of ARs and COs was the same as for the standard $\overline{EMD}_{\overline{\odot}}$ described in section 7.2, i.e. ARs$=$ 40% and COs varying from 6% to 60%. The percentage coverage of FLs was instead modified for the second and third $\overline{EMD}_{FL\overline{\odot}_M}$, assumed to go from 0% to 10%. A higher coverage fraction of FLs than the one previously

adopted is required to reproduce the observed T_{av}, since these two flare EMDs have a lower emission measure and a lower temperature compared to the previous EMDs, as can be noticed in Figure 7.4.1.

These three grids were treated as explained in section 7.2: for each combination of magnetic structures in the modified $\overline{EMD}_{\odot}$ I synthesized 1000 times the corresponding spectra and I analysed them in the same way as for the spectra of ε Eri (subsection 6.5.2). Then the analytic match was performed. The selected EMDs are shown in Figure 7.4.2, 7.4.3 and 7.4.4 . The coding of these plots follows the same chosen for Figure 7.2.5. Also the ratio of the spectral parameters of ε Eri over the selected best-fitting parameters were calculated and plotted in Figure 7.4.5.

7.4.1 Contributions of flares at soft and hard energies

Some of the observations now require a smaller coverage fraction of COs because of the additional soft emission of the flare $EM(T)$. The discrepancies between observed and synthetic parameters are somewhat smaller than in the previous case, but they show the same pattern (compare blue symbols in Figure 7.4.5 with Figure 7.3.1). The differences are still large, particularly for the third component of the emission measure.

7.4.2 Flares in the decay phase at soft and hard bands

The selected EMDs for this case are composed of a significantly lower CO coverage fraction than the previous ones, and the FL fraction is up to $\sim 7\%$. The observed and simulated spectral parameters are now in much better agreement. A major improvement is obtained for the hot component, where the ratios for both kT_3 and EM_3 are now much closer to 1. The parameters representing the other two spectral components also show somewhat a better agreement than before. This suggests that flare plasma with a lower temperature, such as solar flares during the decay phase, better describes the phenomena in the corona of ε Eri.

7.4.3 Flare in the decay phase at hard band

Compared to the flares in decay that included soft emission (subsection 7.4.2), the FL coverage is smaller and more COs are present. The results are very similar to the ones in subsection 7.4.2. The red symbols in Figure 7.4.5 are partially superimposed to the green ones, meaning that it is not possible to distinguish which of these two flare distributions better matches the EMD of ε Eri.

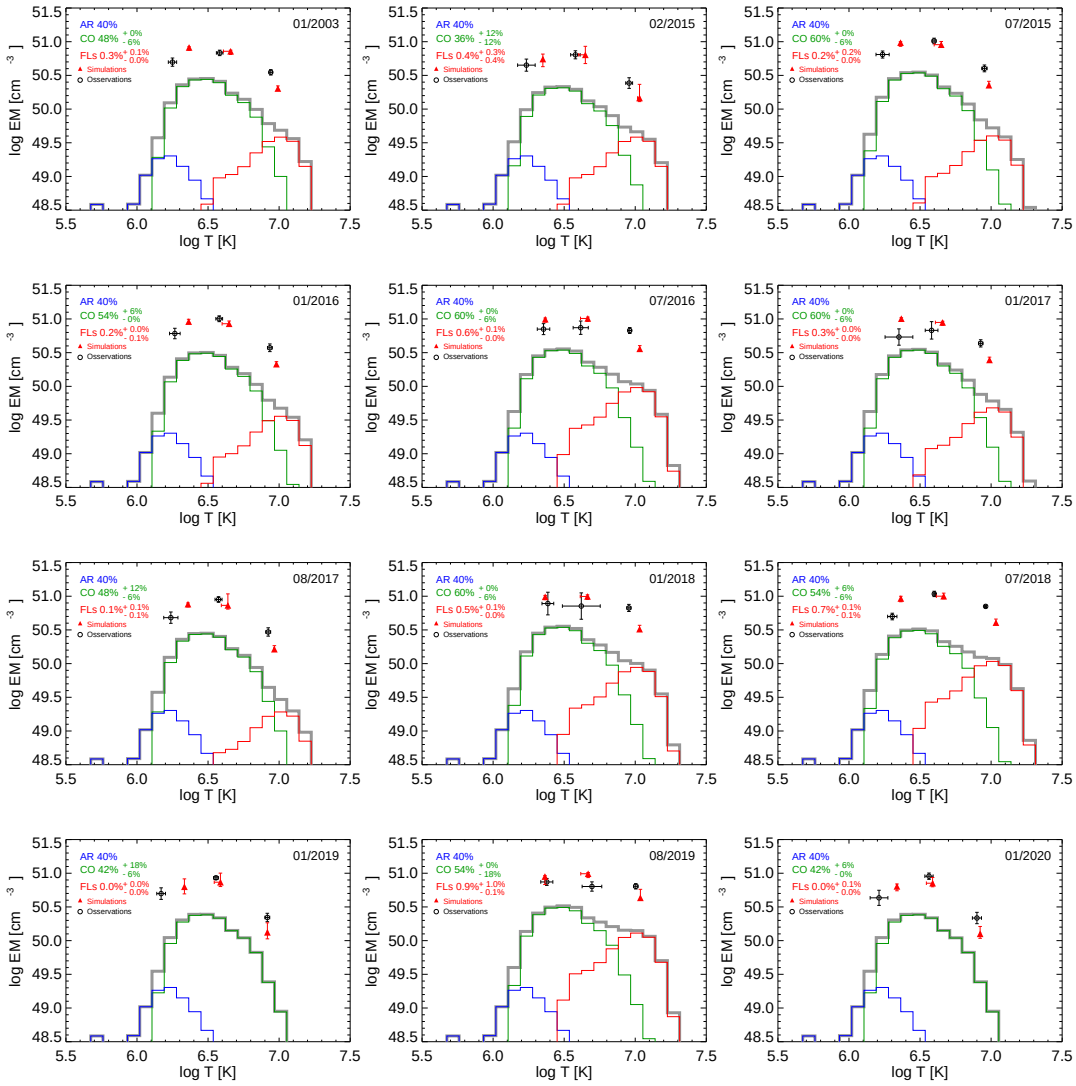

Figure 7.4.2: Best-matching EMDs composed by ARs (blue distribution), COs (green distribution) and FLs (red distribution), where the $\overline{EMD}_{FL\overline{\odot}'_M}$ includes only flares of class M observed with the hard and soft filters. The coding of plot is the same of Figure 7.2.5 (Coffaro et al. (2020) updated with new observations).

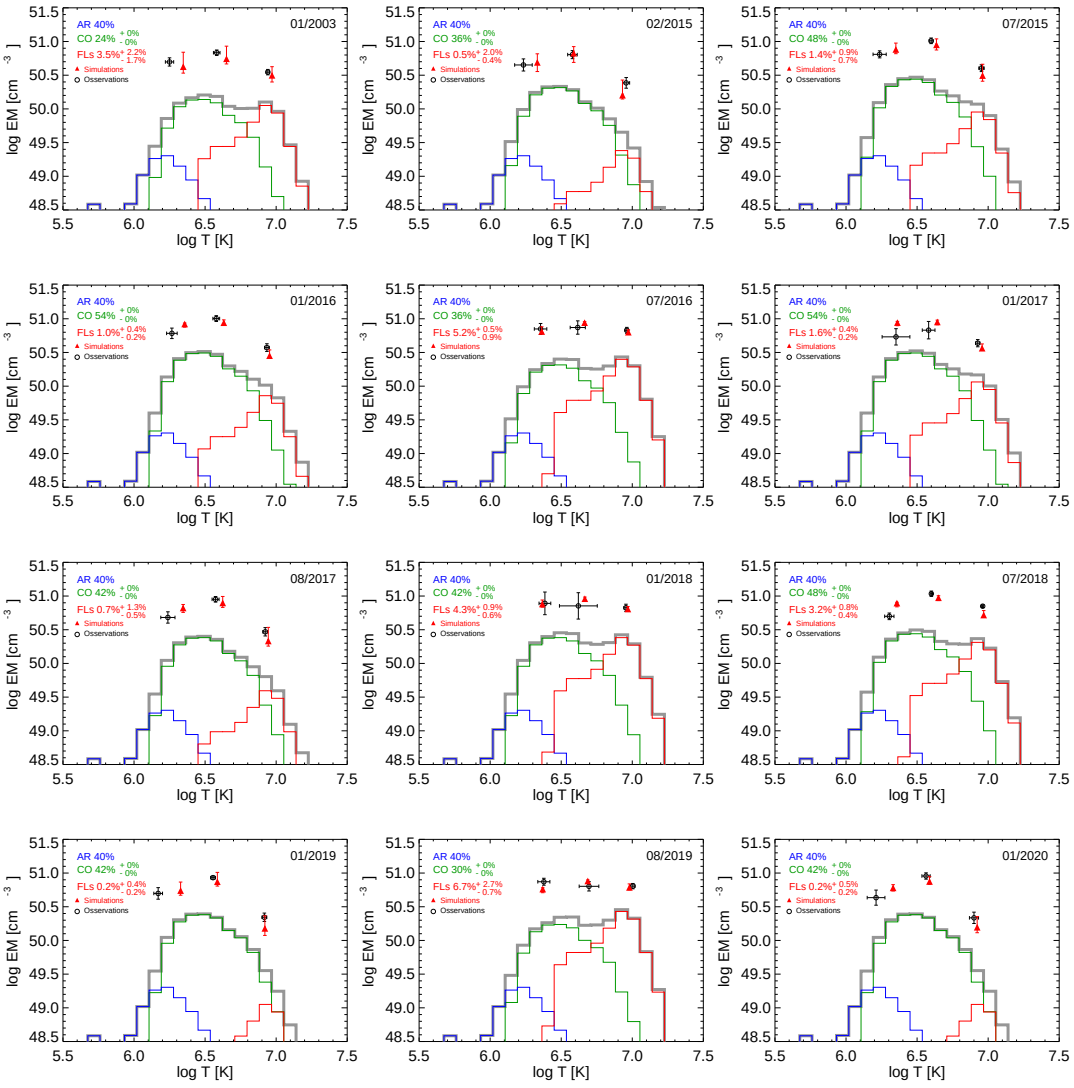

Figure 7.4.3: Best-matching EMDs composed by ARs (blue distribution), COs (green distribution) and FLs (red distribution), where the $\overline{EMD}_{FL\overline{\odot}''_M}$ includes only flares of class M observed with the hard and soft filters in the decay phase. The coding of plot is the same of Figure 7.2.5 (Coffaro et al. (2020) updated with new observations).

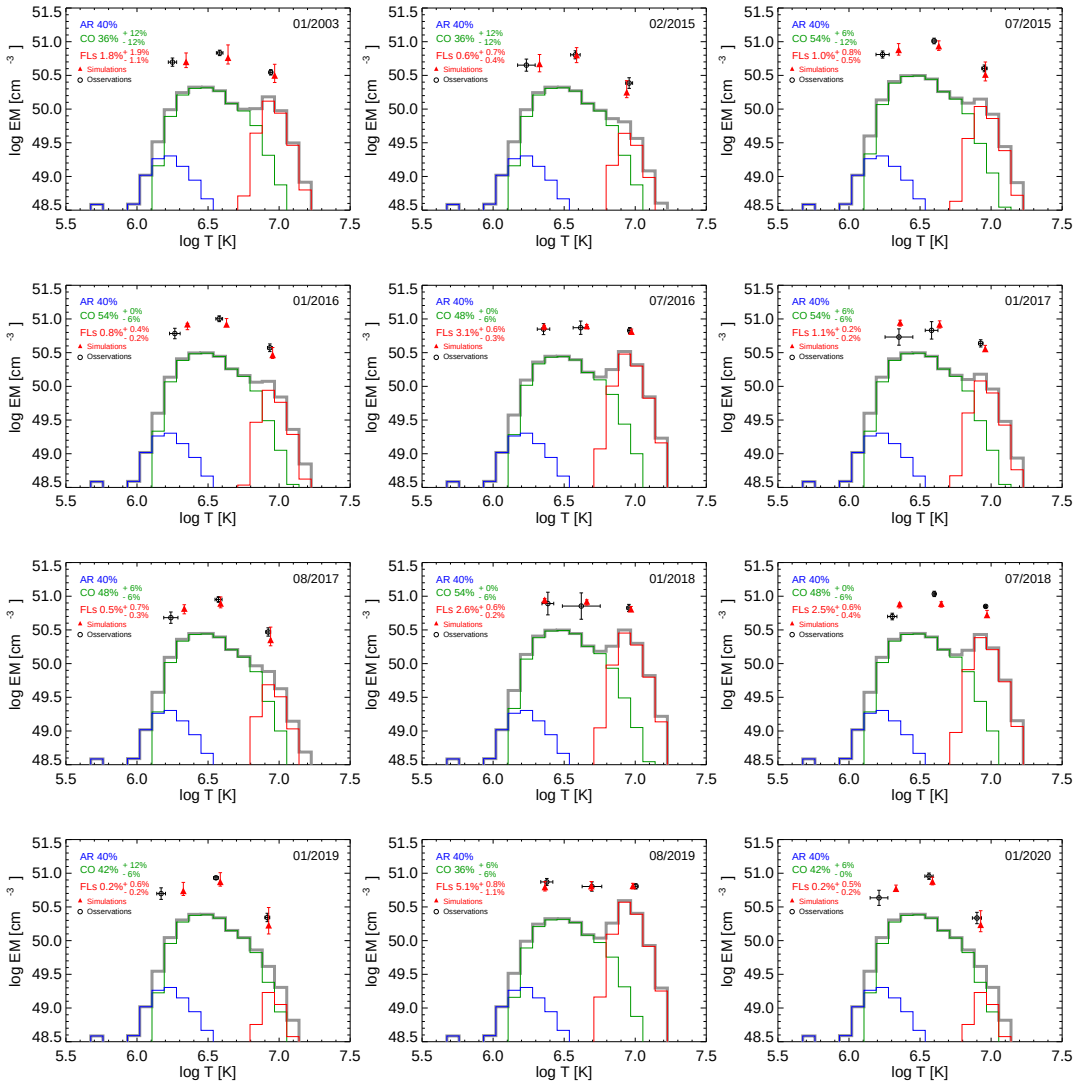

Figure 7.4.4: Best-matching EMDs composed by ARs (blue distribution), COs (green distribution) and FLs (red distribution), where the $\overline{EMD}_{FL\overline{\odot}_M'''}$ includes only flares of class M observed with the hard in the decay phase. The coding of plot is the same of Figure 7.2.5 (Coffaro et al. (2020) updated with new observations).

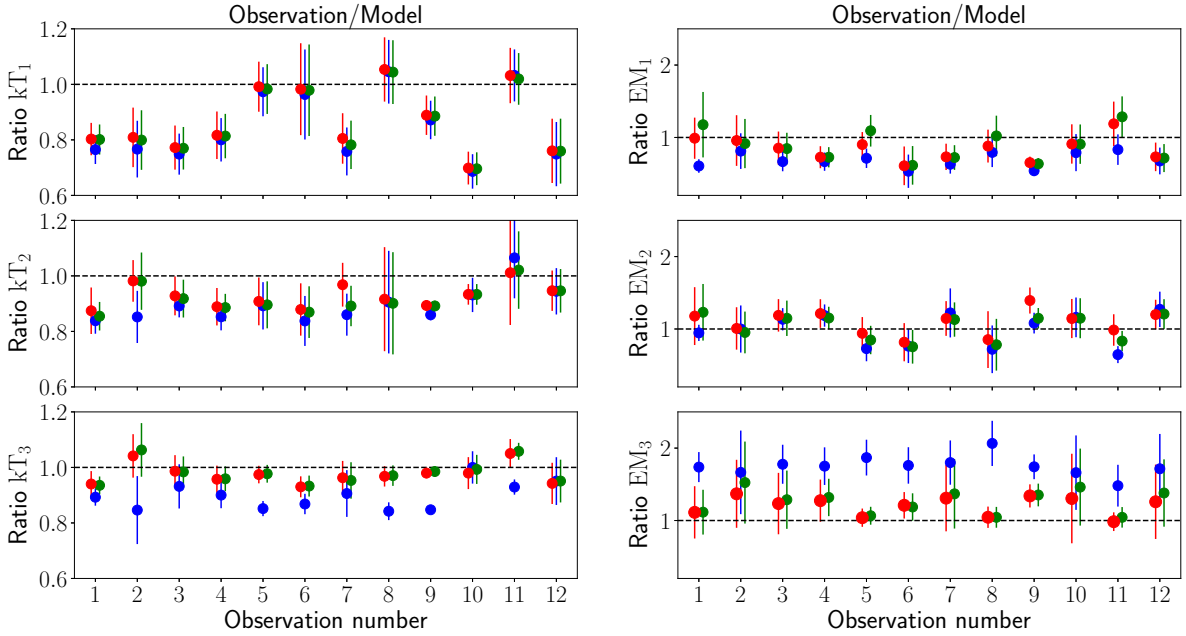

Figure 7.4.5: Ratio of best-fit parameters of ε Eri over the same parameters selected from the grid with ARs 40%, COs 6 – 60%. The color code follows Figure 7.4.1. *Blue circles* - FLs 0 – 2% of COs for M class flares at soft and hard energies ($\overline{EMD}_{FL\odot'_M}$); *green circles* - FLs 0 – 10% of COs for M class flares at soft and hard energies in the decay phase ($\overline{EMD}_{FL\odot''_M}$); *red circles* - FLs 0 – 10% of COs for M class flares at hard energies in the decay phase ($\overline{EMD}_{FL\odot'''_M}$). The error bars are the errors on the ratios found from error propagation taking into account both the uncertainties of observed best-fitting parameters and of the 10% and 90% percentiles of the 1000 selected representations (Coffaro et al. (2020) updated with new observations).

7.5 Final results

The last two EMDs tested, respectively the ones that are composed by flares in the decay phase, are the distributions that best represent the observations of ε Eri. However, we can not distinguish which one of the two EMDs is better. Thus, to discuss the obtained results, I decided to take as reference the outcomes of the $\overline{EMD}_{FL\overline{\odot}''_M}$ where the FLs are of M class, observed with the soft and hard filters in the decay phase. As matter of fact, even if the test made with the $\overline{EMD}_{FL\overline{\odot}'''_M}$, where the FLs are of M class, but observed only with hard filters in the decay phase, gives similar results, the exclusion of the soft component in the flare emission is artificial.

The main evidence provided by the simulations is that the emission measure distributions of ε Eri match the solar templates only when flares, that are not representative of the solar average flare distribution and are in the decay phase, are assumed. During the decay phase, in fact, the flaring events taking place on the stellar surface are cooling and, therefore, their EMD results shifted to lower temperatures with respect to the time-averaged solar flare EMD. The explanation is that the actual flare distribution on ε Eri at any given time might be dominated by flares in their late stage of evolution, implying that the X-ray flares on ε Eri last longer than their solar counterparts. This could be due to the lower metallicity, compared to the Sun, that makes radiative losses less efficient, as seen also in Equation 7.1. Thus, one of the major outcomes of this work is that, through this approach, it was possible to constrain the nature of flares on ε Eri.

In Figure 7.5.1 I show the coverage fraction of COs and FLs found for each observation as function of the X-ray luminosity of ε Eri. The first notable thing is the variation of COs with the luminosity: overall, as the luminosity increases, the percentage of COs in the surface of ε Eri increases too. To this evidence, the observations with the highest luminosity (namely the observations 5,8,9 and 11) and the observation 1 make an exception. These are the same observations that show a short-term variability, i.e. a flaring-like event, in their lightcurve and, as matter of fact, the corresponding percentage of flares (denoted with the red squares in the bottom panel) results higher than the other observations. Thus, it is plausible that the short-term variability seen in the lightcurves of those observations might be indeed due to flare events occurring on the surface on ε Eri.

During the minimum and the maximum of the X-ray cycle in Figure 6.6.1 (observations 2 and 9), the percentage coverage fraction of COs in these phases goes from 36% to 48%, meaning that in total the corona of ε Eri is covered throughout its cycle from 76% to 88% with magnetic structures (ARs+COs). As a contrast, in the Sun Orlando et al. (2001) have noticed that the cores of active regions result absent in the cycle minimum and feeble in the cycle maximum with respect to the active

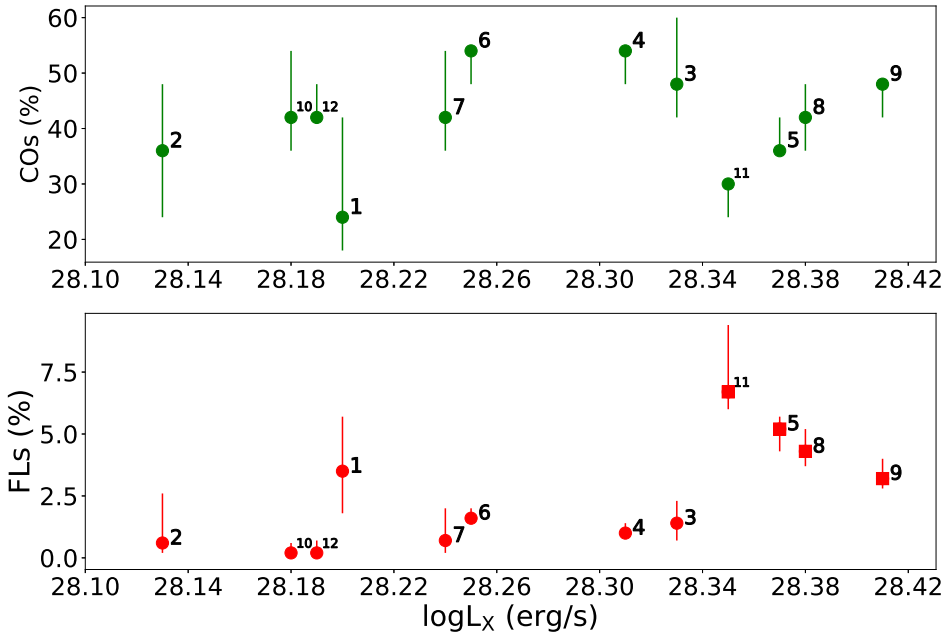

Figure 7.5.1: Coverage fraction of COs and FLs as function of the X-ray luminosity of ε Eri. The top panel refers to the variation of percentage of COs that cover the surface of the star throughout its cycle. The bottom panel shows the variation in percentage of the flaring component. The squares correspond to the observations with a flaring-like event in the short term lightcurve. The error bars are the percentile at 10% and 90% of the 1000 best-matching representations selected for each observation (Coffaro et al. (2020) updated with new observations).

regions (see Figure 3.1.4). Therefore, the high X-ray luminosity of ε Eri is the result of high magnetic filling factor in the corona and the small amplitude of the X-ray cycle of ε Eri can be indeed explained as a lack of additional space for enhancing the covering fraction throughout the cycle. Therefore, this study answers quantitatively to the third question of this PhD project. Extrapolating from the high X-ray luminosity and low cycle amplitude of ε Eri and ι Hor, it can be speculated that even younger active stars could be covered with an even higher basal surface coverage of magnetic structures.

In the past, the corona of ε Eri was observed by EUVE satellite in 1993 and *Chandra* satellite in the 2000s (Drake et al., 2000; Sanz-Forcada et al., 2003, 2004). The resulting high-resolution spectra of these observations were studied, obtaining a $EM(T)$ distribution of the corona of ε Eri. Thus, I compared these latter $EM(T)$ distributions obtained by Drake et al. (2000) and Sanz-Forcada et al. (2003, 2004) with the best-matching $\overline{EMD}_{\odot}$ of the minimum and maximum of the cycle of ε Eri, retrieved from the simulations. In Figure 7.5.2 the EMDs of Drake et al. (2000) and Sanz-Forcada et al. (2003, 2004) (green and black dots) are shown and compared to the emission measure distributions of the Sun during the minimum and the maximum of the solar cycle (April 1996 and December 1991;

dashed distributions) and the EMDs of ε Eri during the minimum and the maximum of the X-ray cycle derived from the simulations (February 2015 and August 2018; solid distributions).

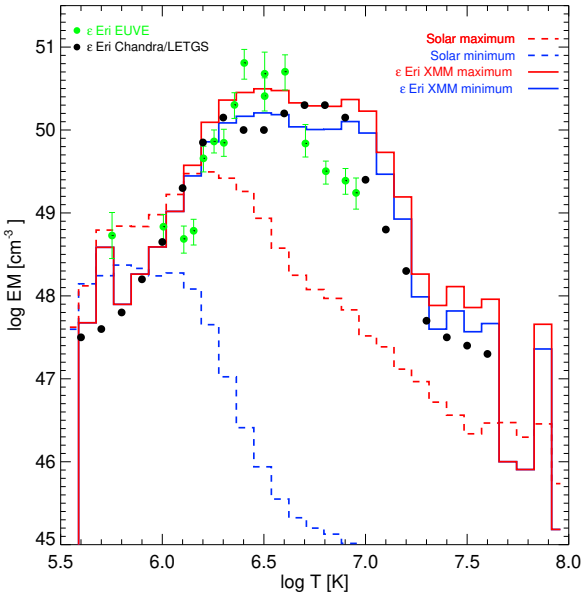

Figure 7.5.2: Comparison between the solar EMDs during the minimum and the maximum of the cycle (dotted blue and red lines) and the EMDs of ε Eri during the minimum and the maximum of the cycle (solid blue and red lines). Overplotted are the EMDs of ε Eri from high-resolution spectra obtained with EUVE and *Chandra* (green and black circles) (Coffaro et al., 2020).

The EMDs found through the simulations are in good agreement with the X-ray EMD derived by Sanz-Forcada et al. (2004) with *Chandra*, strengthening the validity of this analysis that, even if low-resolution spectra were used (EPIC/pn spectra), is able to reproduce results based on high-resolution spectra. I can reproduce at low temperatures ($T \sim 10^6 K$) the emission measure obtained from EUVE observations and the rise towards higher temperatures that reaches a first peak at $T \sim 10^{6.5} K$. At high temperatures the X-ray emission measures, both from *Chandra* spectra and EPIC/pn spectra, show a different maximum than the EUVE data. The peak at $\sim 10^7 K$ in the X-ray emission measures found in my analysis are the contribution of the flaring events. The absence of this peak in the EMD obtained with EUVE shows is due to the fact than these longer-λ observations have no sensitivity for the flaring component. Moreover, at the time of EUVE observations in 1993 ε Eri did not show the 3-yr chromospheric cycle, i.e. the EMD could have been different, and thus it is reasonable to think that the current corona of ε Eri has more flaring events than it had 27 years ago. Moreover, it can be seen from Figure 7.5.2 that the EMDs of ε Eri are very different from those of the Sun throughout its

activity cycle. As noticed by Drake et al. (2000), this difference may lay on the fact that active stars may be covered with more active regions than the Sun, an hypothesis that has been quantitatively verified in this thesis.

8

Kepler 63

Contents

In the context of searching for X-ray activity cycles in young solar-like stars, I started a new X-ray monitoring campaign of a promising target, Kepler 63. The observation campaign (Obs ID: 084123; PI M.Coffaro) was granted in late 2018 and the first observation was acquired by *XMM-Newton* in May 2019.

Kepler 63 was extensively observed by the NASA satellite *Kepler*, who had the goal of monitoring and collecting observations of stars from the constellations of Cygnus and Lyra and discovering Earth-sized planets. The mission started in 2009 and lasted for 7 years, during which more than 500000 stars were observed and a few thousands of new exoplanets were discovered.

Kepler 63 was catalogued as a solar-like star with spectral type G2V (Morris et al., 2019) and it is 200 ± 15 pc away (Sanchis-Ojeda et al., 2013). It is younger than the stars previously studied in the context of X-ray activity cycles: the age is estimated to 210 ± 45 Myr (Sanchis-Ojeda et al., 2013). It is a fast rotator with a rotational period of ~ 5.4 days, determined from the *Kepler* lightcurves. Around the star, a Jupiter-like planet is orbiting with a polar orbit of 9.43 days (Sanchis-Ojeda et al., 2013).

The magnetic activity of the star was characterized by Estrela et al. (2016) and Netto et al. (2020): the cycle period is estimated to be 1.27 yr. Back at the time when the magnetic cycle was studied by Estrela et al. (2016) and Netto et al. (2020), there was not an homogeneous data set of the chromospheric activity of Kepler 63: the star had been observed only once with the spectrograph HIRES at the Keck observatory in Hawaii in 2009, providing a chromospheric S-index of 0.37. Also at the present time, a monitoring data of the chromospheric activity is still missing. In the absence of a chromospheric monitoring campaign, Estrela et al. (2016) and Netto et al. (2020) used a different method to assess the presence of an activity cycle applied to the *Kepler* lightcurves, called *spot transit* method. In section 8.1 I briefly summarize this technique, used by Estrela et al. (2016) to identify the magnetic activity of Kepler 63.

Its young age, its fast rotational period and an activity cycle make Kepler 63 an ideal target for an X-ray monitoring campaign in search of its coronal cycle. Moreover, because the cycle period is only slightly longer than a year, I could obtain the first results within a single *XMM-Newton* observing season. In section 8.2 I present and discuss the X-ray observations that I acquired between 2019 and 2020 with the *XMM-Newton* satellite. In section 8.3 I give the preliminary conclusions on the X-ray study of Kepler 63.

8.1 The activity cycle of Kepler 63

As discussed in chapter 2, one of the most common proxies of activity cycles is the photospheric spot variation on the stellar surface. On the Sun we have seen that every 11 years the spots display a cyclic

variation, defining the solar activity cycle.

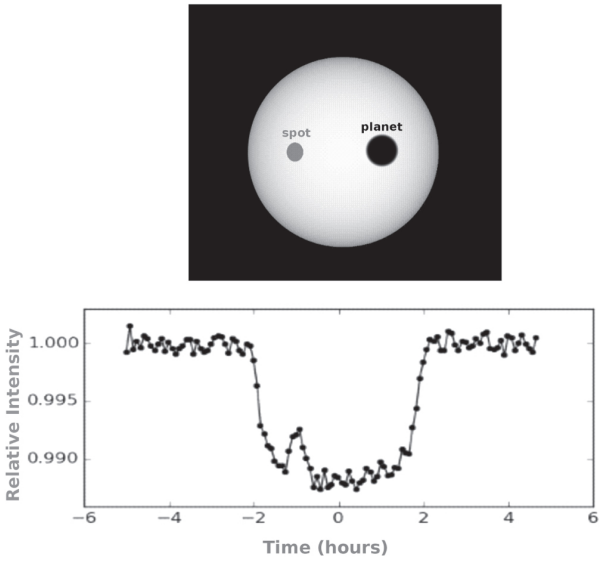

Figure 8.1.1: *Top:* simulated image of a star, with a transiting planet (black circle) and a stellar spot (grey circle) occurring on the surface. *Bottom*: the corresponding lightcurve of the simulated image with the "bump" due to the spot-crossing transit (Estrela et al., 2016).

To assess the presence of an activity cycle on Kepler 63, Estrela et al. (2016) took advantage of the spots detected by the *Kepler* satellite on the stellar surface of Kepler 63. The spots can not be directly imaged on the surface as in the case of the Sun, but the number of spots occurring on the surface can be detected from the lightcurves. As the planet transits in front of the star, it obscures a portion of the stellar surface proportional to its size causing a decrease of the flux. If a spot is present on the stellar surface during the transit of the planet and it is occulted by the planet, a slight increase in the luminosity during a short time of the transit is registered and it translates into a "bump" in the lightcurve. This is due to the fact that the spots are darker and colder than the photosphere and they have thus a decreased intensity with respect to the total stellar surface. An example of a spot-crossing transit is given in Figure 8.1.1.

Kepler 63 was observed for 4 years with the *Kepler* satellite, and during this time a total of 122 transits showed such bumps. As first step, the authors applied the *spot transit* method, previously proposed by Silva (2003), to characterize the properties of the spots: the model consists on simulating the spot-crossing transit on a star and then fitting the lightcurve using the simulated model. The fitting provides as best-fitting values the size of the spot, its intensity $I_{\rm spot}$ and the position on the photosphere. For each of the 122 transits with a bump (i.e. 122 starspots), Estrela et al. (2016) retrieved these parameters.

The activity cycle of the star was then characterized by monitoring both the variation of the spots numbers and the flux deficit that each spot presented. The flux deficit was defined at the beginning as

$$F \approx \sum (1 - f_i) \left(R_{\rm spot}\right)^2 \tag{8.1}$$

where $R_{\rm spot}$ is the radius of one spot and comes from the fitting model (Estrela et al., 2016) and f_i is

the fraction of spot intensity with respect to the central stellar intensity I_c, i.e. $f_i = \frac{I_{\rm spot}}{I_{\rm star}}$. However, in a most recent work it was noticed that the radius of the spot changes accordingly to the position (Netto et al., 2020): low latitude spots are larger close to the equator, whereas the high latitude spots increase in size toward the pole. This tendency can introduce a degeneracy in the calculation of the flux deficit, since either a darker small spot or a large brighter spot may produce similar signals in the transit light curve. Thus, the authors redefined the flux deficit of each spot as follows:

$$F = \pi \left(R_{\rm spot}\right)^2 \left(I_{\rm spot}/I_c\right) \tag{8.2}$$

Finally, they calculated the flux deficit for each transit and performed a Lomb-Scargle periodogram analysis to search for a periodicity. In the top panel of Figure 8.1.2, the final periodogram is shown. The most significant peak is found at 460 days, equal to 1.27 yr. This same result was found by the authors in their first version of this study, and cross-checked by performing the Lomb-Scargle periodogram analysis on the spots number variation (bottom panel of Figure 8.1.2).

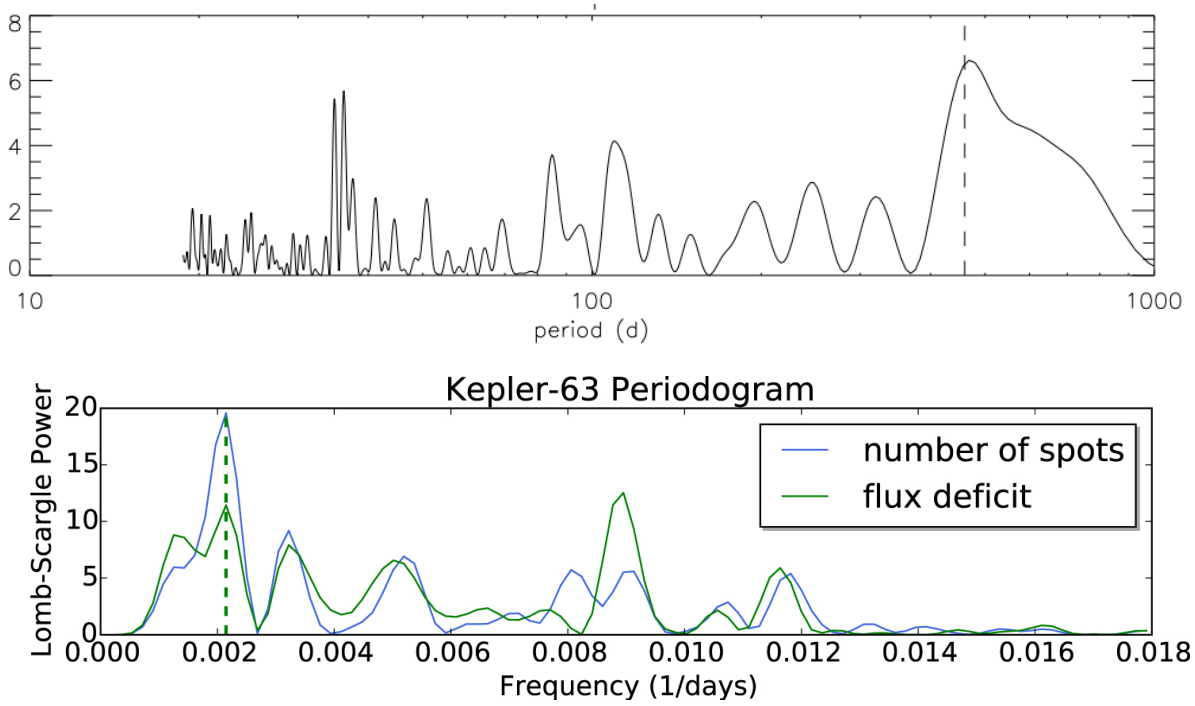

Figure 8.1.2: *Top*: Lomb-Scargle periodogram of the flux deficit calculated for Kepler 63 using Equation 8.2. The dashed line indicates the significant period, found at 1.27 yr (Netto et al., 2020). *Bottom*: Lomb-Scargle periodogram for the variation of the spot number (blue line) and of the flux deficit calculated using Equation 8.1. The dashed line indicates also here the significant peak (Estrela et al., 2016).

8.2 Search for an X-ray activity cycle

My *XMM-Newton* monitoring campaign (Obs ID: 084123; PI M.Coffaro) of Kepler 63 started in 2019 and comprises in total four snapshots of the star. As a result of the short cycle period of the star, in few snapshots the presence of X-ray variability can be proved or disproved. The observations of Kepler 63 during my monitoring campaign covered 4/5 of the total cycle period. Previous to my campaign, the star had already been observed with *XMM-Newton* in September 2014 and this observation was included in the analysis.

Kepler 63 was observed with all three XMM-Newton instruments: EPIC, RGS and OM. For a preliminary analysis presented in this PhD project, I gave priority to the EPIC/pn data, which was the prime instrument of my observations and which provides the highest sensitivity. The observing log of the X-ray monitoring campaign with EPIC is given in Table 8.2.1.

Date	Rev.	Science Mode	Exposure Time	
		EPIC	EPIC/pn	EPIC MOS
2014-09-28	0743460301[a]	Full Frame	27.0 ks	29.0 ks
2019-05-05	0841230201	Full Frame	15.9 ks	17.7 ks
2019-08-21	0841230301	Full Frame	15.6 ks	17.5 ks
2019-10-31	0841230401	Full Frame	9, 5 ks	11.4 ks
2020-03-06	0841230501	Full Frame	5.7 ks	7.6 ks

[a] Archival observation carried out prior to my *XMM-Newton* campaign.

Table 8.2.1: Observational log of my X-ray monitoring campaign of Kepler 63, including the observation in the *XMM-Newton* archive.

8.2.1 EPIC data extraction

In general, the steps for the extraction procedure of the EPIC data are the same followed for ε Eri. Since these procedures were extensively discussed in section 6.3 and represent the standard procedure to follow when handling an *XMM-Newton* observation, I will not repeat the details.

However, during the data extraction, one step needed to be performed with more attention: the definition of the GTI. As a matter of fact, the detector background registered in the EPIC/pn camera during some of the observations was high and the standard threshold suggested by the SAS manual (ESA: XMM-Newton SOC, 2019) could not be applied.

In Figure 8.2.1 the lightcurves of the detector for each observation are shown. In some observations (panel b, d and e) the background was variable during the monitoring of the target and the level of noise was higher than the threshold suggested by *XMM-Newton* and SAS manuals, i.e. higher than 0.4 cnt/s (XMM-Newton SOC, 2019; ESA: XMM-Newton SOC, 2019). Because of this, the GTI were defined in a different way for each background lightcurve, keeping in mind that, by definition, the GTI are those time intervals in the lightcurve where the background is low and constant during time.

Each observation thus requires a choice of GTI *ad hoc*, different for each case. For the observations of September 2014 and August 2019 (panel a and c in Figure 8.2.1) the standard cuts could be applied, i.e. I selected as GTI all the intervals where the events are below 0.4 cnt/s. In the case of the observations taken on May 2019 and October 2019 (panel b and d in Figure 8.2.1) the threshold was chosen at 5 cnt/s and at 1 cnt/s respectively. For the observation of March 2020 (panel e in Figure 8.2.1), where the background is the most variable, I selected three time intervals where the background results low and constant. In this way, because the background of this latter observation is more variable that in the others, I avoided to exclude too many events from the final event list. The three chosen intervals are highlighted in Figure 8.2.1e.

Because Kepler 63 is a faint source and because of the level of noise, in the images it is not possible to distinguish by eye the star. However, the SAS source detection procedure was able to detect Kepler 63 in all snapshots of my campaign. In Figure 8.2.2, I show as an example a portion of two EPIC/pn images of the observations of September 2014 and October 2019 respectively. The first observation in panel a is the one found in the archive: because of its exposure time (27.5 ks), 2-5 times longer than the observations of my campaign, Kepler 63 can be better visualized in the EPIC/pn image. On the other hand, in the image of the observation of October 2019, that has an exposure time of 9.5 ks, the star is less visible. Nevertheless, the source detection successfully identified it. Finally, in these two images in Figure 8.2.2 also the source regions and background regions, used for the extraction of lightcurves and spectra, are overplotted in red.

8.2.2 EPIC/pn lightcurves

The EPIC/pn lightcurves of Kepler 63 were all extracted in the soft energy band of *XMM-Newton*, i.e. from 0.2 to 2.0 keV. The time bin size was set to 1000 s.

In Figure 8.2.3 all five EPIC/pn lightcurves of the observations of Kepler 63 are shown. The red dots represent the lightcurves of the background regions chosen in each observation. The green dots are

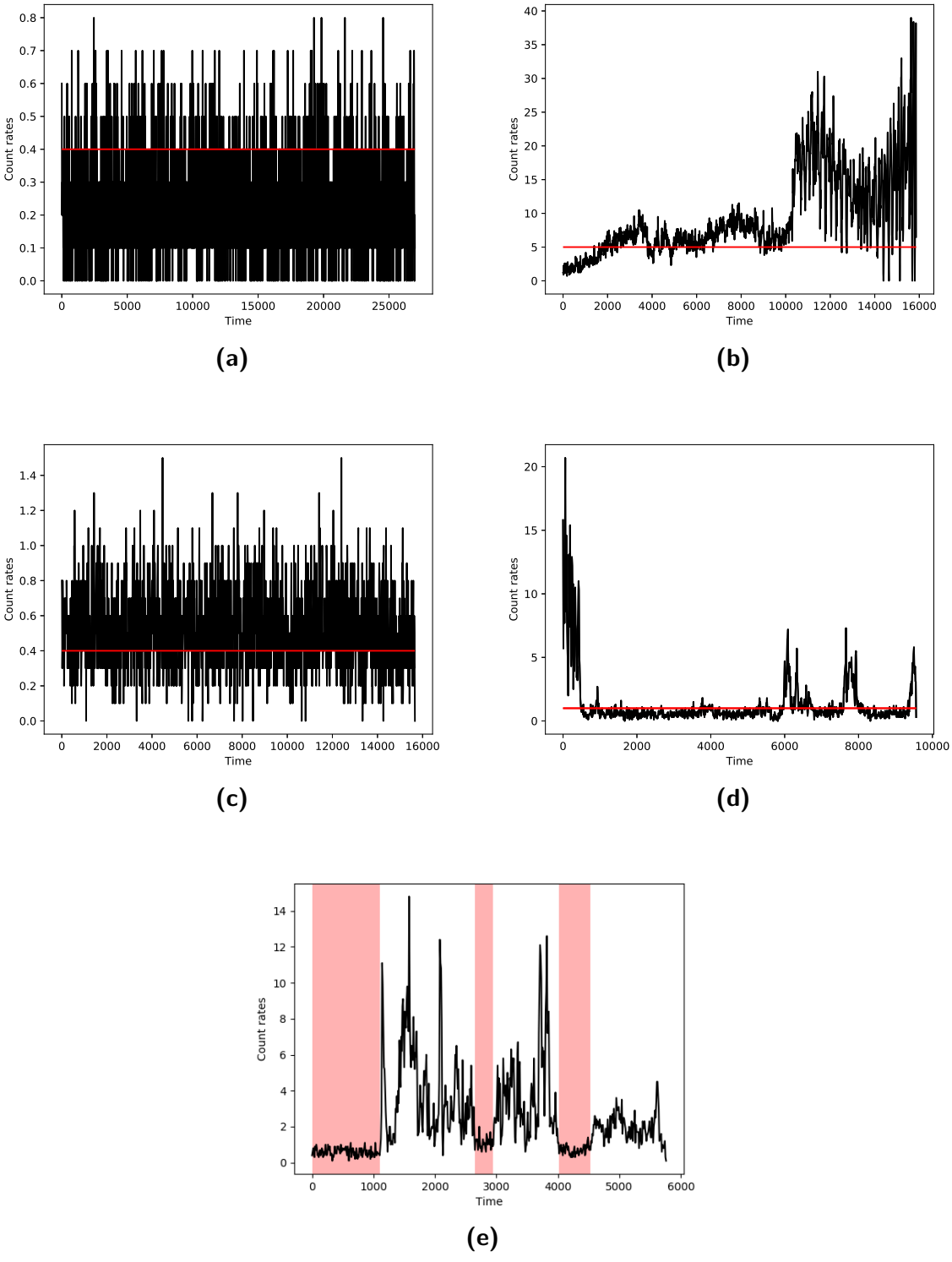

Figure 8.2.1: Lightcurves of the EPIC/pn detector. *Panel a*: September 2014; *Panel b*: May 2019; *Panel c*: August 2019; *Panel d*: October 2019; *Panel e*: March 2020.

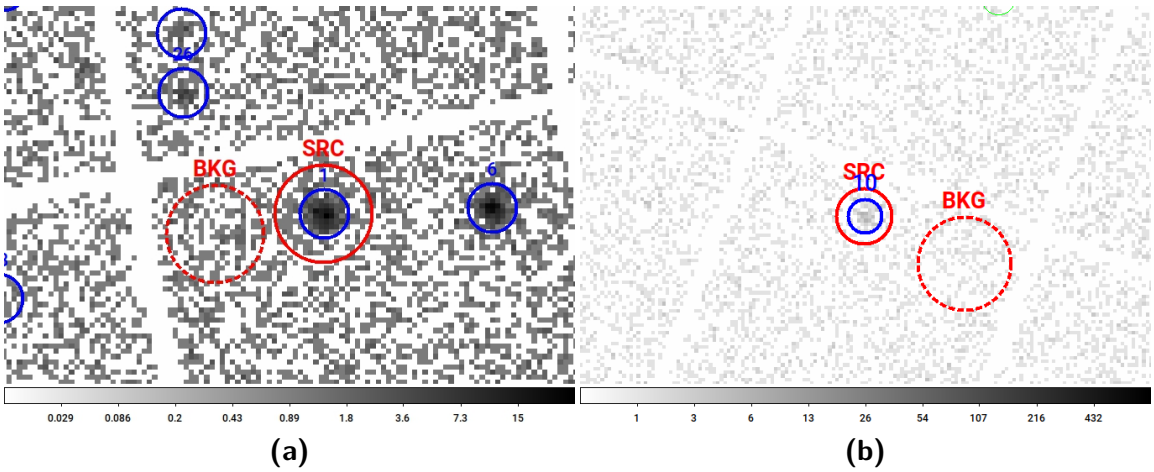

Figure 8.2.2: Two examples of EPIC/pn images in the region of Kepler 63. The source regions and the background regions chosen for the subsequent analysis are overlaid in red. The sources detected with the SAS procedure are highlighted with blue circles. Kepler 63 had the source ID no. 1 (panel a) and 10 (panel b). *Panel a*: September 2014; *Panel b*: October 2019.

the lightcurves of the source regions, i.e. the lightcurves to be still corrected for the background. The black dots are the final lightcurves, i.e. the background-subtracted lightcurves. As mentioned already in section 6.4, the SAS procedure `epiclccorr` that generates the background-subtracted lightcurve takes into account different effects and does not produce the final lightcurve as a simple subtraction between the source count rates and the background. One of the effects is the GTI correction. In the plots, I show the GTIs selected for each observation highlighted in grey. The count rates of the source and the background regions that lay outside the GTIs are not taken in consideration by the `epiclccorr` procedure, as can be seen for the observations of May 2019 and March 2020. Moreover, the bins that lay on the border of the GTIs are those with a large error bar and an example of this is evident in the lightcurve of the observation of May 2019. The other bins in the background-subtracted lightcurves, that also show large error bars, contain most probably counts influenced by other effects, such as exposure time and dead time of the CCDs.

For each background-subtracted lightcurve, I calculated the mean count rate. These values are plotted in Figure 8.2.3 with the solid blue line. The uncertainties are calculated as the standard deviation of the mean and are plotted with the dotted blue lines [1]. These values are also reported in Table 8.2.2 and compared with the count rates of each observation obtained by the SAS source detection procedure. From both these quantities, it is obvious that the lightcurves do not show a significant long-term

[1] In the lightcurve of the observation of May 2019 (Figure 8.2.3) the dotted blue lines are not visible in the plot because the value of the standard deviation of the mean is high and it is thus located outside the limit of y-axis.

variability: the mean count rate does not show a significant variability throughout the monitoring of Kepler 63. This indicates that in the corona the star does not show a cyclic behaviour.

Obs. date	Count rate lightcurve cnt/s	Count rate source detection cnt/s
September 2014	0.019 ± 0.005	0.019 ± 0.005
May 2019	0.027 ± 0.100	0.019 ± 0.004
August 2019	0.012 ± 0.010	0.015 ± 0.003
October 2019	0.016 ± 0.005	0.017 ± 0.002
March 2020	0.015 ± 0.008	0.020 ± 0.005

Table 8.2.2: In the second column, the mean count rate calculated from each lightcurve of Kepler 63 is shown. The errors are the uncertainties calculated as the standard deviation of the count rates. In the third column, the count rates derived from the source detection procedure are reported.

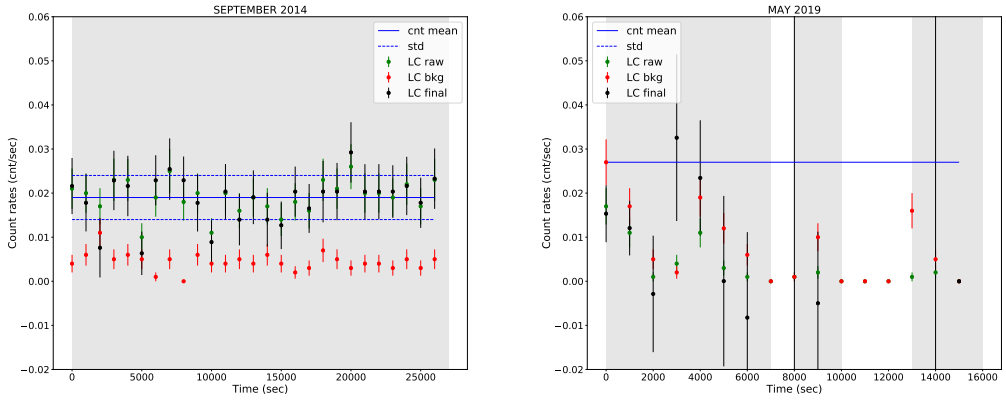

Figure 8.2.3: EPIC/pn lightcurves of all observations of Kepler 63. The red and green dots are the lightcurves of the source region and of the background region respectively. The black dots are referring to the background-corrected lightcurve. The blue line is the mean count rate calculated as average of all background-subtracted count rates in each observation. The dotted blue lines are the standard deviation of the mean.

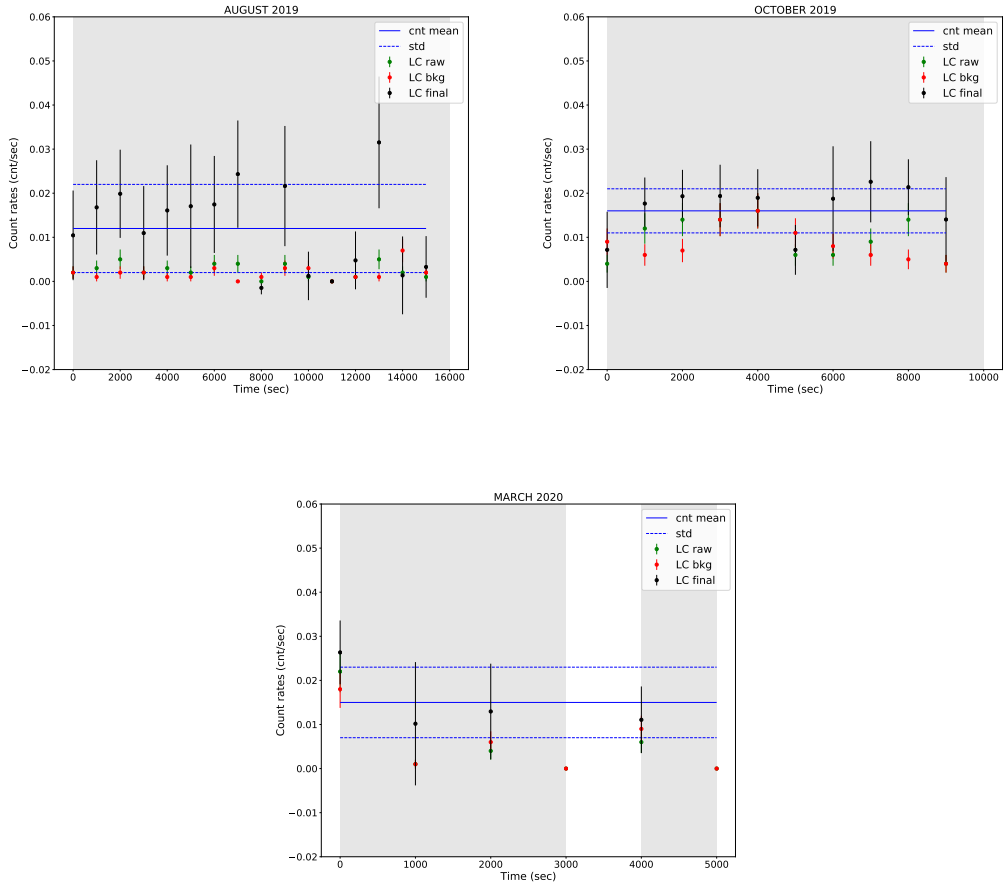

Figure 8.2.3: (continued)

8.2.3 EPIC/pn spectra

The EPIC/pn spectra of Kepler 63 were extracted following the threads described in section 6.3. For the observations of my monitoring campaign (2019-2020), the spectra of the source region and the ones of the background region were grouped with a minimum of 5 counts per bin. The spectrum of the archival observation (September 2014) was instead grouped with a minimum of 15 counts per bin. As a matter of fact, for spectra of my campaign I could not use a grouping size greater than 5 because the counts (on average 80 counts) are much less than in the archival observation (= 647 counts) and a larger grouping size would have produced spectra with too few bins for spectral fitting. This is due

to the fact that my observations have a smaller exposure time than the first archival observation and thus less X-ray photons are registered by the EPIC cameras.

The spectra were all analysed using the software `xspec` (version 12.10; Arnaud, 1996) and in Table 8.2.3 the best-fitting parameters are shown. Because of the few counts in the spectra of the 2019-2020 monitoring campaign, I adopted the simplest spectral model: a 1-T APEC model where the metal abundances are frozen at $1.0 Z_{\odot}$ in the fitting procedure. This value was adopted from the literature, where the metal abundance in the photosphere of Kepler 63 is found to be $[Fe/H] = 0.07 - 0.14$ dex, corresponding to $1.1 - 1.4\ Z_{\odot}$ (Huber et al., 2013; Frasca et al., 2016; Morris et al., 2019). The spectrum extracted from the archive (September 2014) was instead fitted with a 2-T APEC spectral model, keeping also frozen the metal abundances on $1.0 Z_{\odot}$.

The fitting of the 2019-2020 observations provides best-fitting parameters that are not well constrained for some of the spectra. In particular this problem occurred for the observations of May 2019 and March 2020. In fact, the command `error` can not find upper limits for the best-fitting parameters. When the `error` command fails on the determination of the uncertainties, the command `steppar` is helpful: this command performs the fit while stepping the best-fitting values of two parameters through a given range and determines the confidence ranges of the parameters. The results of this procedure can be visualized in contour plots: in these plots the reduced χ^2, obtained for each pair of the values tested during the stepping, are shown and the corresponding confidence levels are plotted on the graph. In the Figure D 1 of Appendix D, the contour plots retrieved from running the command `steppar` applied to the temperatures and normalizations are shown: the contours correspond to 1σ (red line), 2σ (green line) and 3σ (blue line) confidence level. For the observation of May 2019 it can be seen that both temperatures and emission measures show two contours within the 1σ confidence range, suggesting thus the presence of two possible values for each parameter. For the observation of March 2020 the 1σ confidence range is so large that it is not possible to properly constrain the temperature. Moreover, the range of temperatures and normalizations identified within the 1σ contour does not include values physically reasonable for a stellar corona.

Thus, the best-fitting parameters obtained for my observations are not statistically solid due to the limited number of counts in the spectra. To retrieve spectral information and to search for variability, I therefore resorted to the hardness ratio, defined as:

$$HR = \frac{H - S}{H + S} \tag{8.3}$$

where H is the count rate in a chosen hard band of the spectrum and S is the count rate a the chosen soft band of the spectrum. The bands chosen to calculate the hardness ratio are $E_S = [0.2 - 0.9]$ keV

Obs.	kT_1 [keV]	kT_2 [keV]	$logEM_1$ [cm^{-3}]	$logEM_2$ [cm^{-3}]	F_X 10^{-14} [erg/cm^{-2}/s]	$\overline{\chi}^2$	d.o.f.
2775	$0.40^{+0.89}_{-0.06}$	$1.13^{+0.23}_{-0.19}$	51.42 ± 0.08	51.21 ± 0.17	1.56 ± 0.21	0.88	28
3553	$1.82^{+0}_{-0.59}$		51.78 ± 0.77		1.56 ± 0.92	0.77	7
3607	$0.69^{+1.74}_{-0.37}$		51.21 ± 0.16		1.17 ± 0.44	1.17	4
3643	$0.76^{+1.65}_{-0.13}$		51.43 ± 0.11		1.89 ± 0.44	0.73	16
3707	$3.76^{+0}_{-3.01}$		52.32 ± 0.67		4.05 ± 1.66	0.40	3

Table 8.2.3: Best-fitting parameters of the observations Kepler 63. The archival observation (Orb. 2775) is the only one with sufficient photon statistics that a 2-T APEC model could be applied. The observations of my X-ray monitoring campaign (from 3553 to 3707) were instead fitted with a 1-T APEC model. In both spectral models I kept the metal abundances frozen at the value $1.0 Z_{\odot}$. The last column shows the degree of freedom (d.o.f.) of each fitting procedure.

and $E_H = [0.9 - 2.0]$ keV. Both count rates were calculated by the source detection. If the energy bands are given as input to the source detection procedure, the source detection calculates the count rates in each band for each detected source. In Figure 8.2.4, the time-evolution of the hardness ratio for five observations of Kepler 63 is shown.

Any spectral variability in the X-ray corona of Kepler 63 is expected to show up in Figure 8.2.4. However, within the uncertainties the hardness ratio of Kepler 63 is not variable (see Figure 8.2.4). Clearly, the low statistics of each spectrum makes difficult to identify small changes in the hardness ratio from one snapshot to the next one.

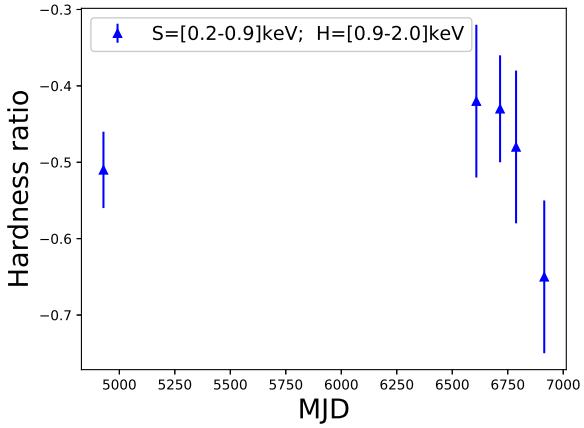

Figure 8.2.4: Hardness ratio of each observation of Kepler 63. The chosen soft and hard bands are given in the legend on the plot.

Combining all four spectra from my campaign improves the signal and thus enables a comparison to the archival observation of 2014. Therefore, I merged the spectra of the 2019-2020 campaign with SAS and proceeded on spectral fitting of the merged spectrum (with a total number of counts of 315).

In Figure 8.2.5 on the left the merged spectrum is shown. The bottom panel of the figure shows the residuals of the fit. The fit was first performed by keeping the metal abundances frozen on the value found in the literature, i.e. $1.0 Z_{\odot}$, (Figure 8.2.5a) and in a second run the fitting was repeated

	Z $[Z_\odot]$	kT [keV]	$logEM$ $[cm^{-3}]$	F_X $10^{-14} erg/cm^2/s$	$\overline{\chi}^2$	d.o.f
Merged spectrum	1.0 (frozen)	0.92	51.58	2.35	3.55	7
	0.16 ± 0.08	0.92 ± 0.12	52.18 ± 0.11	2.98 ± 0.35	0.26	6
Orb. 2711	0.18 ± 0.10	0.63 ± 0.09	52.06 ± 0.14	1.56 ± 0.21	1.22	29

Table 8.2.4: Best-fitting parameters of the merged spectrum and the archival spectrum. The merged spectrum is obtained by considering only my X-ray campaign (2019-2020) and it is fit with a 1-T APEC spectral model, when in one case the metal abundances are frozen and in the second case they are free to vary. The archival observation is also fit with a 1-T APEC model, but only in the case of the metal abundances kept thawed. The last column shows the degree of freedom (d.o.f.) of each fitting procedure.

leaving the abundances free (Figure 8.2.5b). In Table 8.2.4 the best-fitting parameters obtained are shown. When the metal abundances are fixed at $1.0 Z_\odot$, the reduced χ^2 is high, and the errors on the best-fitting parameters can not be calculated. On the other hand, when the abundances are left free during the procedure, the fit of the merged spectrum has better statistics with a small reduced χ^2. The residuals of the fit do not show a systematic behaviour, indicating thus that the fitting procedure yields a statistically acceptable result. To check if the best-fitting parameters are well constrained by the fit, I again used the `xspec` command `steppar`. In Appendix D the contour plot is shown (Figure D 2). Here, the contours are well defined and thus the obtained values are well constrained by the fitting procedure.

The merged spectrum was then compared to the archival observation: the spectrum of this observation with the best-fitting spectral model is shown in Figure 8.2.5c and Table 8.2.4 reports also the best-fitting values for the parameters. For the sake of an appropriate comparison, the archival observation was here fitted with a 1-T APEC model with the metal abundance free to vary during the procedure. Overall, the residuals of this fitting are statistically reasonable, but the reduced χ^2 is larger than the value obtained for the 2-T fit (see Table 8.2.3) and thus a 2-T APEC model is more suitable for the archival observation. Because of the difference in counts between the two spectra, the archival observation shows a number of degree of freedom higher than the merged spectrum that as a consequence shows a smaller reduced χ^2.

The metal abundances obtained for both spectra are comparable within their uncertainties. However, the values are considerably lower than the one found in the literature. This is due to the fact that those metal abundances $[Fe/H]$ refer to the abundances in the photosphere of the star and it is reasonable that instead in the corona Zs are reduced.

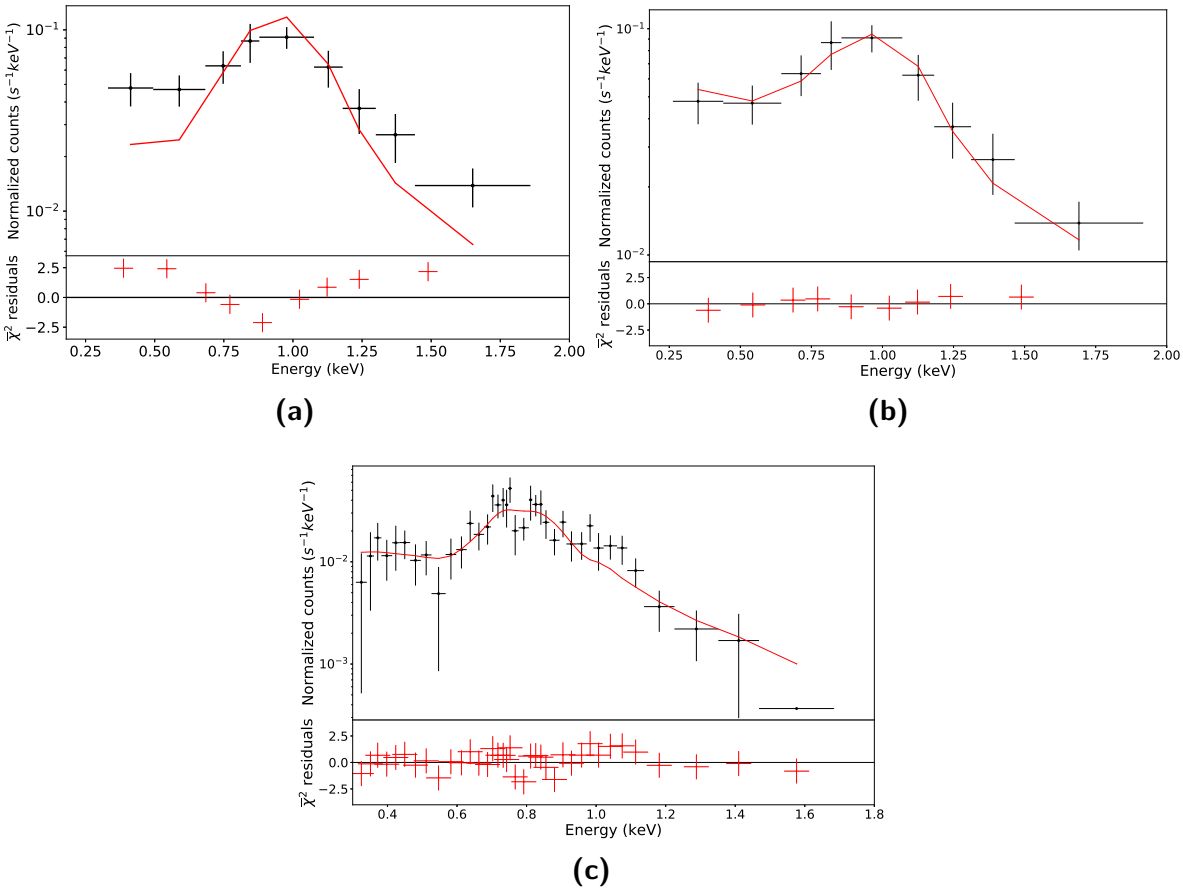

Figure 8.2.5: EPIC/pn spectra of the merged observations of Kepler 63 obtained in 2019 and 2020 (panel a-b) and of the archival observation (panel c). The best-fitting spectral models, 1-T APEC, are overlaid in red. Panel a shows the best-fitting model when the abundances are frozen to the solar abundances, whereas in panel b and c the abundances are free during the fitting procedure. The bottom panels show the residuals of the fit.

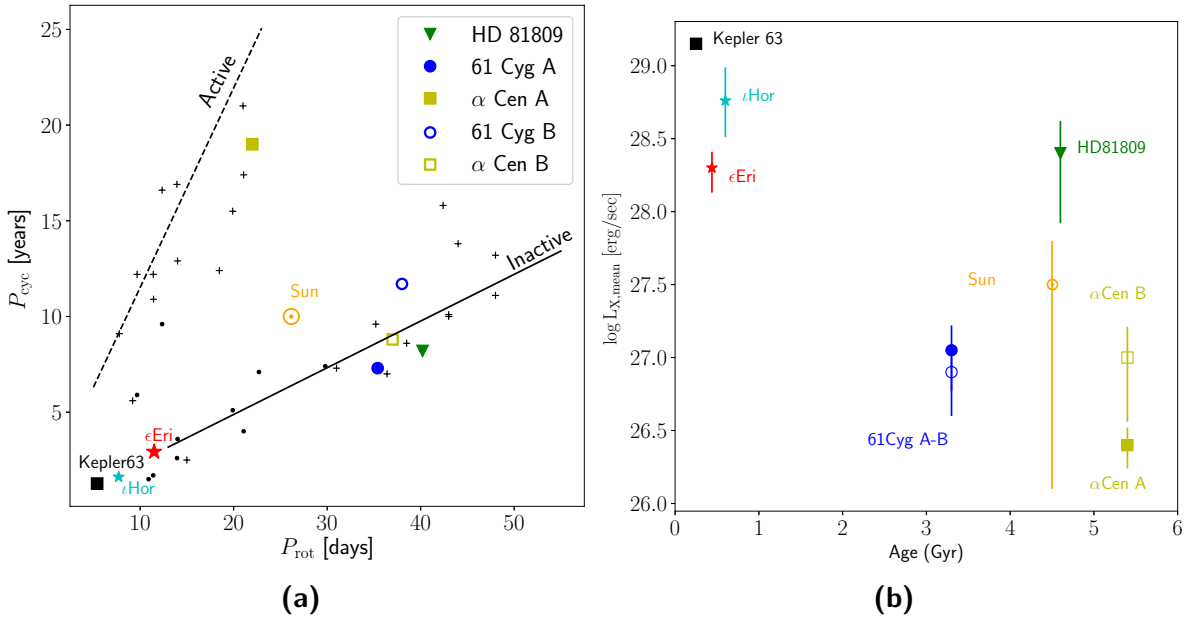

Figure 8.3.1: Panel a: the $P_{cyc} - Prot$ diagram with Kepler 63 included. Panel b: the X-ray luminosity-age relationship is shown. The coding of the plots follows Figure 3.3.1.

8.3 Preliminary conclusion on the X-ray monitoring campaign of Kepler 63

To summarize, the X-ray monitoring campaign of Kepler 63 provided four snapshots. Even if the star is faint, the source detection detected Kepler 63 in all four observations. We have also noticed that the observations of May 2019, October 2019 and March 2020 show a higher detector background than the ones of the other two snapshots: this could be due to a massive presence of soft protons occurring during the 2019-2020 observations.

From the analysis of the X-ray lightcurves no long-term variability was detected during the monitoring of Kepler 63, indicating that the star likely has no coronal activity cycle. Moreover, the analysis of the spectra and the calculation of the hardness ratio show no evidence for X-ray spectral variability.

The merged spectrum of the four spectra taken from 2019 to 2020 provides an X-ray luminosity of 1.4×10^{29}erg/s. If thus Kepler 63 is included in the X-ray luminosity-age relation (Figure 8.3.1b), among all stars with known X-ray activity cycle it is the star with the highest X-ray activity level. The outcome is in agreement with what it is expected for young solar-like stars: young star shows high X-ray activity level and a low amplitude of the cycle is expected. Thus, although no X-ray variability was detected during my monitoring campaign, Kepler 63 is expected to be one of the star with the highest activity level.

Part III

Future prospectives

9

Outlook

Contents

In this last chapter I summarize the main findings that I achieved during my PhD project. Moreover, I give some insights on further studies that can be done in the future with the three stars presented here, i.e. ε Eridani, ι Horologii and Kepler 63.

9.1 ε Eridani and future studies

In this PhD project I established the clear evidence of a coronal X-ray cycle for the young solar-like star ε Eridani (chapter 6). Together with ι Horologii, these two stars are the youngest stars monitored at X-ray wavelengths so far and they have the shortest activity cycles.

Interestingly the age of ε Eridani ($\sim$ 400 Myr) and of ι Horologii ($\sim$ 600 Myr) corresponds to the age of the Sun when life started to appear on our planet. Therefore, it is quite important to characterize the magnetic activity cycle in such young targets, not only for growing our knowledge on the stellar dynamo mechanism, but also to better understand if and in which measure the magnetic field can play a role in the evolution of exoplanets.

The coronal cycle of ε Eridani was discovered thanks to the synergistic studies conducted with *XMM-Newton* (chapter 4) and with ground-based optical telescopes such as TIGRE at La Luz Observatory in Mexico. The dedicated monitoring campaign on the Ca II H&K lines was the benchmark to follow for characterizing the X-ray variability. As a matter of fact, from a qualitative and quantitative correlation, I verified the presence of an X-ray cycle lasting 2.93 yr in excellent agreement with the chromospheric counterpart.

Chromospheric and coronal cycle In Figure 6.6.1 I showed the final lightcurve of ε Eridani including both the X-ray fluxes and the Ca II measurements. Until late 2018, both activity indicators are in good agreement and they follow roughly the sinusoidal function approximating the activity cycle. However, in January 2019 a departure between the expected cycle and the observations is clear: both Ca II measurements and the X-ray fluxes are at a minimum and not at the maximum expected for that observing season. Moreover, after early 2019, the X-ray fluxes returned to be in good agreement with the sinusoidal function. However, the lack of Ca II measurements for the same time range makes it difficult to understand if changes in the activity cycle of ε Eridani are occurring.

The 3-yr cycle of ε Eridani became dominant only 10 years ago (Metcalfe et al., 2013). Now, again after roughly a decade, new changes of the cycle appear to occur. Thus, the chromospheric and coronal cycle of ε Eridani are entering in an interesting phase that provides the possibility to understand how cycles dramatically change in a long-term run. Hence, new monitoring campaigns of both activity indicators will be carried out in the immediate future. With *XMM-Newton* a new observation is soon to

be acquired (in August 2020). With the ground-based telescopes, and more specifically with TIGRE and SMARTS, new observations were taken in the last year and they are under analysis. In particular TIGRE is observing ε Eridani with an almost daily cadence in this last year, with the further goals to better understand the surface distribution of activity on the star and to re-calculate its rotation period[1]. These new campaigns will shed light of the ongoing changes on the activity cycle behaviour.

Simulations of the coverage fraction of magnetic structures Another key point of my PhD project was the characterization of the X-ray cycle of ε Eridani in terms of solar magnetic structures on the stellar surface (chapter 7). As a matter of fact, the amplitude of the X-ray cycle found from my spectral analysis is the smallest of all stars with known X-ray cycles and I have quantified that this might be due to a lack of space for magnetic structures to arise on the surface and evolve. To this end, since it is not possible to spatially and temporally resolved such structures on a stellar surface, I took advantage the study "The Sun as an X-ray star" (section 3.1). The approach consisted on simulating the X-ray spectra of solar magnetic structures as if they were on the corona of ε Eridani and observed by *XMM-Newton*. This allowed me to assign for each state of the X-ray cycle a percentage of coverage fraction of the magnetic active regions, cores of active regions and flares. The main result from this analysis was that during the minimum of the X-ray cycle the star appears to be covered by magnetic structures at 75% and during the maximum the magnetic structures reach 95% of the total surface, confirming that indeed the X-ray luminosity of ε Eridani can not vary strongly because of lack of space on the stellar surface.

Interestingly, the observations that are affected by short-term variability (flare-like events) result to be also the ones with the highest percentage of flares in their composite emission measure distribution. These observations comprise one third of all the X-ray observations of ε Eridani acquired by *XMM-Newton* in the last three years, influencing hence the X-ray cycle monitored during this project. Thus, it is interesting in the future to apply again the method of "The Sun as an X-ray star" on those X-ray spectra acquired during the flare-like events. A possible approach can be simulating a grid of emission measure distributions for which the only contribution is given by flares. As a matter of fact, from the study "The Sun as an X-ray star" a collection of different flares at different evolutionary phases is available and, thus, it is possible to perform a comparison between the X-ray spectra of ε Eridani representative of flare-like events and the spectra extracted from these solar events. This can give the possibility to understand if the short-term variability is actually ascribable to flare events occurring on ε Eridani and, if so, gain more information on the nature of these events. At the present, the method I applied results successful, i.e. the simulations and the X-ray observations actually match, if the flare

[1]The last measurement of the rotational period of ε Eridani dates back to 1995 (Gray et al., 1995).

contribution to the total emission measure distribution comes from flares that are decaying (i.e. they last longer than in the Sun) and are of class M (i.e. of intermediate energy).

Analysis of the high-resolution X-ray spectra of ε Eridani As said in section 6.2, ε Eridani was also observed using the RGS detector on board of *XMM-Newton* and designed for high resolution spectroscopy. Here, I summarize the steps followed in the extraction procedure of the RGS data and the preliminary results I obtained.

The scientific products are extracted from the ODFs through the SAS task `rgsproc`. This task processes different stages without starting from scratch. The different entry and exit points are called *processing stages* and they generate the following products in order: 1) the source-independent calibrations; 2) the filtered events and the exposure maps; 3) the spectra; 4) the response matrices; 5) the lightcurves. The user can choose to go through all stages or to run some of them. In the case of ε Eridani, the `rgsproc` was stopped at the third stage where the spectra are generated.

Once the main scientific files are produced, the user should only check for the source coordinates and for the possible presence of high background. To check for the source coordinates, the plots called *dispersion vs cross dispersion* and *dispersion vs energy images* are generated directly with the SAS task `evselect`: on these plots the dispersion masks are also overplotted. To create the dispersion masks, the coordinates stored in the header of the RGS event files are used. If the source detected by RGS is not included in the dispersion masks, then the coordinates need to be modify. In the case of ε Eridani this problem was not present, as shown in Figure 9.1.1.

To check for high background, the procedure is identical to the one of the EPIC event files (section 6.3). First, the lightcurve of the detector is produced. By inspecting this lightcurve, the GTIs are identified and the GTI table is produced. Finally, the SAS task `rgsproc` is run again with the time filtering option `auxgtitables` that will produce the event files and the spectra within the chosen GTIs.

During this PhD project, the RGS spectra of each observation of ε Eridani were not analysed individually. Instead, a merged spectrum comprising all observations was produced for the first and the second spectral order of the RGS detectors. The spectrum of the first order is shown in Figure 9.1.2. Contrary to the low-resolution EPIC spectrum, the RGS spectrum allows to identify individual emission lines by eye. In particular important ions, easily recognized from the spectrum, are for example O VII triplet, O VIII, Fe XVII and Ne X.

The future goal is to analyse the RGS spectra individually, so that the metal abundances on the corona of ε Eridani can be better defined. In this way, I can analyse again the EPIC spectra, but adopt-

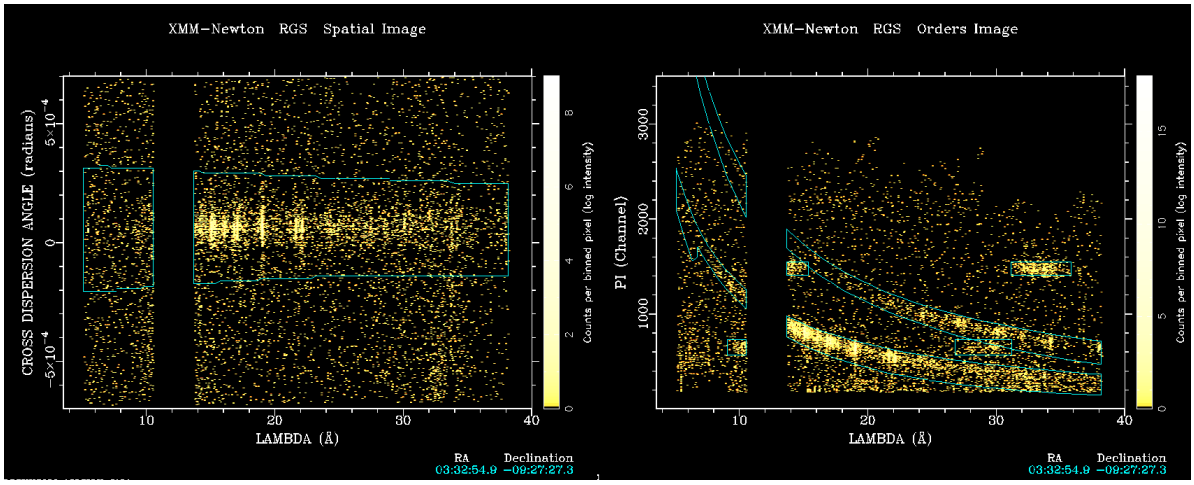

Figure 9.1.1: Plots of the cross dispersion and of the energy channel as function of the wavelength, on the left and on the right respectively. The dispersion masks, retrieved from the source coordinates stored in the header of the RGS event files, are overplotted in blue. ε Eridani is within the dispersion masks, i.e. it was correctly detected by the RGS detectors. Moreover, on the right plot the dispersions masks highlight the two spectral orders of the X-ray emission.

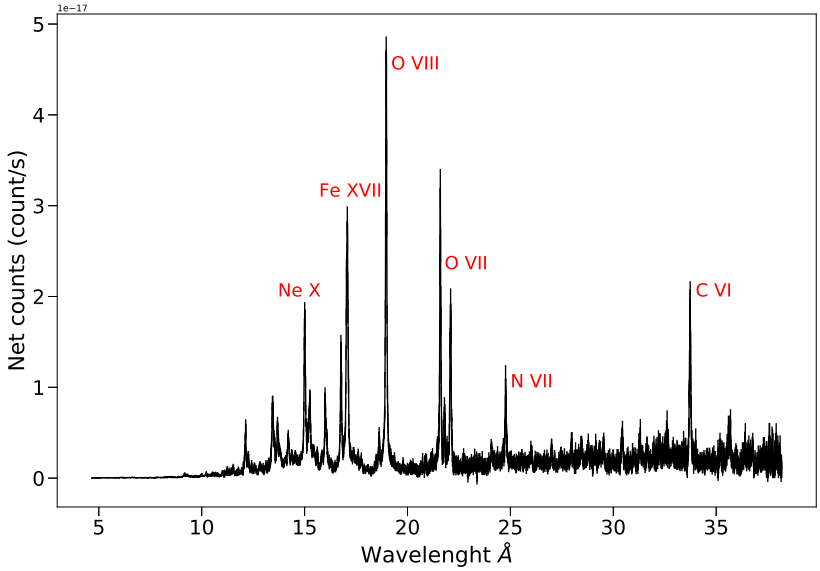

Figure 9.1.2: Merged RGS spectrum of all observations of ε Eri. The most important emission lines, visible by eye, are highlighted in red.

ing as spectral model a 3-T VAPEC model where the metal abundances are not global and are treated individually. Thus, I will have a more precise estimation of the coronal abundances of ε Eridani.

Moreover, an interesting future prospective is to apply the study "The Sun as an X-ray star" to the

RGS observations.

9.2 Conclusions and future prospectives of ι Horologii and Kepler 63

The characterization of the activity cycle of ι Horologii was a side project during my Phd. Its X-ray activity cycle had been identified by Sanz-Forcada et al. (2013) and with the subsequent X-ray observations the short cycle of 1.6 yr was confirmed (Sanz-Forcada et al., 2019). Similar to ε Eridani, this star is a fast rotator and it shows also a small amplitude of its X-ray activity cycle. Thus, it would be interesting here to characterize the coronal cycle of ι Horologii applying the method developed in the context "The Sun as an X-ray star" as done during this PhD for ε Eridani. Extending this analysis to a second, similar star would be important to confirm if young fast rotating stars are actually showing small cycle amplitudes because of a massive presence of magnetic structures on the stellar surfaces. The application of this method on ι Horologii can strengthen the method refined during this PhD project.

Kepler 63 was the last target I analysed in my PhD. Contrary to the other two stars, the Ca II H&K lines of Kepler 63 have not be monitored during a dedicated and continuing campaign. Thus, as explained in section 8.1, the activity cycle of Kepler 63 was characterized through a photometric study, where a short cycle of 1.27 yr was found. In particular, Estrela et al. (2016) obtained the number of starspots and their evolution on the surface of Kepler 63 from the transit lightcurve of the planet of Kepler 63 (section 8.1). My X-ray monitoring campaign started with the goal of detecting a periodic X-ray variability of the same timescale of the variability seen by Estrela et al. (2016) in the photosphere of the star. However, no such variability was found. Kepler 63 is the youngest star I monitored in the context of this PhD project and it shows also the shortest activity cycle. In the *HK project* such short cycles were not detected. Thus, it would be interesting to undertake a monitoring campaign of the chromospheric activity index that can prove or disprove the 1.27-yr cycle detected from the reconstruction of the starspot behaviour of Kepler 63.

Bibliography

Anglada-Escudé, G. and R. P. Butler (June 2012). "The HARPS-TERRA Project. I. Description of the Algorithms, Performance, and New Measurements on a Few Remarkable Stars Observed by HARPS". In: *The Astrophysical Journal Supplement Series* 200.2, 15, p. 15. DOI: 10.1088/0067-0049/200/2/15.

Arnaud, K. A. (1996). "XSPEC: The First Ten Years". In: *Astronomical Data Analysis Software and Systems V*. Ed. by G. H. Jacoby and J. Barnes. Vol. 101. Astronomical Society of the Pacific Conference Series, p. 17.

Ayres, T. R. (Mar. 2014). "The Ups and Downs of α Centauri". In: *Astronomical Journal* 147.3, 59, p. 59. DOI: 10.1088/0004-6256/147/3/59.

Babcock, H. W. (Nov. 1960). "The 34-KILOGAUSS Magnetic Field of HD 215441." In: *Astrophysical Journal* 132, p. 521. DOI: 10.1086/146960.

Baliunas, S. L. et al. (Jan. 1995). "Chromospheric Variations in Main-Sequence Stars. II." In: *Astrophysical Journal* 438, p. 269. DOI: 10.1086/175072.

Baliunas, S. L. et al. (Jan. 1998). "Activity Cycles in Lower Main Sequence and POST Main Sequence Stars: The HK Project". In: *Cool Stars, Stellar Systems, and the Sun*. Ed. by Robert A. Donahue and Jay A. Bookbinder. Vol. 154. Astronomical Society of the Pacific Conference Series, p. 153.

Baraffe, I. et al. (May 2015). "New evolutionary models for pre-main sequence and main sequence low-mass stars down to the hydrogen-burning limit". In: *Astronomy and Astrophysics* 577, A42, A42. DOI: 10.1051/0004-6361/201425481.

Barnes, S. A. (Nov. 2007). "Ages for Illustrative Field Stars Using Gyrochronology: Viability, Limitations, and Errors". In: *Astrophysical Journal* 669.2, pp. 1167–1189. DOI: 10.1086/519295.

Barnes, S. A., F. Spada, and J. Weingrill (Sept. 2016). "Some aspects of cool main sequence star ages derived from stellar rotation (gyrochronology)". In: *Astronomische Nachrichten* 337.8-9, p. 810. DOI: 10.1002/asna.201612377.

Bayo, A. et al. (Dec. 2008). "VOSA: virtual observatory SED analyzer. An application to the Collinder 69 open cluster". In: *Astronomy and Astrophysics* 492.1, pp. 277–287. DOI: 10.1051/0004-6361:200810395.

Berdyugina, S. V. (Dec. 2005). "Starspots: A Key to the Stellar Dynamo". In: *Living Reviews in Solar Physics* 2.1, 8, p. 8. DOI: 10.12942/lrsp-2005-8.

Böhm-Vitense, E. (Mar. 2007). "Chromospheric Activity in G and K Main-Sequence Stars, and What It Tells Us about Stellar Dynamos". In: *Astrophysical Journal* 657.1, pp. 486–493. DOI: 10.1086/510482.

Brandenburg, A., S. Mathur, and T. S. Metcalfe (Aug. 2017). "Evolution of Co-existing Long and Short Period Stellar Activity Cycles". In: *Astrophysical Journal* 845.1, 79, p. 79. DOI: 10.3847/1538-4357/aa7cfa.

Brandenburg, A., S. H. Saar, and C. R. Turpin (May 1998). "Time Evolution of the Magnetic Activity Cycle Period". In: *Astrophysical Journal, Letters* 498.1, pp. L51–L54. DOI: 10.1086/311297.

Buccino, A. P. and P. J. D. Mauas (June 2008). "Mg II h+k emission lines as stellar activity indicators of main sequence F-K stars". In: *Astronomy and Astrophysics* 483.3, pp. 903–910. DOI: 10.1051/0004-6361:20078925.

Cayrel de Strobel, G. (Jan. 1996). "Stars resembling the Sun". In: *Astronomy and Astrophysics Reviews* 7.3, pp. 243–288. DOI: 10.1007/s001590050006.

Charbonneau, Paul (June 2020). "Dynamo models of the solar cycle". In: *Living Reviews in Solar Physics* 17.1, 4, p. 4. DOI: 10.1007/s41116-020-00025-6.

Coffaro, M. et al. (Apr. 2020). "An X-ray activity cycle on the young solar-like star $\in$ Eridani". In: *Astronomy and Astrophysics* 636, A49, A49. DOI: 10.1051/0004-6361/201936479.

Di Folco, E. et al. (Nov. 2004). "VLTI near-IR interferometric observations of Vega-like stars. Radius and age of α PsA, β Leo, β Pic, $\in$ Eri and τ Cet". In: *Astronomy and Astrophysics* 426, pp. 601–617. DOI: 10.1051/0004-6361:20047189.

Donahue, R. A., S. H. Saar, and S. L. Baliunas (July 1996). "A Relationship between Mean Rotation Period in Lower Main-Sequence Stars and Its Observed Range". In: *Astrophysical Journal* 466, p. 384. DOI: 10.1086/177517.

Drake, J. J. et al. (Dec. 2000). "On Stellar Coronae and Solar Active Regions". In: *Astrophysical Journal* 545.2, pp. 1074–1083. DOI: 10.1086/317820.

Epstein, C. R. and M. H. Pinsonneault (Jan. 2014). "How Good a Clock is Rotation? The Stellar Rotation-Mass-Age Relationship for Old Field Stars". In: *Astrophysical Journal* 780.2, 159, p. 159. DOI: 10.1088/0004-637X/780/2/159.

ESA: XMM-Newton SOC (2019). *Users Guide to the XMM-Newton Science Analysis System*. Issue 15.0.

Estrela, R. and A. Valio (Nov. 2016). "Stellar Magnetic Cycles in the Solar-like Stars Kepler-17 and Kepler-63". In: *Astrophysical Journal* 831.1, 57, p. 57. DOI: 10.3847/0004-637X/831/1/57.

Favata, F. et al. (2004). "High-amplitude, long-term X-ray variability in the solar-type star HD 81809: The beginning of an X-ray activity cycle?" In: *A&A* 418.1, pp. L13–L16. DOI: 10.1051/0004-6361:20040105.

Favata, F. et al. (Nov. 2008). "The X-ray cycle in the solar-type star HD 81809. XMM-Newton observations and implications for the coronal structure". In: *Astronomy and Astrophysics* 490.3, pp. 1121–1126. DOI: 10.1051/0004-6361:200809694.

Frasca, A. et al. (Oct. 2016). "Activity indicators and stellar parameters of the Kepler targets. An application of the ROTFIT pipeline to LAMOST-Kepler stellar spectra". In: *Astronomy and Astrophysics* 594, A39, A39. DOI: 10.1051/0004-6361/201628337.

Fuhrmann, K. (Jan. 2004). "Nearby stars of the Galactic disk and halo. III." In: *Astronomische Nachrichten* 325.1, pp. 3–80. DOI: 10.1002/asna.200310173.

Fuhrmann, K. et al. (Feb. 2017). "Multiplicity among Solar-type Stars". In: *Astrophysical Journal* 836.1, 139, p. 139. DOI: 10.3847/1538-4357/836/1/139.

Gondoin, P. (Sept. 2018). "Magnetic activity evolution on Sun-like stars". In: *Astronomy and Astrophysics* 616, A154, A154. DOI: 10.1051/0004-6361/201731541.

Gray, D. F. and S. L. Baliunas (Mar. 1995). "Magnetic Activity Variations of epsilon Eridani". In: *Astrophysical Journal* 441, p. 436. DOI: 10.1086/175368.

Hale, G. E. (Nov. 1908). "On the Probable Existence of a Magnetic Field in Sun-Spots". In: *Astrophysical Journal* 28, p. 315. DOI: 10.1086/141602.

Hall, J. C., G. W. Lockwood, and B. A. Skiff (Mar. 2007). "The Activity and Variability of the Sun and Sun-like Stars. I. Synoptic Ca II H and K Observations". In: *Astronomical Journal* 133.3, pp. 862–881. DOI: 10.1086/510356.

Hatzes, A. P. et al. (Dec. 2000). "Evidence for a Long-Period Planet Orbiting ε Eridani". In: *Astrophysical Journal, Letters* 544, pp. L145–L148. DOI: 10.1086/317319.

Hempelmann, A. et al. (Dec. 2006). "Coronal activity cycles in 61 Cygni". In: *Astronomy and Astrophysics* 460.1, pp. 261–267. DOI: 10.1051/0004-6361:20065459.

Huber, D. et al. (Apr. 2013). "Fundamental Properties of Kepler Planet-candidate Host Stars using Asteroseismology". In: *Astrophysical Journal* 767.2, 127, p. 127. DOI: 10.1088/0004-637X/767/2/127.

Isaacson, H. and D. Fischer (Dec. 2010). "Chromospheric Activity and Jitter Measurements for 2630 Stars on the California Planet Search". In: *Astrophysical Journal* 725.1, pp. 875–885. DOI: 10.1088/0004-637X/725/1/875.

Kaastra, J. S. (1992). "An X-ray Spectral Code for Optically Thin Plasmas". In: *Internal Report, updated version 2.0 (SRON-Leiden)*.

Keenan, P. C. and R. C. McNeil (Oct. 1989). "The Perkins Catalog of Revised MK Types for the Cooler Stars". In: *The Astrophysical Journal Supplement Series* 71, p. 245. DOI: 10.1086/191373.

Killick, R. and I. Eckley (2014). "changepoint: An R Package for Changepoint Analysis". In: *Journal of Statistical Software, Articles* 58.3, pp. 1–19. ISSN: 1548-7660. DOI: 10.18637/jss.v058.i03.

Killick, R., P. Fearnhead, and I. A. Eckley (Oct. 2012). "Optimal Detection of Changepoints With a Linear Computational Cost". In: *Journal of the American Statistical Association* 107.500, pp. 1590–1598. ISSN: 1537-274X. DOI: 10.1080/01621459.2012.737745.

Kürster, M. et al. (Jan. 2000). "An extrasolar giant planet in an Earth-like orbit. Precise radial velocities of the young star iota Horologii = HR 810". In: *Astronomy and Astrophysics* 353, pp. L33–L36.

Lebreton, Y., J. Fernandes, and T. Lejeune (Aug. 2001). "The helium content and age of the Hyades:. Constraints from five binary systems and Hipparcos parallaxes". In: *Astronomy and Astrophysics* 374, pp. 540–553. DOI: 10.1051/0004-6361:20010757.

Lomb, N. R. (Feb. 1976). "Least-Squares Frequency Analysis of Unequally Spaced Data". In: *Astrophysics and Space Science* 39.2, pp. 447–462. DOI: 10.1007/BF00648343.

Mauas, P. J. D. et al. (July 2012). "12 years of stellar activity observations in Argentina". In: *Comparative Magnetic Minima: Characterizing Quiet Times in the Sun and Stars*. Ed. by Cristina H. Mandrini and David F. Webb. Vol. 286. IAU Symposium, pp. 317–323. DOI: 10.1017/S1743921312005029.

Metcalfe, T. S. et al. (Nov. 2010). "Discovery of a 1.6 Year Magnetic Activity Cycle in the Exoplanet Host Star Horologii". In: *Astrophysical Journal, Letters* 723.2, pp. L213–L217. DOI: 10.1088/2041-8205/723/2/L213.

Metcalfe, T. S. et al. (Feb. 2013). "Magnetic Activity Cycles in the Exoplanet Host Star epsilon Eridani". In: *Astrophysical Journal, Letters* 763.2, L26, p. L26. DOI: 10.1088/2041-8205/763/2/L26.

Mewe, R., J. S. Kaastra, and D. A. Liedhal (1995). In: *Legacy* 6, p. 16.

Mewe, R., J. R. Lemen, and G. H. J. van den Oord (Sept. 1986). "Calculated X-radiation from optically thin plasmas. VI - Improved calculations for continuum emission and approximation formulae for nonrelativistic average Gaunt factors". In: *Astronomy and Astrophysics, Supplement* 65, pp. 511–536.

Mittag, M. et al. (June 2016). "Chromospheric activity and evolutionary age of the Sun and four solar twins". In: *Astronomy and Astrophysics* 591, A89, A89. DOI: 10.1051/0004-6361/201527542.

Morris, B. M. et al. (Sept. 2019). "Stellar Properties of Active G and K Stars: Exploring the Connection between Starspots and Chromospheric Activity". In: *Astronomical Journal* 158.3, 101, p. 101. DOI: 10.3847/1538-3881/ab2e04.

Narain, U. and P. Ulmschneider (Feb. 1996). "Chromospheric and Coronal Heating Mechanisms II". In: *Space Science Reviews* 75.3-4, pp. 453–509. DOI: 10.1007/BF00833341.

Ness, J. -U. and C. Jordan (Apr. 2008). "The corona and upper transition region of epsilon Eridani". In: *Monthly Notices of the RAS* 385.4, pp. 1691–1708. DOI: 10.1111/j.1365-2966.2007.12757.x.

Netto, Y. and A. Valio (Mar. 2020). "Stellar magnetic activity and the butterfly diagram of Kepler-63". In: *Astronomy and Astrophysics* 635, A78, A78. DOI: 10.1051/0004-6361/201936219.

Noyes, R. W. et al. (Apr. 1984). "Rotation, convection, and magnetic activity in lower main-sequence stars." In: *Astrophysical Journal* 279, pp. 763–777. DOI: 10.1086/161945.

Orlando, S., G. Peres, and F. Reale (Jan. 2000). "The Sun as an X-Ray Star. I. Deriving the Emission Measure Distribution versus Temperature of the Whole Solar Corona from theYohkoh/Soft X-Ray Telescope Data". In: *Astrophysical Journal* 528, pp. 524–536. DOI: 10.1086/308137.

— (Oct. 2001). "The Sun as an X-Ray Star. IV. The Contribution of Different Regions of the Corona to Its X-Ray Spectrum". In: *Astrophysical Journal* 560, pp. 499–513. DOI: 10.1086/322333.

— (Sept. 2004). "The Sun as an X-ray star: Active region evolution, rotational modulation, and implications for stellar X-ray variability". In: *Astronomy and Astrophysics* 424, pp. 677–689. DOI: 10.1051/0004-6361:20040207.

Orlando, S. et al. (Sept. 2017). "Fifteen years in the high-energy life of the solar-type star HD 81809. XMM-Newton observations of a stellar activity cycle". In: *Astronomy and Astrophysics* 605, A19, A19. DOI: 10.1051/0004-6361/201731301.

Peres, G. et al. (Jan. 2000). "The Sun as an X-Ray Star. II. Using theYohkoh/Soft X-Ray Telescope-derived Solar Emission Measure versus Temperature to Interpret Stellar X-Ray Observations". In: *Astrophysical Journal* 528, pp. 537–551. DOI: 10.1086/308136.

Pourbaix, D. (Aug. 2000). "Resolved double-lined spectroscopic binaries: A neglected source of hypothesis-free parallaxes and stellar masses". In: *Astronomy and Astrophysics, Supplement* 145, pp. 215–222. DOI: 10.1051/aas:2000237.

Preibisch, T. and E. D. Feigelson (Oct. 2005). "The Evolution of X-Ray Emission in Young Stars". In: *The Astrophysical Journal Supplement Series* 160.2, pp. 390–400. DOI: 10.1086/432094.

Pye, J. P. et al. (Sept. 2015). "A survey of stellar X-ray flares from the XMM-Newton serendipitous source catalogue: HIPPARCOS-Tycho cool stars". In: *Astronomy and Astrophysics* 581, A28, A28. DOI: 10.1051/0004-6361/201526217.

Quillen, A. C. and S. Thorndike (Oct. 2002). "Structure in the ϵ Eridani Dusty Disk Caused by Mean Motion Resonances with a 0.3 Eccentricity Planet at Periastron". In: *Astrophysical Journal, Letters* 578, pp. L149–L152. DOI: 10.1086/344708.

Raetz, St., B. Stelzer, and A. Scholz (May 2020). "The rotation-activity relation of M dwarfs: From K2 to TESS and PLATO". In: *Astronomische Nachrichten*, arXiv:2005.08688.

Reale, F., G. Peres, and S. Orlando (Aug. 2001). "The Sun as an X-Ray Star. III. Flares". In: *Astrophysical Journal* 557, pp. 906–920. DOI: 10.1086/321598.

Ribas, I. et al. (Mar. 2005). "Evolution of the Solar Activity over Time and Effects on Planetary Atmospheres. I. High-Energy Irradiances (1-1700 Å)". In: *Astrophysical Journal* 622.1, pp. 680–694. DOI: 10.1086/427977.

Robrade, J., J. H. M. M. Schmitt, and F. Favata (July 2012). "Coronal activity cycles in nearby G and K stars. XMM-Newton monitoring of 61 Cygni and α Centauri". In: *Astronomy and Astrophysics* 543, A84, A84. DOI: 10.1051/0004-6361/201219046.

Saar, S. H. and A. Brandenburg (Oct. 1999). "Time Evolution of the Magnetic Activity Cycle Period. II. Results for an Expanded Stellar Sample". In: *Astrophysical Journal* 524.1, pp. 295–310. DOI: 10.1086/307794.

Salabert, D. et al. (Nov. 2016). "Photospheric and chromospheric magnetic activity of seismic solar analogs. Observational inputs on the solar-stellar connection from Kepler and Hermes". In: *Astronomy and Astrophysics* 596, A31, A31. DOI: 10.1051/0004-6361/201628583.

Sanchis-Ojeda, R. et al. (Sept. 2013). "Kepler-63b: A Giant Planet in a Polar Orbit around a Young Sun-like Star". In: *Astrophysical Journal* 775.1, 54, p. 54. DOI: 10.1088/0004-637X/775/1/54.

Sanz-Forcada, J., N. S. Brickhouse, and A. K. Dupree (Mar. 2003). "The Structure of Stellar Coronae in Active Binary Systems". In: *The Astrophysical Journal Supplement Series* 145.1, pp. 147–179. DOI: 10.1086/345815.

Sanz-Forcada, J., F. Favata, and G. Micela (Mar. 2004). "Coronal versus photospheric abundances of stars with different activity levels". In: *Astronomy and Astrophysics* 416, pp. 281–290. DOI: 10.1051/0004-6361:20034466.

Sanz-Forcada, J., B. Stelzer, and T. S. Metcalfe (May 2013). "Horologi, the first coronal activity cycle in a young solar-like star". In: *Astronomy and Astrophysics* 553, L6, p. L6. DOI: 10.1051/0004-6361/201321388.

Sanz-Forcada, J. et al. (Aug. 2011). "Estimation of the XUV radiation onto close planets and their evaporation". In: *Astronomy and Astrophysics* 532, A6, A6. DOI: 10.1051/0004-6361/201116594.

Sanz-Forcada, J. et al. (Nov. 2019). "Multi-wavelength variability of the young solar analog Horologii. X-ray cycle, star spots, flares, and UV emission". In: *Astronomy and Astrophysics* 631, A45, A45. DOI: 10.1051/0004-6361/201935703.

Scargle, J. D. (Dec. 1982). "Studies in astronomical time series analysis. II. Statistical aspects of spectral analysis of unevenly spaced data." In: *Astrophysical Journal* 263, pp. 835–853. DOI: 10.1086/160554.

Schröder, C., A. Reiners, and J. H. M. M. Schmitt (Jan. 2009). "Ca II HK emission in rapidly rotating stars. Evidence for an onset of the solar-type dynamo". In: *Astronomy and Astrophysics* 493.3, pp. 1099–1107. DOI: 10.1051/0004-6361:200810377.

Shkolnik, E.L. (Mar. 2013). "An Ultraviolet Investigation of Activity on Exoplanet Host Stars". In: *Astrophysical Journal* 766.1, 9, p. 9. DOI: 10.1088/0004-637X/766/1/9.

Silva, A. V. R. (Mar. 2003). "Method for Spot Detection on Solar-like Stars". In: *Astrophysical Journal, Letters* 585.2, pp. L147–L150. DOI: 10.1086/374324.

Skumanich, A. (Feb. 1972). "Time Scales for CA II Emission Decay, Rotational Braking, and Lithium Depletion". In: *Astrophysical Journal* 171, p. 565. DOI: 10.1086/151310.

Song, I. et al. (Apr. 2000). "Ages of Late Spectral Type Vega-like Stars". In: *Astrophysical Journal, Letters* 533.1, pp. L41–L44. DOI: 10.1086/312597.

Thomas, J. H. and N. O. Weiss (2008). *Sunspots and Starspots*. Cambridge Astrophysics. Cambridge University Press. DOI: 10.1017/CBO9780511536342.

Usoskin, I. G. et al. (Sept. 2015). "The Maunder minimum (1645-1715) was indeed a grand minimum: A reassessment of multiple datasets". In: *Astronomy and Astrophysics* 581, A95, A95. DOI: 10.1051/0004-6361/201526652.

van Leeuwen, F. (Nov. 2007). "Validation of the new Hipparcos reduction". In: *Astronomy and Astrophysics* 474.2, pp. 653–664. DOI: 10.1051/0004-6361:20078357.

Vauclair, S. et al. (May 2008). "The exoplanet-host star Horologii: an evaporated member of the primordial Hyades cluster". In: *Astronomy and Astrophysics* 482.2, pp. L5–L8. DOI: 10.1051/0004-6361:20079342.

Vernazza, J. E., E. H. Avrett, and R. Loeser (Apr. 1981). "Structure of the solar chromosphere. III. Models of the EUV brightness components of the quiet sun." In: *The Astrophysical Journal Supplement Series* 45, pp. 635–725. DOI: 10.1086/190731.

Wargelin, B. J. et al. (Jan. 2017). "Optical, UV, and X-ray evidence for a 7-yr stellar cycle in Proxima Centauri". In: *Monthly Notices of the RAS* 464.3, pp. 3281–3296. DOI: 10.1093/mnras/stw2570.

XMM-Newton SOC (2019). *XMM-Newton Users Handbook*. Issue 2.17.

Zechmeister, M. and M. Kürster (Mar. 2009). "The generalised Lomb-Scargle periodogram. A new formalism for the floating-mean and Keplerian periodograms". In: *Astronomy and Astrophysics* 496.2, pp. 577–584. DOI: 10.1051/0004-6361:200811296.

A

Analysis techniques

A.1 The General Lomb-Scargle periodogram

The General Lomb-Scargle periodogram (Lomb, 1976; Scargle, 1982) is a widely used tool in astronomy to estimate and characterize periodicity in unevenly sampled time-series. Across my PhD project, we saw several applications of this analysis, e.g. to look for the cycle period of ι Horologii (chapter 5) and ε Eridani (chapter 6).

In this section I review and see the main properties of the Lomb-Scargle periodogram, starting from the mathematical interpretations in subsection A.1.1. In subsection A.1.2 I describe the software used during the PhD project.

A.1.1 Mathematical interpretations of the general Lomb-Scargle Periodogram

The main mathematical method to compute the periodogram of a data set is the estimation of the Fourier power spectrum of the signal we want to characterize. Given a continuous signal $g(t)$, the Fourier transform is:

$$\widehat{g}(f) \equiv \int_{-\infty}^{\infty} g(t) e^{-2\pi i f t} dt \equiv \mathcal{F}\{g\} \tag{A.1}$$

where $i \equiv \sqrt{-1}$ is the imaginary unity. Thus, the Fourier transform represents the continuous signal in the domain of the frequency, f.

This expression is valid for a signal that is observed during an infinite time period. However, in reality we deal with finite signals, i.e. with real observations that take place during a finite amount of time. Thus, Equation A.1 needs to be rewritten in its discrete form.

A real observed signal $g_{obs}(t)$ can be defined as the product between the true underlying continuous signal $g(t)$ with the so-called *window function* $W(t)$, describing the real observation. The Fourier

transform of $g_{obs}(t)$ is then the convolution of the signal transform $\mathcal{F}\{g\}$ and the window transform $\mathcal{F}\{W\}$. The window function that describes a real signal is the Dirac comb, $III_{\Delta t}(t) \equiv \sum_{n=-\infty}^{\infty} \delta(n\Delta t)$, i.e an infinite sequence of Dirac delta functions placed at even time intervals Δt (n is the infinite time range). This kind of window function is quite useful because its Fourier transform is always a Dirac comb and allows to pass to the discrete form of the Fourier transform with few calculations. Thus we can rewrite Equation A.1 in its discrete form for a real observed signal as:

$$\widehat{g}_{obs}(f) = \sum_{n=0}^{N} g(n\Delta t) e^{-2\pi i f t_n} \tag{A.2}$$

where the sum is limited up to the N times the signal is observed.

The power spectrum of a Fourier transform is defined as $\mathcal{P}_g \equiv |\mathcal{F}\{g\}|^2$ and it is a positive real-valued function of the frequency f that quantifies the contribution of each frequency f to the total signal. The power spectrum of Equation A.2 represents indeed the periodogram computed in 1898 by Schuster:

$$P_S(f) = \frac{1}{N} \left| \sum_{n=1}^{N} g_n e^{-2\pi i f t_n} \right|^2 \tag{A.3}$$

However, it is important to keep in mind that the periodogram in Equation A.3 and the general definition of power spectrum are conceptually two different things, as noted by Scargle (1982): *the periodogram (the statistics to compute from the data) is an estimator of the power spectrum (the underlying continuous function of interest).*

Equation A.3 was rewritten by Lomb (1976) and Scargle (1982) in a different way, and its new form is called the General Lomb-Scargle Periodogram:

$$\begin{aligned} P_S(f) &= \frac{1}{N} \left| \sum_{n=1}^{N} g_n e^{-2\pi i f t_n} \right|^2 = \\ &= \frac{1}{N} \left[\left(\sum_n g_n cos(2\pi f t_n) \right)^2 + \left(\sum_n g_n sin(2\pi f t_n) \right)^2 \right] \\ &= \frac{A^2}{2} \left(\sum_n g_n cos\left(2\left[t_n - \tau\right]\right) \right)^2 + \frac{B^2}{2} \left(\sum_n g_n sin\left(2\left[t_n - \tau\right]\right) \right)^2 \end{aligned} \tag{A.4}$$

The coefficients A, B and τ are arbitrary functions of the frequency f and they can be chosen univocally such that the periodogram represents equally spaced observations (even if they are not), the periodogram's distribution is analytically computable and the periodogram is insensitive to global time shifts in the data.

The interpretation of the Lomb-Scargle periodogram can be extended to different mathematical methods, such as the *least-squares* method. The method consists in fitting a model to the observed signal at each candidate frequency and selecting the frequency that maximizes the likelihood. Math-

ematically speaking, a sinusoidal model is proposed:

$$y(t;f) = y_0(f) + A_f \sin(2\pi f(t - \varphi_f)) \tag{A.5}$$

$y_0(f)$ is an offset term for which, if it is not included, the data would be pre-centred around the mean value of the unknown signal. A_f is the amplitude, φ_f is the phase, and both are functions of the frequency f. These terms are the parameters to fit to the data and their best-fitting values are the ones that minimize the χ^2 statistics at each frequency:

$$\chi^2(f) = \sum_n (y_n - y(t_n;f))^2 \tag{A.6}$$

By calling the best model $\widehat{y}(t;f)$, Scargle (1982) redefined Equation A.4 as:

$$P_S(f) = \frac{1}{2}\left[\widehat{\chi}_0^2 - \widehat{\chi}^2(f)\right] \tag{A.7}$$

where $\widehat{\chi}_0^2$ is a non-varying reference model.

A.1.2 The GLS software

The software GLS (Zechmeister et al., 2009) that I used during the PhD project is based on the least-squares periodogram interpretation and written in the FORTRAN language. An output plot provided by the software can be seen in Figure 6.1.4.

The software calculates the normalized periodogram that from Equation A.7 is[1]

$$P_{norm}(f) = 1 - \frac{\widehat{\chi}^2(f)}{\widehat{\chi}_0^2} \tag{A.8}$$

Thus, the normalized periodogram is unitless and is always between 0 and 1. Moreover, GLS provides the best-fitting values of the functions A_f, φ_f, $y_0(f)$ and the corresponding best frequency f, i.e. the most significant peak in the periodogram. From these values it is then possible to generate the best fitting sine model to be overplotted onto the observed data (see as an example Figure 6.1.5).

In the output plot, other peaks can be present. Thus, from a practical point of view, we need to be sure that these other peaks in the power spectrum provided by the software are not also significant and then representing a second periodicity in the data set. To solve this issue, two more important outputs are provided by software: the *False Alarm Probability* (FAP) and the residuals of sinusoidal fitting.

The FAP measures the significance of the peak by calculating the probability that a data set with no signal would lead to a peak of a similar height. Or, to put in other words, the FAP answers to the question: "*What is the probability that this data set is not periodic given these observations?*". Thus, the smaller the FAP is the more significant is the peak.

[1] If the sinusoidal model perfectly fits the data at f_0, then $\widehat{\chi}^2(f_0) = 0$ and the maximum value of the periodogram is thus $\widehat{\chi}_0^2/2$. This is the value to use to normalize the periodogram in Equation A.7.

The residuals can also be used to assess the presence of secondary peaks. By running GLS on the residuals of the data set, then the periodogram will show no significant peaks if there are no aliases.

Thus, when inspecting a periodogram, for GLS (or for other software) it is more important to define the significance of the peak, rather than the uncertainty in locating the period of the peak. However, as we are used to associate errors to measured quantities, especially in those cases where two or more measures are compared, I needed an alternative method to find the errors of the cycle periods. In this sense, one way to estimate the uncertainty was to simulate N times the data set, so that each point of the simulated data set is randomly drawn from a normal distribution within the observed standard deviation around the measured data point; then, GLS can be run on each simulated data set and the corresponding significant peaks will be Gaussian distributed; the standard deviation of that distribution will be the uncertainty of the period. For the chromospheric cycle period of ε Eridani and the coronal cycle period of ι Horologii the estimation of the errors following this approach is explained in section 5.2 and section 6.1 where I also show the plots derived from simulating the data sets.

A.2 The *changepoint* analysis

In many branches of science, it is of particular interest to identify the location of multiple change points within time series.

In simple terms, the requirement is to determine a point at which the statistical properties of a sequence of observations change. In mathematical terms, this means that, given a sequence of data, $y_{1:n} = (y_1, \ldots, y_n)$, a single change point occurs within the data set when a time $\tau \in \{1, \ldots, n-1\}$ exists such that the statistical properties of $\{y_1, \ldots, y_\tau\}$ and $\{y_{\tau+1} \ldots y_n\}$ are different. Extending this notion to multiple changes translates to have m change points at their time positions $\tau_{1:m} = (\tau_1, \ldots, \tau_m)$, where each position is an integer between 1 and $n-1$ inclusive. Thus, the first and the last position of the change point are: $\tau_0 = 0$ and $\tau_{m+1} = n$. By assuming that the change points are ordered so that $\tau_i < \tau_j$ if, and only if, $i < j$, we will have as consequence that the m change points split the data into $m+1$ segments, where the ith segment contains the data $y_{(\tau_{i-1}+1)+1}$.

Several algorithms that answer to this need are available and they date back to the 1970s. They are all implemented in the most recent analysis software.

For the analysis of the lightcurves of ε Eridani (section 6.4), I made used of the program R, a software environment for statistical computing and graphics, and its package `changepoint` (Killick et al., 2014), to look for short-term variability in the count rates of each *XMM-Newton* observation of the star. In the package `changepoint` several algorithms to estimate multiple change points are available and I adopted the PELT algorithm (Pruned Exact Linear Time; Killick et al., 2012). This algorithm works iteratively: first one change point is estimated and the time series is split into two subsets; the algorithm then looks for other change points in the two new subsets separately; if a new change point is found, another subset will be generated and the process will start again. The algorithm stops when there are no new change points in the segmented data set. Moreover, I requested that the change point is that point in time where the subsets result statistically different in mean and variance simultaneously.

In Appendix B, the lightcurves divided into the segments where a change point occurs are shown.

A.3 Correlation study and the Pearson coefficient

When characterizing two independent data sets, one might want to determine if the variables of each set are somehow correlated. Establishing a correlation by eye is not possible and trustful because for example the variables could appear in the plot scattered and there is no clue of their uncertainties, and consequentially a clear correlation can not be visualized.

To solve this issue, in statistics a correlation analysis can be performed calculating the Pearson coefficient r. It quantifies the linear dependence, if any, between two variables and is given by the following equation:

$$r = \frac{\sum_n (x_n - m_{x_n})(y_n - m_{y_n}}{\sqrt{\sum_n (x_n - m_{x_n})^2 \sum_n (y_n - m_{y_n})^2}} \tag{A.9}$$

where x_n and y_n are the variables with vectors of length n to correlate and m_{x_n} and m_{y_n} are the mean values of the corresponding variable. The Pearson's coefficient can be equal to zero, lower or greater than zero. The first case ($r = 0$) occurs when the two variables are not correlated at all. The second case ($r < 0$ or $r > 0$) occurs when there is a linear correlation, negative or positive respectively.

As for any statistical study, it is also here important to check if the found correlation is statistically correct. For this reason, the so-called *p-value* is used , calculated as follows

$$p = 2\left(1 - \texttt{tcdf}\left(\texttt{t}, \texttt{N} - 2\right)\right), \tag{A.10}$$

where $t = |r\sqrt{\frac{N-1}{1-r^2}}|$, N is the number of freedoms and `tcdf` is the Student's cumulative distribution function. In simple words, the p-value defines the probability that, under certain hypothesis on the data sets, the value r can be different from the observed one. In the case of correlation studies, the hypothesis on the data sets, called *null-hypothesis*, is *"We hypothesise that the two sets of variables are not correlated, i.e. $r = 0$"*. The null hypothesis is rejected when the p-value results smaller than a significance level a that is arbitrarily set, by convention, to e.g. 5%, 1%, 0.5%, or 0.1%. Since these latter values of the significance level are small, the smaller the p-value is, the higher is the statistical significance of r.

B

X-ray lightcurves of ε Eridani

Here, the lightcurves of the observations of ε Eridani are shown. The extraction procedure and the analysis of the lightcurves are explained in section 6.3 and section 6.4 respectively.

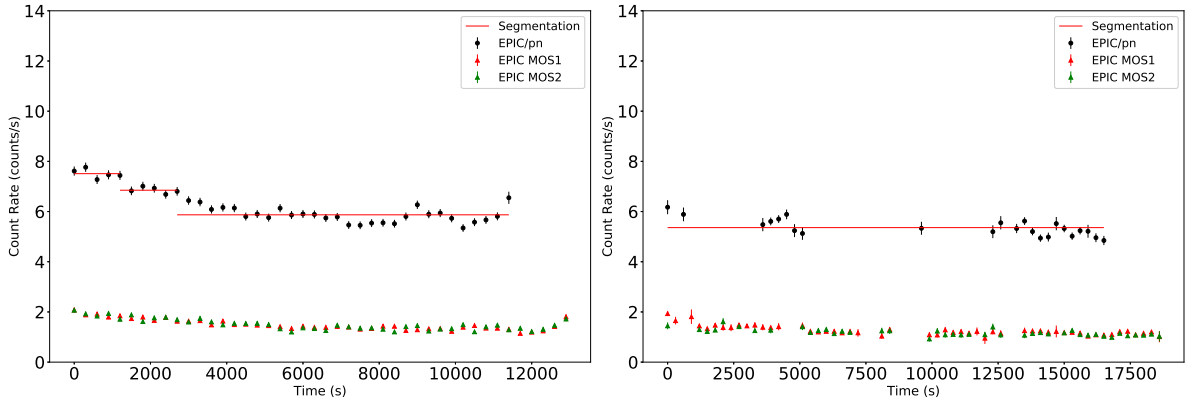

(a) January 2003 **(b)** February 2015

Figure B 3: EPIC lightcurves of ε Eri. The EPIC/pn lightcurves are plotted with the black dots, while the EPIC MOS lightcurves are plotted in red (MOS 1) and in green (MOS 2). The solid red lines highlight each time interval where a change in the count rates is found through the `changepoint` procedure (see section 6.4 and section A.2).

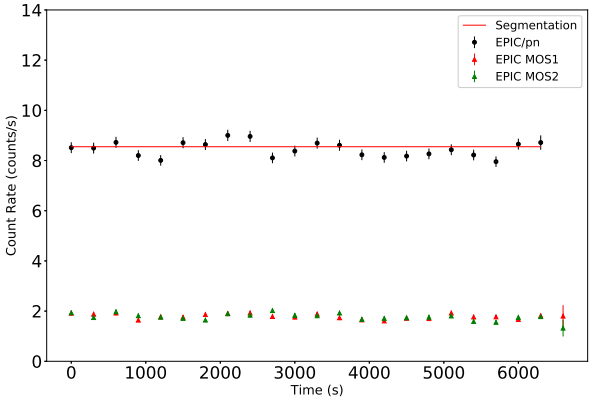

(c) July 2015

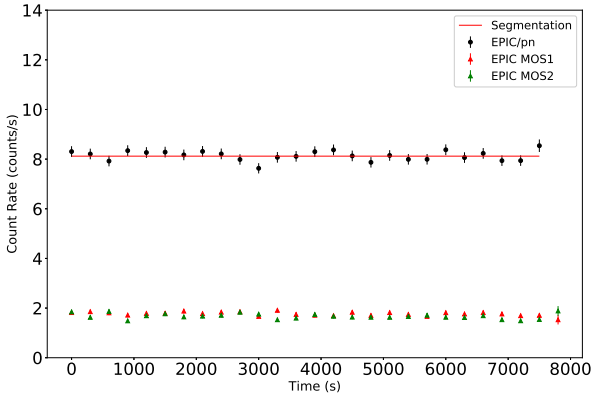

(d) January 2016

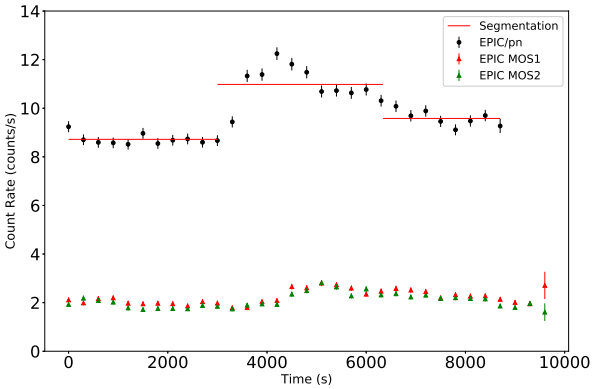

(e) July 2016

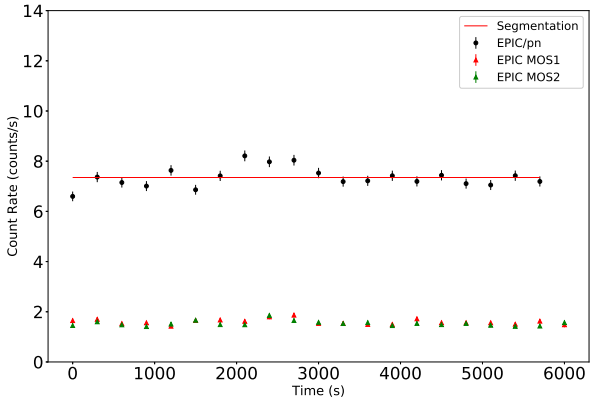

(f) January 2017

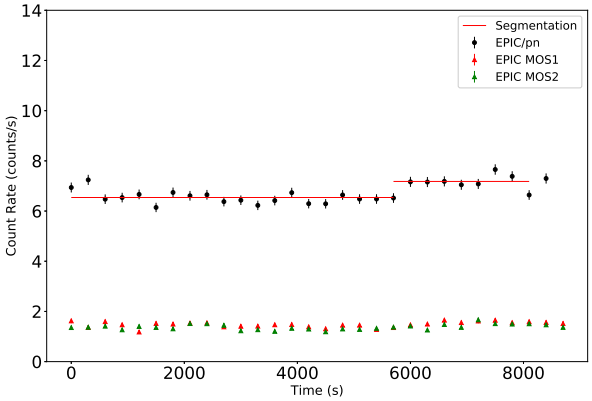

(g) August 2017

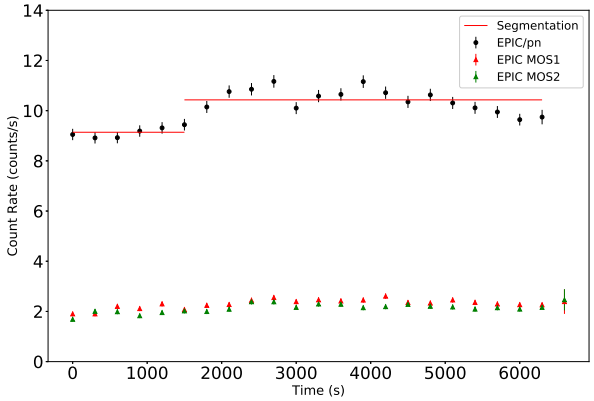

(h) January 2018

Figure B 3: (continued)

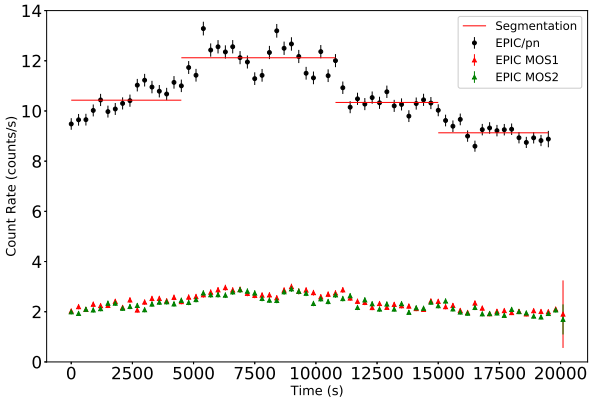

(i) August 2018

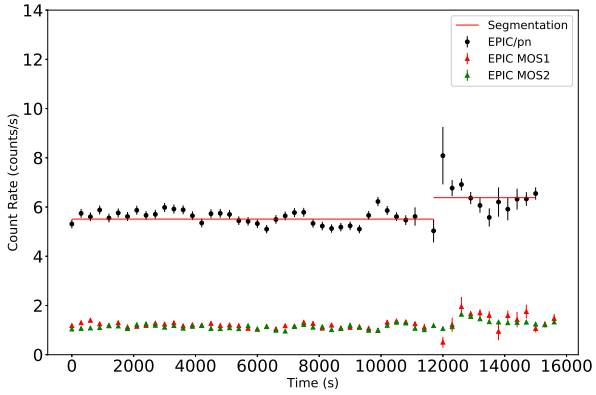

(j) January 2019

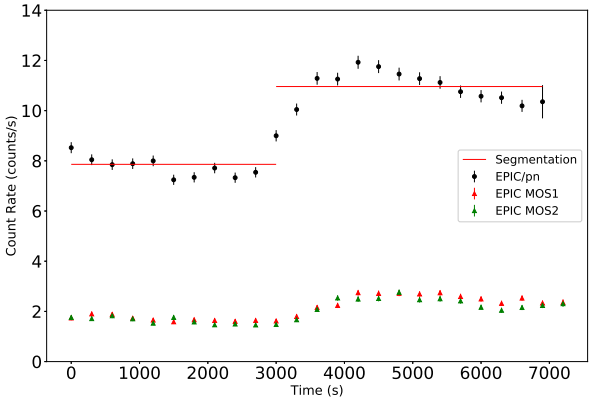

(k) August 2019

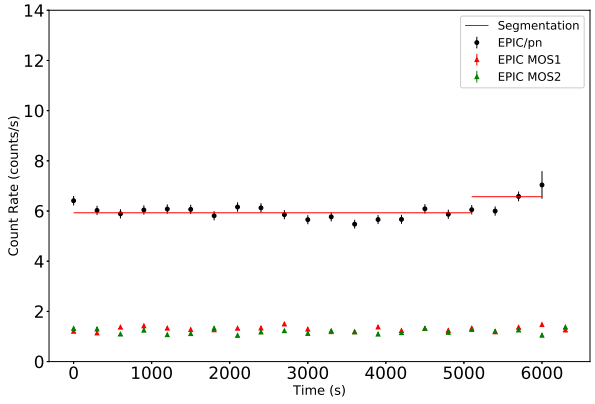

(l) January 2020

Figure B 3: (continued)

C

EPIC/pn spectra of ε Eridani

Here, the EPIC/pn spectra of the observations of ε Eridani and the corresponding best-fitting parameters are shown. In particular, Figure C 1 shows the spectra fitted with a 3-T APEC model when the metal abundances are left free to vary during the fitting (left panels) and when they are kept frozen at $0.3 Z_{\odot}$ (right panels). The corresponding best-fitting parameters are reported in Table C 1 and Table C 2 respectively.

In Figure C 2 the spectra of those observations with a flare-like event are shown, where the left column shows the spectra of a quiescent state of the corresponding observations whereas the spectra of the flare-like events are shown in the right column. The spectral model used in the fitting procedure is a 3-T APEC model with the abundances kept frozen and the best-fitting parameters of this procedure are reported in Table C 3.

In each spectrum the spectral models adopted in the analysis are overplotted in red and the bottom panels in each plot are the reduced χ^2 residuals of the fitting. The fitting procedures are described in subsection 6.5.2.

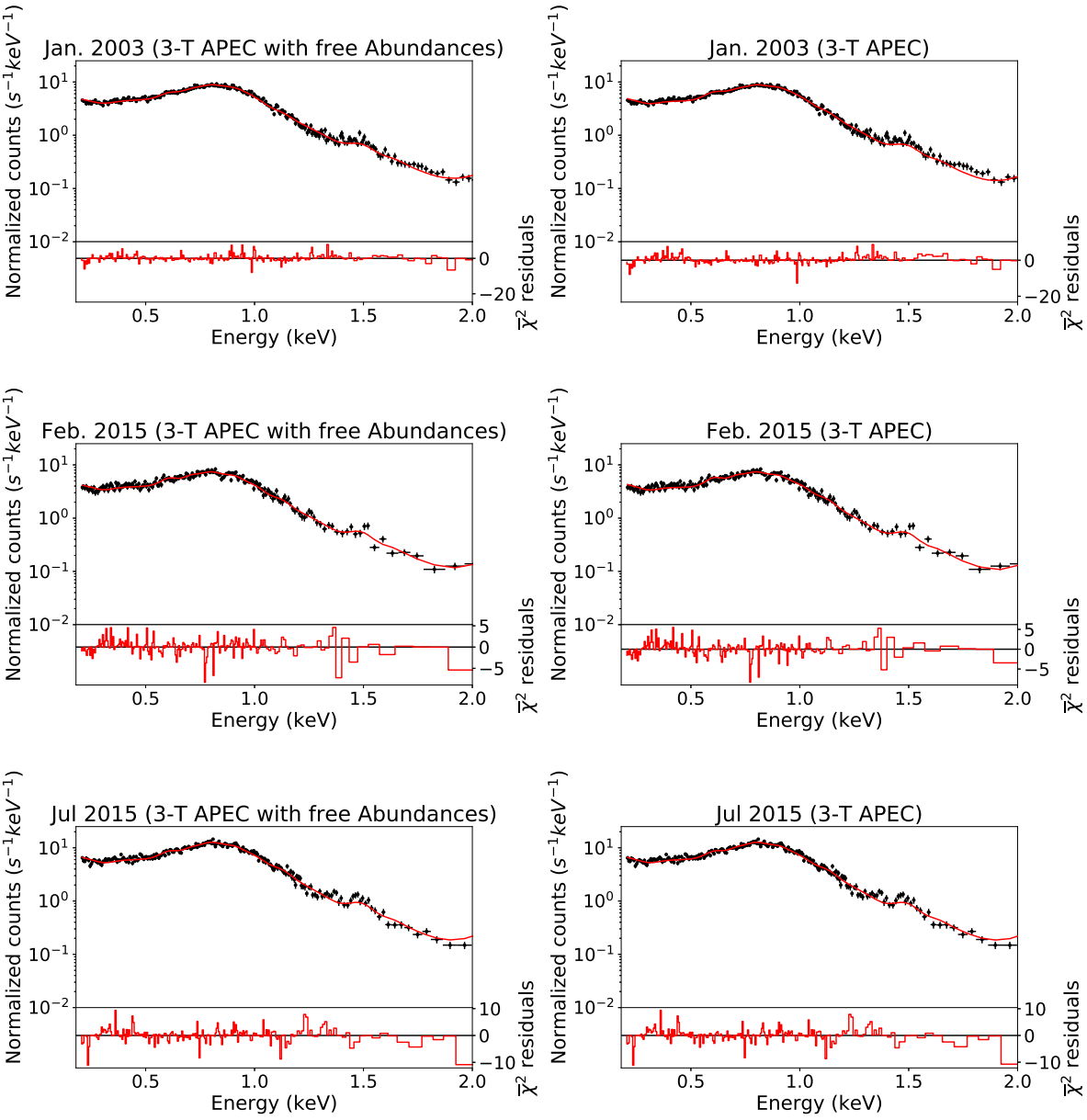

Figure C 1: Spectra of each observation of ε Eridani fitted with a 3-T APEC model (red solid line). The spectra on the right are fitted keeping the metal abundances frozen during the fitting procedures, whereas for the spectra on the left the abundances are free to vary in the fitting. The bottom panels show the reduced χ^2 residuals.

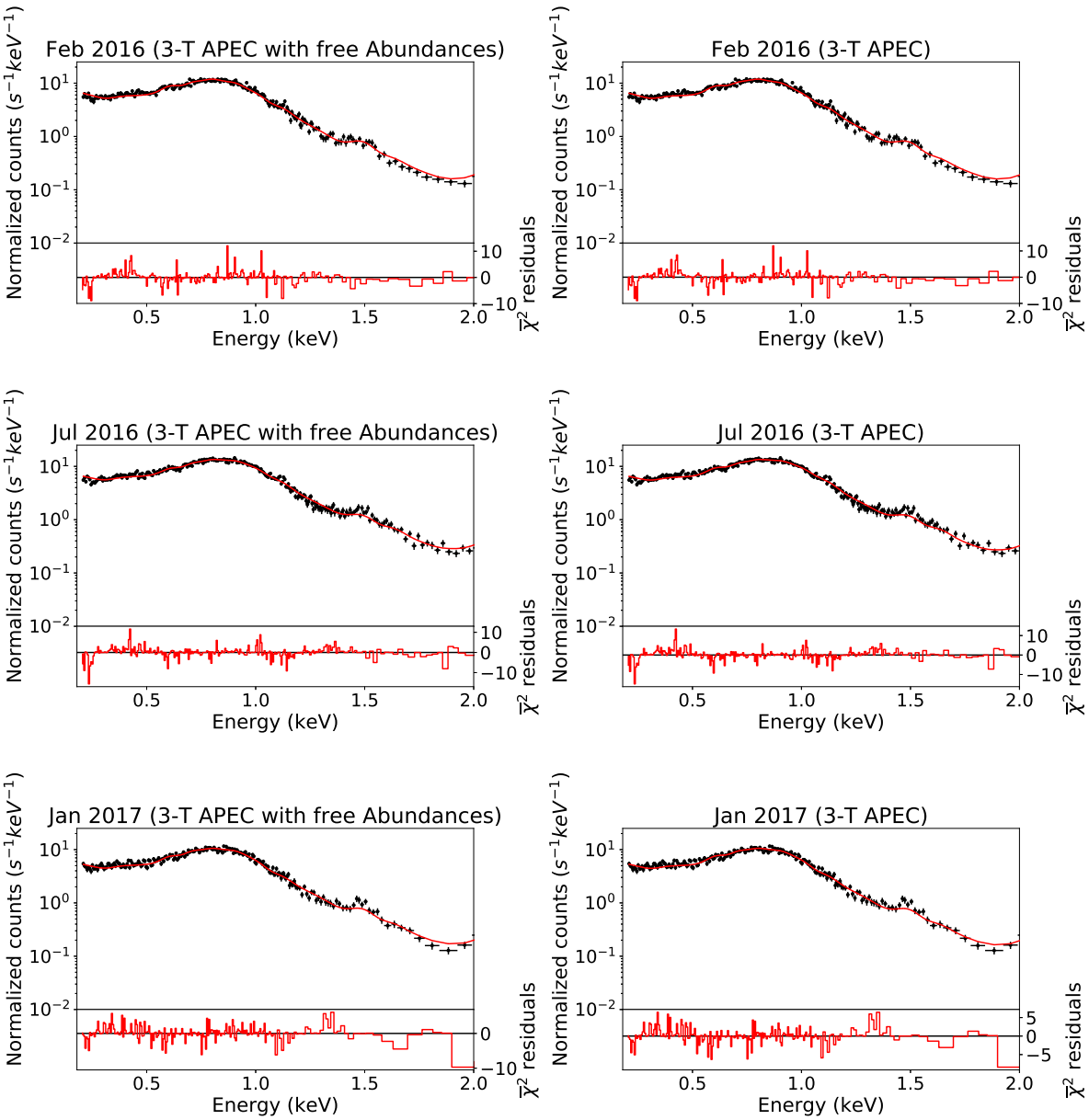

Figure C 1: (continued)

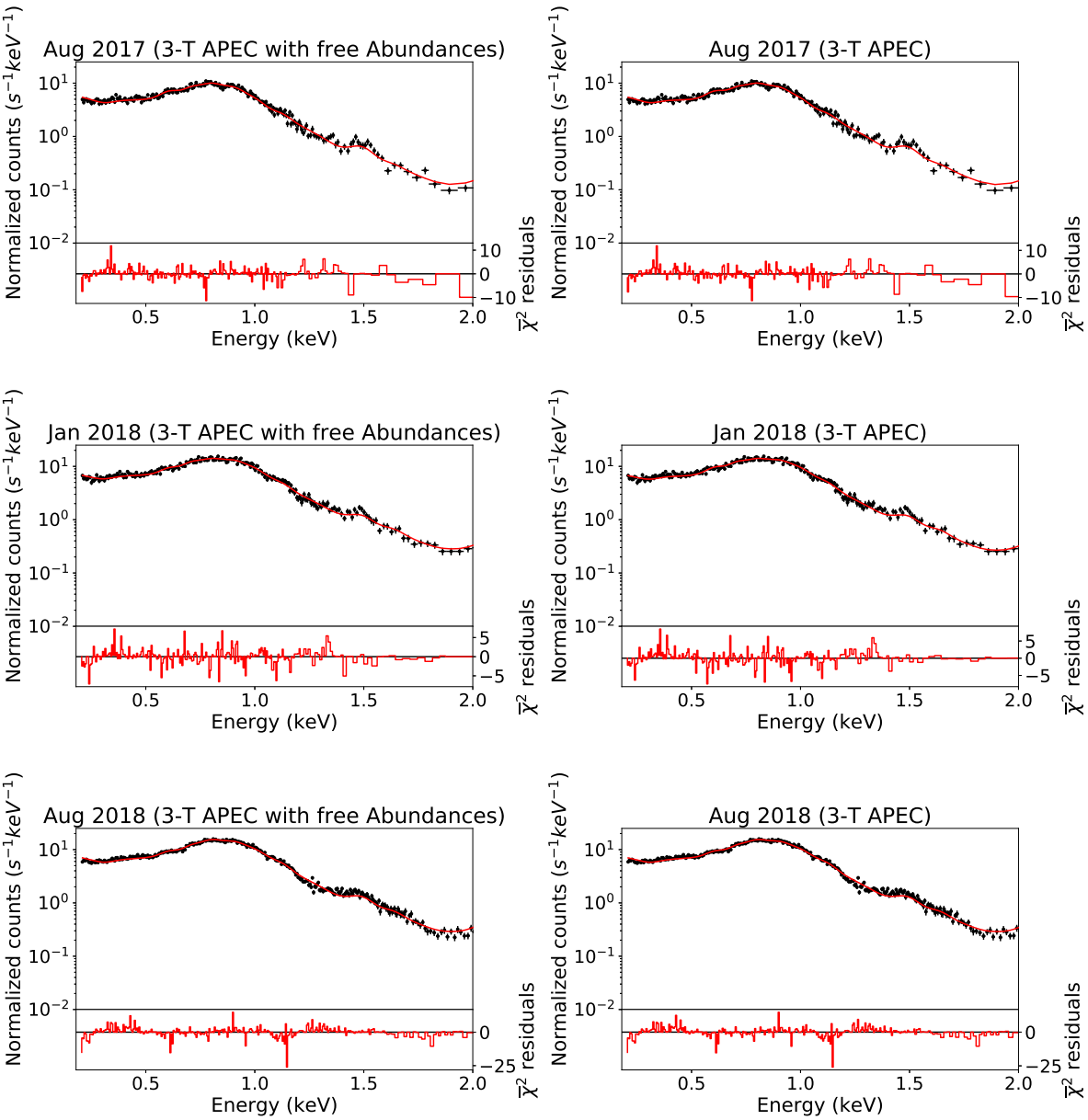

Figure C 1: (continued)

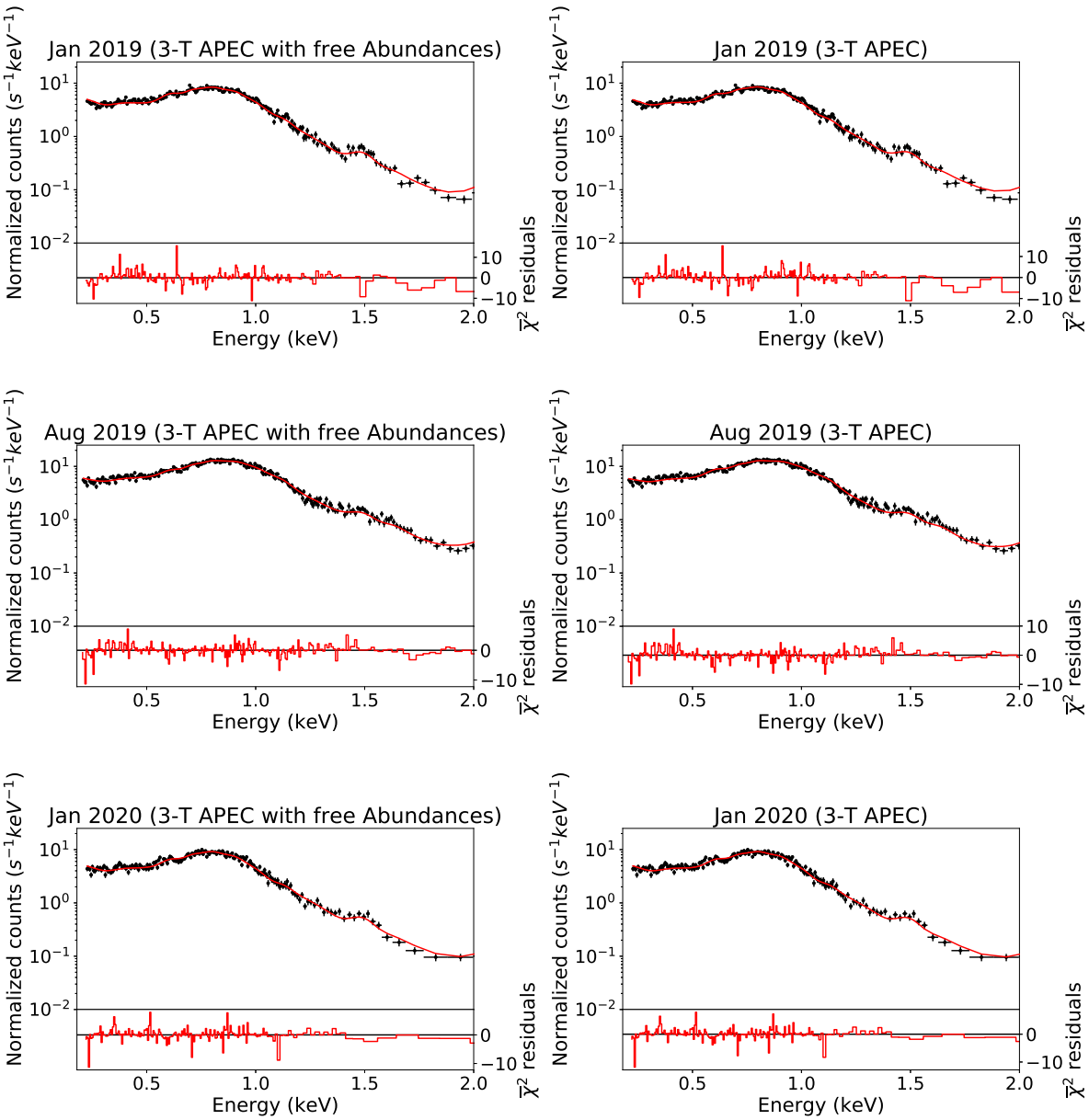

Figure C 1: (continued)

ID Obs.	Abundances $[Z_\odot]$	kT_1 [keV]	kT_2 [keV]	kT_3 [keV]	$logEM_1$ [cm^{-3}]	$logEM_2$ [cm^{-3}]	$logEM_3$ [cm^{-3}]	F_X 10^{-11}[erg/cm^2/s]	$\overline{\chi}^2$	d.o.f.
0112880501	0.21 ± 0.02	0.19 ± 0.04	0.34 ± 0.04	0.72 ± 0.02	50.78 ± 0.08	50.88 ± 0.08	50.69 ± 0.03	1.27 ± 0.01	1.04	247
0748010101	0.22 ± 0.04	0.17 ± 0.06	0.34 ± 0.06	0.76 ± 0.05	50.69 ± 0.10	50.88 ± 0.08	50.49 ± 0.04	1.08 ± 0.01	0.86	191
0760490301	0.30 ± 0.05	0.15 ± 0.03	0.34 ± 0.03	0.77 ± 0.04	50.81 ± 0.07	51.01 ± 0.06	50.61 ± 0.03	1.74 ± 0.02	1.16	227
0760490401	0.29 ± 0.05	0.16 ± 0.05	0.33 ± 0.04	0.74 ± 0.03	50.79 ± 0.08	51.01 ± 0.06	50.58 ± 0.03	1.68 ± 0.02	1.16	215
0780240101	0.25 ± 0.02	0.20 ± 0.04	0.36 ± 0.08	0.78 ± 0.03	50.90 ± 0.09	50.89 ± 0.11	50.89 ± 0.05	1.92 ± 0.01	1.21	248
0780240201	0.26 ± 0.04	0.21 ± 0.07	0.34 ± 0.07	0.71 ± 0.03	50.83 ± 0.16	50.80 ± 0.19	50.70 ± 0.04	1.46 ± 0.02	1.03	206
0801160301	0.29 ± 0.05	0.15 ± 0.04	0.32 ± 0.04	0.72 ± 0.04	50.69 ± 0.09	50.96 ± 0.06	50.48 ± 0.03	1.40 ± 0.01	1.23	215
0801160401	0.25 ± 0.02	0.22 ± 0.03	0.36 ± 0.09	0.76 ± 0.03	50.94 ± 0.11	50.89 ± 0.13	50.89 ± 0.06	1.97 ± 0.02	0.96	231
0820070201	0.30 ± 0.02	0.17 ± 0.03	0.34 ± 0.01	0.79 ± 0.01	50.70 ± 0.05	51.04 ± 0.04	50.85 ± 0.02	2.08 ± 0.01	1.83	295
0820070301	0.39 ± 0.08	0.12 ± 0.02	0.31 ± 0.02	0.73 ± 0.03	50.71 ± 0.07	50.83 ± 0.08	50.25 ± 0.03	1.27 ± 0.01	1.37	214
0843450301	0.24 ± 0.02	0.21 ± 0.03	0.43 ± 0.10	0.85 ± 0.03	50.91 ± 0.06	50.85 ± 0.10	50.88 ± 0.06	1.85 ± 0.02	0.96	242
0843450401	0.27 ± 0.07	0.15 ± 0.06	0.32 ± 0.04	0.68 ± 0.05	50.64 ± 0.12	50.99 ± 0.08	50.35 ± 0.03	1.27 ± 0.02	0.95	186

Table C 1: Best-fitting parameters of a 3-T APEC model and global abundances that are free to vary during the procedure, obtained from fitting each individual observation of ε Eridani. The uncertainties of the temperatures and of the fluxes are calculated directly with *xspec* through the command *error*, whereas the errors on the emission measures are calculated with the error propagation. The fluxes are calculated over the soft energy band of *XMM-Newton*, i.e. $0.2 - 2.$keV.

ID Obs.	kT_1 [keV]	kT_2 [keV]	kT_3 [keV]	$logEM_1$ [cm^{-3}]	$logEM_2$ [cm^{-3}]	$logEM_3$ [cm^{-3}]	F_X 10^{-11}[erg/cm^2/s]	$\overline{\chi}^2$	d.o.f.
0112880501	0.15 ± 0.01	0.33 ± 0.02	0.75 ± 0.02	50.70 ± 0.06	50.83 ± 0.04	50.55 ± 0.04	1.29 ± 0.01	1.02	248
0748010101	0.15 ± 0.02	0.33 ± 0.03	0.78 ± 0.05	50.65 ± 0.09	50.81 ± 0.06	50.39 ± 0.08	1.10 ± 0.03	0.81	192
0760490301	0.15 ± 0.02	0.34 ± 0.02	0.77 ± 0.04	50.81 ± 0.05	51.01 ± 0.04	50.60 ± 0.05	1.74 ± 0.02	1.08	228
0760490401	0.16 ± 0.02	0.33 ± 0.02	0.74 ± 0.04	50.78 ± 0.08	51.00 ± 0.04	50.57 ± 0.06	1.69 ± 0.02	1.00	216
0780240101	0.19 ± 0.02	0.36 ± 0.03	0.79 ± 0.03	50.85 ± 0.08	50.87 ± 0.10	50.83 ± 0.04	1.92 ± 0.02	1.00	249
0780240201	0.19 ± 0.03	0.33 ± 0.04	0.73 ± 0.03	50.73 ± 0.12	50.83 ± 0.13	50.64 ± 0.05	1.47 ± 0.02	0.95	207
0801160301	0.15 ± 0.02	0.32 ± 0.02	0.72 ± 0.04	50.68 ± 0.08	50.95 ± 0.04	50.47 ± 0.06	1.40 ± 0.01	1.17	216
0801160401	0.21 ± 0.02	0.36 ± 0.08	0.78 ± 0.03	50.89 ± 0.17	50.85 ± 0.20	50.83 ± 0.05	1.97 ± 0.02	0.90	232
0820070201	0.17 ± 0.01	0.34 ± 0.01	0.79 ± 0.01	50.70 ± 0.05	51.03 ± 0.04	50.85 ± 0.02	2.08 ± 0.01	1.60	296
0820070301	0.13 ± 0.01	0.31 ± 0.01	0.71 ± 0.03	50.70 ± 0.09	50.93 ± 0.06	50.34 ± 0.06	1.25 ± 0.02	1.369	215
0843450301	0.21 ± 0.02	0.43 ± 0.05	0.87 ± 0.05	50.87 ± 0.05	50.80 ± 0.05	50.81 ± 0.07	1.85 ± 0.08	1.02	243
0843450401	0.14 ± 0.02	0.31 ± 0.02	0.68 ± 0.03	50.64 ± 0.11	50.96 ± 0.05	50.34 ± 0.08	1.28 ± 0.03	0.95	187

Table C 2: Best-fitting parameters of a 3-T APEC model and the global abundances that are kept frozen on $0.3 Z_\odot$, obtained from fitting each individual observation of ε Eridani. The uncertainties are calculated as in Table C 1. The fluxes are calculated over the soft energy band of *XMM-Newton*, i.e. $0.2 - 2$.keV.

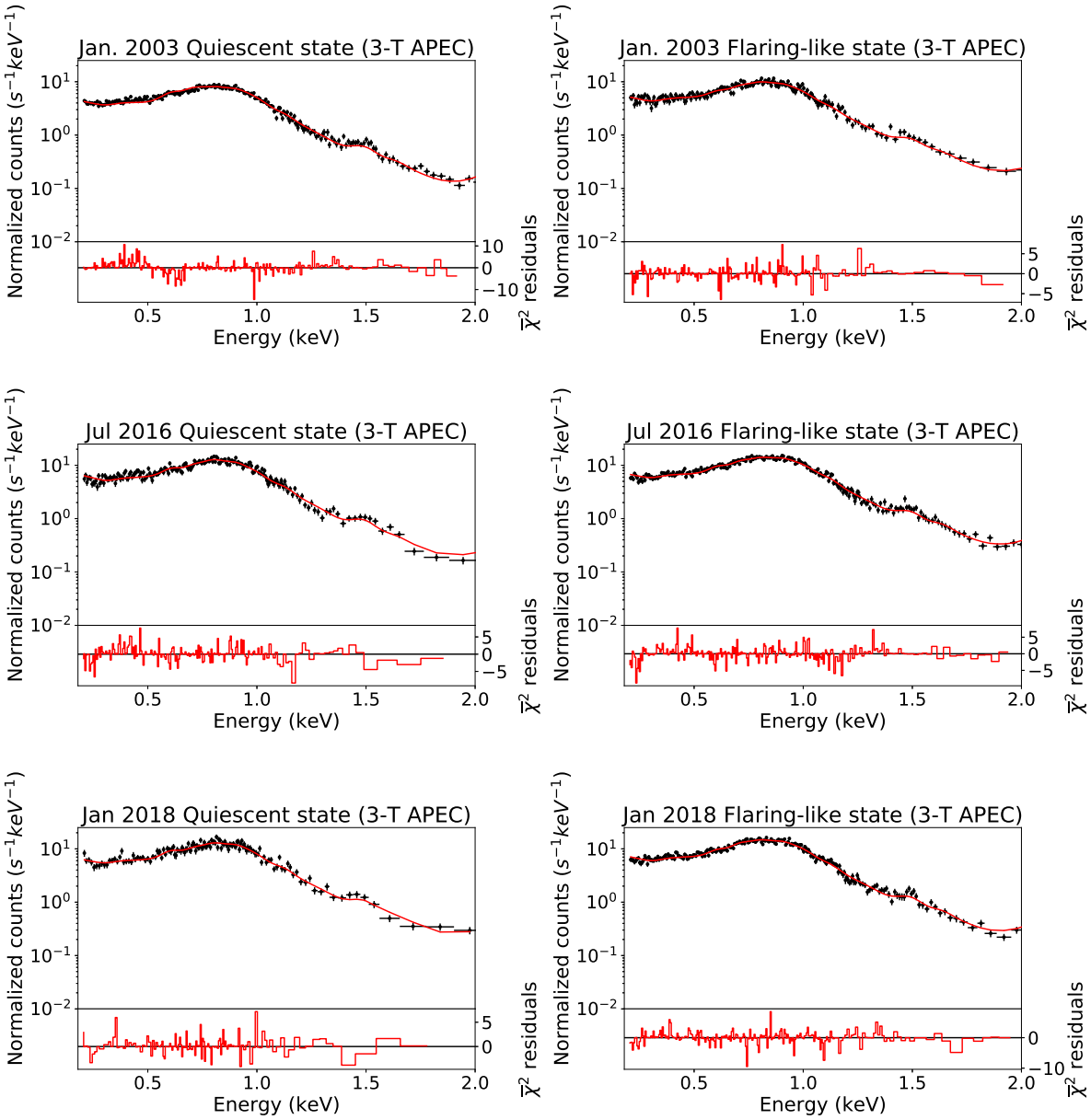

Figure C 2: Spectra of those observations of ε Eridani that show variability in the short-term lightcurves. The spectra on the left are those extracted from a quiescent state of the observation, while on the right there are the spectra extracted in the flaring-like state. The spectra are all fitted with a 3-T APEC model, keeping the abundances frozen on $0.3Z_{\odot}$ during the procedure. The spectral model is overplotted with the solid red line. The bottom panels show the reduced χ^2 residuals of the fitting procedures.

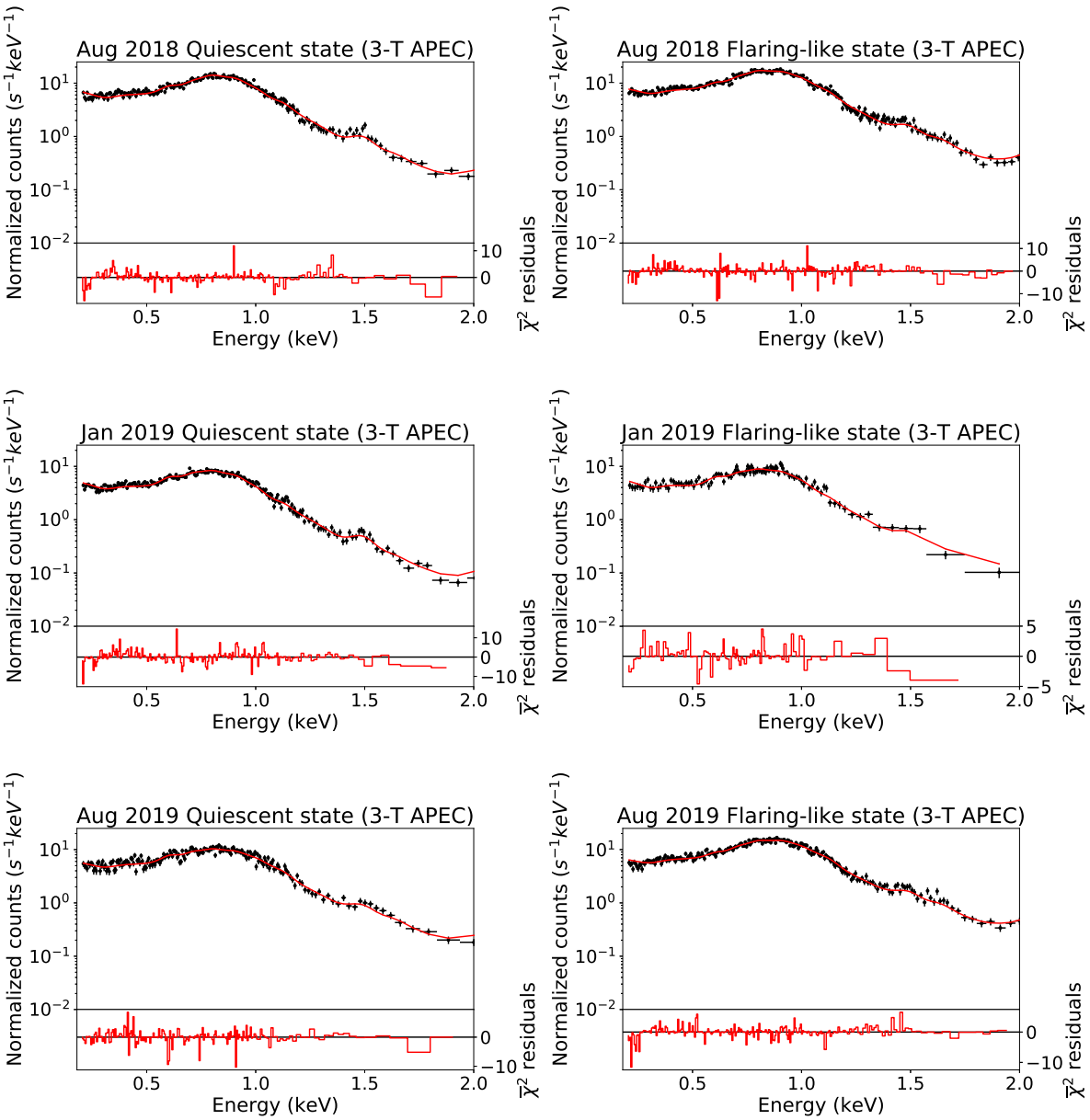

Figure C 2: (continued)

ID Obs.	F_X $10^{11} erg/cm^2/s$		kT_1 [keV]		kT_2 [keV]		kT_3 [keV]	
	Quiescent	Flaring	Quiescent	Flaring	Quiescent	Flaring	Quiescent	Flaring
0112880501	1.23 ± 0.01	1.47 ± 0.02	0.15 ± 0.01	0.15 ± 0.03	0.33 ± 0.02	0.32 ± 0.03	0.74 ± 0.03	0.78 ± 0.04
0780240101	1.76 ± 0.03	2.03 ± 0.02	0.16 ± 0.02	0.21 ± 0.02	0.34 ± 0.03	0.39 ± 0.05	0.75 ± 0.04	0.81 ± 0.03
0801160301	1.80 ± 0.04	2.05 ± 0.02	0.20 ± 0.04	0.22 ± 0.02	0.49 ± 0.17	0.34 ± 0.03	0.84 ± 0.52	0.77 ± 0.03
0820070201	1.86 ± 0.02	2.37 ± 0.02	0.16 ± 0.02	0.17 ± 0.02	0.34 ± 0.02	0.34 ± 0.01	0.74 ± 0.03	0.80 ± 0.02
0820070301	1.20 ± 0.01	1.33 ± 0.03	0.15 ± 0.02	0.12 ± 0.05	0.31 ± 0.01	0.30 ± 0.06	0.70 ± 0.03	0.72 ± 0.08
0843450301	1.56 ± 0.03	2.08 ± 0.02	0.18 ± 0.04	0.22 ± 0.02	0.35 ± 0.05	0.47 ± 0.06	0.84 ± 0.05	0.88 ± 0.04
ID Obs.	$LogEM_1$ $[cm^{-3}]$		$LogEM_2$ $[cm^{-3}]$		$LogEM_3$ $[cm^{-3}]$		$\overline{\chi}^2$	
	Quiescent	Flaring	Quiescent	Flaring	Quiescent	Flaring	Quiescent	Flaring
0112880501	50.70 ± 0.07	50.65 ± 0.16	50.82 ± 0.05	50.88 ± 0.08	50.49 ± 0.05	50.68 ± 0.08	1.10	0.81
0780240101	50.80 ± 0.08	50.93 ± 0.12	50.97 ± 0.10	50.79 ± 0.16	50.69 ± 0.07	50.88 ± 0.11	1.00	1.01
0801160301	50.97 ± 0.06	50.89 ± 0.19	50.86 ± 0.22	50.85 ± 0.20	50.55 ± 0.31	50.87 ± 0.05	0.75	0.97
0820070201	50.75 ± 0.07	50.73 ± 0.08	51.03 ± 0.05	51.05 ± 0.06	50.69 ± 0.06	50.96 ± 0.04	0.98	1.13
0820070301	50.63 ± 0.08	50.67 ± 0.27	50.91 ± 0.04	50.90 ± 0.09	50.31 ± 0.07	50.57 ± 0.13	1.44	0.76
0843450301	50.77 ± 0.16	50.87 ± 0.06	50.87 ± 0.16	50.84 ± 0.06	50.65 ± 0.07	50.89 ± 0.04	1.00	0.87

Table C 3: Best-fitting parameters obtained with a 3-T APEC model for observations with short-term variability. For each parameter the values for the quiescent spectrum and the flaring spectrum are shown. The uncertainties are calculated as in Table C 1. The fluxes are calculated over the soft energy band of *XMM-Newton*, i.e. $0.2 - 2.\text{keV}$.

D

Contour plots for X-ray spectral parameters of Kepler 63

Here, the contour plots of the best-fitting values retrieved from the fitting procedures of the EPIC/pn spectra of Kepler 63 are shown. The fitting procedures applied to these observations are explained in subsection 8.2.2.

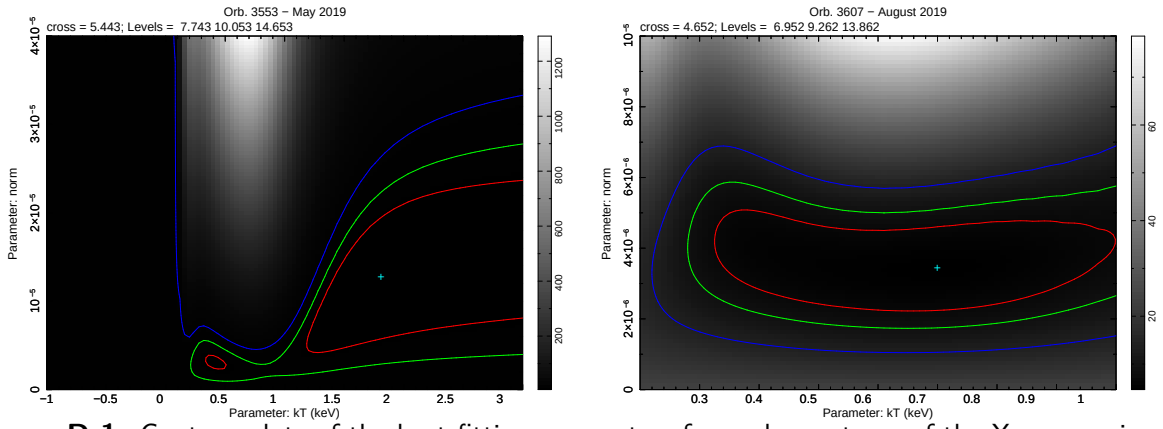

Figure D 1: Contour plots of the best-fitting parameters for each spectrum of the X-ray monitoring campaign in 2019-2020 of Kepler 63: the red contour is the 1σ confidence level; the green one the 2σ; the blue one the 3σ. The fitting procedure applied to each observation uses the 1-T APEC spectral model with metal abundances kept frozen during the fit. The results of these fits are reported in Table 8.2.3.

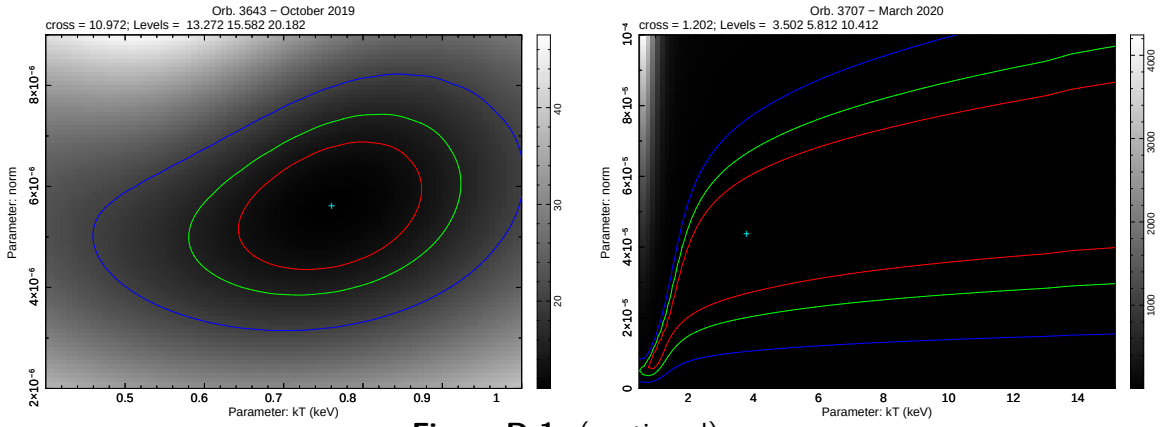

Figure D 1: (continued)

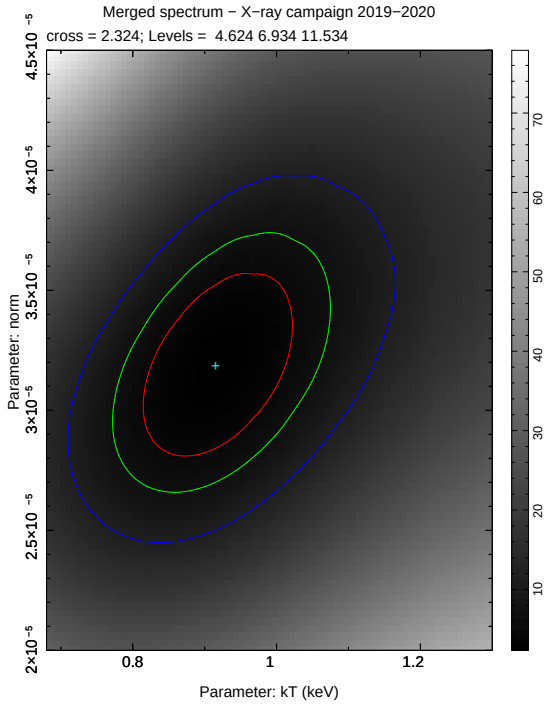

Figure D 2: Contour plots of the best-fitting parameters of the merged spectrum obtained from the 2019-2020 observing campaign of Kepler 63. The color coding of the plot is the same of Figure D 1. The results of this fit are reported in Table 8.2.4.

Acknowledgments

These last three years were fruitful and challenging for my career and my formation and I am proud to have accomplished another important step in my life: a PhD degree. However, I would not be able to arrive here without the help of many wonderful people. Thus, a heartfelt thanks is in order.

First, I want to thank my supervisor Prof. Dr. Beate Stelzer from whom I learnt a lot in these last three years. She also assembled a wonderful working group composed of people who supported me in any regards. In particular, I thank Stefanie, who helped me going through some chapters of this thesis, and Enza, who psychologically supported me while I was writing this manuscript. I also found an amazing and wonderful friend in Enza, and not only a co-worker.

A big thanks goes also to Prof. Dr. Andrea Santangelo for welcoming me in Tübingen many years ago.

I thank all my colleagues at the Institute für Astronomie und Astrophysik in Tübingen, who between a coffee break and another have made our institute not only a stimulating workplace but also a happy environment where to go everyday. In particular, I thank Jörg who always helped me when the German bureaucracy was not easy for me to understand; Alejandro and Samu, who were always able to make me laugh even in the bad days; Manfredi who was always able to make the day a better one with his jokes.

During my PhD, I also had the opportunity of working with other people from other institutes. Thus, I want to thank the Osservatorio Astronomico di Palermo and in the specific Dr. Salvatore Orlando for welcoming me in his working group even if for a short time. Moreover, I want to thank Dr. Jorge Sanz-Forcada with whom I worked in Madrid.

I want also to thank all my friends outside the working environment. Giulia, Gabriele, Carlo, Nadia, Francesco and Stefano followed my path from the very beginning to the very end and I appreciated always their unconditional support. I also met many other amazing people, as Paolo, Annalisa and Irene, who deserve a thanks for being there and cheer me up in these last years.

Last but not least, a big thanks goes to my incredible family, my mother and my sister. My work brought me far away from them, but they have been with me in every moment and they have given me a lot of support.